CORA Cork Open Research Archive
Cartlann Taighde Oscailte Chorcaí

Title	The design of curved optical waveguides : analytical and numerical analysis
Authors	Sheehan, Robert N.
Publication date	2013
Original Citation	Sheehan, R. N. 2013. The design of curved optical waveguides : analytical and numerical analysis. PhD Thesis, University College Cork.
Type of publication	Doctoral thesis
Rights	© 2013, Robert N. Sheehan - http://creativecommons.org/licenses/by-nc-nd/3.0/
Download date	2026-10-27 20:14:21
Item downloaded from	https://hdl.handle.net/10468/1377



UCC
University College Cork, Ireland
Coláiste na hOllscoile Corcaigh

The Design of Curved Optical Waveguides

Analytical and Numerical Analysis

Robert Noel Sheehan

BSc



NATIONAL UNIVERSITY OF IRELAND, CORK

Faculty of Science

Department of Physics

Integrated Photonics Group

Thesis submitted for the degree of
Doctor of Philosophy

14 - 8 - 2013

Supervisor: Dr. Frank Hudson Peters

Head of Department: Prof. John McInerney

Research supported by The Centre for Telecommunications Research (CTVR)

I, Robert Noel Sheehan, certify that this thesis is my own work and I have not obtained a degree in this university or elsewhere on the basis of the work submitted in this thesis.

Robert Noel Sheehan

Contents

Acknowledgements v
List of Publications vi
List of Acronyms vii
List of Symbols viii
Abstract x
Introduction xi

1 The Physics of Curved Optical Waveguides 1
1.1 Introduction 1
1.2 Modal Analysis for Optical Waveguides 5
1.2.1 One-dimensional straight slab waveguide 8
1.2.2 One-dimensional curved slab waveguides 12
1.2.3 Analytical estimates for curved waveguide loss 15
1.3 Conformal Mapping Approach to Curved Optical Waveguides 16
1.4 Discussion 21

2 Waveguide Mode Calculation 22
2.1 Introduction 22
2.2 Rayleigh-Ritz Finite Element Method 23
2.3 FEM for Two-Dimensional Waveguides 24
2.3.1 Planar elements in two-dimensions 25
2.3.2 Elemental matrices in two-dimensions 27
2.3.3 Global matrices in two-dimensions 29
2.3.4 The generalised eigenvalue problem 30
2.4 SFEM_Modes: An object oriented waveguide mode solver 31
2.4.1 Mesh generation 31
2.4.2 Numerical analysis 35
2.5 Testing SFEM_Modes 36
2.5.1 Comparison of 1D analytical and 1D numerical 36
2.5.2 Propagation constant convergence 38
2.5.3 Straight waveguides modes and propagation constants 48
2.6 Discussion 55

3 Optical Wave Propagation 56
3.1 Introduction 56
3.2 Galerkin Finite Element Method 57
3.3 FE-BPM for Three-Dimensional Waveguides 58
3.3.1 Application of the Padé approximation technique 60
3.3.2 Numerical integration of the propagation equation 61
3.3.3 Updating the propagation constant 62
3.4 Boundary Conditions for Beam Propagation 63
3.4.1 Transparent boundaries 64
3.4.2 Perfectly matched layers 65
3.5 SFEM_Propagation: An object oriented waveguide mode propagator 67
3.5.1 The propagation algorithm 67

3.6 Testing SFEM_Propagation . . . 69
3.6.1 Free-Space simulations in two-dimensions . . . 69
3.6.2 Gaussian beam propagation in a rib waveguide . . . 78
3.7 Discussion . . . 83

4 The Design of Optical Waveguide Bends **84**
4.1 Introduction . . . 84
4.2 Techniques for the Reduction of Losses in Waveguide Bends . . . 85
4.3 Curvature Based Bend Construction . . . 89
4.3.1 Constant curvature bends . . . 90
4.3.2 Linear curvature bends . . . 91
4.3.3 Trapezoidal curvature bends . . . 94
4.3.4 Mode optimised bends . . . 98
4.3.5 A bend construction algorithm . . . 100
4.3.6 Application of the bend construction algorithm . . . 102
4.4 Discussion . . . 108

5 Results **109**
5.1 Introduction . . . 109
5.2 Curved Waveguide Modes and Propagation Constants . . . 109
5.3 Mode Optimised Bend Construction . . . 113
5.4 Comparison of the Bend Design Schemes . . . 114
5.4.1 Shallow etch waveguides . . . 116
5.4.2 Deep etch waveguides . . . 121
5.5 Discussion . . . 128

6 Conclusions and Future Work **129**
6.1 Conclusions . . . 129
6.2 Future Work . . . 130

A Complex Analysis **132**
A.1 Complex valued functions and their derivatives . . . 132
A.2 Proof of the conformal mapping theorem . . . 134

B The Variational Principle **136**
B.1 Proof of the variational principle . . . 136

C Sparse Matrix Manipulation **138**
C.1 Row-indexed Sparse Storage Mode . . . 138
C.2 Testing the objects . . . 140
C.3 Discussion . . . 141

D Algorithms **142**

Bibliography **159**

"Enter ye in at the narrow gate: for
wide is the gate and broad is the way
that leadeth to destruction, and many
there are who go in thereat.
How narrow is the gate, and strait
is the way that leadeth to life: and few
there are that find it!"
Matthew 7: 13 - 14

Tiomnaithe do chuimhne Eibhlís Ní Laoire

Acknowledgements

Firstly, I would like to thank my supervisor Dr. Frank Peters for his support, guidance and friendship over the years. Frank has been a constant source of help and encouragement in matters both physical and spiritual. I look forward to many more debates, both heated and cordial, in the future.

I also want to thank past and present members of the Integrated Photonics Group and the III-V Materials and Devices Group for their help and suggestions. Specifically, special thanks are due to Brian Corbett, Brendan Roycroft and James O'Callaghan for giving me advice and the benefit of their expertise.

I would like to thank my neighbour, David Goulding, for encouraging me to study Physics in the first place and for his helpful comments and suggestions regarding this manuscript during its preparation.

I would like to thank the Centre for Telecommunications Research for their generous financial support.

In my time at UCC I've made many friends and they have all made me a better person. Thank you Dan Hurley, Chris Daunt, Rory Conboye, Patrick Tuite, Brian O'Sullivan, Eddie Cotter, Padraic Morrissey, Niall Kelly and Owen McConnell. Our conversations over tea, or pints of Murphy's, have always been enjoyable in the most enlightening and entertaining of ways. I look forward to many more conversations in the future.

I want to especially thank my family for everything they have done for me over the years. My mam and dad, Alice and Paul, my brother and sister, Trevor and Aishling, have always been there for me; encouraging me to write and supporting me whenever I needed help. Thank you for everything. I would also like to thank Harry, Patty and Becky Cummins for all their help over the years.

I want to thank the Lord, Our God, for granting me the strength and the ability to bring this work to its conclusion.

Finally, I would like to thank my fianceé Tracey. Your support, understanding and encouragement has given me the strength to persevere through the difficult days. Your constant love has helped me through the bad nights to see the better days ahead. There are no words to express my gratitude to you for all you've done. Thank you.

Robert Sheehan
30 - 7 - 2013

List of Publications

- P. E. Morrissey, D. Goulding, R. Sheehan, B. Roycroft and F. H. Peters, "Experimental Technique for Quick and Efficient Lensed Fiber to Ridge Waveguide Coupling", IET Optoelectronics, 7(2), 2013.
- R. N. Sheehan and F. H. Peters, "Low-Loss Curved Optical Waveguide Design for Integrated Photonics", Proc. Photonics Ireland, Cork, September, 2009.
- R. N. Sheehan, S. Horne and F. H. Peters, "The Design of Low-Loss Curved Waveguides", Optical and Quantum Electronics, 40, 1211-1218, 2009.
- R. N. Sheehan and F. H. Peters, "The Design of Continuous Curvature Waveguides", Proc. 8^{th} International Conference on Numerical Simulation of Optoelectronic Devices, Nottingham, England, September, 2008.
- R. Sheehan and F. Peters, "Curvature Based Optimisation of Waveguide Bends for Integrated Photonics", Proc. Photonics Ireland, Galway, September, 2007.

List of Acronyms

Acronym	Explanation
CTVR	Centre for Telecommunications Research
TE	Transverse Electric
TM	Transverse Magnetic
EIM	Effective Index Method
FDM	Finite Difference Method
FEM	Finite Element Method
MOL	Method of Lines
EEM	Eigenmode Expansion Method
BPM	Beam Propagation Method
FDTD	Finite Difference Time Domain
FE-BPM	Finite Element-Beam Propagation Method
ABC	Absorbing Boundary Condition
TBC	Transparent Boundary Condition
PML-BC	Perfectly Matched Layer-Boundary Condition
BCGM	Bi-Conjugate Gradient Method
PIC	Photonic Integrated Circuit
SOI	Silicon-On-Insulator
AWG	Arrayed Waveguide Grating
CC	Constant Curvature
LC	Linear Curvature
TC	Trapezoidal Curvature
RISSM	Row Indexed Sparse Storage Mode

List of Symbols

Symbol	Explanation
κ	Curvature
L_T	Transition Loss
L_b	Bending loss
α	Power attenuation coefficient / Imaginary part of propagation constant
$\mathbf{E}$	Electric field vector
$\mathbf{H}$	Magnetic field vector
$\mathbf{D}$	Electric flux density
$\mathbf{B}$	Magnetic flux density
$\mathbf{J}$	Current density
ϵ	Electrical permittivity
ϵ_r	Relative permittivity
μ	Magnetic permeability
μ_r	Relative permeability
ρ	Charge density
σ_e	Electrical conductivity
σ_m	Magnetic conductivity
n	Refractive index
n_{eff}	Effective refractive index
k_0	Wavenumber
λ	Wavelength
ω	Angular frequency
ϕ	A component of the electromagnetic field
ψ	Phase of a wave in a slab waveguide
A	Normalisation constant for the slab waveguide
β	Real part of the propagation constant
h, p, q	Wavenumber components of the slab waveguide
P, Q	Polarisation dependent coefficients of the governing equations

Symbol	**Explanation**
$\hat{r}$, $\hat{x}$, $\hat{z}$, $\hat{\theta}$ etc.	Variables to indicate coordinate axis directions
γ	Complex propagation constant
$\zeta = x + i\,z$	Complex number in the $(x,\, z)$ plane
Ω	Region in space over which a solution is computed
$\partial\,\Omega$	Boundary of the region in space over which a solution is computed
Γ	Curvature dependent term in the governing equations
$\mathfrak{L}$	Operator representation of a differential equation
$\delta\,F$	Variational of the functional F
N_j^e	Basis function at the j^{th} node of the e^{th} element in a 2D mesh
a^e, b^e, c^e	Interpolation coefficients for the 2D mesh
Δ^e	Area of the e^{th} element of a 2D mesh
l_e	Length of the e^{th} element of a 1D mesh
s	PML parameter
$\phi(s)$	Bending angle as a function of pathlength
L_{cc}	Length of a CC bend
L_{lc}	Length of an LC bend
L_{tc}	Length of a TC bend
α_l	Slope of the LC curvature profile
α_t	Slope of the TC curvature profile
σ	Length of the linear portion of a TC bend
f	Fraction of a TC bend that has linear curvature

Abstract

A model for understanding the formation and propagation of modes in curved optical waveguides is developed. A numerical method for the calculation of curved waveguide mode profiles and propagation constants in two dimensional waveguides is developed, implemented and tested. A numerical method for the analysis of propagation of modes in three dimensional curved optical waveguides is developed, implemented and tested. A technique for the design of curved waveguides with reduced transition loss is presented. A scheme for drawing these new waveguides and ensuring that they have constant width is also provided. Claims about the waveguide design technique are substantiated through numerical simulations.

Introduction

Motivation:

Given that today's photonic systems require more power to handle increasing traffic, using devices with higher functionality and lower footprint, there is a strong emphasis on reducing the size of photonic integrated circuits while maintaining, or increasing, functionality at reduced cost [1–4]. One possible method for reducing the size of photonic integrated circuits is to use curved waveguides to connect devices on chip, this allows for more compact system design. One technique for achieving footprint reduction is to reduce the bend radius of curved waveguides connecting two devices, this increases the waveguide curvature. Increased curvature can lead to an increase in optical losses, so there is a need for curved waveguide designs that can have high curvature while exhibiting low losses. These new low loss bends can then be employed as components of devices, such as arrayed waveguide gratings, echelle gratings, s-bends, in photonic integrated circuits whose overall size can be reduced.

To enable a low loss curved waveguide to be designed, the mode properties of curved waveguides must be understood. The interaction of modes from straight and curved waveguides is one of the causes of loss in curved waveguides. Another source of loss is that which occurs while a wave is propagating in a device. The aim of this thesis is to design a curved waveguide that allows for a reduction in certain aspects of the total loss associated with curved waveguides. In designing these low loss bends the total size of a device can be reduced because a bend with a lower radius of curvature can be used.

The design of these new waveguide bends is accomplished by application of analytical and numerical design techniques. The resulting design schemes are simple to implement, require no extra fabrication steps and ensure a reduction in the total loss associated with a waveguide bend.

Thesis Outline:

This thesis comprises five chapters. Chapter 1 describes the background theory necessary for understanding optical waveguides. The effects of waveguide curvature on mode properties are described. The mechanisms that induce loss in curved waveguides are introduced. The model currently used to explore curved waveguides is presented and extended from two to three spatial dimensions. The extension of the curved waveguide model produces a partial differential equation whose solution describes the mode behaviour in curved optical waveguides.

The technique used to compute the mode solutions in curved optical waveguides is presented in Chapter 2. The finite element method is applied to the extended curved waveguide model so that the mode profiles and propagation constants of curved waveguides can be calculated numerically. An implementation of an object oriented code that can compute the required solutions is discussed.

Chapter 3 presents the details necessary for understanding the propagation of modes in curved optical waveguides. Absorbing boundary conditions, i.e. perfectly matched layer boundary conditions, are used in conjunction with finite element beam propagation method to step a mode through a waveguide. A custom computer code is written to realise this. With this tool it will be possible to characterise the loss associated with curved optical waveguides.

Chapter 4 applies the knowledge developed in Chapters 1 - 3 to design a new type of curved

optical waveguide. The techniques currently being used to design curved waveguides are presented. Then, by application of a known technique, a new type of curved waveguide bend is designed. It will be seen that this new bend type will ensure a reduction in total losses associated with a curved waveguide via a reduction in what is known as mode transition loss. The method used to design the new waveguides are presented in detail.

Over the course of this thesis a series of tools were developed to help in the understanding of the curved waveguide problem, see Section 2.4 in Chapter 2 and Section 3.5 in Chapter 3. In Chapter 5 the results of the application of these new tools to the curved waveguide problem are presented. It will be seen that the new waveguide bend design technique, see Section 4.3 of Chapter 4, does in fact result in a waveguide in which the light propagates with lower loss. These results are arrived at through a study of the propagation of light in curved waveguide structures enabled by the computer code written as part of this thesis.

Appendix A contains a detailed discussion of a result from the theory of complex variables that underpins the extended curved waveguide model described in Section 1.3. Appendix B contains a discussion of the variational principle that is the foundation of the theory of the finite element method when it used to compute mode profiles, see Section 2.3, and enable propagation calculations, see Section 3.3. Appendix C contains a description of a data structure that is used to ensure certain numerical operations are completed in a timely fashion. Lastly, Appendix D contains the algorithms used to perform certain tasks inside the computer programs that were written as part of this thesis.

Throughout this thesis light is assumed to have a wavelength of $\lambda = 1.55\,(\mu\text{m})$ unless otherwise stated. Quoted refractive index values are also specified at this wavelength.

Chapter 1

The Physics of Curved Optical Waveguides

Summary: *An outline of the theory necessary for understanding optical waveguide modes is presented. The loss mechanisms associated with curved waveguides are presented. The curved slab waveguide model is extended to three dimensions using the conformal mapping technique.*

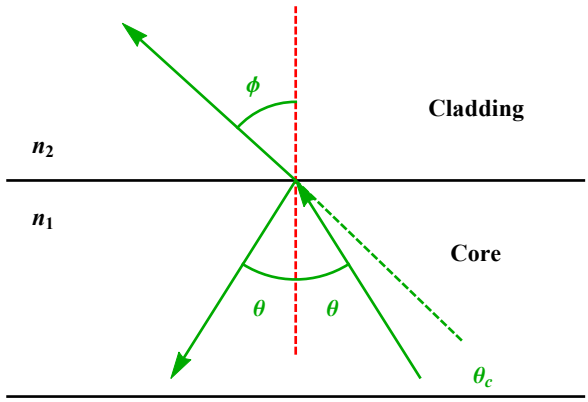
1.1 Introduction

An optical waveguide is a region of high refractive index material, called a core, surrounded by a region of lower refractive index, usually referred to as the cladding. The refractive index difference between the core and the cladding enables, under certain circumstances, light to be confined inside the core and from there to propagate in the high index region. The conditions under which light is confined are determined by the material properties of the dielectrics, the wavelength of the light, and the cross section geometry of the waveguide. The mechanism by which light is confined is known as total internal reflection [5]. When light, propagating in the core, impinges on a dielectric boundary an amount of the light is reflected and an amount is transmitted into the adjoining medium of lower refractive index, allowing the propagation of a light-wave in that medium, see Figure 1.1(a). For certain propagation angles no light is transmitted from the core into the cladding region, this is known as confinement, see Figure 1.1(b). The critical angle

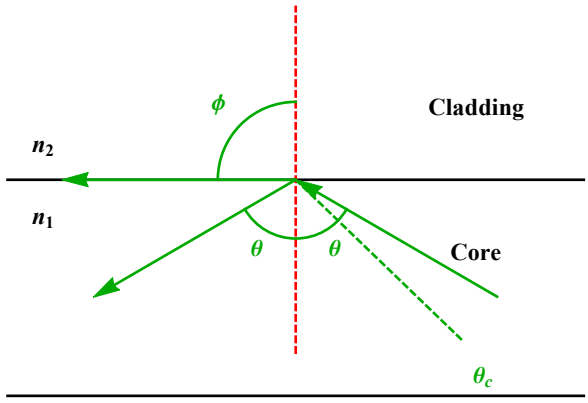
$$\theta_c = \sin^{-1}\left(\frac{n_2}{n_1}\right) \tag{1.1}$$

defines the angle above which total internal reflection will occur.

This ray picture, while providing a basic illustration of the confinement mechanism, is incomplete. The optical waveguide is, in its essence, a resonance chamber with certain "fundamental vibrations", these "fundamental vibrations" are known as the modes of the waveguide. A mode is a type of wave that can propagate in the waveguide once it has been excited. It has a distinct shape and propagation constant. The mode propagation constant is a number that defines the phase velocity of the mode in the waveguide through $v_p = \omega/\beta$, for a wave with angular frequency ω and propagation constant β. Understanding how waveguide modes behave is critical for the design of photonic devices.



(a) Internal reflection

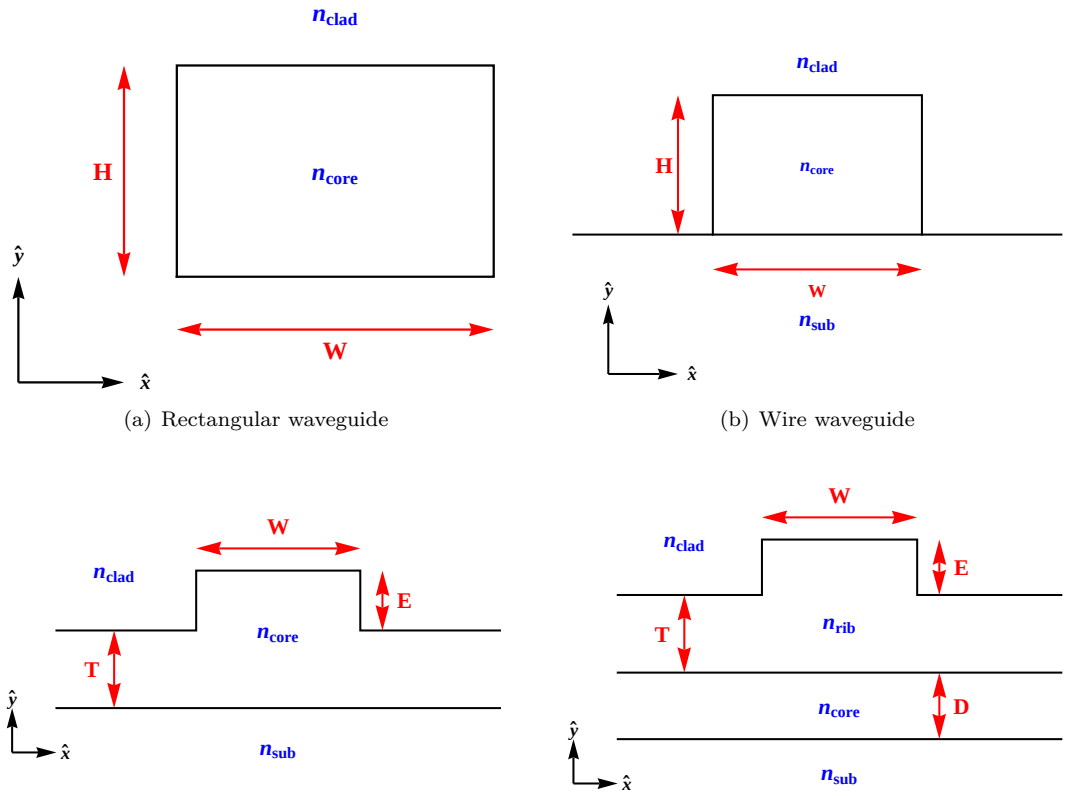


(b) Total internal reflection

Figure 1.1: Ray diagrams illustrating reflection and refraction at a dielectric boundary where $n_1 > n_2$.

The cross-sectional geometry of the waveguide, the material properties and the wavelength of the light determine the shape and number of bound state modes that can propagate in a waveguide, some common waveguide structures are presented in Figures 1.2(a) - 1.2(d). Another factor that can affect a waveguide's behaviour is its curvature, κ, along the axis of propagation. If a waveguide has zero curvature along its axis of propagation then it is a straight waveguide and its behaviour and properties are already well understood [6–9]. However, when the waveguide curvature becomes non-zero the behaviour of the light inside the waveguide is changed. It becomes more difficult to confine the light because the non-zero curvature means that more light can escape through the curved boundaries of the waveguide walls. This is because the mode is shifted from the centre towards the outer wall of the waveguide. This shift in the mode position is caused by the bending of the waveguide and becomes more pronounced as the curvature increases, as observed in [10, 11]. The curvature of the waveguide also affects the shape of the waveguide mode, the mode is no longer symmetric about a central axis as would be the case in a straight waveguide.

This mode shape difference, or mode mismatch, can be problematic in photonic devices, for example, if a straight waveguide is connected to a curved waveguide the mode from the straight section must convert to the mode in the curved section, this leads to transition loss. Transition



(a) Rectangular waveguide

(b) Wire waveguide

(c) Rib waveguide

(d) Ridge waveguide

Figure 1.2: Common optical waveguide structures

loss is defined as as the power coupling efficiency between the mode in the straight section and the mode in the bent section [12]. Transition loss is computed by the overlap integral method using the formula [12–17]

$$L_T = 10 \log_{10} T \quad \text{(dB)} \tag{1.2}$$

where the overlap integral T is computed from

$$T = \frac{\iint_\Omega \psi_s \psi_b \, d\Omega}{\left(\iint_\Omega \psi_s \psi_s \, d\Omega \iint_\Omega \psi_b \psi_b \, d\Omega \right)^{1/2}} \tag{1.3}$$

In equation (1.3) ψ_s represents the mode from the straight section and ψ_b represents the mode from the bend section. Transition loss reduction techniques are discussed in Chapter 4. The effects of back-reflection are not included in this estimate for transmission loss.

A second loss mechanism that arises is known as pure bending loss [10, 18–28]. As a mode propagates in a straight waveguide its phase front is orthogonal to the direction of propagation. In a waveguide bend the field and phase front must rotate about the centre of curvature of the bend with constant angular velocity. Away from the waveguide bend the phase front curvature starts to increase because the phase velocity must increase if it is to remain in step with the mode profile. Since the phase velocity cannot exceed the speed of light there will be a point at which the phase velocity cannot remain in step with the bend mode, the field in the region beyond this point becomes radiative. The resulting radiation is known as bend loss. This phenomenon is known as electromagnetic tunelling [11,22], the point at which it occurs is known

as a caustic [10]. The amount of energy lost increases with increasing curvature. Bending loss is also dependent on the waveguide materials and geometry, for example a waveguide bend that has a low index contrast will be more lossy than a bend with a high index contrast because less light is confined in a low index contrast bend, similarly rib waveguides, see Figure 1.2(c), with low etch depth will only be able to provide weak confinement for waveguide modes [25]. Numerical methods, such as the finite element method, have been used to show that the bend loss, due to propagation in a curved rib waveguide, can be computed by [16, 17, 29, 30]

$$L_b = 20 \log_{10} e^{\frac{\pi}{2} R \beta_i} \quad (\text{dB}/90^\circ) \tag{1.4}$$

$$= 4.342 \pi R \beta_i \quad (\text{dB}/90^\circ) \tag{1.5}$$

where β_i is the imaginary part of the propagation constant.

Another type of loss mechanism that is frequently cited is the power attenuation coefficient [24]. This is often computed as

$$\Delta P = 10 \log_{10} \left(\frac{P(z)}{P(0)} \right) \quad (\text{dB}) \tag{1.6}$$

where $P(z)$ is the power at some point along the direction of propagation and $P(0)$ is the power in the straight section of the guide. The average power of an an optical wave is computed from the real part of the Poynting vector of the electromagnetic field.

Other sources of loss that occur when dealing with photonic devices include scattering loss and insertion loss. Scattering loss is caused by sidewall roughness. Sidewall roughness is a periodic deformation of an optical waveguide caused by the fabrication process. If the device is carefully made errors due to sidewall roughness and hence scattering loss can be kept to a minimum [14]. Another source of loss in photonic devices is insertion loss, the loss that occurs when attempting to get light into a device. Reduction of insertion loss is a major topic of interest in its own right and will not be given much consideration in this thesis.

Analytical models for the solution of the curved waveguide problem have been proposed. For one-dimensional curved slabs a field matching method, similar to that which is used to analyse the slab waveguide, can be used to determine a dispersion equation whose solution provides the complex propagation constants for the curved waveguide [31]. This technique has the advantage of being quasi-analytical, however, the resulting equation is very difficult to solve numerically because its solution requires the evaluation of Bessel and Hankel functions of very large, complex order [31]. Perturbative techniques have also been used to study the waveguide bend propagation characteristics [16, 32, 33]. These techniques are generally able to re-produce the mode profiles in curved slab waveguides, which will allow for a study of the transition loss, but not able to produce information required to compute the bending loss. Field-matching techniques have been developed for two-dimensional waveguides but apply only to special cases of waveguides, such as rectangular waveguides [19, 30].

A technique that has proven to be very successful when applied to curved waveguides is the conformal mapping approach developed by Heiblum and Harris [34]. This method converts a curved waveguide section into an equivalent straight section using a conformal mapping. The effect of the conformal mapping is to mathematically induce a change in the refractive index profile in the equation whose solution provides the mode shape in the bend, effectively, the refractive index gains a slope that is proportional to the waveguide curvature. The advantage of this approach is that it can be extended from two to three spatial dimensions, without

necessitating a change in coordinates and it also explains many of the radiation features that have been observed from experiments with curved waveguides [10, 11].

In Section 1.2 the physics necessary for understanding optical waveguides is introduced. The solution of the slab waveguide in straight and curved configurations is discussed in Sections 1.2.1 and 1.2.2 respectively. Approximate models for estimating the loss associated with curved waveguides are briefly discussed in Section 1.2.3. This chapter closes by showing how to map the curved waveguide problem onto an equivalent straight waveguide. It will be seen how the transformation of the problem effects the equations involved and how this transformed problem will lead onto the numerical calculation of curved waveguide modes and propagation in curved waveguides.

1.2 Modal Analysis for Optical Waveguides

The behaviour of light inside an optical waveguide is well described by Maxwell's equations [6–9].

$$\nabla \times \mathbf{E} = -\frac{\partial \mathbf{B}}{\partial t} \qquad \nabla \times \mathbf{H} = \mathbf{J} + \frac{\partial \mathbf{D}}{\partial t}$$

$$\nabla \cdot \mathbf{D} = \rho \qquad \nabla \cdot \mathbf{B} = 0$$

$$\mathbf{D} = \epsilon\, \mathbf{E} \qquad \mathbf{B} = \mu\, \mathbf{H}$$

$$\mathbf{J} = \sigma_e\, \mathbf{E} \qquad \nabla \cdot \mathbf{J} + \frac{\partial \rho}{\partial t} = 0$$

The quantities described are the electric field $\mathbf{E}$, magnetic field $\mathbf{H}$, electric flux density $\mathbf{D}$, magnetic flux density $\mathbf{B}$, current density $\mathbf{J}$, electrical permittivity ϵ, magnetic permeability μ, charge density ρ and electrical conductivity σ_e. Active devices are not being considered, so terms describing the distribution of the charge inside a waveguide are neglected. It is also assumed that the refractive index of the waveguide is linear, isotropic and homogenous, this means that the relative electrical permittivity, ϵ_r, can be written as a scalar function of position i.e. $\epsilon_r = \epsilon_r(x, y, z)$. The electrical permittivity, ϵ, is defined as the product of the vacuum permittivity ϵ_0 and the relative permittivity ϵ_r. The magnetic permeability, μ, is similarly defined as the product of the vacuum permeability μ_0 and the relative permeability μ_r. Since magnetic devices are not being considered, we set $\mu_r = 1$ hence $\mu = \mu_0$. Under these assumptions Maxwell's curl and divergence equations reduce to the following [6–9].

$$\nabla \times \mathbf{E} = -\mu_0 \frac{\partial \mathbf{H}}{\partial t} \qquad \nabla \times \mathbf{H} = \epsilon_0\, \epsilon_r \frac{\partial \mathbf{E}}{\partial t} \tag{1.7}$$

$$\nabla \cdot (\epsilon_r\, \mathbf{E}) = 0 \qquad \nabla \cdot \mathbf{H} = 0 \tag{1.8}$$

The refractive index, n, of the material is defined as the ratio of the speed of the wave in vacuo and the speed of the wave in the medium [35]. In a vacuum the speed of an electromagnetic wave is the speed of light, c, defined by $c = (\mu_0\, \epsilon_0)^{-1/2}$. In a material the speed of the wave is reduced by its interaction with the material, this speed is given by $u = (\mu\, \epsilon)^{-1/2}$. The ratio of these speeds is the material refractive index $n = c/u$, substituting for μ and ϵ it is seen that the refractive index is given by $n = \sqrt{\epsilon_r}$ or $\epsilon_r = n^2$ [35].

Waveguide structures commonly used for telecommunication's applications, see Figures 1.2(a) - 1.2(d), support the propagation of waves of a certain polarisation. These were classified by

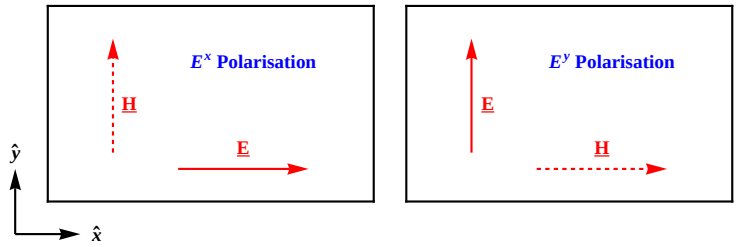


Figure 1.3: The polarisation directions of the electric and magnetic fields for the E^x and E^y polarisations

Marcatilli as the E^x and E^y waves [36,37], also known as the EH and HE waves [8] or hybrid waves [9]. The waves are assumed to have a time-dependence of the form $e^{i\,\omega\,t}$, where ω is the angular frequency of the wave, ω is related to the wavelength λ by the wavenumber k_0, defined as $k_0 = \frac{2\,\pi}{\lambda} = \frac{\omega}{c}$.

The E^x wave has its electric field polarised along the $\hat{\mathbf{x}}$ direction, the wave is dominated by the electric field along the $\hat{\mathbf{x}}$ direction and the magnetic field along the $\hat{\mathbf{y}}$ direction. It has no electric field component along the $\hat{\mathbf{y}}$ direction and only a very weak magnetic field component along the $\hat{\mathbf{z}}$ direction. The electric field of the E^x wave is represented by equation (1.9) and its magnetic field is given by equation (1.10), where it has been assumed that the time-dependence of all field components can be decoupled from the spatial variation.

$$\mathbf{E^x}(\mathbf{r},\,t) = \{E_x(\mathbf{r}),\,0,\,E_z(\mathbf{r})\}\,e^{i\,\omega\,t} \tag{1.9}$$

$$\mathbf{H^x}(\mathbf{r},\,t) = \{H_x(\mathbf{r}),\,H_y(\mathbf{r}),\,H_z(\mathbf{r})\}\,e^{i\,\omega\,t} \tag{1.10}$$

The E^y wave has its electric field polarised along the $\hat{\mathbf{y}}$ direction, the E^y wave is dominated by the x component of the magnetic field and the y component of the electric field. It has no magnetic field along the $\hat{\mathbf{y}}$ direction and a very weak electric field along the $\hat{\mathbf{x}}$ direction. The electric field of the E^y wave is given by equation (1.11) and its magnetic field is given by eqref (1.12), with a decoupled time-dependence. The polarisation directions of the electric and magnetic fields for both polarisations are shown in Figure 1.3.

$$\mathbf{E^y}(\mathbf{r},\,t) = \{E_x(\mathbf{r}),\,E_y(\mathbf{r}),\,E_z(\mathbf{r})\}\,e^{i\,\omega\,t} \tag{1.11}$$

$$\mathbf{H^y}(\mathbf{r},\,t) = \{H_x(\mathbf{r}),\,0,\,H_z(\mathbf{r})\}\,e^{i\,\omega\,t} \tag{1.12}$$

Substitution of equations (1.9) and (1.10) into Maxwell's curl and divergence conditions, (1.7) and (1.8), allows the governing equations for the E^x polarisation to be determined. The components of the E^x polarised field are expressed in E_x because that is assumed to be the dominating

term for that polarisation. The components of the E^x polarised waves are described by

$$\frac{\partial^2 E_x}{\partial x^2} + \frac{\partial^2 E_x}{\partial y^2} + \frac{\partial^2 E_x}{\partial z^2} + k_0^2\, n^2\, E_x = 0 \tag{1.13}$$

$$\frac{\partial E_z}{\partial z} = -\frac{\partial E_x}{\partial x} \tag{1.14}$$

$$H_x = \frac{i}{\omega\,\mu_0}\frac{\partial E_z}{\partial y} \tag{1.15}$$

$$H_y = \frac{i}{\omega\,\mu_0}\left(\frac{\partial E_x}{\partial z} - \frac{\partial E_z}{\partial x}\right) \tag{1.16}$$

$$H_z = -\frac{i}{\omega\,\mu_0}\frac{\partial E_x}{\partial y} \tag{1.17}$$

In a similar manner, substitution of equations (1.11) and (1.12) into the curl equations (1.7) and the divergence condition (1.8) allows the governing equations for the E^y polarisation to be found. The components of the E^y polarised field are expressed in H_x because that is assumed to be the dominating term for that polarisation. The governing equations for the components of the E^y polarised waves are found to be

$$\frac{\partial^2 H_x}{\partial x^2} + \frac{\partial^2 H_x}{\partial y^2} + \frac{\partial^2 H_x}{\partial z^2} + k_0^2\, n^2\, H_x = 0 \tag{1.18}$$

$$\frac{\partial H_z}{\partial z} = -\frac{\partial H_x}{\partial x} \tag{1.19}$$

$$E_x = -\frac{i}{\omega\,\epsilon_0\, n^2}\frac{\partial H_z}{\partial y} \tag{1.20}$$

$$E_y = -\frac{i}{\omega\,\epsilon_0\, n^2}\left(\frac{\partial H_x}{\partial z} - \frac{\partial H_z}{\partial x}\right) \tag{1.21}$$

$$E_z = \frac{i}{\omega\,\epsilon_0\, n^2}\frac{\partial H_x}{\partial y} \tag{1.22}$$

Equations (1.13) - (1.17) and (1.18) - (1.22) describe the behaviour of the electromagnetic field for E^x and E^y polarised waves. These equations form the basis of the analysis required to understand optical waveguides.

In an optical waveguide only waves of a certain shape are allowed to propagate. These waves are known as the normal modes of the waveguide, or simply the waveguide modes. To examine the behaviour of modes in optical waveguides the z-dependence of the fields for the E^x and E^y polarised waves is assumed to be of the form $e^{-i\,\beta\,z}$, where β is the propagation constant of the mode in the waveguide. Taking this dependence into account changes equations (1.13) and (1.18). The E_x component of the E^x polarised wave is described by the solution of equation (1.23) [37, 38].

$$\frac{\partial^2 E_x}{\partial x^2} + \frac{\partial^2 E_x}{\partial y^2} + (k_0^2\, n^2 - \beta^2)\, E_x = 0 \tag{1.23}$$

The H_x component of the E^y wave is described by the solution of equation (1.24) [37, 38].

$$\frac{1}{n^2}\frac{\partial^2 H_x}{\partial x^2} + \frac{1}{n^2}\frac{\partial^2 H_x}{\partial y^2} + \left(k_0^2 - \frac{\beta^2}{n^2}\right) H_x = 0 \tag{1.24}$$

The solutions of equations (1.23) and (1.24) cannot be determined analytically because the value of the mode propagation constant is not known. The mode propagation constant is determined by the waveguide geometry, material parameters, and wavelength of the light in the waveguide. The conditions inside the waveguide restrict the set of allowed values of β for a given optical

waveguide. This is most easily seen by performing an analysis of a one-dimensional waveguide known as a slab waveguide. This analysis is presented in Section 1.2.1.

Semi-analytical approximations to waveguide propagation constants, and the corresponding mode profiles, in two-dimensional waveguides can be obtained for certain geometries using Marcatilli's method [6–9, 35]. A technique known as the effective index method (EIM) can be used to approximate the propagation constants of more complicated geometries [6–9], however, the EIM cannot be used to approximate the shape of an optical mode except in the case of rectangular waveguides. To solve equations (1.23) and (1.24) for arbitrary waveguide cross-section, advanced numerical techniques are required. These numerical techniques are discussed in detail in Chapter 2.

Since this thesis is concerned with the design of curved waveguides then it would seem reasonable to start analysing equations (1.13) - (1.17) and (1.18) - (1.22) in cylindrical polar coordinates. This approach has the disadvantage of requiring the radius of the bend to be constant all the way along the bend. On a more practical level, this would also require the writing of two different numerical codes, one for analysing straight waveguides in Cartesian coordinates, and one for computing curved mode profiles in cylindrical polar coordinates. This is not, in itself, an unreasonable request, however, in order that the loss in the waveguides may be characterised correctly it will also be required to numerically propagate waves in straight and curved geometries, requiring the writing of at least two more codes to handle the different coordinate systems. Another issue that can arise with the analysis of Maxwell's equations in cylindrical polar coordinates is having to work with Bessel functions of large complex order. This issue is discussed in Section 1.2.2.

To analyse the curved waveguide problem a conformal mapping is employed to transform the curved waveguide structure that lives in cylindrical polar coordinates into a straight waveguide section that lives in Cartesian coordinates. The mapping changes the refractive index profile in the transformed structure, but more importantly the code that was written to compute the modes of straight waveguides can be used, with minor modifications, to analyse curved waveguides. Similarly, in the case of propagation codes. The details of this analysis are presented in Section 1.3.

1.2.1 One-dimensional straight slab waveguide

The slab waveguide is a one-dimensional waveguide comprised of slabs of dielectric material. The refractive index varies along the $\hat{\mathbf{x}}$ direction, the direction of $\hat{\mathbf{x}}$ being taken from Figure 1.4. In this structure the field is described by the solution of

$$P\,\frac{d^2\phi}{dx^2} + Q\,k_0^2\,\phi(x) - P\,\beta^2\,\phi(x) = 0 \tag{1.25}$$

Equation (1.25) is obtained by neglecting the contributions of the y-dependent terms in equations (1.23) and (1.24). The definitions of P and Q change according to the polarisation being analysed, see Table 1.1.

It should be noted that when the problem is reduced from two to one dimensions certain field components can no longer form part of the propagating field. In the case of E^x polarised waves the H_x and H_z components are discarded, see equations (1.15) and (1.17), for E^y polarised waves the E_x and E_z components are discarded, see equations (1.20) and (1.22). Thus a one-

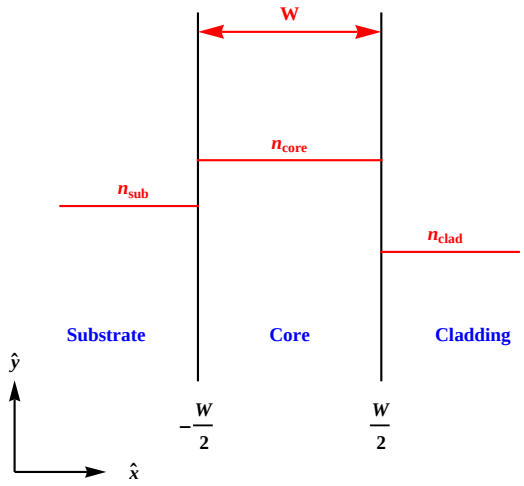


Figure 1.4: Slab waveguide structure centred on the origin

Table 1.1: Definitions for the coefficients in equation (1.25)

Polarisation	ϕ	P	Q
$E^y(TE)$	E_y	1	n^2
$E^x(TM)$	H_y	$1/n^2$	1

dimensional E^x polarised wave is the same as a TM polarised wave, and a one-dimensional E^y wave is the same as a TE polarised wave.

It is assumed that the refractive index, $n(x)$, of a slab waveguide is a piecewise constant function of position

$$n(x) = \begin{cases} n_{clad}, & x > \frac{W}{2} \\ n_{core}, & |x| \leq \frac{W}{2} \\ n_{sub}, & x < -\frac{W}{2} \end{cases} \tag{1.26}$$

with $n_{clad} \leq n_{sub} < n_{core}$, see Figure 1.4. An ansatz for the solution of equation (1.25) is

$$\phi(x) = A \begin{cases} e^{-q\,(x\,-\,W/2)}, & x > \frac{W}{2} \\ \cos\,(h\,x\,-\,\psi), & |x| \leq \frac{W}{2} \\ e^{p\,(x\,+\,W/2)}, & x < -\frac{W}{2} \end{cases} \tag{1.27}$$

where $\phi(x)$ represents E_x or H_x depending on the polarisation, ψ is related to the phase of the wave. The term A, used to normalise the field amplitude, is defined by

$$A = \begin{cases} \sqrt{\dfrac{\omega\,\mu_0}{\beta\,d_{eff}}}, & E^y(\text{TE}) \text{ polarisation} \\ \sqrt{\dfrac{\omega\,\epsilon_0\,n_c^2}{\beta\,d_{eff}}}, & E^x(\text{TM}) \text{ polarisation} \end{cases} \tag{1.28}$$

The term d_{eff} is known as the effective width of the mode, this is in reference to the fact that a waveguide mode will penetrate beyond the actual width of the slab waveguide. It is defined by

$$d_{eff} = \begin{cases} W + \dfrac{1}{p} + \dfrac{1}{q}, & E^y(\text{TE}) \text{ polarisation} \\ W + \dfrac{1}{g_1\,p} + \dfrac{1}{g_2\,q}, & E^x(\text{TM}) \text{ polarisation} \end{cases}$$

where the terms g_1 and g_2 are defined by [9]

$$g_1 = \frac{\beta^2}{k_0^2\, n_{core}^2} + \frac{\beta^2}{k_0^2\, n_{sub}^2} - 1$$
$$g_2 = \frac{\beta^2}{k_0^2\, n_{core}^2} + \frac{\beta^2}{k_0^2\, n_{clad}^2} - 1$$

The terms h, p and q are the transverse components of the field wavenumber in the core, substrate and cladding regions [6–9].

$$h = \sqrt{k_0^2\, n_{core}^2 - \beta^2}$$
$$p = \sqrt{\beta^2 - k_0^2\, n_{sub}^2}$$
$$q = \sqrt{\beta^2 - k_0^2\, n_{clad}^2}$$

$\phi(x)$ provides the necessary physical characteristics for a bound mode of an optical waveguide; inside the core region it is oscillatory, outside the core region the wave decays to zero. The requirement that the field decay to zero is a consequence of the fact that a mode is not considered to be confined if it is radiating energy away from the waveguide [9]. In general the propagation constants for bound modes must satisfy $k_0\, n_{sub} < \beta < k_0\, n_{core}$. If this condition is not satisfied then either p or q can become complex, which would imply that the waveguide is radiating energy into the substrate or cladding.

To determine the bound mode propagation constants electromagnetic boundary conditions are applied at the core-cladding and core-substrate interfaces, with equation (1.27) representing the field. Physically, this is equivalent to requiring total internal reflection at the core-cladding and core-substrate interfaces [39]. Upon application of the field matching technique it is found that the propagation constants of bound modes must satisfy

$$W\, h = \tan^{-1}\left(\eta_{ccl}\frac{q}{h}\right) + \tan^{-1}\left(\eta_{cs}\frac{p}{h}\right) + (m-1)\,\pi \tag{1.29}$$

The phase term is computed from

$$2\,\psi = \tan^{-1}\left(\eta_{ccl}\frac{q}{h}\right) - \tan^{-1}\left(\eta_{cs}\frac{p}{h}\right) + (m-1)\,\pi \tag{1.30}$$

where the terms η_{ccl} and η_{cs} are defined by

$$\eta_{ccl} = \begin{cases} 1, & E^y(\text{TE}) \text{ polarisation} \\ \dfrac{n_{core}^2}{n_{clad}^2}, & E^x(\text{TM}) \text{ polarisation} \end{cases} \tag{1.31}$$

$$\eta_{cs} = \begin{cases} 1, & E^y(\text{TE}) \text{ polarisation} \\ \dfrac{n_{core}^2}{n_{sub}^2}, & E^x(\text{TM}) \text{ polarisation} \end{cases} \tag{1.32}$$

The integer constant m, present in equations (1.29) and (1.30), is related to the mode being considered, e.g. $m = 1$ for the fundamental mode, $m = 2$, 3, 4 ... etc. for higher order modes. The convention for defining the η parameters is adopted from [7].

To compute the propagation constants for a slab waveguide equation (1.29) must be solved numerically. A root-finding algorithm is employed to determine the bound-mode values of β

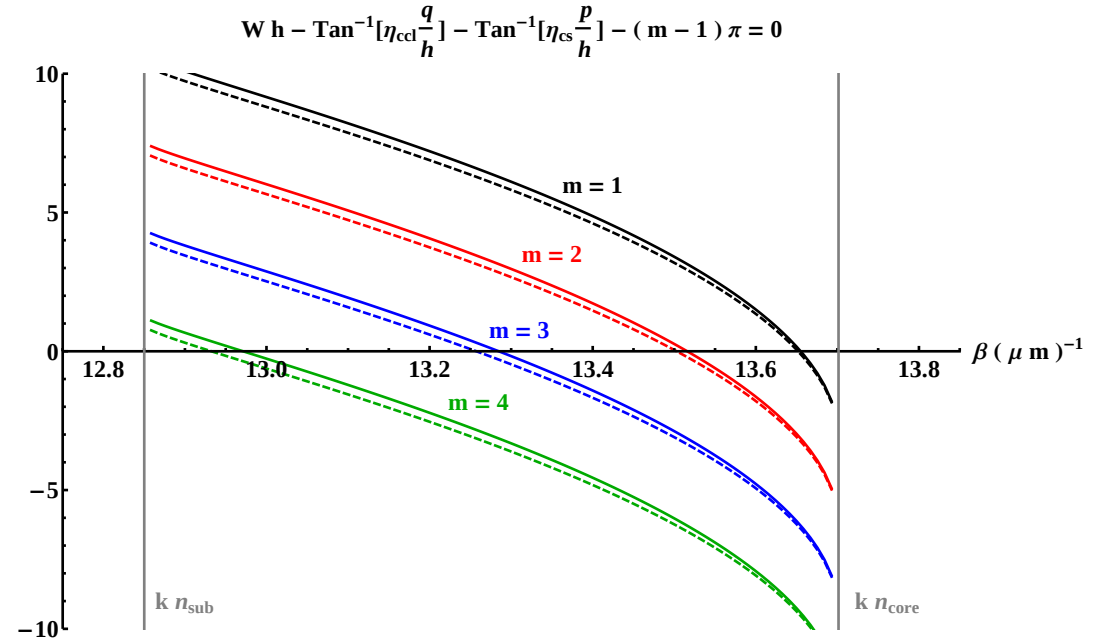


Figure 1.5: TE (solid) and TM (dashed) dispersion equations for the modes in a $2.5\,\mu m$ wide InGaAsP on InP slab waveguide with air cladding.

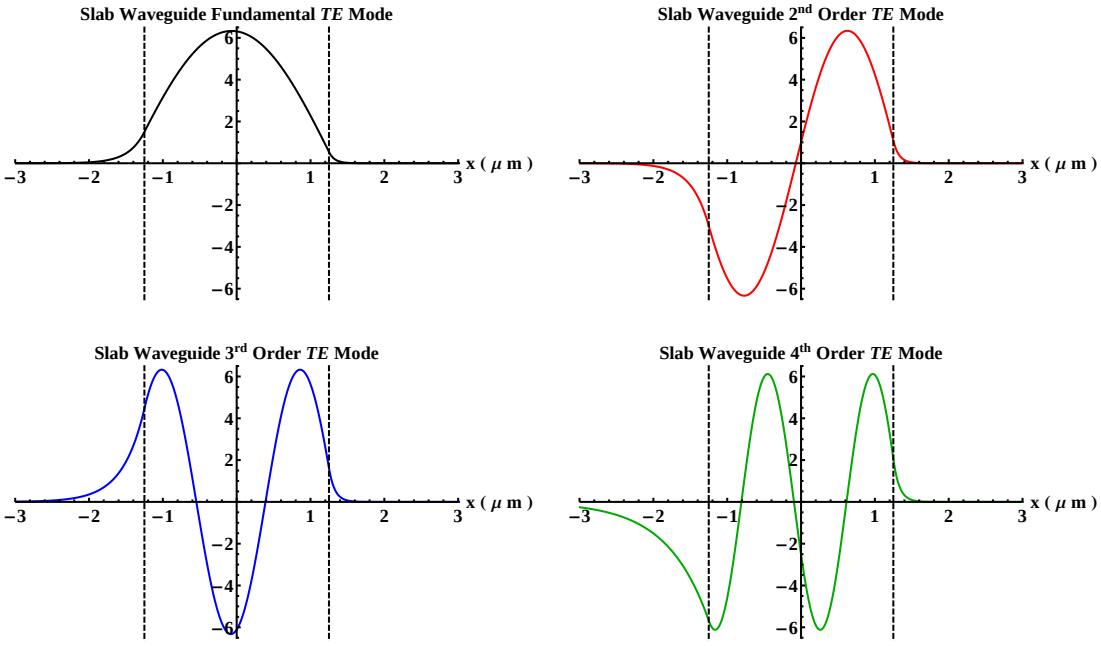


Figure 1.6: TE bound-mode profiles in a $2.5\,\mu m$ wide InGaAsP on InP slab waveguide with air cladding. The E_y components are shown here with $n_{core} = 3.38$, $n_{sub} = 3.17$ and $n_{clad} = 1.0$.

in the range $k_0\, n_s < \beta < k_0\, n_c$. The roots are located at the points where the curves in Figure 1.5 cut the horizontal axis. As an example, consider a $2.5\,\mu m$ wide InGaAsP layer on an InP substrate with air cladding. The refractive indices at a wavelength of $\lambda = 1.55\,\mu m$ in the core, substrate and cladding regions are $n_{core} = 3.38$, $n_{sub} = 3.17$ and $n_{clad} = 1$. There will be a total of eight modes in this waveguide, four TE polarised and four TM polarised. The dispersion curve is plotted for each of the eight modes in Figure 1.5. The values for the roots of equation (1.29) are determined using an implementation of Brent's root finding method [40]

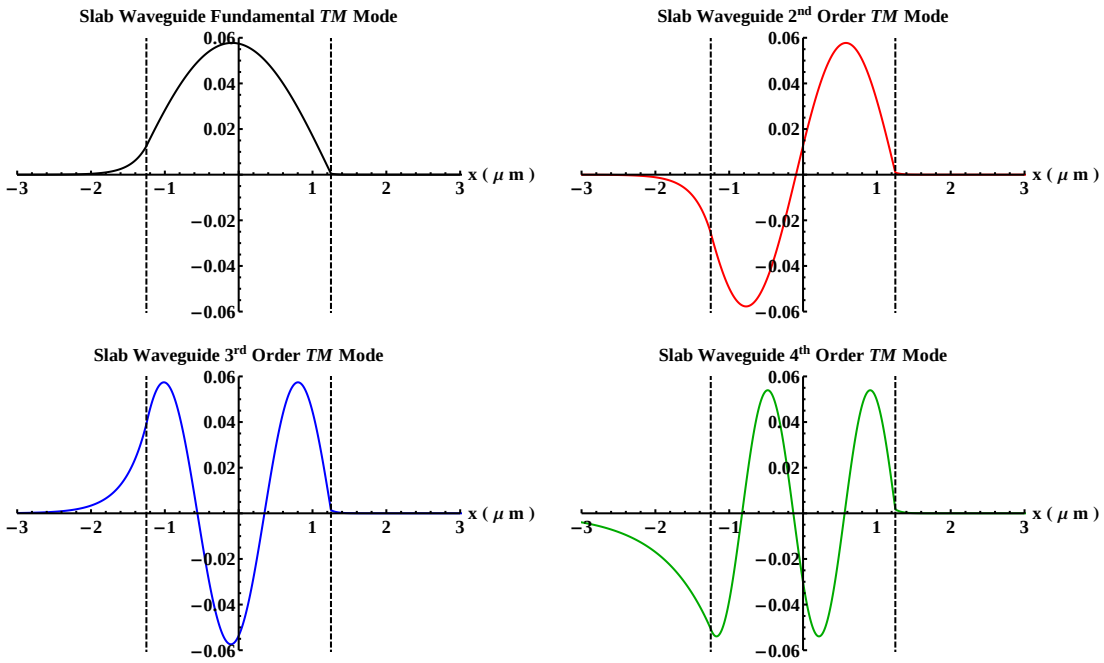


Figure 1.7: TM bound-mode profiles in a 2.5 μm wide InGaAsP on InP slab waveguide with air cladding. The H_y components are shown here with $n_{core} = 3.38$, $n_{sub} = 3.17$ and $n_{clad} = 1.0$.

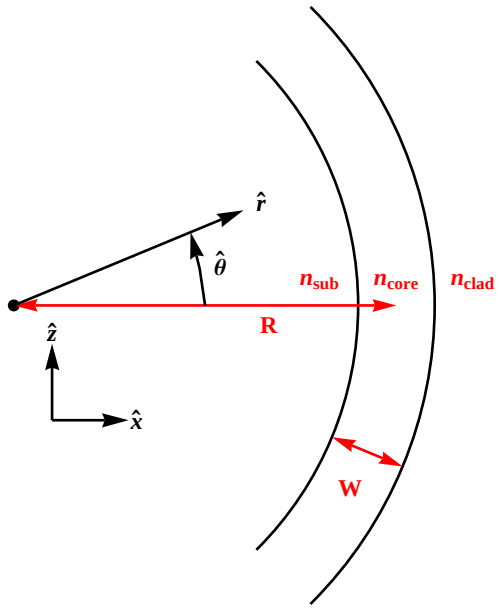
From Figure 1.5 it is seen that β decreases in value for higher order modes, this can tell us about the shape of the modes. Looking at the definitions of the wavenumber parameters h, p and q it is seen that h increases with decreasing β, which means the frequency of oscillations in the core will increase for higher order modes, by equation (1.27). Also, as β decreases p and q decrease, which implies that the slope of the exponential decay increases meaning that higher order modes are less well confined. In general large β means low frequency oscillations in the core region and a sharp decay at the core-substrate and core-cladding interfaces, small β means high frequency oscillations in the core region and a gradual decay of the field at the core-substrate and core-cladding interfaces. This behaviour is observed when the mode profiles are plotted, see Figures 1.6 and 1.7.

1.2.2 One-dimensional curved slab waveguides

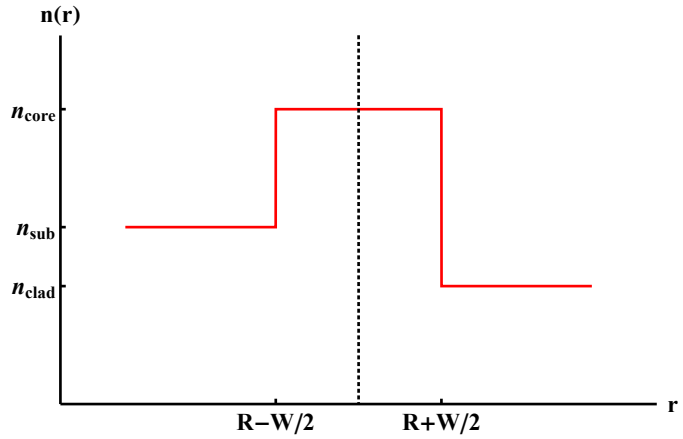
Figure 1.8(a) shows a plan view of a curved slab waveguide of width W and radius of curvature R in the Cartesian (x, z) plane. In cylindrical coordinates the slab waveguide has its boundaries located at $r = R - \frac{W}{2}$ and $r = R + \frac{W}{2}$. Conversion of the waveguide boundary between the Cartesian and cylindrical coordinates is achieved by means of the transformation (1.33).

$$x = r\cos\theta, \qquad z = r\sin\theta \tag{1.33}$$

It is assumed, for now, that the waveguide radius of curvature does not change with θ, this then is a constant curvature waveguide. The refractive index for a curved slab waveguide having constant curvature is defined in a cylindrical coordinate system by (1.34), similar to



(a) Curved dielectric slab



(b) Curved slab index profile

Figure 1.8: Curved slab waveguide structure and index profile

equation (1.26) for straight slab waveguides.

$$n(r,\,\theta) = \begin{cases} n_{clad}, & r > R + \frac{W}{2} \\ n_{core}, & R - \frac{W}{2} \leq r \leq R + \frac{W}{2} \\ n_{sub}, & 0 \leq r < R - \frac{W}{2} \end{cases} \tag{1.34}$$

If Maxwell's equations are expressed in cylindrical coordinates, the electric and magnetic fields are described by a Bessel equation whose solution can be written in the form (1.35) [31]. The field component represented by $\phi(r,\,\theta)$ is E_y in the case of TE polarisation, and H_y in the case of TM polarisation. The fields propagate along the $\hat{\theta}$ direction and vary transversely along the

$\hat{\mathbf{r}}$ direction.

$$\phi(r,\,\theta) \,=\, e^{i(\omega\,t\,-\,\nu\,\theta)} \begin{cases} A_{cl}\,H_{\nu}^{(2)}(k_0\,n_{clad}\,r), & \text{if } r \,>\, R+\frac{W}{2} \\ A_c\,J_{\nu}(k_0\,n_{core}\,r) \,+\, B_c\,Y_{\nu}(k_0\,n_{core}\,r), & \text{if } R-\frac{W}{2} \,\leq\, r \,\leq R+\frac{W}{2} \\ A_{sub}\,J_{\nu}(k_0\,n_{sub}\,r), & \text{if } 0 \,\leq\, r \,<R-\frac{W}{2} \end{cases} \tag{1.35}$$

In (1.35) ν is related to field propagation constant, $J_{\nu}(\cdot)$ and $Y_{\nu}(\cdot)$ are the ordinary Bessel functions of order ν, and $H_{\nu}^{(2)}(\cdot)$ is the Hankel function of the 2^{nd} kind of order ν [41], A_{cl}, A_c, B_c and A_{sub} are unknown constants. The Hankel function of the 2^{nd} kind is defined by

$$H_{\nu}^{(2)}(\cdot) = J_{\nu}(\cdot) - iY_{\nu}(\cdot) \tag{1.36}$$

$H_{\nu}^{(2)}(\cdot)$ satisfies the physical criteria that the field must travel away from the waveguide at large distances from the waveguide and also that the field in a curved slab loses energy by radiation [19–21,31]. To see how the field decays and loses energy consider the value of the field far away from the waveguide. For large positive argument, $\xi \gg R$, the Hankel function can be expressed by its asymptotic approximation [41].

$$H_{\nu}^{(2)}(\xi) \,\sim\, e^{i\,(2\,\nu\,+\,1)\,\frac{\pi}{4}}\,e^{-i\,\xi}\,\left(\frac{2}{\pi\,\xi}\right)^{1/2} \quad \text{as} \quad \xi \to \infty \tag{1.37}$$

From (1.37) it is seen that $H_{\nu}^{(2)}(\xi)$ is oscillatory in its complex exponential term and decays as $\xi^{-1/2}$. Contrast this with the behaviour of the straight slab waveguide solution far from the waveguide core, recall that the field is real and decays as $\sim\, e^{-\,p\,r}$, equation (1.27). Thus the straight slab solution decays to zero at large distances from the waveguide, while the curved slab solution is oscillatory far away from the waveguide, this means that the curved slab waveguide loses energy by radiation.

The field also depends on the order parameter ν of the Bessel and Hankel functions. To decide upon the value of ν required it first needs to be defined. For large R the curved waveguide is treated as a small perturbation away from the straight configuration [20]. Near the outer boundary of the curved waveguide, the region $r \,\simeq\, R+\frac{W}{2}$ in Figure 1.8(a), the field of the curved waveguide is assumed to be similar to the field of the equivalent straight waveguide, that is a waveguide having the same dimensions and material parameters but zero curvature. Under this equal fields assumption $e^{-i\,\nu\,\theta} \,\approx\, e^{-i\,\beta_s\,z}$ near the waveguide, where $\hat{\mathbf{z}}$ is the direction of propagation for the straight waveguide and β_s is the propagation constant for the equivalent straight waveguide. This allows us to determine an approximate value for the order parameter ν of the Bessel and Hankel functions in equation (1.35).

$$\beta_s\,z \,\approx\, \nu\,\theta \quad \Rightarrow \nu \,\approx\, \beta_s\,R \quad \because z \,=\, R\,\theta$$

Since $R \gg \lambda$ then ν must be a very large number, also, since light propagating in a curved waveguide loses energy due to radiation then ν must be complex to include the attenuation coefficient, α, of the field. So the order parameter of the field in the curved waveguide is defined as the product of a complex propagation constant $\gamma \,=\, \beta_c \,+\, i\,\alpha_c$ and the radius of curvature of the waveguide [31].

$$\nu \,=\, \gamma\,R \,=\, (\beta_c \,+\, i\,\alpha_c)\,R \tag{1.38}$$

To determine the complex propagation constant a field matching method, similar to that which is used to analyse the straight slab waveguide, is used to determine a non-linear equation whose roots are the propagation constants of the bound modes of the curved slab waveguide. This analysis was carried out by Hiremath et al. in [31]. The fields of a TE or TM polarised wave, equation (1.35), were matched at $r = R-t$ and $r = R+t$, with $t = \frac{W}{2}$. A system of equations arises from the analysis, and this equation has a non-trivial solution if and only if condition

$$T_1 \cdot T_2 - T_3 \cdot T_4 = 0 \tag{1.39}$$

is satisfied. The solutions of (1.39) are the complex propagation constants, $\gamma = \nu/R$, for the curved slab waveguide. The terms in (1.39) are defined by equations (1.40) - (1.45) [31], with the primes indicating differentiation with respect to the coordinate r.

$$\begin{aligned} T_1 =& J_\nu\left(k_0\, n_{core}\,(R-t)\right) J'_\nu(k_0\, n_{sub}\,(R-t)) \\ &- q_s\, J_\nu(k_0\, n_{sub}\,(R-t))\, J'_\nu(k_0\, n_{core}\,(R-t)) \end{aligned} \tag{1.40}$$

$$\begin{aligned} T_2 =& Y_\nu(k_0\, n_{core}\,(R+t))\, H_\nu^{(2)'}(k_0\, n_{clad}\,(R+t)) \\ &- q_c\, H_\nu^{(2)}(k_0\, n_{clad}\,(R+t))\, Y'_\nu(k_0\, n_{core}\,(R+t)) \end{aligned} \tag{1.41}$$

$$\begin{aligned} T_3 =& Y_\nu(k_0\, n_{core}\,(R-t))\, J'_\nu(k_0\, n_{sub}\,(R-t)) \\ &- q_s\, J_\nu(k_0\, n_{sub}\,(R-t))\, Y'_\nu(k_0\, n_{core}\,(R-t)) \end{aligned} \tag{1.42}$$

$$\begin{aligned} T_4 =& J_\nu(k_0\, n_{core}\,(R+t))\, H_\nu^{(2)'}(k_0\, n_{clad}\,(R+t)) \\ &- q_c\, H_\nu^{(2)}(k_0\, n_{clad}\,(R+t))\, J'_\nu(k_0\, n_{core}\,(R+t)) \end{aligned} \tag{1.43}$$

$$q_s = \begin{cases} \frac{n_{core}}{n_{sub}} & \text{TE waves} \\ \frac{n_{sub}}{n_{core}} & \text{TM waves} \end{cases} \tag{1.44}$$

$$q_c = \begin{cases} \frac{n_{core}}{n_{clad}} & \text{TE waves} \\ \frac{n_{clad}}{n_{core}} & \text{TM waves} \end{cases} \tag{1.45}$$

Equation (1.39) does not possess an analytical solution. It is also very difficult to solve numerically because ν is very large and complex [31], this difficulty is compounded because the solution must be sought in the complex-plane without the aid of standard implementations of the Bessel functions for large complex arguments [31]. Approximate analyses, based on perturbation techniques [20], can provide accurate results as long as the bend radius is sufficiently large.

1.2.3 Analytical estimates for curved waveguide loss

Two dimensional models for the loss in optical waveguides exist [19, 30], but their applicability is generally restricted to rectangular waveguide structures, see Figure 1.2(a). The analysis by Marcatilli says that the attenuation per radian in a curved waveguide should go as [19]

$$\alpha_{slab} = A_1\, e^{-B_1\, R_c}$$

A_1, B_1 are independent of the bend radius R_c. Specifically, Marcatilli talks about the attenuation per radian of a waveguide bend, this is defined as the attenuation in a length of guide equal to the bend radius R [19]. The analysis by Marcatilli is approximate, it assumes that the field in a two-dimensional waveguide is composed of the outer product of the fields of two one-

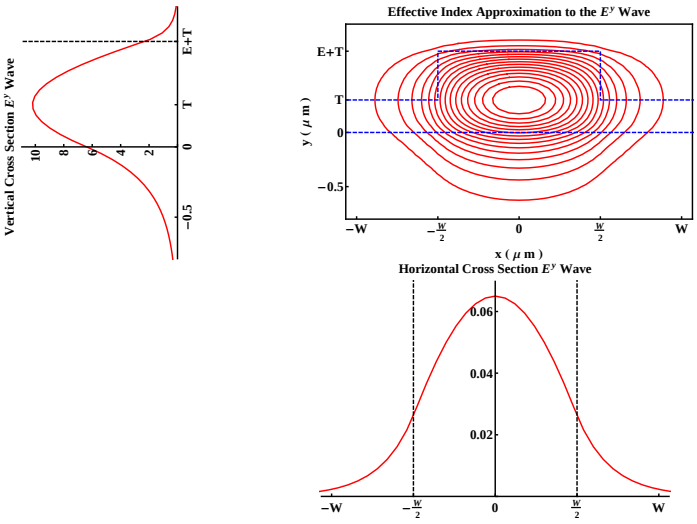


Figure 1.9: Approximation to a mode of a rib waveguide constructed using the effective index method

dimensional waveguides [19]. This is a reasonable approximation for rectangular waveguides but it is not appropriate for other waveguide structures such as rib or ridge waveguides, see Figures 1.2(c) and 1.2(d) respectively. For example, Figure 1.9 shows an attempt to construct the fundamental mode of a rib waveguide from the vertical and horizontal approximations that arise as a result of the application of the effective index method. The approximation does not reproduce the expected features of a mode in a rib waveguide.

The analysis by Sewell while being more accurate requires the solution of non-linear equations involving Bessel functions of large order, it is also restricted to waveguides of a certain type [30]. The problems associated with this approach have already been explained in Section 1.2.2. The volume current method was used to obtain a formula for the bend loss of a curved rib waveguide structure [27]. The authors suggest that for strongly guiding waveguides the following formula may approximate the bend loss [27]

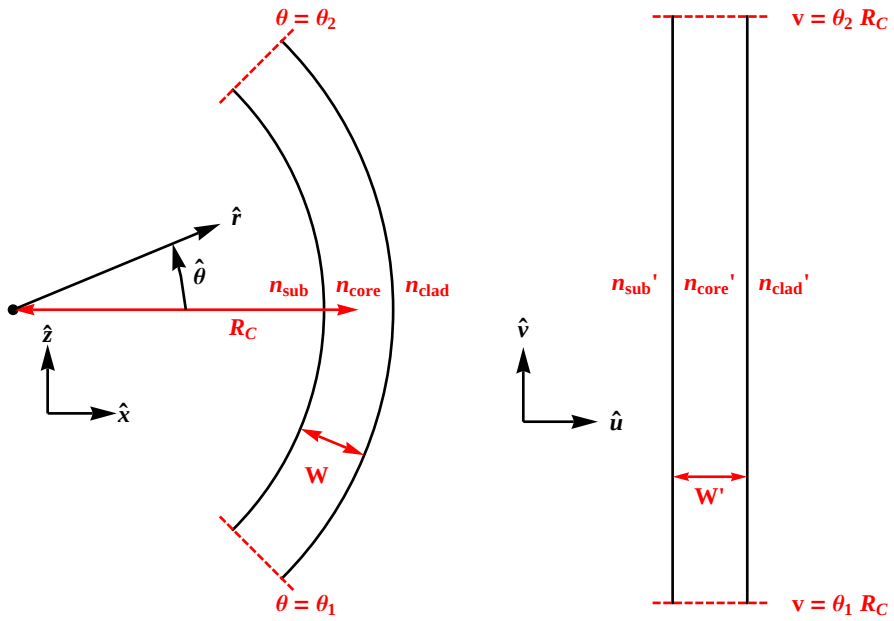
$$\alpha_{rib} \;=\; A_3\, R_c^{-3/2}\, e^{-B_1\, R_c}$$

where the constants A_3 and B_1 are defined by the waveguide parameters.

Given the difficulties associated with analytical models of curved waveguides an extension of an existing model for curved one-dimensional slab waveguides is presented in an attempt to determine the optical properties of curved two-dimensional optical waveguides. This model is discussed in the next section.

1.3 Conformal Mapping Approach to Curved Optical Waveguides

The conformal mapping technique was introduced by Heiblum and Harris in [34]. The technique introduced in their paper has been used repeatedly to analyse curved waveguide structures [10, 11, 15, 16, 32, 42–52]. The Heiblum-Harris method maps the curved waveguide structure of Figure 1.10(a) onto an equivalent straight waveguide with a transformed refractive index profile



(a) Curved structure in ζ-plane (b) Straight structure in w-plane

Figure 1.10: Waveguide structures before and after conformal transformation

and waveguide width, see Figure 1.10(b). The curved structure is mapped onto an equivalent straight structure by a conformal transformation [53, 54]. Specifically, a circular section, of radius R_c, of the $(x,\, z)$ plane, see Figure 1.10(a), is mapped onto a rectangular section of the complex $(u,\, v)$ plane, see Figure 1.10(b), by the transformation $w = f(\zeta) = u + i\, v$, where u and v are real valued functions of x and y, and $\zeta = x + i\, z = r\, e^{i\,\theta}$. To transform the circular region, of radius R_c, of the ζ-plane into the rectangular section of the w-plane apply the mapping

$$w = R_c \log \frac{\zeta}{R_c} \tag{1.46}$$

to the coordinates that define the circular region [34]. Expanding the complex logarithm function it is seen that the real and imaginary parts of (1.46) are defined by

$$u(x,\, z) = R_c \log \frac{r}{R_c} \quad v(x,\, z) = R_c\, \theta \tag{1.47}$$

If local coordinates are used and the $\hat{\mathbf{r}}$ axis is aligned with the $\hat{\mathbf{x}}$ axis then (1.47) can be written as (1.48), because $r = x + R_c$.

$$u(x,\, z) = R_c \log \left\{ 1 + \frac{x}{R_c} \right\} \quad v(x,\, z) = R_c\, \theta \tag{1.48}$$

The transformed structure is a rectangle in the $(u,\, v)$ plane, see Figure 1.10(b). The length of the rectangle is $L = R_c\, (\theta_2 - \theta_1)$, the width of the new structure is given by (1.49).

$$W' = R_c \left(\log \left(1 + \frac{W}{2\, R_c} \right) - \log \left(1 - \frac{W}{2\, R_c} \right) \right) \tag{1.49}$$

However, given $W \ll R_c$ the width of the transformed structure is approximately the same $W' \approx W$, since $\log (1 \pm \epsilon) \approx \pm \epsilon - O(\epsilon^2)$ for $|\epsilon| < 1$.

The geometry of the problem has been transformed. The effect of the transformation on the

governing equations will now be discussed. It has been shown in Section 1.2 that the modes in optical waveguides are described by equations (1.13) and (1.18). Since $n(x,\, y,\, z)$ is piecewise constant equations (1.13) and (1.18) can be represented by the same Helmholtz equation, equation (1.50) where for E^x polarisation $\phi = E_x$ and for E^y polarisation $\phi = H_x$.

$$\frac{\partial^2\phi}{\partial x^2} + \frac{\partial^2\phi}{\partial y^2} + \frac{\partial^2\phi}{\partial z^2} + k_0^2\, n^2(x,\, y,\, z)\, \phi = 0 \tag{1.50}$$

Using a result from the theory of complex variables the effect of a conformal mapping on equation (1.50) can be found. The result is stated in theorem 1.3.1 [53, 54], a proof of this result in given in Appendix A.

Theorem 1.3.1. *Under the transformation $w = f(\zeta) = u + i\, v$, where u and v are real valued functions, $f(\zeta)$ is analytic and $f'(\zeta) \neq 0$, if $\phi(x,\, z) = \phi(x(u, v),\, z(u,\, v))$ is a real valued function then $\nabla^2_{x,y}\phi = |f'(\zeta)|^2\, \nabla^2_{u,v}\phi$.*

$$\frac{\partial^2\phi}{\partial\, x^2} + \frac{\partial^2\phi}{\partial\, z^2} = |f'(\zeta)|^2 \left(\frac{\partial^2\phi}{\partial\, u^2} + \frac{\partial^2\phi}{\partial\, v^2} \right) \tag{1.51}$$

Theorem 1.3.1 provides a way of computing the Cartesian transverse Laplacian operator $\nabla^2_{x,\,z}$ in terms of a complex valued function $f(\zeta)$ and the transverse Laplacian operator in the w-plane $\nabla^2_{u,\,v}$. When the result is applied to (1.50) the resulting equation can be numerically solved to provide the bound mode propagation constants and mode profiles as a function of the waveguide curvature. The same equation can also be used to numerically examine the propagation properties of bound modes in curved waveguides. The details of these new numerical methods will be provided in Chapters 2 and 3.

To obtain the equation whose solution will provide the propagation constants and mode profiles of a curved waveguide transform equation (1.13) between the ζ-plane and the w-plane by application of theorem 1.3.1, similarly for equation (1.18). Then substitute the conformal mapping that maps the curved waveguide of the ζ-plane onto the straight waveguide of the w-plane. Theorem 1.3.1 can be applied in this case since the mapping function (1.46) is analytic and its derivative is not equal to zero, at least not in the region of interest. Application of equation (1.51) to (1.50) gives

$$\frac{\partial^2\phi}{\partial u^2} + \frac{\partial^2\phi}{\partial v^2} + \frac{1}{|f'(\zeta)|^2}\frac{\partial^2\phi}{\partial y^2} + \frac{1}{|f'(\zeta)|^2}\, k_0^2\, n^2(x,\, y,\, z)\, \Phi = 0 \tag{1.52}$$

The derivative of $f(\zeta)$ can be inverted as follows

$$|f'(\zeta)| = \left|\frac{dw}{d\zeta}\right| \Rightarrow |f'(\zeta)|^{-1} = \left|\frac{d\zeta}{dw}\right|$$

So that equation (1.52) becomes

$$\frac{\partial^2\phi}{\partial u^2} + \frac{\partial^2\phi}{\partial v^2} + \left|\frac{d\zeta}{dw}\right|^2 \frac{\partial^2\phi}{\partial z^2} + \left|\frac{d\zeta}{dw}\right|^2 k_0^2\, n^2(x,\, y,\, z)\, \phi = 0 \tag{1.53}$$

When mapping a circular section onto a straight section the mapping is given by equation (1.46). The inverse mapping in this case is defined by

$$\zeta = R_c\, e^{w/R_c} \tag{1.54}$$

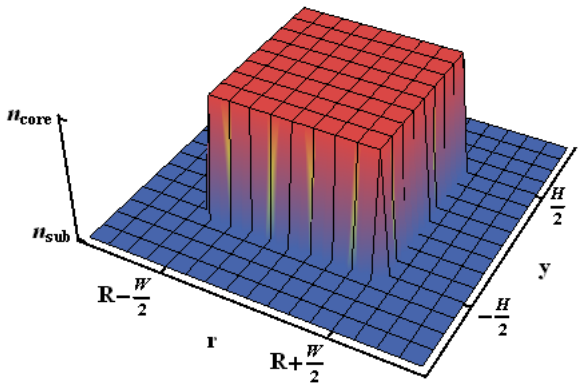


Figure 1.11: Refractive index profile prior to application of conformal mapping

The absolute value of the derivative of this mapping is given by

$$\begin{aligned}\left|\frac{d\zeta}{dw}\right| &= \left|\frac{R_c}{R_c}\,e^{w/R_c}\right| = |e^{w/R_c}| = |e^{(u+i\,v)/R_c}| \\ &= |e^{u/R_c}|\cdot|e^{i\,v/R_c}| \\ &= e^{u/R_c} \quad \because |e^{i\,v/R_c}| = 1 \end{aligned} \tag{1.55}$$

Substituting in equation (1.53) for the absolute value of the derivative of the inverse mapping results in

$$\frac{\partial^2\phi}{\partial u^2} + \frac{\partial^2\phi}{\partial v^2} + e^{2\,u/R_c}\,\frac{\partial^2\phi}{\partial y^2} + k_0^2\,n^2(x,\,y,\,z)\,e^{2\,u/R_c}\,\phi = 0 \tag{1.56}$$

The effect of the conformal mapping is to alter the refractive index of the transformed structure. Consider the refractive index profile of a uniform rectangular waveguide prior to transformation, see Figure 1.11. The refractive index in a uniform rectangular waveguide has a value of n_{core} in the core and n_{sub} outside the core. The refractive index in the transformed waveguide, see Figure 1.12, acts like the refractive index in the original waveguide multiplied by the absolute value of the derivative of the inverse mapping. In the case of a mapping from a curved structure onto a straight one, the refractive index in the transformed structure gains a slope that is proportional the curvature of the original waveguide, because the exponential function is approximately linear for small arguments $e^{u/R_c} \approx 1 + u/R_c + O((u/R_c)^2)$. To see the effect of the mapping more clearly, consider Figure 1.13. This figure shows a cross section through a uniform rectangular waveguide prior to transformation and the same cross section after transformation, the original refractive index profile is red and the refractive index profile in the transformed structure in blue.

To enable mode and propagation calculations it is assumed that the field term in equation (1.56), either E_x or H_x depending on polarisation, can be written as $\phi(u,\,v,\,y) = \phi(u,\,v,\,y)\,e^{-i\,\gamma\,v}$, where $\gamma = \beta + i\,\alpha$ is the complex propagation constant for a mode in a curved waveguide. Making this substitution results in

$$\frac{\partial^2 E_x}{\partial u^2} + e^{2\,u/R_c}\,\frac{\partial^2 E_x}{\partial y^2} + \frac{\partial^2 E_x}{\partial v^2} - 2\,i\,\gamma\,\frac{\partial E_x}{\partial v} + (k_0^2\,n^2\,e^{2\,u/R_c} - \gamma^2)\,E_x = 0 \tag{1.57}$$

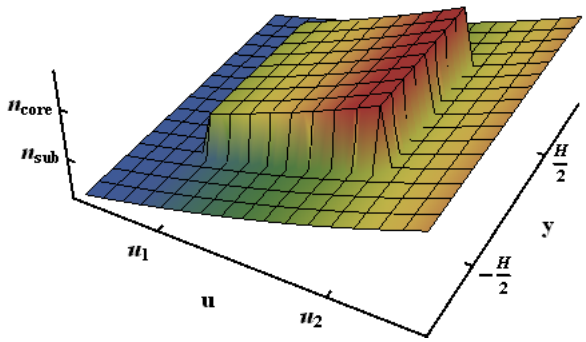


Figure 1.12: Refractive index profile after application of conformal mapping

for E^x waves and

$$\frac{1}{n^2}\frac{\partial^2 H_x}{\partial u^2} + \frac{e^{2\,u/R_c}}{n^2}\frac{\partial^2 H_x}{\partial y^2} + \frac{1}{n^2}\frac{\partial^2 H_x}{\partial v^2} - \frac{2\,i\,\gamma}{n^2}\frac{\partial H_x}{\partial v} + \left(k_0^2\,e^{2\,u/R_c} - \frac{\gamma^2}{n^2}\right) H_x = 0 \quad (1.58)$$

for E^y waves. The direction of propagation in the transformed structure is assumed to be along the $\hat{v}$ direction.

To simplify the programming of the numerical methods equations (1.57) and (1.58) are represented by a single equation, with coefficients defined differently depending on polarisation [38]. This combined equation is

$$P\frac{\partial^2\phi}{\partial u^2} + P\,\Gamma\frac{\partial^2\phi}{\partial y^2} + P\frac{\partial^2\phi}{\partial v^2} - 2\,i\,\gamma\,P\frac{\partial\phi}{\partial v} + k_0^2\,Q\,\Gamma\,\phi - P\,\gamma^2\,\phi = 0 \quad (1.59)$$

and the coefficients are defined in Table 1.2[1].

Equation (1.59) will be the primary focus of analysis for the thesis. When computing mode profiles the solution of

$$P\frac{\partial^2\phi}{\partial u^2} + P\,\Gamma\frac{\partial^2\phi}{\partial y^2} + k_0^2\,Q\,\Gamma\,\phi - P\,\beta^2\,\phi = 0 \quad (1.60)$$

with real propagation constants is sought. A numerical scheme for computing the solution of (1.60) is derived in Chapter 2. The scheme is based on the finite element method. The propagation properties of a wave can be analysed by computing the solution of

$$2\,i\,\gamma\,P\frac{\partial\phi}{\partial v} - P\frac{\partial^2\phi}{\partial v^2} = P\frac{\partial^2\phi}{\partial u^2} + P\,\Gamma\frac{\partial^2\phi}{\partial y^2} + k_0^2\,Q\,\Gamma\,\phi - P\,\gamma^2\,\phi \quad (1.61)$$

A numerical scheme for doing just this is derived in Chapter 3. The propagation technique is known as the finite element beam propagation method.

The advantage of the approach taken here is that it allows for a non-constant curvature to be included along the direction of propagation [47]. This is in contrast to the analytical models that assume a fixed curvature along the length of the waveguide bend [19, 30, 31]. The model proposed here should be valid as long as the curved waveguide is not in the whispering gallery

[1]For a bend of fixed radius $\kappa = 1/R_c$

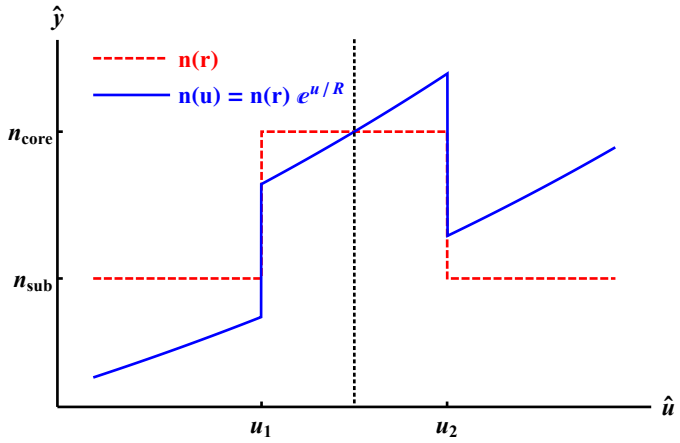


Figure 1.13: Refractive index profile in the equivalent straight waveguide after application of the conformal mapping

Table 1.2: Term definitions for the coefficients in equations (1.59)

Polarisation	ϕ	P	Q	Γ
E^x	E_x	1	n^2	$e^{2\kappa u}$
E^y	H_x	$1/n^2$	1	$e^{2\kappa u}$

regime, i.e. as long as

$$R_c > \frac{W}{2}\left(\log\left(\frac{n_{core}}{n_{eff}}\right)\right)^{-1}$$

This model may break down in the presence of polarisation coupling, which can occur in curved waveguides. However, this effect is not considered in this thesis.

1.4 Discussion

The theory of optical waveguides has been described. The curved waveguide and its properties have been described and the various methods used to approximate its solution have been presented. The extension of the curved slab waveguide model, based on a conformal transformation, has been extended to enable it to deal with curved three dimensional waveguides.

In the next chapter a method for numerically calculating the optical modes and their propagation constants is developed. The method will be applicable to straight and curved optical waveguide structures.

Chapter 2

Waveguide Mode Calculation

Summary: *The numerical method necessary for computing the modes in a curved optical waveguide is presented. It is shown how the finite element method is used to compute the mode profiles and propagation constants of an optical waveguide via the calculation of matrix eigenvalues and associated eigenvectors. A computer code that implements the finite element method is presented. Some useful rules concerning the choice of computational domain parameters are provided. The applicability of the finite element method is demonstrated by its application to some waveguide problems.*

2.1 Introduction

It was shown in Chapter 1 that the equation whose solution determines the shape of the E^x and E^y polarised waves in two dimensional waveguides is given by

$$P\,\frac{\partial^2\phi}{\partial u^2} + P\,\Gamma\,\frac{\partial^2\phi}{\partial y^2} + k_0^2\,Q\,\Gamma\,\phi - P\,\beta^2\,\phi = 0 \tag{2.1}$$

where the terms ϕ, P, Q and Γ are defined in Table 1.2. This problem cannot be formulated as a standard boundary value problem because neither the bound mode propagation constants nor the value of the field at the dielectric interfaces are known. Numerical methods must be used to compute the solution.

A large number of methods are available for solving (2.1). Some are based on classical methods such as the finite difference method (FDM) [55–57], the finite element method (FEM) [38, 58–64] and fourier methods [65]. Other methods were developed specifically to deal with the waveguide problem, such as the method of lines (MOL) [66] and the eigenmode expansion method (EEM) [67]. In general the solution procedure can be summarised as follows: the region surrounding a waveguide is discretised according to some recipe, for example with FDM, eigenmode expansion and Fourier methods. Equation (2.1), is reduced to a system of linear equations which are then solved to obtain the propagation constants and an approximation to the electromagnetic field at each of the points around the waveguide. The manner of the discretisation, the construction of the equations, their resulting form and solution is what changes between the methods. Another approach to mode solving is to actually simulate the propagation of light in the structure via a Beam Propagation Method (BPM) [68] or the Finite

Difference Time Domain Method (FDTD) [69]. However, these propagation techniques can require long simulation times to allow the initial beam to settle down into the correct shape and propagation constant of a waveguide mode.

The technique used here is the Finite Element Method (FEM). The reason for choosing FEM over alternative methods is that formal techniques exist that allow for an error bound on the solution of an equation to be derived [64]. The error associated with a solution is proportional to the size of the elements used to compute the solution, so to make the solution more accurate all that is required is to reduce the size of the elements. The computational procedure and implementation of the FEM for computing the solution of equation (2.1) is described in this chapter. Details of the FEM as it is applied in the field of Photonics can be found in [6, 37, 38, 58, 59, 70]. The mathematical foundations of the FEM are presented in [63, 64].

2.2 Rayleigh-Ritz Finite Element Method

To solve equation (2.1) the Rayleigh-Ritz finite element method is used. This approach re-writes an equation $\mathfrak{L}\,\phi = f$ as an equivalent functional and invokes the variational principle. A functional $F(\phi)$ is a function of a function defined by

$$F(\phi) = \frac{1}{2}(\mathfrak{L}\,\phi,\, \phi) - (\phi,\, f) \tag{2.2}$$

for a differential operator $\mathfrak{L}$ with an inner product defined by

$$(\phi,\, \psi) = \int_{\Omega} \phi\, \psi \, d\Omega \tag{2.3}$$

An operator is defined as being self-adjoint (symmetric) when the following condition is satisfied.

$$(\mathfrak{L}\,\phi,\, \psi) = (\phi,\, \mathfrak{L}\,\psi) \tag{2.4}$$

The variational principle states that solving $\mathfrak{L}\,\phi = f$ is the same as computing the minimum of $F(\phi)$ when $\mathfrak{L}$ is self-adjoint [63, 64, 70][1]. The variation of a functional, $\delta\, F(\phi)$, is defined by

$$\delta\, F(\phi) = F(\phi + \delta\phi) - F(\phi). \tag{2.5}$$

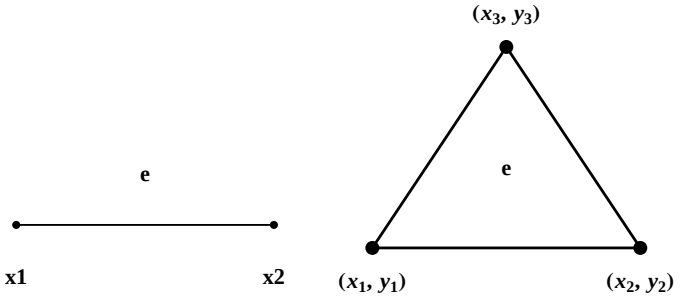
The functional $F(\phi)$ is stationary when the variation of the functional equals zero, i.e. $\delta\, F = 0$. It can be shown that the variation of the functional $F(\phi)$ is given by [70]

$$\delta\, F = (\delta\phi,\, \mathfrak{L}\,\phi) - (\delta\phi,\, f) = (\delta\phi,\, \mathfrak{L}\,\phi - f). \tag{2.6}$$

If $\delta\, F = 0$ then $\mathfrak{L}\,\phi - f = 0$ because $\delta\phi \neq 0$. The operator associated with equation (2.1) is self-adjoint, by (2.4), therefore the variational principle can be invoked to determine the solution of equation (2.1).

The variational principle allows the solution to be theoretically determined, practically speaking though the solution remains unknown. The finite element method is the practical means by which the solution is computed. To compute an approximate solution to an equation proceed by subdividing the computational domain into a set of points called nodes. Collections of nodes

[1] A detailed description of the variational principle is provided in Appendix B



(a) One-dimensional finite element

(b) Two-dimensional finite element

Figure 2.1: Finite element sub-domains used in one and two dimensional meshes

are joined together to form sub-regions, called elements. In one-dimension, elements are linear sections bounded by two nodes, see Figure 2.1(a). In two dimensions elements are triangular regions bounded by three nodes, see Figure 2.1(b). The collection of elements that covers the computational domain is called the mesh. The solution is approximated on each element of the mesh by some interpolating function defined on a single element. The aim is to determine the value of the solution at each node of the mesh.

The approximate solution is arrived at by assuming that the interpolating functions on each of the elements can replace the field terms in the functional. In practice the functional is approximated on each element using the interpolating function for that element. The expression for the functional is then differentiated and the result set equal to zero. This is repeated for all the elements on the mesh to provide what are called the elemental matrices. A system of linear equations is formed by computing a sum over all the elemental matrices in the mesh, the solution of this set of equations approximates the solution at each point in the mesh in accordance with the variational principle [63, 64, 70].

The set of equations, in this case, forms a generalised eigenvalue problem[2] [70, 71] whose eigenvalues are related to the propagation constants and the corresponding eigenvectors are related to the waveguide mode profiles. The eigenvalues and eigenvectors of a large matrix must now be computed. Techniques exist for reducing the generalised eigenvalue problem to the standard eigenvalue problem, and standard algorithms can be used to compute the eigenvalues and eigenvectors of the resulting problem [40, 72, 73].

2.3 FEM for Two-Dimensional Waveguides

The functional equivalent to equation (2.1) is computed using equation (2.2). The expression for the functional is simplified using the first scalar Green's theorem [70] and the fact that $\phi(u,\, y) \rightarrow 0$ as $|u| \rightarrow \infty$ and $|y| \rightarrow \infty$. The functional to be minimised to produce the elemental matrices in accordance with the Rayleigh-Ritz finite element method is

$$\begin{aligned} F(\phi) &= \frac{1}{2} \iint_{\Omega} \left(P \frac{\partial^2 \phi}{\partial u^2} \phi + P \Gamma \frac{\partial^2 \phi}{\partial y^2} \phi + k_0^2 Q \Gamma \phi^2 - \beta^2 P \phi^2 \right) d\Omega \\ &= \frac{1}{2} \iint_{\Omega} \left(k_0^2 Q \Gamma \phi^2 - P \left(\frac{\partial \phi}{\partial u} \right)^2 - P \Gamma \left(\frac{\partial \phi}{\partial y} \right)^2 - \beta^2 P \phi^2 \right) d\Omega \end{aligned} \tag{2.7}$$

[2] See Section 2.3.4

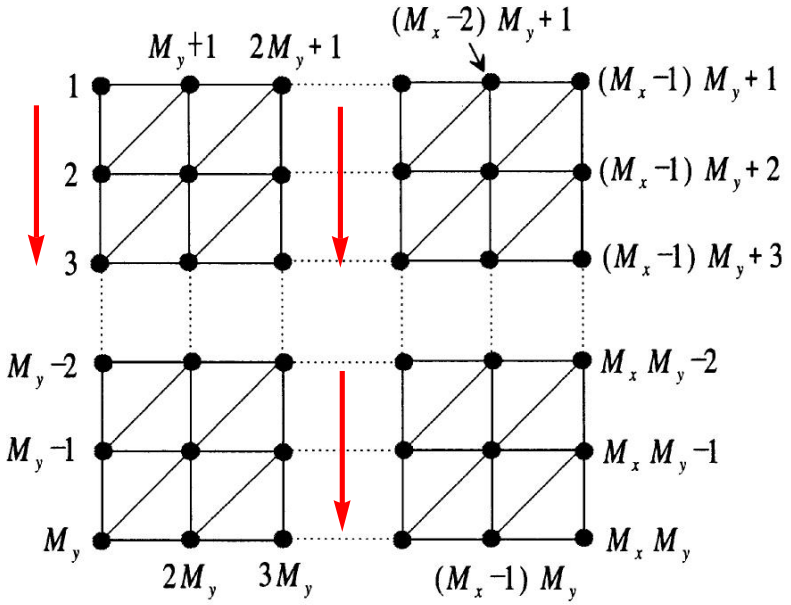


Figure 2.2: Finite element mesh in two dimensions. The numbering of the nodes is illustrated.

2.3.1 Planar elements in two-dimensions

For two-dimensional problems the solution of equation (2.1) is sought on a domain Ω, which is a finite section of the $u\,y$-plane. This domain is discretised by a set of nodes along the horizontal and vertical axes of this domain. The horizontal direction is split into N_u nodes and the vertical direction is split into N_y nodes. The nodes for the entire domain are defined by forming the cartesian product from the sets of vertical and horizontal nodes, this gives a total of $N = N_u\,N_y$ points in Ω of the form $(u_r,\, y_s)$. These nodes are used to form triangular sub-domains called elements, each element comprises three nodes. The set of elements that covers Ω is called the mesh, see Figure 2.2 taken from [37]. There are a total of $M = (N_u - 1)(N_y - 1)$ elements in the mesh.

The numbering of the nodes plays an important role in the formation of a two-dimensional mesh. It can be shown that the node numbering is related to bandwidth of the global matrices used in the calculation of the solution [70]. Here, it is assumed that the nodes along the horizontal direction are numbered left-to-right $1 \leq r_u \leq N_u$, the nodes along the vertical direction are numbered top-to-bottom $1 \leq s_y \leq N_y$. The point pairs inside Ω are then given a global number that is computed according to the rule

$$g = (r_u - 1)\,N_y + s_y. \tag{2.8}$$

Equation (2.8) can be inverted so that a particular node position can be determined from the global number using

$$r_u(g) = \begin{cases} g/N_y, & \text{if } g\%N_y = 0 \\ 1 + g/N_y, & \text{otherwise} \end{cases} \tag{2.9}$$

$$s_y(g) = \begin{cases} N_y, & \text{if } g\%N_y = 0 \\ g\%N_y, & \text{otherwise} \end{cases} \tag{2.10}$$

The elements in the mesh are numbered $1 \leq e \leq M$ in the manner of a raster scan, see Figure 2.2. The global node numbers and the element numbers are related via an array called the connectivity matrix [70], this is an array of size $M \times 3$ in which the e^{th} row holds the global numbers of the nodes in element e. Inside an element the nodes are given a local number $i = 1, 2, 3$. The connection between the local node number and the global node number is used in the assembly of the matrix equations, see Section 2.3.3.

On each element of the mesh the solution is approximated by a planar interpolating function $\phi^e(u, y)$.

$$\phi^e(u, y) = a^e + b^e u + c^e y \tag{2.11}$$

Vandermonde interpolation [72] is used to construct a set of equations for the interpolation coefficients a^e, b^e and c^e.

$$\begin{pmatrix} \phi_1^e \\ \phi_2^e \\ \phi_3^e \end{pmatrix} = \begin{pmatrix} 1 & u_1^e & y_1^e \\ 1 & u_2^e & y_2^e \\ 1 & u_3^e & y_3^e \end{pmatrix} \cdot \begin{pmatrix} a^e \\ b^e \\ c^e \end{pmatrix} \tag{2.12}$$

Solving this system results in

$$\begin{pmatrix} a^e \\ b^e \\ c^e \end{pmatrix} = \frac{1}{2\Delta^e} \begin{pmatrix} u_2^e y_3^e - y_2^e u_3^e & u_3^e y_1^e - y_3^e u_1^e & u_1^e y_2^e - y_1^e u_2^e \\ y_2^e - y_3^e & y_3^e - y_1^e & y_1^e - y_2^e \\ u_3^e - u_2^e & u_1^e - u_3^e & u_2^e - u_1^e \end{pmatrix} \cdot \begin{pmatrix} \phi_1^e \\ \phi_2^e \\ \phi_3^e \end{pmatrix} \tag{2.13}$$

where Δ^e is the area of the e^{th} element.

Substitution of a^e, b^e and c^e into equation (2.11) allows $\phi^e(u, y)$ to be re-written as an expansion over a set of basis functions. The basis functions for the two-dimensional interpolating function, $N_j^e(u, y)$, are given by

$$N_j^e(u, y) = \frac{1}{2\Delta^e} (a_j^e + b_j^e u + c_j^e y) \tag{2.14}$$

where the index j refers to the elements of column j from the matrix in equation (2.13). With these basis functions the solution on the e^{th} element is approximated by

$$\begin{aligned} \phi^e(u, y) &= N_1^e(u, y)\, \phi_1^e + N_2^e(u, y)\, \phi_2^e + N_3^e(u, y)\, \phi_3^e \\ &= \sum_{j=1}^{3} N_j^e(u, y)\, \phi_j^e \end{aligned} \tag{2.15}$$

Equation (2.15) will be used to approximate the solution inside the functional (2.7).

2.3.2 Elemental matrices in two-dimensions

The functional for the mesh is written as a sum over the elemental contributions [70]. The functional in this case is the sum over the double integrals

$$\begin{aligned} F(\phi) &= \sum_{e=1}^{M} F^e(\phi^e) \\ F^e(\phi^e) &= \frac{1}{2}\iint_e k_0^2\, Q^e\, \Gamma^e\, (\phi^e)^2\, du\, dy - \frac{1}{2}\iint_e P^e \left(\frac{\partial \phi^e}{\partial x}\right)^2 du\, dy \\ &\quad - \frac{1}{2}\iint_e P^e\, \Gamma^e \left(\frac{\partial \phi^e}{\partial y}\right)^2 du\, dy - \frac{1}{2}\iint_e \beta^2\, Q^e\, (\phi^e)^2\, du\, dy \end{aligned} \tag{2.16}$$

Substitute for the elemental approximation to the field on the e^{th} element in (2.16) using equation (2.15), assume that the terms P^e, Q^e and Γ^e are constant over an element. The result is

$$\begin{aligned} F^e(\phi^e) &= \frac{1}{2}\, k_0^2\, Q^e\, \Gamma^e \sum_{j=1}^{3}\sum_{k=1}^{3} A^e_{j\,k}\, \phi^e_j\, \phi^e_k \\ &\quad - \frac{1}{2}\, P^e \sum_{j=1}^{3}\sum_{k=1}^{3} B^e_{j\,k}\, \phi^e_j\, \phi^e_k \\ &\quad - \frac{1}{2}\, P^e\, \Gamma^e \sum_{j=1}^{3}\sum_{k=1}^{3} C^e_{j\,k}\, \phi^e_j\, \phi^e_k \\ &\quad - \frac{1}{2}\, \beta^2\, P^e \sum_{j=1}^{3}\sum_{k=1}^{3} A^e_{j\,k}\, \phi^e_j\, \phi^e_k \end{aligned} \tag{2.17}$$

this is an approximation to the functional on the e^{th} element. The terms $A^e_{j\,k}$, $B^e_{j\,k}$ and $C^e_{j\,k}$ are integrals over the basis functions defined by

$$A^e_{j\,k} = \iint_e (N^e_j)(N^e_k)\, du\, dy \tag{2.18}$$

$$B^e_{j\,k} = \iint_e \left(\frac{\partial N^e_j}{\partial u}\right)\left(\frac{\partial N^e_k}{\partial u}\right) du\, dy \tag{2.19}$$

$$C^e_{j\,k} = \iint_e \left(\frac{\partial N^e_j}{\partial y}\right)\left(\frac{\partial N^e_k}{\partial y}\right) du\, dy \tag{2.20}$$

Using the following results [70, 74]

$$\begin{aligned} \iint_e du\, dy &= \Delta^e \\ \iint_e N_1^i\, N_2^j\, N_3^k\, du\, dy &= 2\,\Delta^e\, \frac{i!\, j!\, k!}{(i+j+k+2)!} \end{aligned}$$

the integrals (2.18) - (2.20) are evaluated to give the $2D$ elemental matrices (2.21) - (2.23).

$$A^e_{j\,k} = \frac{1}{12}\,\Delta^e\,(1+\delta_{j\,k}) \tag{2.21}$$

$$B^e_{j\,k} = \frac{1}{4\,\Delta^e}\, b^e_j\, b^e_k \tag{2.22}$$

$$C^e_{j\,k} = \frac{1}{4\,\Delta^e}\, c^e_j\, c^e_k \tag{2.23}$$

The interpolation coefficients b^e and c^e in (2.22) and (2.23) are defined by equation (2.13). Equations (2.21) - (2.23) can be written in matrix form.

$$A^e = \frac{1}{12}\Delta^e \begin{pmatrix} 2 & 1 & 1 \\ 1 & 2 & 1 \\ 1 & 1 & 2 \end{pmatrix}$$

$$B^e = \frac{1}{4\,\Delta^e} \begin{pmatrix} (y_2^e - y_3^e)^2 & (y_2^e - y_3^e)\cdot(y_3^e - y_1^e) & (y_2^e - y_3^e)\cdot(y_1^e - y_2^e) \\ (y_3^e - y_1^e)\cdot(y_2^e - y_3^e) & (y_3^e - y_1^e)^2 & (y_3^e - y_1^e)\cdot(y_1^e - y_2^e) \\ (y_1^e - y_2^e)\cdot(y_2^e - y_3^e) & (y_1^e - y_2^e)\cdot(y_3^e - y_1^e) & (y_1^e - y_2^e)^2 \end{pmatrix}$$

$$C^e = \frac{1}{4\,\Delta^e} \begin{pmatrix} (u_3^e - u_2^e)^2 & (u_3^e - u_2^e)\cdot(u_2^e - u_1^e) & (u_3^e - u_2^e)\cdot(u_2^e - u_1^e) \\ (u_1^e - u_3^e)\cdot(u_3^e - u_2^e) & (u_1^e - u_3^e)^2 & (u_1^e - u_3^e)\cdot(u_2^e - u_1^e) \\ (u_2^e - u_1^e)\cdot(u_3^e - u_2^e) & (u_2^e - u_1^e)\cdot(u_1^e - u_3^e) & (u_2^e - u_1^e)^2 \end{pmatrix}$$

To determine the system of linear equations whose solution approximates that of equation (2.1) differentiate equation (2.17) with respect to the dummy variable ϕ_r^e and compute the resulting sums. When equation (2.17) has been differentiated the result is

$$\begin{aligned} \frac{\partial F^e}{\partial \phi_r^e} &= \frac{1}{2}\,k_0^2\,Q^e\,\Gamma^e \sum_{j=1}^{3}\sum_{k=1}^{3} A_{j\,k}^e \frac{\partial}{\partial \phi_r^e}\left(\phi_j^e\,\phi_k^e\right) \\ &- \frac{1}{2}\,P^e \sum_{j=1}^{3}\sum_{k=1}^{3} B_{j\,k}^e \frac{\partial}{\partial \phi_r^e}\left(\phi_j^e\,\phi_k^e\right) \\ &- \frac{1}{2}\,P^e\,\Gamma^e \sum_{j=1}^{3}\sum_{k=1}^{3} C_{j\,k}^e \frac{\partial}{\partial \phi_r^e}\left(\phi_j^e\,\phi_k^e\right) \\ &- \frac{1}{2}\,\beta^2\,P^e \sum_{j=1}^{3}\sum_{k=1}^{3} A_{j\,k}^e \frac{\partial}{\partial \phi_r^e}\left(\phi_j^e\,\phi_k^e\right) \end{aligned} \tag{2.24}$$

because each of the matrices, $\mathbf{A}^e$, $\mathbf{B}^e$ and $\mathbf{C}^e$, are independent of ϕ^e. The derivative of the product $\phi_j^e\,\phi_i^e$ with respect to ϕ_r^e is given by

$$\begin{aligned} \frac{\partial}{\partial \phi_r^e}\left(\phi_j^e\,\phi_i^e\right) &= \phi_j^e \frac{\partial \phi_i^e}{\partial \phi_r^e} + \phi_i^e \frac{\partial \phi_j^e}{\partial \phi_r^e} \\ &= \phi_j^e\,\delta_{i\,r} + \phi_i^e\,\delta_{j\,r} \end{aligned} \tag{2.25}$$

where $\delta_{i\,k}$ is the Kronecker delta tensor. Replacing the derivative terms in (2.24) using (2.25) results in

$$\begin{aligned} \frac{\partial F^e}{\partial \phi_r^e} &= \frac{1}{2}\,k_0^2\,Q^e\,\Gamma^e \sum_{j=1}^{3}\sum_{k=1}^{3} A_{j\,k}^e \left(\phi_j^e\,\delta_{k\,r} + \phi_k^e\,\delta_{j\,r}\right) \\ &- \frac{1}{2}\,P^e \sum_{j=1}^{3}\sum_{k=1}^{3} B_{j\,k}^e \left(\phi_j^e\,\delta_{k\,r} + \phi_k^e\,\delta_{j\,r}\right) \\ &- \frac{1}{2}\,P^e\,\Gamma^e \sum_{j=1}^{3}\sum_{k=1}^{3} C_{j\,k}^e \left(\phi_j^e\,\delta_{k\,r} + \phi_k^e\,\delta_{j\,r}\right) \\ &- \frac{1}{2}\,\beta^2\,P^e \sum_{j=1}^{3}\sum_{k=1}^{3} A_{j\,k}^e \left(\phi_j^e\,\delta_{k\,r} + \phi_k^e\,\delta_{j\,r}\right) \end{aligned} \tag{2.26}$$

The sums in (2.26) are computed by making use of the properties of the Kronecker delta tensor. Since $\delta_{j\,k} = 1$ only when $j = k$ the sum

$$\sum_{i=1}^{n} R^e_{i\,j}\,\delta_{j\,k} = R^e_{i\,k} \tag{2.27}$$

is valid. Upon application of (2.27) in (2.26) the result is

$$\frac{\partial F^e}{\partial \phi^e_r} = k_0^2\,Q^e\,\Gamma^e \sum_{j=1}^{3} A^e_{j\,r}\,\phi^e_r - P^e \sum_{j=1}^{3} B^e_{j\,r}\,\phi^e_r - P^e\,\Gamma^e \sum_{j=1}^{3} C^e_{j\,r}\,\phi^e_r - \beta^2\,P^e \sum_{j=1}^{3} A^e_{j\,r}\,\phi^e_r. \tag{2.28}$$

Equation (2.28) is the derivative of the functional on the e^{th} element. To determine an approximate solution to the waveguide problem the variational principle is invoked. Equation (2.28) is set equal to zero and the resulting set of equations is written in matrix form. The resulting matrices are known as the elemental matrices.

$$K^e\phi^e = \beta^2\,M^e\phi^e \tag{2.29}$$

$$K^e = k_0^2\,Q^e\,\Gamma^e\,A^e - P^e\,B^e - P^e\,\Gamma^e\,C^e \tag{2.30}$$

$$M^e = P^e\,A^e \tag{2.31}$$

Equation 2.29 is the short form of the equation whose solution provides the propagation constants and mode profiles of an optical waveguides. Equation 2.29 represents the contribution that a single element of the mesh makes to the global problem. Each of these contributions is gathered together in a process known as assembly, this is described in the next section. Once the matrix assembly is complete the eigenvalues and eigenvectors of the resulting matrices form the solution for an optical waveguide.

2.3.3 Global matrices in two-dimensions

Now that the elemental matrices are known the global problem must be constructed. The formation of the global matrices $\hat{\mathbf{K}}$ and $\hat{\mathbf{M}}$ is performed by summing over the contributions from each of the elemental matrices. The summation to assemble the global matrices is carried-out with the aid of the connectivity matrix, labelled C_m. The sums to be computed are given by

$$\hat{\mathbf{K}} = \sum_{e=1}^{M} K^e \tag{2.32}$$

$$\hat{\mathbf{M}} = \sum_{e=1}^{M} M^e \tag{2.33}$$

However, in order to ensure that the contributions from each of the elements is summed to the correct location the members of the elemental matrix $K^e_{i\,j}$ are added to $K_{C_m(e,\,i),C_m(e,\,j)}$ of the global matrix, similarly for $\hat{\mathbf{M}}$ [70]. This process is described by Algorithm 6 in Appendix D.

After computing the sums (2.32) and (2.33) the system of equations is in the form of a generalised eigenvalue problem, the eigenvalues and eigenvectors of which correspond to the bound mode propagation constants and profiles that can exist in the waveguide.

2.3.4 The generalised eigenvalue problem

To solve a generalised eigenvalue problem with eigenvalue Λ

$$(\hat{\mathbf{A}} - \Lambda \hat{\mathbf{B}}) \cdot \mathbf{\Phi} = \mathbf{0} \tag{2.34}$$

it must first be reduced to the standard eigenvalue problem with eigenvalue λ

$$(\hat{\mathbf{C}} - \lambda \hat{\mathbf{I}}) \cdot \mathbf{\Psi} = \mathbf{0} \tag{2.35}$$

where $\hat{\mathbf{C}}$ is some matrix obtained from ($\hat{\mathbf{A}}$, $\hat{\mathbf{B}}$) and $\hat{\mathbf{I}}$ is the identity matrix. It is not clear yet how the eigenvalues and eigenvectors of both problems will be related.

To reduce the generalised eigenvalue problem to the standard eigenvalue problem start by substituting the Cholesky decomposition of $\hat{\mathbf{B}}$ into equation (2.34). Cholesky decomposition is a matrix factorisation procedure for symmetric matrices. The aim of Cholesky decomposition is to write a matrix $\hat{\mathbf{M}}$ as the product of some lower triangular matrix $\hat{\mathbf{L}}$ and its transpose $\hat{\mathbf{L}}^T$ such that $\hat{\mathbf{M}} = \hat{\mathbf{L}} \cdot \hat{\mathbf{L}}^T$ [40, 72, 73]. This is permissable when the matrix $\hat{\mathbf{M}}$ is symmetric and positive definite. Replacing $\hat{\mathbf{B}}$ by its Cholesky decomposition, which is valid since $\hat{\mathbf{B}}$ is symmetric and positive definite, gives

$$\begin{aligned} \hat{\mathbf{A}} \cdot \mathbf{\Phi} &= \Lambda \hat{\mathbf{B}} \cdot \mathbf{\Phi} \\ &= \Lambda (\hat{\mathbf{L}} \cdot \hat{\mathbf{L}}^T) \cdot \mathbf{\Phi} \end{aligned} \tag{2.36}$$

Pre-multiply equation (2.36) by the inverse of the lower triangular factor $\hat{\mathbf{L}}$, i.e. $\hat{\mathbf{L}}^{-1}$, recall that $\hat{\mathbf{I}} = \hat{\mathbf{L}}^{-1} \cdot \hat{\mathbf{L}}$.

$$\begin{aligned} \hat{\mathbf{L}}^{-1} \cdot \hat{\mathbf{A}} \cdot \mathbf{\Phi} &= \Lambda \hat{\mathbf{L}}^{-1} \cdot \hat{\mathbf{L}} \cdot \hat{\mathbf{L}}^T \cdot \mathbf{\Phi} \\ &= \Lambda \hat{\mathbf{I}} \cdot \hat{\mathbf{L}}^T \cdot \mathbf{\Phi} \\ &= \Lambda \hat{\mathbf{L}}^T \cdot \mathbf{\Phi} \end{aligned} \tag{2.37}$$

On the left hand side of (2.37) replace $\hat{\mathbf{A}}$ by $\hat{\mathbf{A}} \cdot \hat{\mathbf{I}}$, and then replace $\hat{\mathbf{I}}$ by the product of $\hat{\mathbf{L}}^T$ with its inverse $\hat{\mathbf{L}}^{-T}$.

$$\begin{aligned} \hat{\mathbf{L}}^{-1} \cdot \hat{\mathbf{A}} \cdot \hat{\mathbf{I}} \cdot \mathbf{\Phi} &= \Lambda \hat{\mathbf{L}}^T \cdot \mathbf{\Phi} \\ \hat{\mathbf{L}}^{-1} \cdot \hat{\mathbf{A}} \cdot (\hat{\mathbf{L}}^{-T} \cdot \hat{\mathbf{L}}^T) \cdot \mathbf{\Phi} &= \Lambda \hat{\mathbf{L}}^T \cdot \mathbf{\Phi} \\ (\hat{\mathbf{L}}^{-1} \cdot \hat{\mathbf{A}} \cdot \hat{\mathbf{L}}^{-T}) \cdot (\hat{\mathbf{L}}^T \cdot \mathbf{\Phi}) &= \Lambda (\hat{\mathbf{L}}^T \cdot \mathbf{\Phi}) \end{aligned} \tag{2.38}$$

Equation (2.38) has the form $\hat{\mathbf{C}} \cdot \mathbf{\Psi} = \lambda \mathbf{\Psi}$, which is a standard eigenvalue problem, with $\hat{\mathbf{C}}$ and $\mathbf{\Psi}$ defined by

$$\hat{\mathbf{C}} = \hat{\mathbf{L}}^{-1} \cdot \hat{\mathbf{A}} \cdot \hat{\mathbf{L}}^{-T} \tag{2.39}$$

$$\mathbf{\Psi} = \hat{\mathbf{L}}^T \cdot \mathbf{\Phi} \tag{2.40}$$

Thus it has been shown that the eigenvalues of the matrix pair ($\hat{\mathbf{A}}$, $\hat{\mathbf{B}}$) in (2.34) and the eigenvalues of $\hat{\mathbf{C}}$ in (2.35) are equal. The matrix pair ($\hat{\mathbf{A}}$, $\hat{\mathbf{B}}$) is related to $\hat{\mathbf{C}}$ via (2.39). It has also been shown that the eigenvectors of (2.34) and (2.35) are related via the transformation (2.40) [40].

In order to apply this technique to the solution of equation (2.1) it must be shown that $\hat{\mathbf{M}}$,

defined by (2.33), is symmetric and positive definite. $\hat{\mathbf{M}}$ is obtained by summing over the elementary matrices (2.31). The matrix A^e, defined in (2.21) is symmetric, therefore M^e is symmetric. Since $\hat{\mathbf{M}}$ is defined as a sum over symmetric matrices then $\hat{\mathbf{M}}$ is also symmetric. To show that $\hat{\mathbf{M}}$ is positive definite it is necessary to show that $\mathbf{x}^T \cdot \hat{\mathbf{M}} \cdot \mathbf{x} > 0$ for all vectors $\mathbf{x}$ in real n-dimensional space. However a more useful test for positive-definiteness exists. The test is simply that if a matrix has a Cholesky decomposition then it is positive-definite [72, 73]. Since the Cholesky decomposition of $\hat{\mathbf{M}}$ can be found the propagation constants and mode profiles of an optical waveguide can be computed by finding the eigenvalues and eigenvectors of a matrix defined according to (2.39) which uses the matrix $\hat{\mathbf{K}}$ in place of the arbitrary $\hat{\mathbf{A}}$ and the Cholesky decomposition of $\hat{\mathbf{M}}$.

2.4 SFEM_Modes: An object oriented waveguide mode solver

In order to quickly and efficiently compute the propagation constants and mode profiles of an optical waveguide it is necessary to have a computer program that can accomplish each of the required steps. There are multiple professional software packages available that can already perform analysis of optical waveguides, such as [75–77]. However, these products can be expensive for a small research group with a limited budget. It is much more educational to write a custom implementation. The advantages of writing your own software, apart from the cost, are many. The code can be customised to specific requirements, can be extended should the need arise, it can be shared by other members of the research group to aid them with their research [78], and it can be incorporated into a larger piece of work so that its useful life is extended beyond a single PhD[3]. There are also disadvantages to writing your own simulation software. The development time depends strongly on the experience of the programmer. Testing of the code must be performed to ensure that it is returning valid results. Once a code is tested and capable of outputting results it can be put to use.

This section describes a code capable of computing the optical properties of a semiconductor waveguide via the SFEM. The code was written in the C++ programming language [79]. Section 2.4.1 describes the implementation of the objects needed to form a mesh for use in a finite element calculation. Section 2.4.2 describes the process for numerically computing the propagation constants and mode profiles of the optical waveguide being studied.

2.4.1 Mesh generation

The SFEM calculation process comprises two parts

1. Mesh generation.
2. Numerical analysis.

The numerical analysis is performed using standard algorithms. Mesh generation can also be performed using software that is freely available [80], however, it was felt at the start of the PhD that a home-made mesh generator would prove more educational. The type of mesh used in the calculations for this thesis are described in section 2.3.1.

[3]To date the mode solver written for this PhD has been incorporated into a larger code framework that is used to layout PICs made in the fabrication facility at Tyndall National Institute.

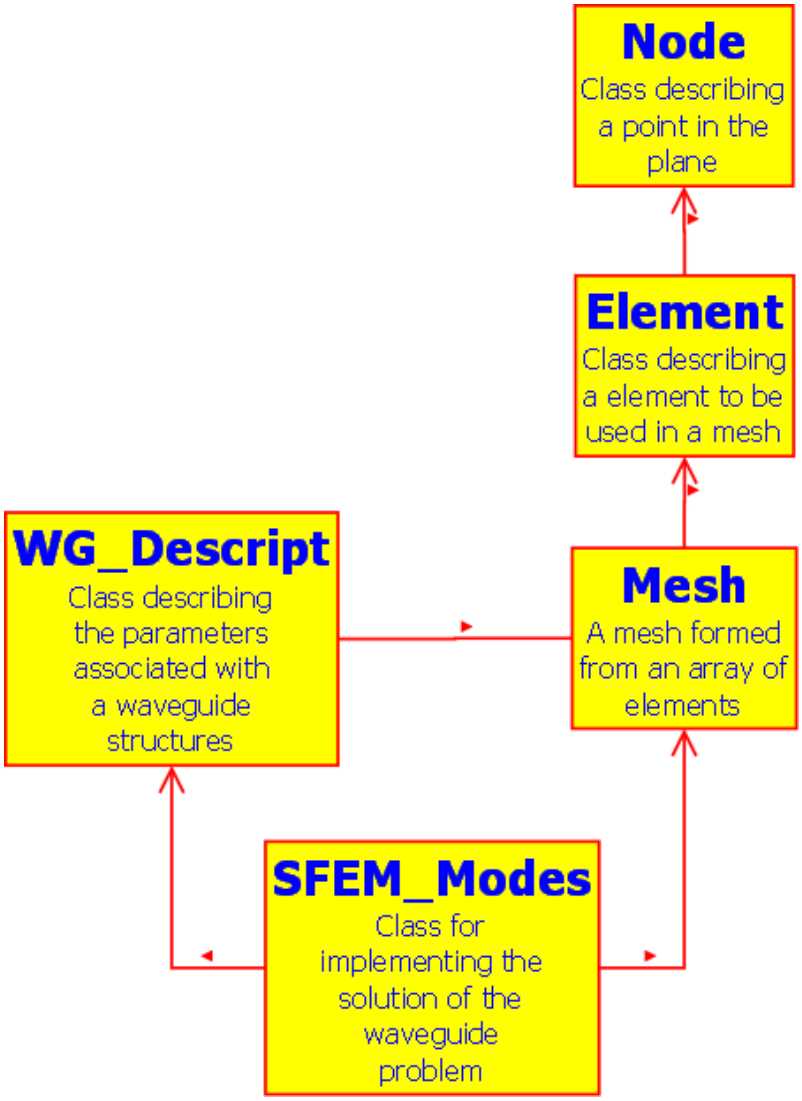


Figure 2.3: Class diagram for the waveguide mode calculation code.

SFEM_Modes must be capable of producing a mesh that discretises the waveguide. The code contains several objects used in the construction of the mesh described in section 2.3.1. The first object needed when building a mesh is one to describe a position in the plane, i.e. a node class. Associated with the node class are the following parameters

- Variables to describe the position of the node
- A variable to store the refractive index at the node
- A variable to store the field value at a particular node
- An integer to store the global number of the node

Once the node object is in place three nodes are joined together to form an element. The positions of the nodes define

- the location of the element centroid
- the element area Δ^e
- the interpolation coefficients, from equation (2.13)
- the field values on a given element
- the elemental matrices defined by (2.30) and (2.31)

The elemental matrices, defined by (2.30) and (2.31), for a given element are defined according to the properties of the nodes and the values of P^e, Q^e and Γ^e. It was decided that the values of P^e, Q^e and Γ^e associated with an element are defined according to the average of the values obtained from the three nodes that define the element.

The next object required is one that can describe an array of node positions in two-dimensions, called *node_arr*. *node_arr* contains the node positions at which the waveguide is sampled. *node_arr* is then used to construct the elements that will eventually form the mesh. To access the mesh information a mesh object has also been written, called *mesh*. *mesh* contains an array of elements and also the very important connectivity matrix that enables the global matrices $\hat{\mathbf{K}}$ and $\hat{\mathbf{M}}$ to be constructed.

Once a mesh object is available the next step is to implement a class that can perform the necessary numerical calculations, this is *SFEM_Modes*. *SFEM_Modes* acts as the control panel for the scalar FEM calculation. All parameters get passed to this object and it tells other classes to return node and mesh objects as required. *SFEM_Modes* constructs the global matrices and then calls numerical libraries to compute the propagation constants and mode profiles from the global matrices.

Once objects that describe the nodes, elements, node-array and mesh are available then the modes of an optical waveguide can be computed simply by passing a set of node positions that discretise the waveguide along the horizontal and vertical directions, along with the refractive index values at those node positions. In an attempt to generate a mesh that closely matches the waveguide structure other objects have also been implemented to aid with the calculation, these are the waveguide description objects, known as *rect*, *rib* and *ridge*. They are used to describe certain waveguide structures, in this case the waveguides shown in Figures 1.2(a) - 1.2(d). This approach was later extended to waveguides of arbitrary cross-section. An example of the type of mesh created for a rib waveguide structure is illustrated in Figure 2.4.

The mesh generation process described here works very well for those waveguides in Figure 1.1 but it is not to be recommended as a general mesh generation process[4]. The relationship between the waveguide discretisation objects and the mesh generation objects is illustrated in Figure 2.3. The remainder of this section details the various algorithms used in the mesh generation process and global matrix construction processes.

To begin with the waveguide structure is discretised along the horizontal and vertical directions. Algorithms 1 and 2, in Appendix D, generate node sets that are matched to the dimensions of a rib waveguide, the process is easily extended for the other structures in Figure 1.1. These algorithms provide nodes that will be uniformly spaced inside the core region of the waveguide

[4]The waveguide description class has been obfuscated in later versions of the code.

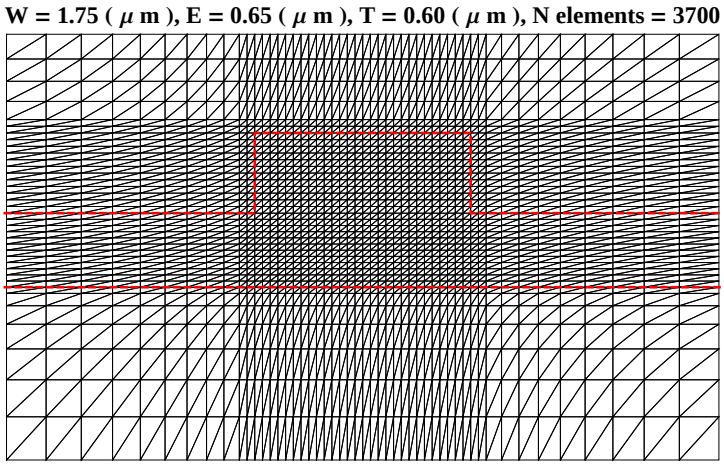


Figure 2.4: Finite element mesh created by the SFEM_Modes class.

while also ensuring that the node spacing increases as you move away from the waveguide core. The uniform spacing inside the core region is achieved by specifying the number of elements into which a particular layer must be split, this number, chosen by the user, is $2\,n_w$ in the case of horizontal discretisation and n_e, or n_t in the case of vertical discretisation. This process will ensure that the resulting mesh will have a large number of small elements inside the core region and a number of larger elements near the mesh boundary, see Figure 2.4. This is a useful property for the mesh to have because the accuracy of a finite element calculation is proportional to the size of the elements used [64], and the waveguide mode solutions will be at their most variable inside the core region.

Once the node positions have been selected the elements of the mesh must be constructed from those nodes. Firstly, a two-dimensional node array must be built, this is accomplished with Algorithm 3, which is effectively a method for computing the cartesian product of two sets. Global node numbers are assigned to the nodes according to formula (2.8).

The next step in the process is to construct the array of elements. The numbering of the node positions follows that described in [37], the node and element numbering is shown in Figure 2.2. The manner in which the nodes are numbered means that the elements can be gathered together by considering odd and even-numbered elements, assuming the numbering starts at 1. So odd numbered elements are built from the nodes with global numbers g, $g+1$ and $g-N_y$. Even numbered elements are built from the nodes with global numbers $g+1$, $g+1-N_y$ and $g-N_y$. The process is described in Algorithm 4 in Appendix D. The connectivity matrix described in Section 2.3.2 lists the global node numbers associated with each element. It is built using Algorithm 5.

The global matrices $\hat{\mathbf{K}}$ and $\hat{\mathbf{M}}$ are then constructed using the properties of the elements in the mesh. Since object oriented code is being used the element properties can be accessed from memory allowing the global matrices to be built very quickly. The global matrix assembly is accomplished using Algorithm 6 in Appendix D.

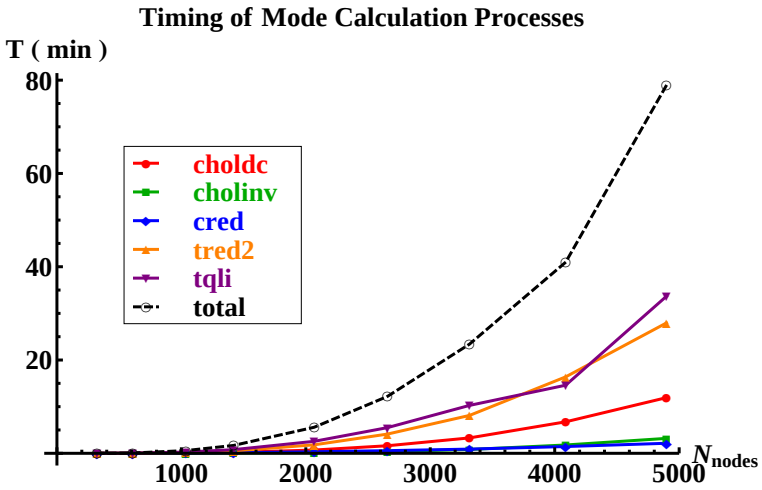


Figure 2.5: Waveguide mode calculation timing. Time, in minutes, for each of the processes required to compute a waveguide mode depending on the number of nodes in the mesh.

2.4.2 Numerical analysis

Once the matrices $\hat{\mathbf{K}}$ and $\hat{\mathbf{M}}$ have been constructed the procedure for finding β and $\mathbf{\Phi}$ can be reduced to a five step process. The first step in the calculation is to compute the Cholesky decomposition of the matrix $\hat{\mathbf{M}}$. The next step is to invert the factors that form the Cholesky decomposition, i.e. compute $\hat{\mathbf{L}}^{-1}$ and $\hat{\mathbf{L}}^{-T}$. Step three of the process is to compute the matrix product $\hat{\mathbf{C}}$ defined by (2.39), with $\hat{\mathbf{K}}$ replacing $\hat{\mathbf{A}}$. This product can be computed using standard matrix multiplication. However, given the sparse nature of $\hat{\mathbf{K}}$, $\hat{\mathbf{L}}^{-1}$ and $\hat{\mathbf{L}}^{-T}$ it is much more efficient to use the sparse matrix object discussed in Appendix C.1. Using this object the non-zero elements of $\hat{\mathbf{K}}$, $\hat{\mathbf{L}}^{-1}$ and $\hat{\mathbf{L}}^{-T}$ can be stored and the matrix $\hat{\mathbf{C}}$ can be computed in a shorter time than would otherwise be possible.

Step four is to compute the eigenvalues and eigenvectors of $\hat{\mathbf{C}}$. This calculation is accomplished in two parts. Firstly, reduce $\hat{\mathbf{C}}$ to a similar symmetric tri-diagonal matrix using the Householder reduction process [40, 72]. The second part of the eigenvalue / eigenvector calculation is the diagonalisation of the similar symmetric tri-diagonal matrix that arises from the application of Householder's method. Diagonalisation is accomplished by a variation of QR factorisation known as Implicit QL reduction [40]. Once diagonalisation is complete the eigenvalues of the matrix $\hat{\mathbf{C}}$, and hence the propagation constants of the waveguide, have been found.

Since only bound mode propagation constants are of interest, a search of the eigenvalues that satisfy $k_0\, n_{sub} < \beta < k_0\, n_{core}$ is made. The valid eigenvalues, and their corresponding eigenvectors are retrieved. The final step is to compute the mode profiles, $\mathbf{\Phi}$, corresponding to the bound mode propagation constants via the transformation (2.40). The entire calculation process is described algorithmically in Algorithm 7 in Appendix D.

SFEM_Modes, as it is written, can be used on problems with up to 5000 nodes, roughly 10,000 elements. This works very well for the types of calculations being performed as part of this PhD. If other variables such as polarisation coupling are to be introduced then modifications to the code will be required. To ensure that SFEM_Modes scales to larger numbers of nodes sparse matrix techniques will have to be employed to reduce the amount of memory being used. To ensure that the eigenvalues and eigenvectors of the resulting matrices can be computed in a reasonable amount of time then iterative techniques, rather than the direct techniques

Table 2.1: Waveguides used to test the mode calculation software

Name	Width (µm)	Etch Depth (µm)	Slab-Height (µm)	Core	Substrate
WG1	1.0	0.3	0.2	InGaAsP	InP
WG4	1.25	0.6	0.4	GaAs	AlGaAs
WG8A	2.0	0.7	0.8	InGaAsP	InP
WG9A	2.0	1.1	0.2	InGaAsP	InP
WG8B	2.0	0.7	0.8	GaAs	AlGaAs
WG9B	2.0	1.1	0.2	GaAs	AlGaAs

employed here, must be utilised. The time required for each step of a mode calculation is shown in Figure 2.5. It can be seen that as the number of nodes increases the time taken for each step also increases. Iterative techniques applied to sparse matrices can help to reduce the total calculation. These techniques are employed in optical mode propagation calculations, see Chapter 3.

2.5 Testing SFEM_Modes

To test the software that was written to compute the modes in optical waveguides various rib waveguide will be used, this structure is shown in Figure 1.1. The properties of the waveguides used for testing the code are listed in Table 2.1. The properties listed in Table 2.1 are to be used for 2D calculations. At a wavelength of $\lambda = 1.55\,(\mu m)$ the following values for refractive index are assumed

$$n_{InP} = 3.17, \quad n_{InGaAsP} = 3.38, \quad n_{AlGaAs} = 3.34, \quad n_{GaAs} = 3.44$$

To perform 1D calculations a reduced waveguide must be constructed from the 2D waveguide. The reduced waveguide is assumed to have the same width it has in 2D. The refractive index of the reduced guide is computed by making an effective index approximation of the 2D refractive index profile. Results for computed propagation constants are expressed as a normalised effective index given by [6]

$$b = \frac{n_{eff} - n_{sub}}{n_{core} - n_{sub}} \tag{2.41}$$

where n_{eff} is the effective refractive index of a waveguide, computed from

$$n_{eff} = \frac{\beta}{k_0}$$

2.5.1 Comparison of 1D analytical and 1D numerical

To test *SFEM_Modes* a comparison was made of solutions computed by an analytical method and the FEM code. As an analytical solution for rib waveguide structures does not exist an equivalent 1D slab was constructed from the data for waveguides WG8A, WG8B, WG9A and WG9B. The refractive index profile of the equivalent slab was computed using the effective index method [6]. The equivalent slab is constructed by applying the first step of the effective index method to the waveguides, i.e. the side and central slab regions are reduced to single effective index values, these values are used to form the reduced refractive index distribution. The resulting refractive index profile is polarisation dependent. The properties of the reduced

Table 2.2: Refractive index properties of equivalent waveguides

Waveguide	Polarisation	Core Index	Substrate Index
WG8A	E^x	3.34908	3.29274
	E^y	3.3522	3.3061
WG8B	E^x	3.41314	3.37305
	E^y	3.41544	3.3806
WG9A	E^x	3.4034	3.17
	E^y	3.3448	3.17
WG9B	E^x	3.40624	3.34
	E^y	3.4094	3.34

Table 2.3: Normalised effective indices for the reduced slab waveguides computed analytically and numerically.

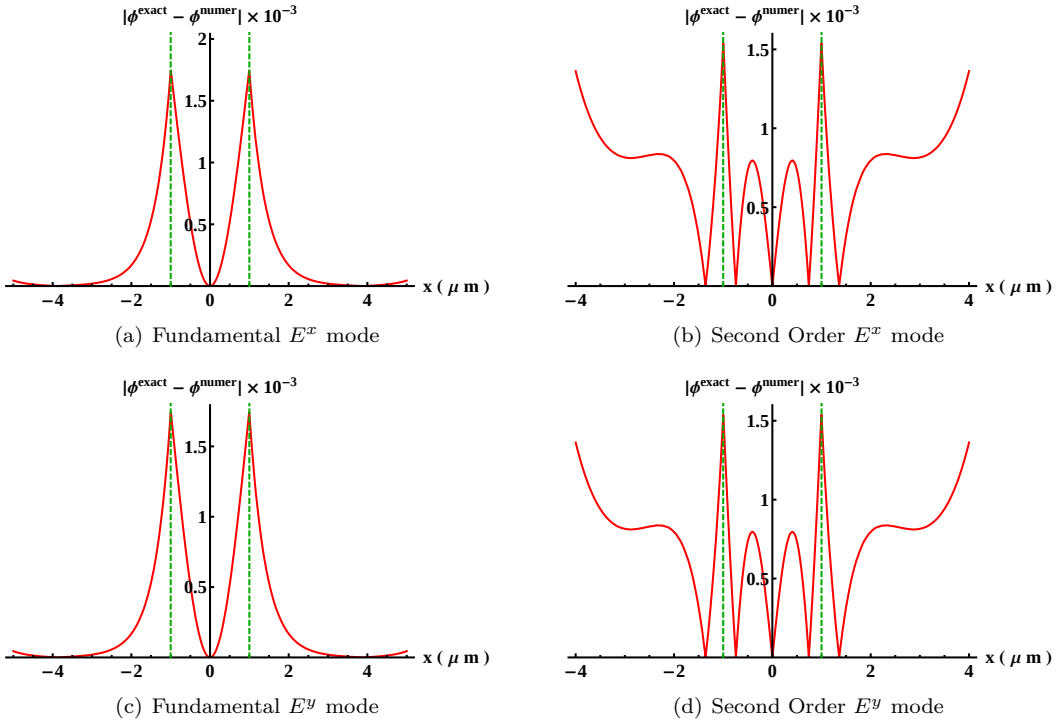
Waveguide	Polarisation	Mode Number	Analytical	Numerical
WG8A	E^x	1	0.799586	0.799381
		2	0.657476	0.656952
	E^y	1	0.817162	0.817
		2	0.689105	0.688714
WG8B	E^x	1	0.63292	0.6326
		2	0.388	0.3874
	E^y	1	0.6597	0.6594
		2	0.4377	0.4377
WG9A	E^x	1	0.74119	0.740857
		2	0.535	0.533857
		3	0.214048	0.211905
	E^y	1	0.759605	0.759286
		2	0.546281	0.545143
		3	0.220043	0.217952
WG9B	E^x	1	0.5466	0.5462
		2	0.2287	0.2273
	E^y	1	0.5745	0.574
		2	0.2478	0.2464

waveguides used in this set of calculations are listed in Table 2.2. A version of *SFEM_Modes* that can compute solutions for one-dimensional structures[5], written by the author, was used to compute the modes for the reduced slab waveguides whose properties are listed in Table 2.2.

The analytical effective indices, computed as the roots of equation (1.29), are compared with the numerical effective indices, computed as the eigenvalues of the matrices that arise from the application of the finite element method to the slab waveguide problem. The normalised effective index values are listed in Table 2.3. There is good agreement between the values computed by both methods. The error in all cases is $O(10^{-4})$.

The difference between the computed mode profiles was also examined. The field, having been computed numerically and analytically, is normalised so its maximum value is unity. The error associated with the numerical calculation is defined to be the maximum of the absolute value of the difference between the computed fields, i.e. $|\phi^{exact} - \phi^{numer}|$. In the case of the fundamental mode profiles the error associated with the finite element calculation is $O(10^{-3})$, see Figures 2.6 - 2.9. The error associated with the higher order modes is also $O(10^{-3})$ with the exception of WG8B, see Figures 2.7(b) and 2.7(d). The error for the higher order WG8B modes grows at the edge of the computational domain where the elements increase in length, but inside the core region the error is $O(10^{-6})$. The error in all cases can be reduced by computing the solution

[5]The 1D calculation procedure is identical to the procedure in 2D described in Section 2.3



(a) Fundamental E^x mode

(b) Second Order E^x mode

(c) Fundamental E^y mode

(d) Second Order E^y mode

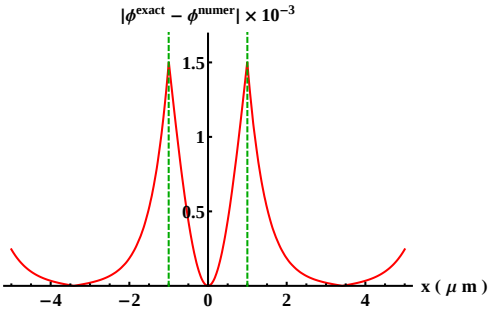
Figure 2.6: Difference between analytical solution and numerical solution in a slab waveguide approximation of WG8A. The refractive index values used to make the approximation are given in Table 2.2. The computed normalised effective indices are given in Table 2.3.

using a larger number of elements, as is well known from the theory associated with the finite element method [63, 64, 70]. Alternatively, a higher order interpolation scheme can be used to generate the solution, although this method is not adopted in this thesis.

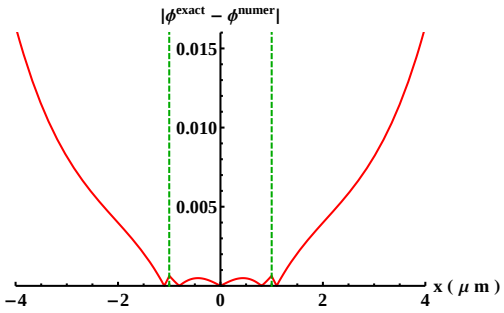
2.5.2 Propagation constant convergence

The calculation of propagation constants and mode profiles for a given waveguide depends not only on the waveguide parameters but also on the choice of computational domain. The principal factor effecting the calculation is the number of elements, N_{elems}, that form the mesh. Too few elements, and the results will not be accurate, too many elements and the calculation will take too long. Unfortunately, there does not seem to be a way to estimate the optimal number of elements a-priori.

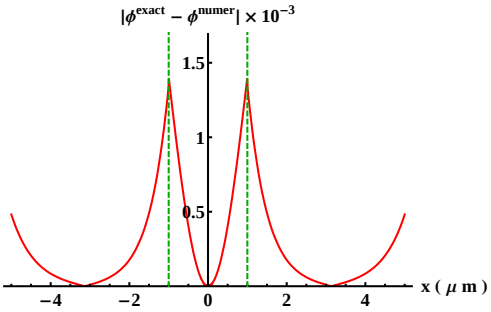
Another factor that effects the accuracy of a calculation is the area of the computational domain, $L_x \times L_y$. If this was a standard boundary value problem then the solution accuracy would depend primarily on the number of nodes, because the size of the domain, and the value of the mode at the domain edge would be specified. In reality waveguide modes decay to zero at large distances from the waveguide centre. On a computer this infinite space has to be truncated for practical reasons. This truncation sets up an artificial boundary some distance from the waveguide, which in turn effects the calculation of the propagation constants. For example, if for some waveguide, global matrices are constructed within a domain of area $L_x \times L_y$ and another domain of area $(2\,L_x) \times (2\,L_y)$, all other parameters being constant, then each domain has a different matrix from which the same propagation constant must be computed. The waveguide propagation constant must be independent of the discretisation used, but the fact that you



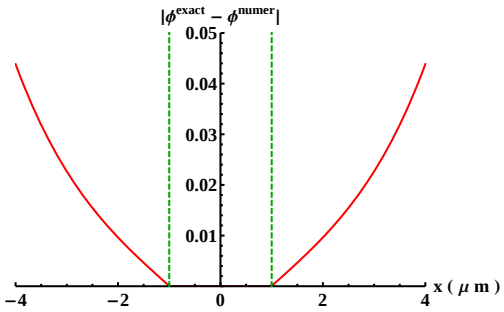
(a) Fundamental E^x mode



(b) Second Order E^x mode

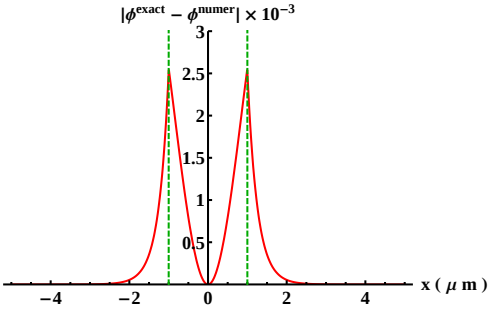


(c) Fundamental E^y mode

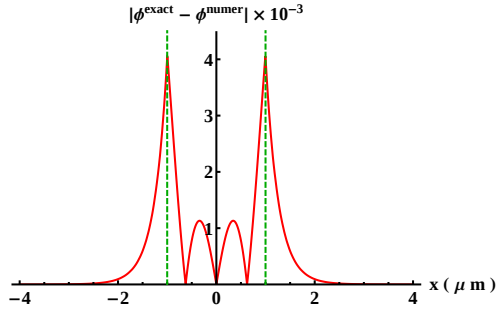


(d) Second Order E^y mode

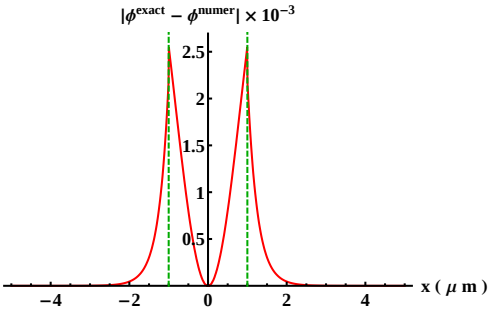
Figure 2.7: Difference between analytical solution and numerical solution in a slab waveguide approximation of WG8B. The refractive index values used to make the approximation are given in Table 2.2. The computed normalised effective indices are given in Table 2.3.



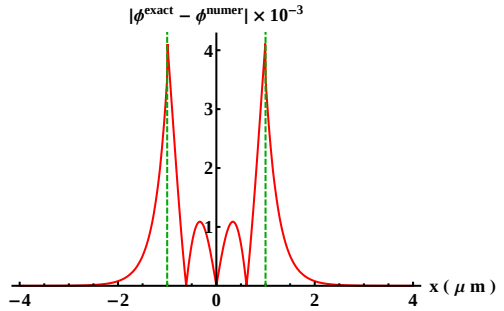
(a) Fundamental E^x mode



(b) Second Order E^x mode

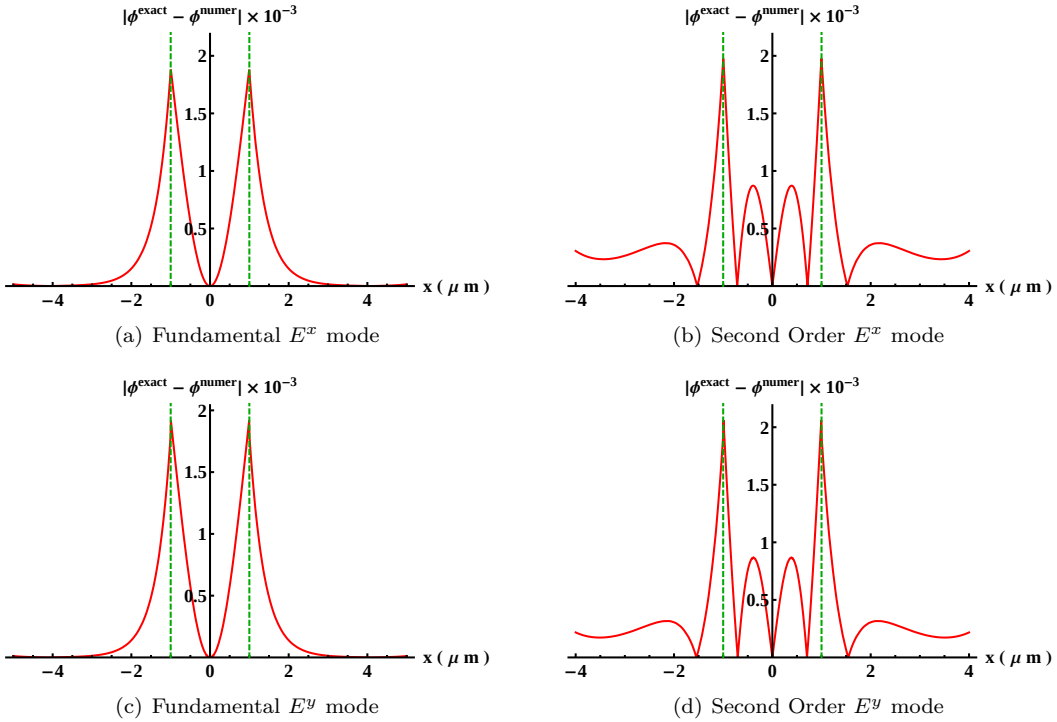


(c) Fundamental E^y mode



(d) Second Order E^y mode

Figure 2.8: Difference between analytical solution and numerical solution in a slab waveguide approximation of WG9A. The refractive index values used to make the approximation are given in Table 2.2. The computed normalised effective indices are given in Table 2.3.



(a) Fundamental E^x mode

(b) Second Order E^x mode

(c) Fundamental E^y mode

(d) Second Order E^y mode

Figure 2.9: Difference between analytical solution and numerical solution in a slab waveguide approximation of WG9B. The refractive index values used to make the approximation are given in Table 2.2. The computed normalised effective indices are given in Table 2.3.

have two different matrices means that the computed propagation constants will differ. The discretisation of the waveguide is as much a part of the solution as the waveguide parameters when dealing with boundary conditions at infinity.

Since the discretisation forms part of the solution it should be possible to determine the values of N_{elems} and L_x for which an accurate solution can be computed. It is not possible in practice to find values of N_{elems} and L_x which will guarantee that a computed solution will be accurate, however, it should be possible to find guidelines to inform our choices for N_{elems} and L_x. The choices of N_{elems} and L_x for which a waveguide mode is assumed to be accurate are to be determined by numerical experiment. It is being assumed that L_y is approximately equal to L_x $L_y \approx L_x > H$, where H is the waveguide height.

The numerical experiment for finding guidelines for choosing N_{elems} and L_x comprises computing the mode profiles and propagation constants of a set of optical waveguides for a series of values of N_{elem}, L_x. The process is depicted in Algorithm 8 of Appendix D. When constructing the mesh for a waveguide problem the variable used to specify the number of nodes along the $\hat{x}$ direction is n_w, see Section 2.4.1 for detailed explanation. The loop over each calculation is actually a loop over a set of n_w values, as n_w increases the overall number of elements will increase. Similarly, an outer loop iterates over a set of values of L_x. A set of solutions corresponding to combinations of N_{elems} and L_x values for multiple waveguides is generated by *SFEM_Modes*. The results from the simulations are analysed and the guidelines for choosing N_{elems} and L_x are determined. Please note that in Figures 2.11, 2.13 and 2.15 the vertical axis is labelled by "z", this should in fact be labelled as "y" in keeping with the notation of equation (2.1).

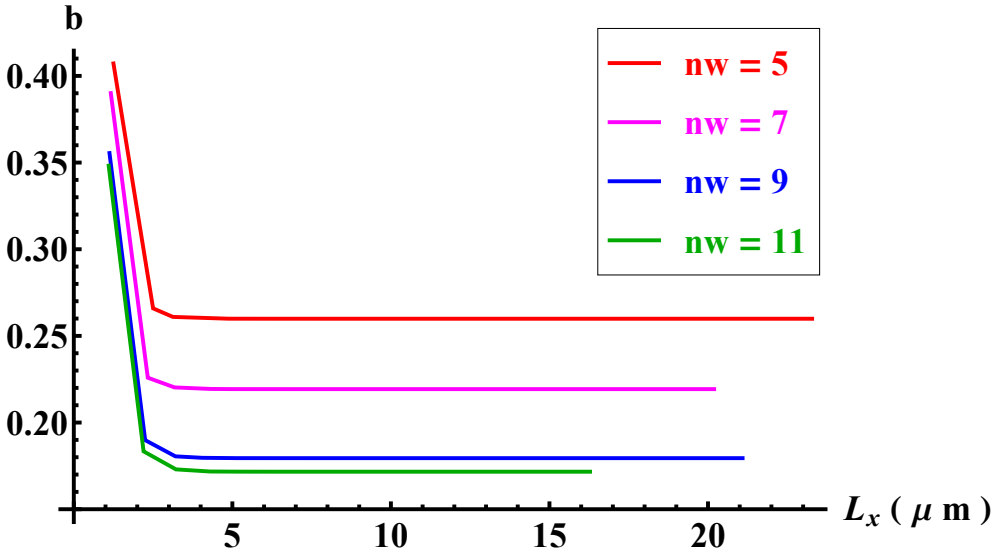
The numerical experiment was performed for waveguides WG1, WG4 and WG8A. For WG1 the

variation of the E^x wave fundamental mode normalised effective index is shown in Figure 2.10. The E^x wave fundamental mode for WG1 is shown in Figure 2.11 for a different values of the size of the computational domain. Figure 2.10 and 2.11 indicate that the solution has converged when $n_w \geq 11$, $L_x > 5\,(\mu\text{m})$.

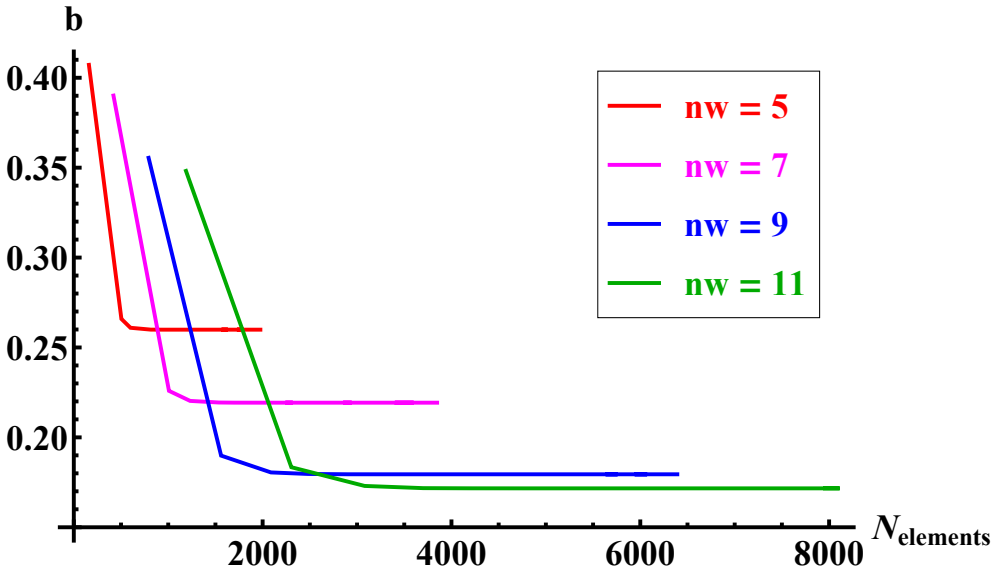
For WG4 the variation of the E^x wave fundamental mode normalised effective index is shown in Figure 2.12. The WG4 E^x wave fundamental mode is shown in Figure 2.13 for a different values of the size of the computational domain. These figures indicate that the solution has converged when $n_w \geq 11$ and $L_x > 5.5\,(\mu\text{m})$.

For WG8A the E^x wave fundamental mode normalised effective index variation is shown in Figure 2.14. The E^x wave fundamental mode for WG8A is shown in Figure 2.15 for a different values of the size of the computational domain. Figures 2.14 and 2.15 show that the solution has converged when $n_w \geq 11$ and $L_x > 10\,(\mu\text{m})$.

From this numerical experiment it can be deduced that calculations for which $n_w > 11$ and $L_x \geq 5\,W$ will converge reasonably well. In each case the solution has converged when $N_{elems} > 4000$. Figures 2.11, 2.13 and 2.15 show that the mode profiles assume the correct shape as the size of the computational domain increases. The conclusions from this experiment are that a choice of $n_w > 11$ and $L_x \geq 5\,W$ should ensure that an accurate solution is being computed. These results will be used as guidelines in future waveguide mode calculations. Further analysis may indicate a non-linear relationship between L_x and W but this is not being pursued at this point.

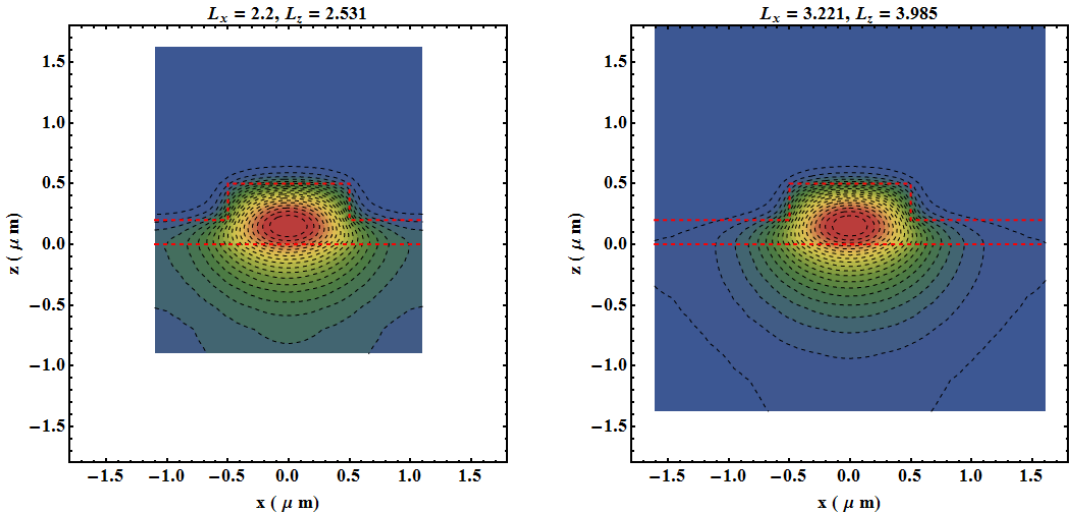


(a) b versus L_x



(b) b versus N_{elems}

Figure 2.10: Variation of the E^x wave fundamental mode normalised effective index in WG1. The waveguide materials and dimensions are available in Table 2.1.



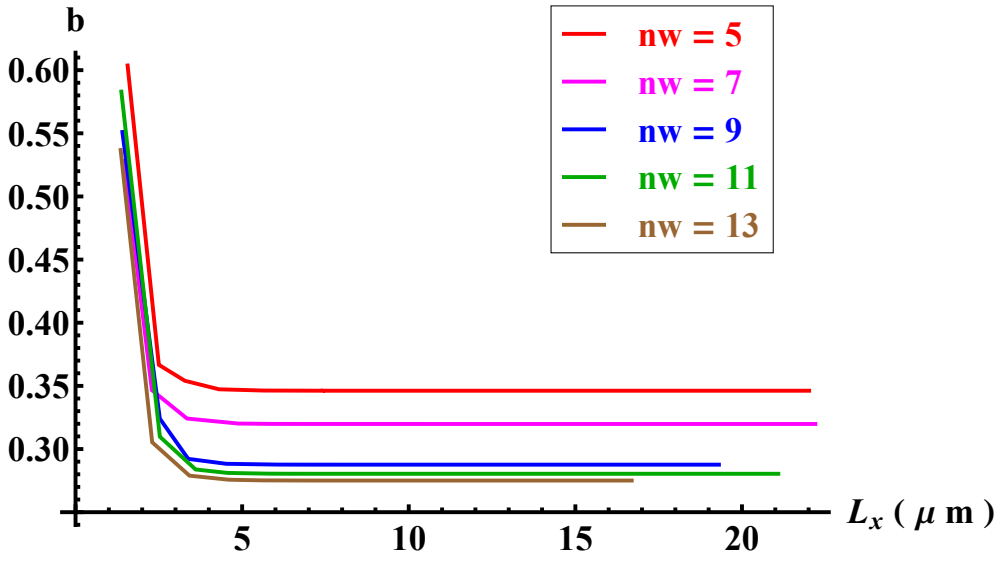
(a) $n_w = 11$, $L_x = 2.2\,(\mu\text{m})$, $L_z = 2.5\,(\mu\text{m})$

(b) $n_w = 11$, $L_x = 3.2\,(\mu\text{m})$, $L_z = 4.0\,(\mu\text{m})$

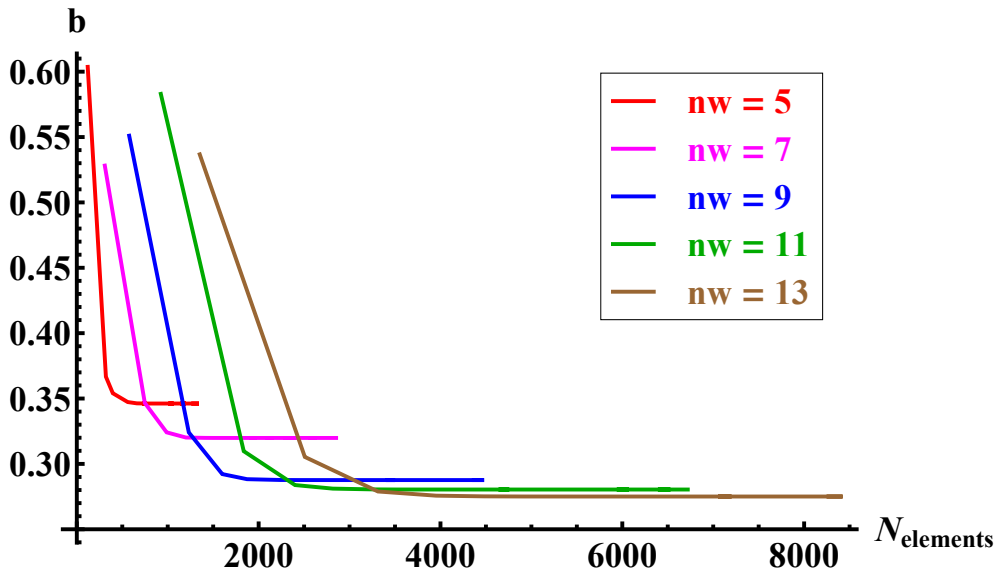
(c) $n_w = 11$, $L_x = 4.3\,(\mu\text{m})$, $L_z = 4.6\,(\mu\text{m})$

(d) $n_w = 11$, $L_x = 5.2\,(\mu\text{m})$, $L_z = 6.8\,(\mu\text{m})$

Figure 2.11: E^x wave fundamental mode of waveguide WG1 for different lengths of the computational domain. The waveguide materials and dimensions are available in Table 2.1.

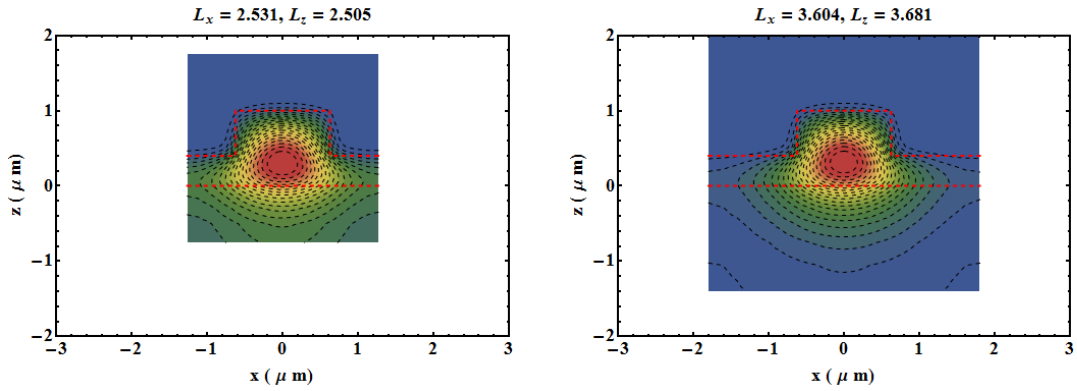


(a) b versus L_x



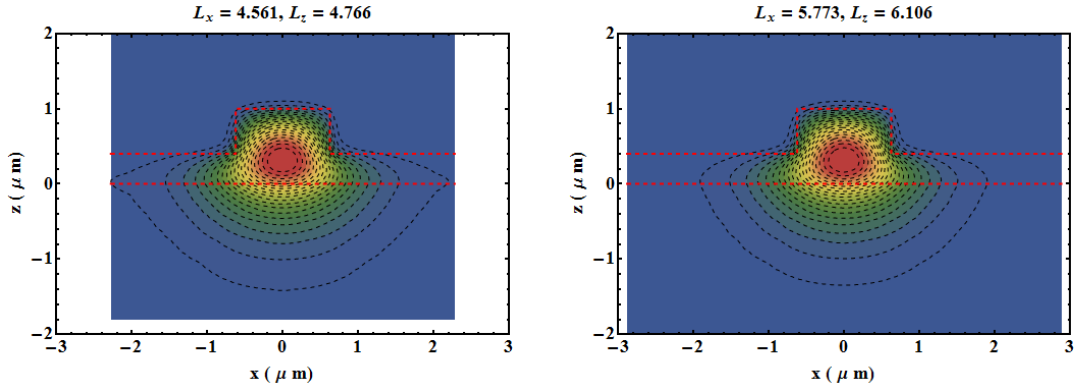
(b) b versus N_{elems}

Figure 2.12: Variation of the E^x wave fundamental mode normalised effective index in WG4. The waveguide materials and dimensions are available in Table 2.1.



(a) $n_w = 11$, $L_x = 2.5\,(\mu\text{m})$, $L_z = 2.5\,(\mu\text{m})$

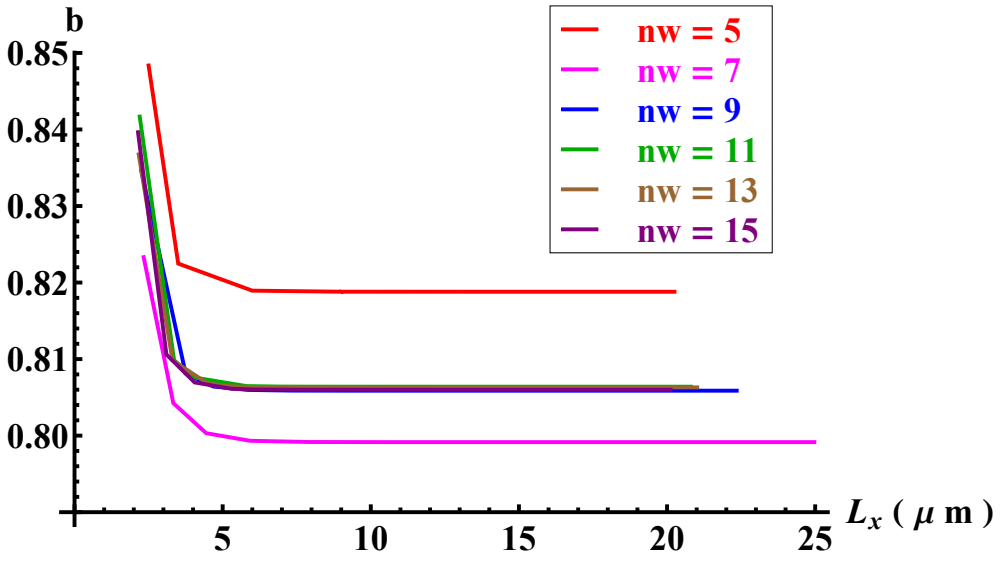
(b) $n_w = 11$, $L_x = 3.6\,(\mu\text{m})$, $L_z = 3.7\,(\mu\text{m})$



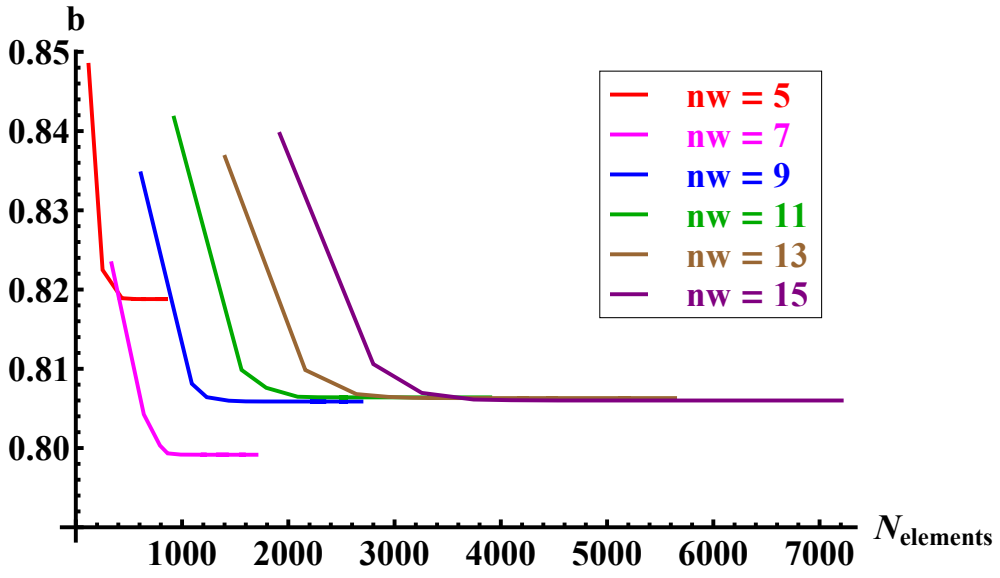
(c) $n_w = 11$, $L_x = 4.6\,(\mu\text{m})$, $L_z = 4.8\,(\mu\text{m})$

(d) $n_w = 11$, $L_x = 5.8\,(\mu\text{m})$, $L_z = 6.1\,(\mu\text{m})$

Figure 2.13: E^x wave fundamental mode of waveguide WG4 for different lengths of the computational domain. The waveguide materials and dimensions are available in Table 2.1.

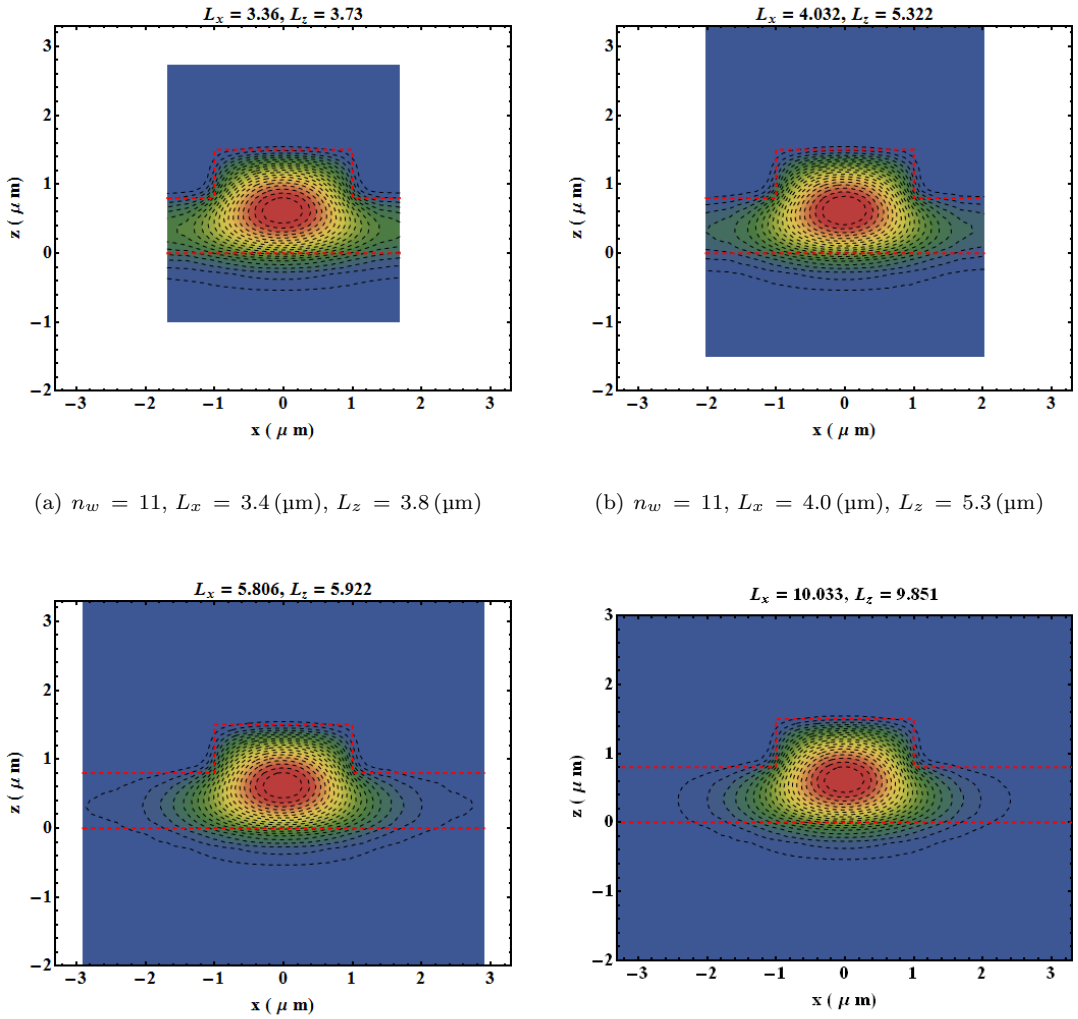


(a) b versus L_x



(b) b versus N_{elems}

Figure 2.14: Variation of the E^x wave fundamental mode normalised effective index in WG8A. The waveguide materials and dimensions are available in Table 2.1.



(a) $n_w = 11$, $L_x = 3.4\,(\mu\text{m})$, $L_z = 3.8\,(\mu\text{m})$

(b) $n_w = 11$, $L_x = 4.0\,(\mu\text{m})$, $L_z = 5.3\,(\mu\text{m})$

(c) $n_w = 11$, $L_x = 5.8\,(\mu\text{m})$, $L_z = 5.9\,(\mu\text{m})$

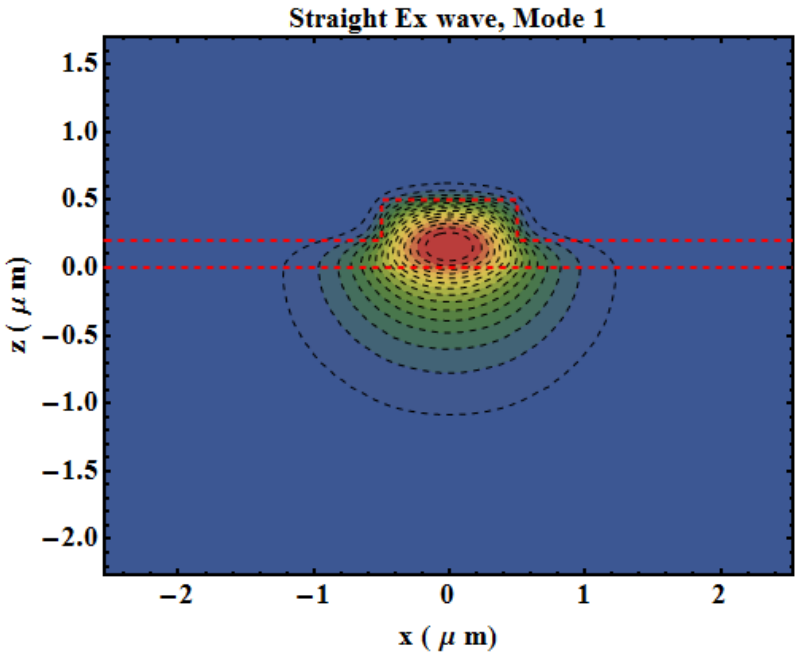
(d) $n_w = 11$, $L_x = 9.8\,(\mu\text{m})$, $L_z = 10\,(\mu\text{m})$

Figure 2.15: E^x wave fundamental mode of waveguide WG8A for different lengths of the computational domain. The waveguide materials and dimensions are available in Table 2.1.

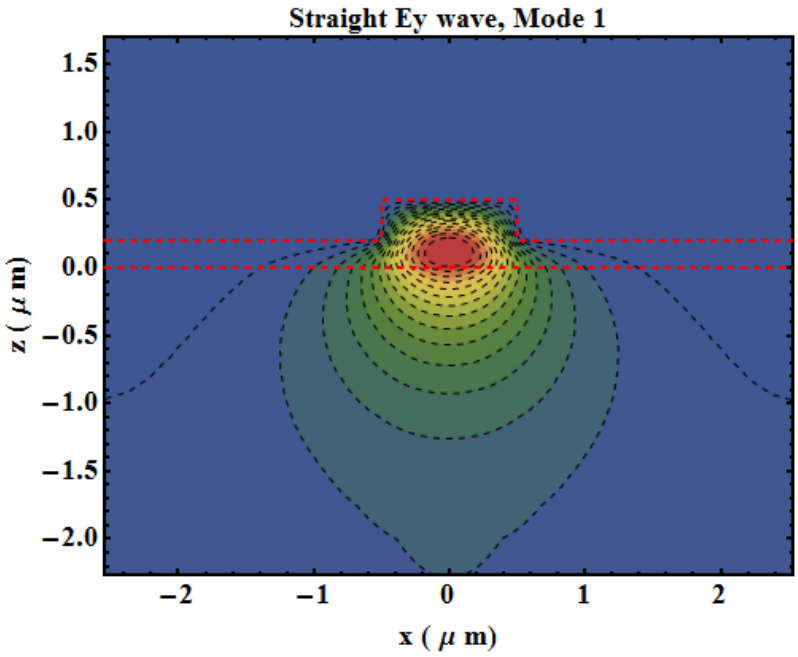
2.5.3 Straight waveguides modes and propagation constants

Using *SFEM_Modes* the propagation constants and mode profiles in an optical waveguide can be computed. The geometry of the waveguide, and its material parameters determine the number of modes that are present in the structure. Waveguides WG1 and WG4 are single mode waveguides, for a given polarisation, as can be seen in Figures 2.16 and 2.17 respectively. These waveguides have a narrow core region that prevents other modes from propagating. Waveguides WG8A and WG8B however, have very large core areas and this allows multiple modes to be excited in the waveguide. The modes corresponding to E^x polarised waves in waveguide WG8A are shown in Figure 2.18. The modes corresponding to E^y polarised waves in waveguide WG8A are shown in Figure 2.19. It should be noted that the boundary of the computational domain is having an effect on the calculation of the higher order modes for WG8A. The modes in Figures 2.18(b) - 2.18(d) and Figures 2.19(b) - 2.19(d) are interacting with the computational domain boundary. The reason for this is because the computational domain is a part of the solution being computed. If L_x was made larger again, the shape of the higher order modes may change. However, as this thesis is principally concerned with the behaviour of waveguide fundamental modes the problem is considered to be beyond the work of this thesis.

On the other hand waveguides WG9A and WG9B have similar core dimensions as WG8A and WG8B, but a very narrow slab section. This large etch depth prevents the excitation of many higher order modes which can be desirable depending on the application. The modes corresponding to E^x polarised waves in waveguide WG9A are shown in Figure 2.20. The modes corresponding to E^y polarised waves in waveguide WG9A are shown in Figure 2.21. These mode profiles also illustrate the effect of polarisation mode dispersion that is present in the waveguides. The effect can be seen by comparing the mode shapes in each of the waveguides for the different polarisations, and also the value of the propagation constants. It can also be seen that the large etch depth is preventing the field from interacting with the computational domain boundary so the shape of the higher modes for WG9A and WG9B is accurate.

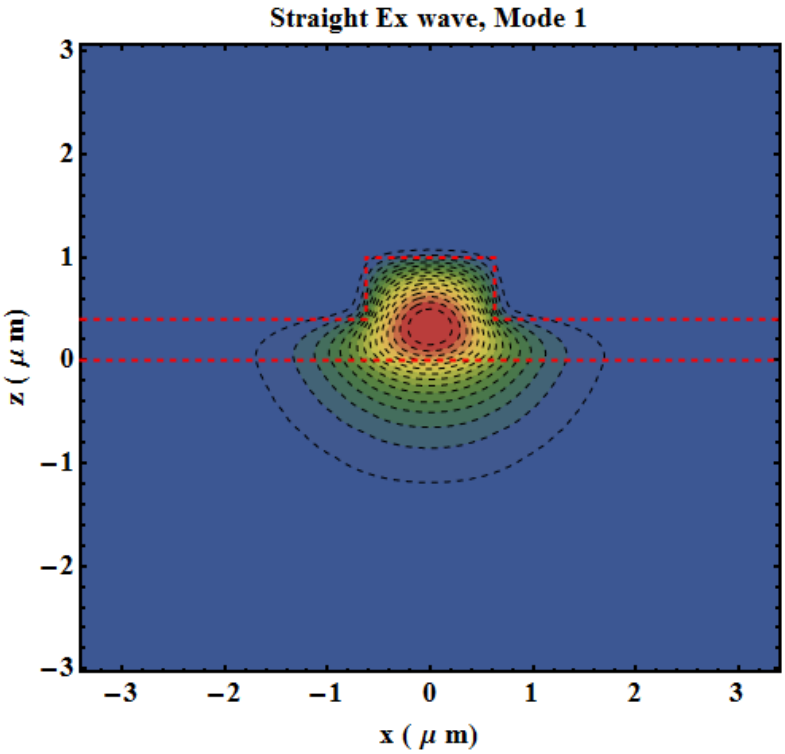


(a) E^x polarisation, $\beta = 12.988\,(\mu\text{m})^{-1}$

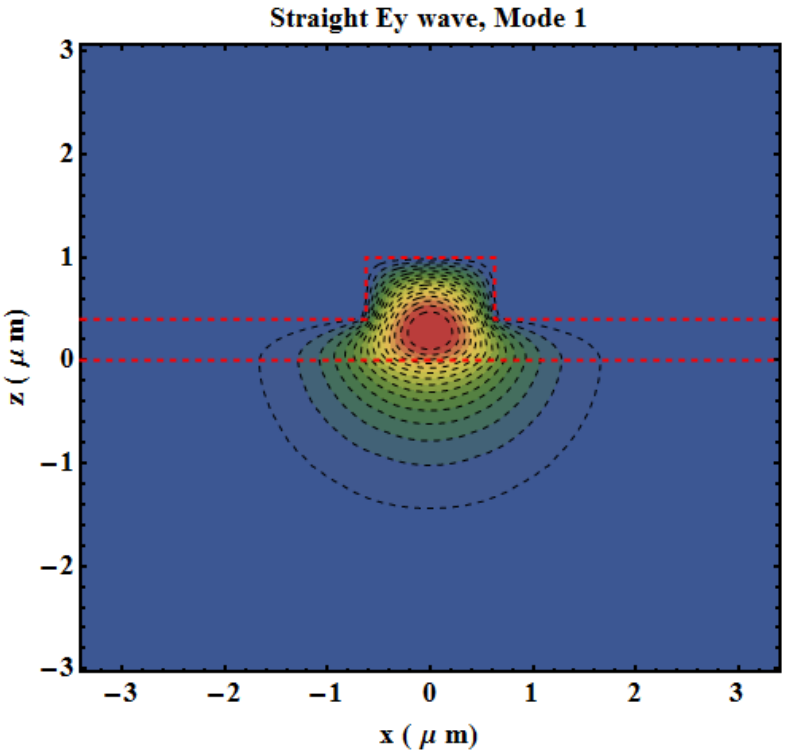


(b) E^y polarisation $\beta = 12.867\,(\mu\text{m})^{-1}$

Figure 2.16: Fundamental modes of WG1. Modes were computed using 75×50 nodes that define 7252 elements in a computational domain with dimensions $5.079 \times 3.97\,(\mu\text{m})^2$. The waveguide materials and dimensions are available in Table 2.1. For waveguide WG1 bound mode propagation constants must satisfy $12.85 < \beta < 13.7$.

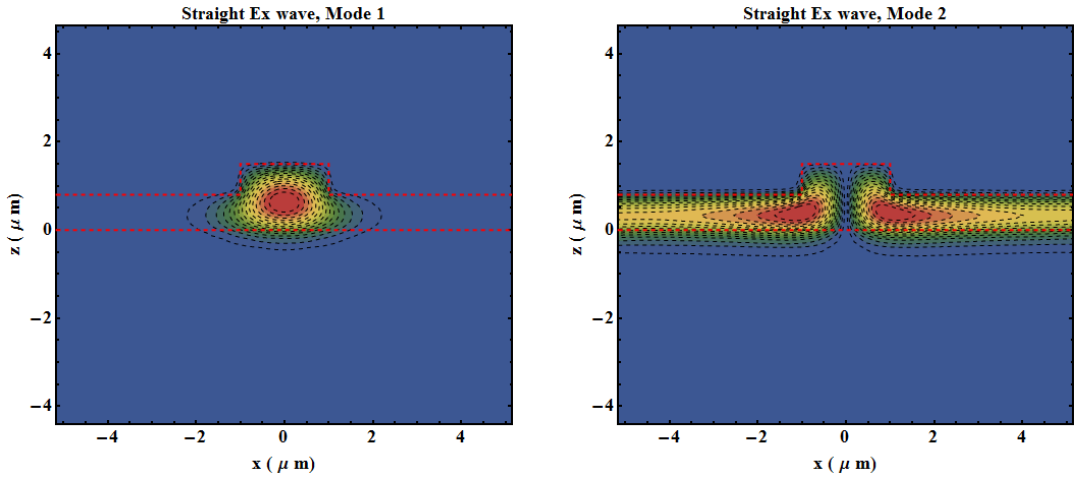


(a) E^x polarisation, $\beta = 13.649\,(\mu\text{m})^{-1}$



(b) E^y polarisation, $\beta = 13.609\,(\mu\text{m})^{-1}$

Figure 2.17: Fundamental modes of WG4. Modes were computed using 71×48 nodes that define 6580 elements in a computational domain with dimensions $6.8 \times 6.102\,(\mu\text{m})^2$. The waveguide materials and dimensions are available in Table 2.1. For waveguide WG4 bound mode propagation constants must satisfy $13.54 < \beta < 13.94$.



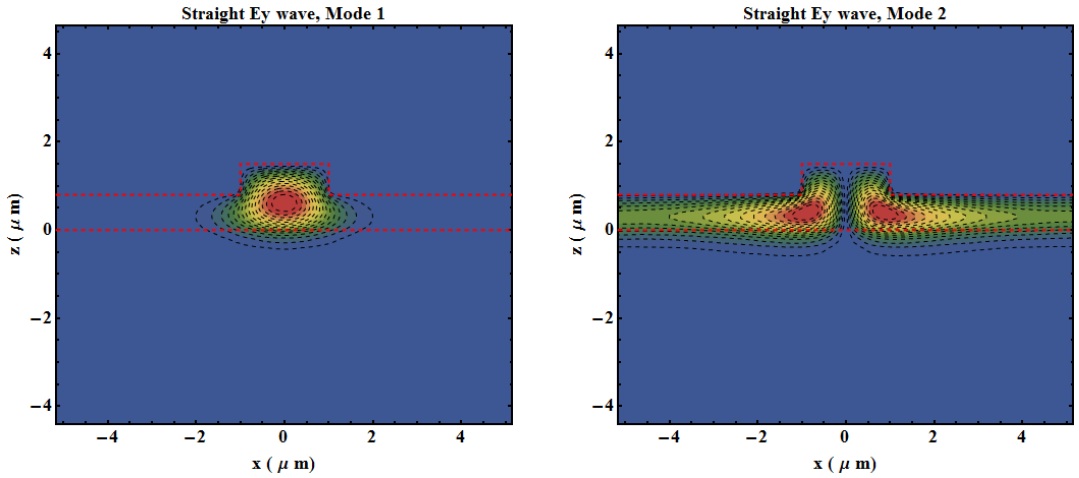
(a) Fundamental mode, $\beta = 13.536\,(\mu\text{m})^{-1}$

(b) Mode 2, $\beta = 13.428\,(\mu\text{m})^{-1}$

(c) Mode 3, $\beta = 13.422\,(\mu\text{m})^{-1}$

(d) Mode 4, $\beta = 13.412\,(\mu\text{m})^{-1}$

Figure 2.18: E^x polarised modes of WG8A. Modes were computed using 59×45 nodes that define 5104 elements in a computational domain with dimensions $10.318 \times 9.034\,(\mu\text{m})^2$. The waveguide materials and dimensions are available in Table 2.1. For waveguide WG8A bound mode propagation constants must satisfy $12.85 < \beta < 13.7$.



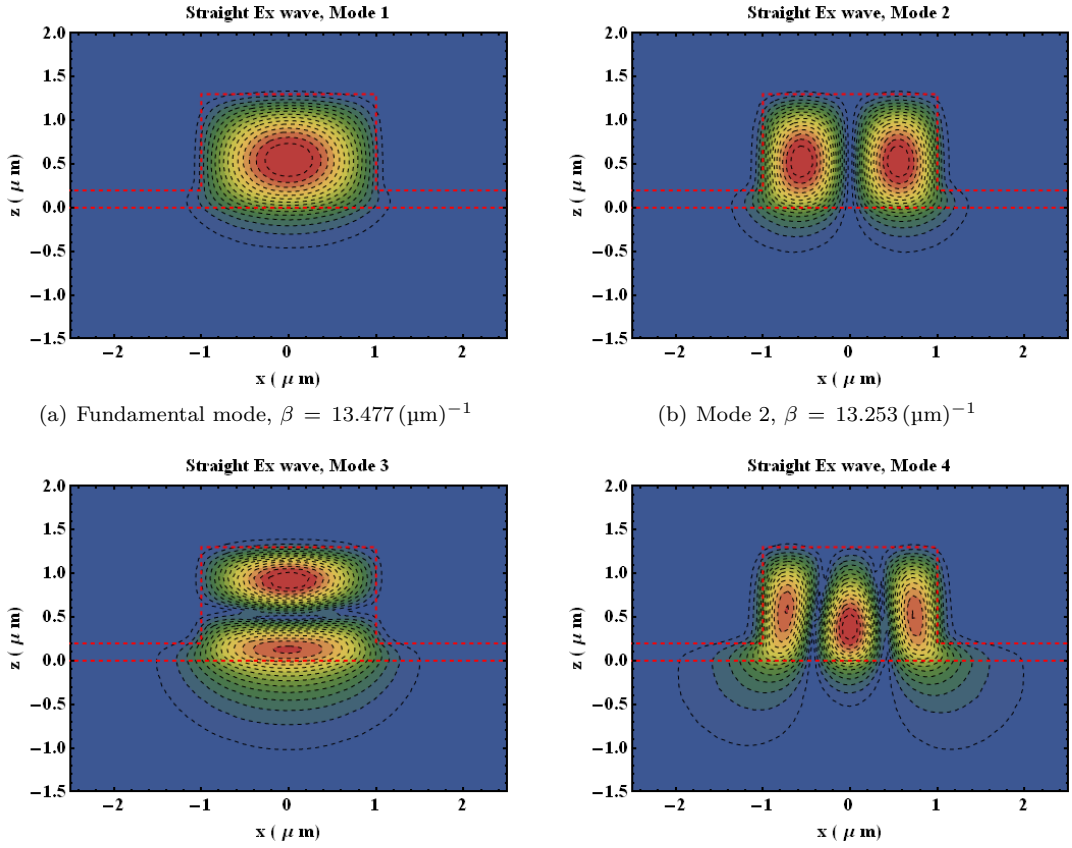
(a) Fundamental mode, $\beta = 13.517\,(\mu\text{m})^{-1}$

(b) Mode 2, $\beta = 13.389\,(\mu\text{m})^{-1}$

(c) Mode 3, $\beta = 13.378\,(\mu\text{m})^{-1}$

(d) Mode 4 , $\beta = 13.371\,(\mu\text{m})^{-1}$

Figure 2.19: E^y polarised modes of WG8A. Modes were computed using 59×45 nodes that define 5104 elements in a computational domain with dimensions $10.318 \times 9.034\,(\mu\text{m})^2$. The waveguide materials and dimensions are available in Table 2.1. For waveguide WG8A bound mode propagation constants must satisfy $12.85 < \beta < 13.7$.



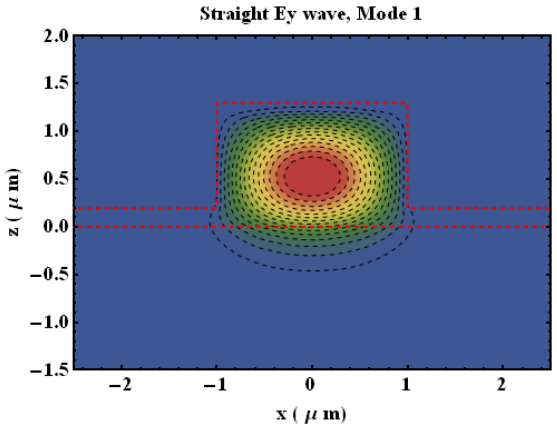
(a) Fundamental mode, $\beta = 13.477\,(\mu\text{m})^{-1}$

(b) Mode 2, $\beta = 13.253\,(\mu\text{m})^{-1}$

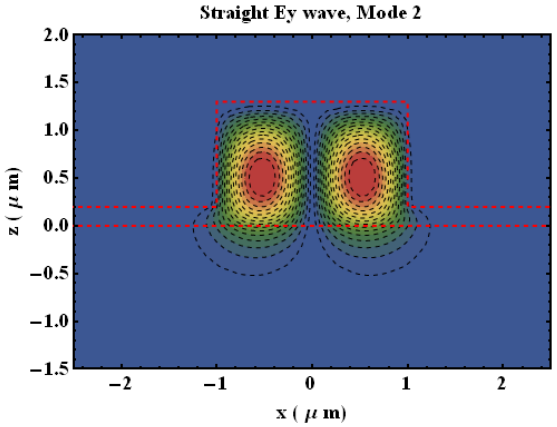
(c) Mode 3, $\beta = 13.043\,(\mu\text{m})^{-1}$

(d) Mode 4, $\beta = 12.881\,(\mu\text{m})^{-1}$

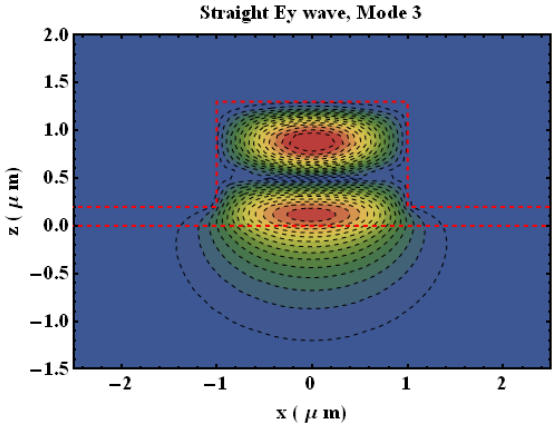
Figure 2.20: E^x polarised modes of WG9A. Modes were computed using 59×57 nodes that define 6496 elements in a computational domain with dimensions $10.318 \times 9.297\,(\mu\text{m})^2$. The waveguide materials and dimensions are available in Table 2.1. For waveguide WG9A bound mode propagation constants must satisfy $12.85 < \beta < 13.7$.



(a) Fundamental mode, $\beta = 13.449\,(\mu\text{m})^{-1}$



(b) Mode 2, $\beta = 13.195\,(\mu\text{m})^{-1}$



(c) Mode 3, $\beta = 12.979\,(\mu\text{m})^{-1}$

Figure 2.21: E^y polarised modes of WG9A. Modes were computed using 59×57 nodes that define 6496 elements in a computational domain with dimensions $10.318 \times 9.297\,(\mu\text{m})^2$. The waveguide materials and dimensions are available in Table 2.1. For waveguide WG9A bound mode propagation constants must satisfy $12.85 < \beta < 13.7$.

2.6 Discussion

The finite element method as it is applied to optical waveguides has been developed. An implementation of this method has been written in C++. The code is capable of analysing straight and, as shall be seen in Section 5.2 of Chapter 5, curved waveguides. Accurate mode profiles can be computed using the code, once the mesh parameters have been chosen correctly.

In the next chapter a method for propagating waves in optical devices in general, and curved structures in particular, is developed. This numerical method will allow for the characterisation of the optical properties of a device.

Chapter 3

Optical Wave Propagation

Summary: *The numerical method necessary for propagating a mode in a curved optical waveguide is presented. It is shown how the finite element beam propagation method is used to propagate a mode in an optical waveguide via the solution of a system of linear equations. A computer code that implements the finite element beam propagation method is presented. The necessary boundary conditions are discussed. The applicability of the finite element beam propagation method is demonstrated by its application to Gaussian beam propagation in free space and in a rib waveguide.*

3.1 Introduction

It was shown in Chapter 1 that a curved structure can be mapped onto an equivalent straight structure by means of a conformal transformation. It was shown that the field in the transformed structure is described by[1]

$$2\,i\,\gamma\,P\,\frac{\partial\phi}{\partial v} - P\,\frac{\partial^2\phi}{\partial v^2} = P\,\frac{\partial^2\phi}{\partial u^2} + P\,\Gamma\,\frac{\partial^2\phi}{\partial y^2} + k_0^2\,Q\,\Gamma\,\phi - P\,\gamma^2\,\phi \tag{3.1}$$

where the field varies transversely along the $\hat{\mathbf{u}}$ and $\hat{\mathbf{z}}$ directions and propagates along the $\hat{\mathbf{v}}$ direction with complex propagation constant $\gamma = \beta + i\,\alpha$, $\alpha < 0$, so that the field components are of the form $\phi(u,\,y,\,v) = \phi(u,\,y,\,v)\,e^{-i\,\beta\,v}\,e^{\alpha\,v}$.

Since γ is not known a-priori the solution of equation (3.1) can only be computed numerically. As is the case with the numerical calculation of waveguide mode profiles there are a large number of techniques currently being used to numerically propagate light in waveguide structures. Propagation of light can be performed using the fast-fourier transform technique [81–83], the finite difference method [84–87], the finite element method [88–99], the method of lines [100] and the eigenmode expansion method [67] to name a few. Techniques that allow for the analysis of waves propagating in more than one direction also exist, these are known as bi-directional beam propagation methods [101,102]. The finite difference time domain method is also used to analyse the propagation of waves in photonic devices [69].

Numerical propagation analysis generally assumes the following procedure: launch a mode profile into the waveguide structure, compute the field a finite distance from the input by a

[1] The terms in the equation are defined in Table 1.2 on page 21

known method, assume the input to the next step is the field from the last computed step, repeat until you have propagated the desired distance. The propagation step is accomplished by means of the solution of a set of linear equations that link the field from the previous step with the field at the next step, i.e. $\hat{\mathbf{A}} \cdot \phi^{new} = \hat{\mathbf{B}} \cdot \phi^{old}$ for matrices $\hat{\mathbf{A}}$ and $\hat{\mathbf{B}}$ that describe the waveguide cross-section at each step. Boundary conditions that remove numerical reflections from the edge of the computational domain are required to prevent the wave being propagated from being distorted [103–112].

In keeping with Chapter 2 a beam propagation method based on the finite element method (FE-BPM) is used to perform the propagation simulations for this thesis. Analysis of FE-BPM and its application to the solution of equation (3.1) is presented in Sections 3.2 and 3.3. The boundary conditions that remove non-physical reflections from the computational domain are discussed in Section 3.4. An object oriented C++ implementation of FE-BPM is presented in Section 3.5 and finally, for this chapter, the testing of the FE-BPM code for two and three dimensional simulations is discussed in Section 3.6.

3.2 Galerkin Finite Element Method

It was shown in Chapter 2 how the Rayleigh-Ritz finite element method is used to determine the numerical solution to equations of the form $\mathfrak{L}\,\phi = f$. The Rayleigh-Ritz approach is applicable when the differential operator $\mathfrak{L}$ is self-adjoint[2]. Testing equation (3.1) for self-adjointness leads to

$$(\mathfrak{L}\,\phi,\, \psi) - (\phi,\, \mathfrak{L}\,\psi) = 2\,i\,\gamma \iint_{\Omega} P \left(\phi \frac{\partial \psi}{\partial v} - \psi \frac{\partial \phi}{\partial v} \right) d\Omega \tag{3.2}$$

The r.h.s. of (3.2) is non-zero only if ϕ or ψ is zero, therefore the differential operator $\mathfrak{L}$ associated with (3.1) is not self-adjoint and the Rayleigh-Ritz finite element method cannot be used to compute a solution to (3.1).

There is, however, a generalised version of the variational principle that can be used to compute the solution to (3.1), it is known as the weak form of the variational principle and it can be used to express equations in variational form when the differential operator is not self-adjoint [63,64]. The technique is known as the Galerkin finite element method. The effect of the application of the Galerkin FEM is to reduce a differential equation to an equivalent set of equations, the solution of which is a stationary point of the functional associated with the differential equation. This is in contrast to the Rayleigh-Ritz FEM, which when applied yields a set of equations whose solution is a global minimum of the associated functional. The Galerkin finite element method requires that you find some function u such that $(\mathfrak{L}u - f,\, v) = 0$ is satisfied for some function v and inner product operator $(\cdot,\, \cdot)$[3].

Application of this method, for admissable functions, provides a set of equations whose solution is a stationary point of the functional associated with the problem and hence approximates the solution to the original equation. The integral $(\mathfrak{L}u - f,\, v) = 0$ is sometimes known as the weighted residual integral [70]. The Galerkin finite element method will be applied to equation (3.1) in order to approximate its solution numerically[4]. Upon application of the

[2] Defined on page 23
[3] Defined on page 23
[4] It should be noted that if the weak variational principle had been applied to equation (2.1) the exact same generalised eigenvalue problem would have been the result.

Galerkin FEM equation (3.1) will be reduced to an equivalent second order ordinary differential equation for the field along the direction of propagation.

3.3 FE-BPM for Three-Dimensional Waveguides

Assume a finite element subdivision of the computational domain where the field on each element is approximated by

$$\phi^e(u,\, y,\, v) \,=\sum_{j=1}^{3} N_j^e(u,\, y)\, \phi_j^e(v) \tag{3.3}$$

with the basis functions $N_j^e(u,\, y)$ being defined by equation (2.14). The difference between the function defined in equation (3.3) and the earlier basis function used in the mode profile analysis, equation (2.15), is that in this case it is assumed that ϕ depends on the position v along the direction of propagation as well as its value along the transverse coordinates u and y. Define the weighting function for the weighted residual integral to be $\psi^e \,=\, N_j^e(u,\, y)$ and assume that ϕ^e can be represented by equation (3.3). The residual integral is computed by calculating $(\mathfrak{L}\,\phi - f,\, \psi) \,=\, 0$ for equation (3.1). This amounts to computing the integral

$$R \,=\, \int_\Omega \psi\,(\mathfrak{L}\,\phi)\, d\Omega \,=\, 0$$

with $\mathfrak{L}$ being the differential operator for equation (3.1). This integral can be broken into a sum over contributions from each of the elements in the mesh. The weighted residual integral on the e^{th} element is given by

$$\begin{aligned} R^e \,=\, & \iint_e \psi^e\, P^e\, \frac{\partial^2 \phi^e}{\partial v^2}\, du\, dy \,-\, 2\, i\, \gamma \iint_e \psi^e\, P^e\, \frac{\partial \phi^e}{\partial v}\, du\, dy \\ & + \iint_e \psi^e\, P^e\, \frac{\partial^2 \phi^e}{\partial u^2}\, du\, dy \,+\, \iint_e \psi^e\, P^e\, \Gamma^e\, \frac{\partial^2 \phi^e}{\partial y^2}\, du\, dy. \\ & + \iint_e \psi^e\, (k_0^2\, Q^e\, \Gamma^e \,-\, \gamma^2\, P^e)\, \phi^e\, du\, dy \end{aligned} \tag{3.4}$$

The integrals containing derivatives with respect to u and y can be reduced using integration by parts [37, 70]. Performing these integrations results in

$$\begin{aligned} R^e \,=\, & \iint_e P^e\, \frac{\partial^2 \phi^e}{\partial v^2}\, \psi^e\, du\, dy \,-\, 2\, i\, \gamma \iint_e P^e\, \frac{\partial \phi^e}{\partial v}\, \psi^e\, du\, dy \\ & + \iint_e k_0^2\, Q^e\, \Gamma^e\, \phi^e\, \psi^e\, du\, dy - \iint_e P^e\, \frac{\partial \phi^e}{\partial u}\, \frac{\partial \psi^e}{\partial u}\, du\, dy\,. \\ & - \iint_e P^e\, \Gamma^e\, \frac{\partial \phi^e}{\partial y}\, \frac{\partial \psi^e}{\partial y}\, du\, dy \,-\, \iint_e \beta^2\, P^e\, \phi^e\, \psi^e\, du\, dy \end{aligned} \tag{3.5}$$

Substitution of $\phi^e(u,\, y,\, v)$ and $\psi^e(u,\, y)$ into equation (3.5) gives

$$\begin{aligned} R^e \;=\; & \iint_e P^e \sum_{j=1}^{3} N_j^e(u,\, y)\, \frac{d^2\phi_j^e}{dv^2}\, N_k^e(u,\, y)\, du\, dy \\ & -\; 2\, i\, \gamma \iint_e P^e \sum_{j=1}^{3} N_j^e(u,\, y)\, \frac{d\phi_j^e}{dv}\, N_k^e(u,\, y)\, du\, dy \\ & +\; \iint_e k_0^2\, Q^e\, \Gamma^e \sum_{j=1}^{3} N_j^e(u,\, y)\, \phi_j^e(v)\, N_k^e(u,\, y)\, du\, dy \\ & -\; \iint_e P^e \sum_{j=1}^{3} \frac{\partial N_j^e}{\partial u}\, \phi_j^e(v)\, \frac{\partial N_k^e}{\partial u}\, du\, dy \\ & -\; \iint_e P^e\, \Gamma^e \sum_{j=1}^{3} \frac{\partial N_j^e}{\partial y}\, \phi_j^e(v)\, \frac{\partial N_k^e}{\partial y}\, du\, dy \\ & -\; \iint_e \gamma^2\, P^e \sum_{j=1}^{3} N_j^e(u,\, y)\, \phi_j^e(v)\, N_k^e(u,\, y)\, du\, dy \end{aligned} \quad . \tag{3.6}$$

Re-arranging the v dependent terms, and assuming that p^e, q^e are constant across an element, the weighted residual integral reduces to equation

$$\begin{aligned} R^e \;=\; & \sum_{j=1}^{3} P^e\, A_{j\,k}^e\, \frac{d^2\phi_j^e}{dv^2} \;-\; 2\, i\, \gamma \sum_{j=1}^{3} P^e\, A_{j\,k}^e\, \frac{d\phi_j^e}{dv} \\ & +\; \sum_{j=1}^{3} k_0^2\, Q^e\, \Gamma^e\, A_{j\,k}^e\, \phi_j^e(v) \;-\; \sum_{j=1}^{3} P^e\; B_{j\,k}^e\, \phi_j^e(v). \\ & -\; \sum_{j=1}^{3} P^e\, \Gamma^e\, C_{j\,k}^e\, \phi_j^e(v) \;-\; \sum_{j=1}^{3} \gamma^2\, P^e\, A_{j\,k}^e\, \phi_j^e(v) \end{aligned} \tag{3.7}$$

where the terms $A_{j\,k}^e$, $B_{j\,k}^e$ and $C_{j\,k}^e$ are matrices defined by the integrals (2.18) - (2.20), see page 27.

Equation (3.7) represents the weighted residual integral for a single element, the weighted residual integral for the entire mesh is computed by summing over the contributions from each of the mesh elements. Setting this sum to zero yields the semi-discrete analogue of equation (3.1) [90–94, 96–98]

$$\hat{\mathbf{M}}\, \frac{d^2\hat{\mathbf{\Phi}}}{dv^2} \;-\; 2\, i\, \gamma\, \hat{\mathbf{M}}\, \frac{d\hat{\mathbf{\Phi}}}{dv} \;+\; (\hat{\mathbf{K}} \;-\; \gamma^2\, \hat{\mathbf{M}})\, \hat{\mathbf{\Phi}} \;=\; \mathbf{0}. \tag{3.8}$$

$$\hat{\mathbf{\Phi}} \;=\; \sum_{e=1}^{M} \phi^e(v) \tag{3.9}$$

$$\hat{\mathbf{M}} \;=\; \sum_{e=1}^{M} P^e\, A^e \tag{3.10}$$

$$\hat{\mathbf{K}} \;=\; \sum_{e=1}^{M} k_0^2\, Q^e\, \Gamma^e\, A^e \;-\; P^e\, B^e \;-\; P^e\, \Gamma^e\, C^e \tag{3.11}$$

Equation (3.8) is a 2^{nd} order ordinary differential equation that describes the field along the direction of propagation. $\hat{\mathbf{\Phi}}$, defined in equation (3.9), is a vector representing the solution at each node of the mesh, $\hat{\mathbf{M}}$ and $\hat{\mathbf{K}}$, defined in equations (3.10) and (3.11) respectively, are the

global matrices that characterise the mesh along the direction of propagation. Note that $\hat{\mathbf{M}}$ and $\hat{\mathbf{K}}$ have the same structure as when they are used to compute the mode profiles of a waveguide, see Section 2.3.2. If in (3.8) the terms involving the derivatives are neglected it reduces to the generalised eigenvalue problem that was encountered when computing the waveguide mode profiles. The complex propagation constant, γ, is unknown. However, in a waveguide whose properties will change along the direction of propagation it is necessary to have some method whereby the propagation constant during propagation, in Section 3.3.3 a formula for updating the propagation constant during propagation is derived [89–94, 96–98].

It remains to discuss how the solution of (3.8) is computed at each propagation step. The first step in this process is to make an approximation of equation (3.8), i.e. its order is reduced to that of an equivalent first order equation. The method for achieving this is presented in Section 3.3.1 [91, 93, 94, 96, 98, 113]. The second step is to solve the reduced equation using numerical integration. The numerical integration algorithm used is detailed in Section 3.3.2.

3.3.1 Application of the Padé approximation technique

To numerically compute the propagation of a light beam through a waveguide equation (3.8) must be solved at each step along the direction of propagation. The usual method for numerically solving 2^{nd} order ordinary differential equations is to re-write the equation as a pair of coupled 1^{st} order ordinary differential equations [40]. However, the Padé approximation technique, introduced by Hadley [113], enables a 2^{nd} order ordinary differential equation to be written as a single 1^{st} order ordinary differential equation, the solution of which closely approximates that of the original 2^{nd} order equation. The resulting 1^{st} order equation can then be solved by numerical integration with the trapezoidal rule [91, 93, 94, 96, 98].

To apply the Padé approximation technique re-write equation (3.8) by bringing the derivative terms to the left and the non-derivative terms to the right.

$$2\,i\,\gamma\,\hat{\mathbf{M}}\,\frac{d\hat{\mathbf{\Phi}}}{dv} - \hat{\mathbf{M}}\,\frac{d^2\hat{\mathbf{\Phi}}}{dv^2} = (\hat{\mathbf{K}} - \gamma^2\,\hat{\mathbf{M}})\,\hat{\mathbf{\Phi}} \tag{3.12}$$

Multiply equation (3.12) by $\hat{\mathbf{M}}^{-1}/2\,i\,\gamma$ to obtain

$$\frac{d\hat{\mathbf{\Phi}}}{dv} - \frac{1}{2\,i\,\gamma}\,\frac{d^2\hat{\mathbf{\Phi}}}{dv^2} = \frac{1}{2\,i\,\gamma}\,\hat{\mathbf{M}}^{-1}\,(\hat{\mathbf{K}} - \gamma^2\,\hat{\mathbf{M}})\,\hat{\mathbf{\Phi}}. \tag{3.13}$$

A derivative operator can be factored from the left hand side of equation (3.13) to leave

$$\frac{d}{dv}\left(1 - \frac{1}{2\,i\,\gamma}\,\frac{d}{dv}\right)\hat{\mathbf{\Phi}} = \frac{1}{2\,i\,\gamma}\,\hat{\mathbf{M}}^{-1}\,(\hat{\mathbf{K}} - \gamma^2\,\hat{\mathbf{M}})\,\hat{\mathbf{\Phi}}. \tag{3.14}$$

From (3.14) a recurrence relation between the left and right hand sides, can be defined.

$$\left.\frac{d}{dv}\right|_n = \frac{\hat{\mathbf{M}}^{-1}}{2\,i\,\gamma}\,\frac{(\hat{\mathbf{K}} - \gamma^2\,\hat{\mathbf{M}})}{1 - \frac{1}{2\,i\,\gamma}\left.\frac{d}{dv}\right|_{n-1}} \quad \text{with} \quad \left.\frac{d}{dv}\right|_{-1} = 0 \tag{3.15}$$

This recurrence relation is used to construct the Padé approximation to equation (3.8) [113].

The first Padé approximation is obtained by taking $n = 0$ in equation (3.15), this is equivalent to the Fresnel approximation of ignoring 2^{nd} order derivatives of the field along the direction

of propagation [91, 93, 94, 96, 98, 113].

$$\begin{aligned}\left.\frac{d}{dv}\right|_0 &= \frac{\hat{\mathbf{M}}^{-1}}{2\,i\,\gamma}\frac{(\hat{\mathbf{K}}-\gamma^2\,\hat{\mathbf{M}})}{1-\left.\frac{1}{2\,i\,\gamma}\,\frac{d}{dv}\right|_{-1}}\\ &= \frac{\hat{\mathbf{M}}^{-1}}{2\,i\,\gamma}\frac{(\hat{\mathbf{K}}-\gamma^2\,\hat{\mathbf{M}})}{1-0}\\ &= \frac{\hat{\mathbf{M}}^{-1}}{2\,i\,\gamma}\,(\hat{\mathbf{K}}-\gamma^2\,\hat{\mathbf{M}})\\ \Rightarrow\; 2\,i\,\gamma\,\hat{\mathbf{M}}\,\frac{d\hat{\mathbf{\Phi}}}{dv} &= (\hat{\mathbf{K}}-\gamma^2\,\hat{\mathbf{M}})\,\hat{\mathbf{\Phi}}\end{aligned} \tag{3.16}$$

The Fresnel approximation of (3.8) is given by equation (3.16).

The second Padé approximation is obtained by taking $n = 1$, this is the wide angle approximation that is used for beam propagation analysis [91, 93, 94, 96, 98, 113].

$$\begin{aligned}\left.\frac{d}{dv}\right|_1 &= \frac{\hat{\mathbf{M}}^{-1}}{2\,i\,\gamma}\frac{(\hat{\mathbf{K}}-\gamma^2\,\hat{\mathbf{M}})}{1-\left.\frac{1}{2\,i\,\gamma}\,\frac{d}{dv}\right|_0}\\ &= \frac{\hat{\mathbf{M}}^{-1}}{2\,i\,\gamma}\frac{(\hat{\mathbf{K}}-\gamma^2\,\hat{\mathbf{M}})}{1-\frac{1}{2\,i\,\gamma}\left(\frac{\hat{\mathbf{M}}^{-1}}{2\,i\,\gamma}\,(\hat{\mathbf{K}}-\gamma^2\,\hat{\mathbf{M}})\right)}\\ &= \frac{\hat{\mathbf{M}}^{-1}}{2\,i\,\gamma}\frac{(\hat{\mathbf{K}}-\gamma^2\,\hat{\mathbf{M}})}{1+\frac{\hat{\mathbf{M}}^{-1}}{4\,\gamma^2}\,(\hat{\mathbf{K}}-\gamma^2\,\hat{\mathbf{M}})}\\ \Rightarrow 2\,i\,\gamma\left(\hat{\mathbf{M}}+\frac{1}{4\,\gamma^2}\,(\hat{\mathbf{K}}-\gamma^2\,\hat{\mathbf{M}})\right)\frac{d\hat{\mathbf{\Phi}}}{dv} &= (\hat{\mathbf{K}}-\gamma^2\,\hat{\mathbf{M}})\,\hat{\mathbf{\Phi}}\end{aligned} \tag{3.17}$$

The wide-angle approximation of (3.8) is given by (3.17).

It has been shown that a second order Padé approximation is sufficient to generate an accurate solution of equation (3.8) [91, 93, 94, 96, 98, 113]. In summary, the equation to be solved is

$$2\,i\,\gamma\,\hat{\mathbf{M}}^*\,\frac{d\hat{\mathbf{\Phi}}}{dv} = (\hat{\mathbf{K}}-\gamma^2\,\hat{\mathbf{M}})\,\hat{\mathbf{\Phi}} \tag{3.18}$$

where $\hat{\mathbf{M}}^*$ is defined by

$$\hat{\mathbf{M}}^* = \hat{\mathbf{M}} + \frac{1}{4\,\gamma^2}\,(\hat{\mathbf{K}}-\gamma^2\,\hat{\mathbf{M}}) \tag{3.19}$$

The numerical integration of equation (3.18) is discussed in Section (3.3.2).

3.3.2 Numerical integration of the propagation equation

Equation (3.18) must be integrated numerically over a step-size $\Delta\,v$. The algorithm used to compute the solution over a step is known by a multitude of names; Trapezoidal rule, Crank-Nicholson method [63] and Newmark method [70]. Application of the trapezoidal rule between

the points $(v_j,\, v_{j+1})$ where $\Delta\, v \,=\, v_{j+1} \,-\, v_j$ leads to

$$\begin{aligned} 2\, i\, \gamma_j\, \hat{\mathbf{M}}_j^*\, (\hat{\mathbf{\Phi}}_{j+1} \,-\, \hat{\mathbf{\Phi}}_j) \,= \\ \Delta v\, (\hat{\mathbf{K}}_j \,-\, \gamma_j^2\, \hat{\mathbf{M}}_j)\, \left(\alpha\, \hat{\mathbf{\Phi}}_{j+1} \,+\, (1 \,-\, \alpha)\, \hat{\mathbf{\Phi}}_j\right) \end{aligned} \tag{3.20}$$

Re-arranging (3.20) by putting the $j+1$ terms on the left and the j terms on the right yields

$$\begin{aligned} \left(2\, i\, \gamma_j\, \hat{\mathbf{M}}_j^* \,-\, \Delta v\, \alpha\, (\hat{\mathbf{K}}_j \,-\, \gamma_j^2\, \hat{\mathbf{M}}_j)\right)\, \hat{\mathbf{\Phi}}_{j+1} \,= \\ \left(2\, i\, \gamma_j\, \hat{\mathbf{M}}_j^* \,+\, \Delta v\, (1 \,-\, \alpha)\, (\hat{\mathbf{K}}_j \,-\, \gamma_j^2\, \hat{\mathbf{M}}_j)\right)\, \hat{\mathbf{\Phi}}_j \end{aligned} . \tag{3.21}$$

Equation (3.21) is a linear system of equations that relates the field at step j to the field at step $j+1$.

$$\hat{\mathbf{A}} \cdot \hat{\mathbf{\Phi}}_{j+1} \,=\, \hat{\mathbf{B}} \cdot \hat{\mathbf{\Phi}}_j \tag{3.22}$$

$$\hat{\mathbf{A}} \,=\, 2\, i\, \gamma_j\, \hat{\mathbf{M}}_j^* \,-\, \Delta v\, \alpha\, (\hat{\mathbf{K}}_j \,-\, \gamma_j^2\, \hat{\mathbf{M}}_j) \tag{3.23}$$

$$\hat{\mathbf{B}} \,=\, 2\, i\, \gamma_j\, \hat{\mathbf{M}}_j^* \,+\, \Delta v\, (1 \,-\, \alpha)\, (\hat{\mathbf{K}}_j \,-\, \gamma_j^2\, \hat{\mathbf{M}}_j) \tag{3.24}$$

The matrices necessary for the solution are dependent on the position along the direction of propagation. To ensure stability of the propagation algorithm choose $\frac{1}{2} \,\leq\, \alpha \,\leq\, 1$. This set of equations also holds in the Fresnel approximation case with $\hat{\mathbf{M}}^*$ being replaced by $\hat{\mathbf{M}}$.

In principle it should be possible to apply numerical integration schemes which are known to be more accurate, e.g. Runge-Kutta method order four or a multi-step technique such as the Adams-Bashforth method [72]. I suspect though that the resulting equations will be non-linear and this in turn would require further numerical approximation. In any case a step size of $\Delta\nu \,=\, 0.1\,(\mu\mathrm{m})$ is assumed for all simulations, this is smaller than previously reported step-sizes [91, 93, 94, 96, 98] and as such should ensure an accurate numerical integration along the direction of propagation.

3.3.3 Updating the propagation constant

As a wave propagates inside a waveguide it will change its properties depending on the material parameters and cross-section geometry. If the waveguide structure changes then the propagation constant must alter accordingly. This means that a mechanism for updating the propagation constant of a propagating beam is required as the wave is propagating. The weak-form of the variational principle enables the propagation constant as a function of path-length to be determined. It will be shown that the propagation constant can be computed directly by a series of integrations over the field as it is stepped through a waveguide device. Following that it will be shown that the multiple integrations can be replaced by a series of matrix multiplications with the matrices involved being the global matrices $\hat{\mathbf{K}}$ and $\hat{\mathbf{M}}$.

To obtain the propagation constant apply the weak form of the variational principle to equation (2.1) [89, 114]. Multiply (2.1) by ϕ and integrate over the domain on which the solution is sought, in this case the domain is the waveguide cross-section transverse to the direction of

propagation.

$$\iint \phi\, P\, \frac{\partial^2 \phi}{\partial u^2}\, dudy \,+\, \iint \phi\, P\, \Gamma\, \frac{\partial^2 \phi}{\partial y^2}\, dudy \,+\, k_0^2 \iint \phi\, Q\, \Gamma\, \phi\, dudy \,-\, \gamma^2 \iint \phi\, P\, \phi\, dudy \,=\, 0 \tag{3.25}$$

Integrating equation (3.25) leads to

$$\begin{aligned} &-\iint P \left(\frac{\partial \phi}{\partial u}\right)^2 dudy \,-\, \iint P\, \Gamma \left(\frac{\partial \phi}{\partial y}\right)^2 dudy \\ &+\, k_0^2 \iint Q\, \Gamma\, (\phi)^2\, dudy \,-\, \gamma^2 \iint P\, (\phi)^2\, dudy \,=\, 0 \end{aligned} \tag{3.26}$$

Writing equation (3.26) in inner product notation gives [89]

$$\gamma^2\, (P\phi,\, \phi) \,=\, k_0^2\, (Q\phi,\, \phi) \,-\, \left(P \frac{\partial \phi}{\partial u},\, \frac{\partial \phi}{\partial u}\right) \,-\, \left(P\, \Gamma\, \frac{\partial \phi}{\partial y},\, \frac{\partial \phi}{\partial y}\right) \tag{3.27}$$

If the field profile is known at any point then the propagation constant at that point can be computed using equation (3.27).

Since the finite element method is being used then an approximation of (3.27) can be obtained that replaces a numerical integration with a matrix multiplication. Each of the integrals in equation (3.27) can be approximated by expanding ϕ in the basis of elemental interpolating polynomials. This leads to the following formula for γ^2 [91, 93, 94, 96, 98]

$$\gamma^2 \,=\, \frac{\hat{\mathbf{\Phi}}^T \cdot \hat{\mathbf{K}} \cdot \hat{\mathbf{\Phi}}}{\hat{\mathbf{\Phi}}^T \cdot \hat{\mathbf{M}} \cdot \hat{\mathbf{\Phi}}} \tag{3.28}$$

where $\hat{\mathbf{\Phi}}^T$ is the conjugate transpose and $\hat{\mathbf{K}}$ and $\hat{\mathbf{M}}$ are the global matrices defined earlier by equations (2.32) and (2.33) respectively. This type of expression is known as a generalised Rayleigh quotient. Since $\hat{\mathbf{\Phi}}$ will, in general, be a complex-valued vector the real and imaginary parts of the propagation constant can be computed as a beam is propagated.

The time required for the matrix multiplications in equation (3.28) can be reduced if the matrices $\hat{\mathbf{K}}$ and $\hat{\mathbf{M}}$ are stored using the row-indexed storage format. Details for the time reduction achieved for a matrix triple product are presented in Appendix C.

3.4 Boundary Conditions for Beam Propagation

The method described in Section 3.3 allows for a wave to be propagated in an optical device. However, since the propagation is simulated on a finite domain light will be reflected from the edge of that domain, this reflected light is non-physical and will interfere with the results of any simulation. In order to remove these non-physical reflections appropriate boundary conditions must be employed at the domain edge. For the beam propagation method the type of boundary condition required is known as an absorbing boundary condition (ABC). ABC allow light to exit the computational domain without introducing non-physical reflections back into the propagation region. There are two main types; Transparent boundary conditions (TBC) [103] and perfectly matched layer boundary conditions(PML-BC) [104–112]. Description of these boundary conditions and the manner in which they are employed within FE-BPM are discussed in Sections 3.4.1 and 3.4.2 respectively.

3.4.1 Transparent boundaries

TBC were first introduced by Hadley [103]. In that paper it was shown that if the field near the edge of the computational domain behaves like

$$\phi \sim \phi_0 \, e^{i \, k_x \, x} \tag{3.29}$$

where ϕ_0 and k_x are complex constants and ϕ represents a component of the electromagnetic field being propagated, then a non-zero flux condition can be defined at the edge of the computational domain. This non-zero flux condition allows energy to leave the computational domain without being reflected from the domain edge, in contrast with Dirichlet or Neumann boundary conditions which conserve total energy inside the domain and thus create reflections at the domain edge. The fact that TBC allows light to leave the computational domain means that the nodes at the domain act like absorbers that do not permit reflection back into the domain.

The mechanism that permits this non-zero flux condition is the updating of the complex constant k_x between propagation steps. Hadley showed that the flux at the domain edge was given by [103]

$$F_n = \frac{1}{4 \, \beta \, \Delta x^2} \sin\left(\Re\{k_x\} \, \Delta x\right) \exp\left(-\Im\{k_x\} \, \Delta x\right) \left| \phi_{n-1}^{j} + \phi_{n-1}^{j+1} \right| \tag{3.30}$$

where F_n is the flux through the mesh boundary at node n, β is the propagation constant of the mode being propagated, $\Delta \, x$ is the spacing between the nodes in the mesh, ϕ_{n-1}^{*} is the value of the field at position $n-1$ for steps j and $j+1$, $\Re\{k_x\}$ is the real part of the complex constant k_x and $\Im\{k_x\}$ is its imaginary part. If $\Re\{k_x\}$ satisfies $0 < \Re\{k_x\} < \pi/\Delta x$ then equation (3.30) always has positive value, which means that energy is always flowing out of the computational domain. The value of k_x is determined by the condition

$$\frac{\phi_n^j}{\phi_{n-1}^j} = e^{i \, k_x \, \Delta x} \tag{3.31}$$

between propagation steps [103].

To incorporate the TBC into FE-BPM the following condition is imposed at the edge of the computational domain

$$\left(\frac{\partial \phi}{\partial x} + k_x \, \phi \right) \Bigg|_{\partial \Omega} = 0 \tag{3.32}$$

where k_x is a complex constant that is renewed with each propagation step by solving (3.31). Condition (3.32) is applied to the two dimensional equivalent of equation (3.4) when the integrals are computed. Following an identical analysis to that given in Section 3.3 the partial differential equation is reduced to a second order ODE that contains an extra term which incorporates the influence of the TBC[5] [90–93].

$$\hat{\mathbf{M}} \frac{d^2 \hat{\mathbf{\Phi}}}{dv^2} - 2 \, i \, \gamma \, \hat{\mathbf{M}} \frac{d \hat{\mathbf{\Phi}}}{dv} + (\hat{\mathbf{K}} - \gamma^2 \, \hat{\mathbf{M}}) \, \hat{\mathbf{\Phi}} + \hat{\mathbf{K}}_{\partial \Omega} \, \hat{\mathbf{\Phi}} = \mathbf{0} \tag{3.33}$$

[5] In Section 3.3 Neumann boundary conditions are assumed and this eliminates the extra term that arises here.

The global matrices $\hat{\mathbf{M}}$ and $\hat{\mathbf{K}}$ correspond to those of a one-dimensional slab waveguide [70, 90–93].

$$\hat{\mathbf{K}} = \sum_{e=1}^{M} (k_0^2 \, Q^e \, \Gamma^e \, A^e - P^e \, B^e)$$
$$\hat{\mathbf{M}} = \sum_{e=1}^{M} P^e \, A^e$$

where the matrices A^e and B^e are defined, assuming linear elements, by

$$A^e = \frac{l_e}{6} \begin{pmatrix} 2 & 1 \\ 1 & 2 \end{pmatrix} \qquad B^e = \frac{1}{l_e} \begin{pmatrix} 1 & -1 \\ -1 & 1 \end{pmatrix} \tag{3.34}$$

The extra term $\hat{\mathbf{K}}_{\partial\Omega}$ in equation (3.33) contains the effect of the TBC and in practice is an $n \times n$ matrix that is zero everywhere except at positions [1][1] and $[n][n]$, assuming a mesh containing $n > 1$ nodes. The effect of the $\hat{\mathbf{K}}_{\partial\Omega}$ term can be added into the two-dimensional equivalent of (3.22).

TBC can also be applied in three-dimensional propagation simulations [94]. In practice, however, this requires adding extra types of elements into the mesh which complicates the analysis and assembly of the global matrices required for the propagation [94]. It was felt that mixing different element types would be an extra, time-consuming, complication and for this reason, the TBC were not employed in any three-dimensional simulations as part of this thesis. Testing of the TBC is discussed in Section 3.6.

3.4.2 Perfectly matched layers

PML-BC are another type of absorbing boundary condition. They were introduced by Bérenger in [104]. In that paper it was shown that by placing a region of non-physical material around the computational domain, see Figure 3.1 taken from [112], waves could be absorbed in that domain and not suffer from reflections. The property that allowed for this region to be absorbing was that its conductivity was matched to the conductivity of the computational domain, hence the name perfectly matched layer. It was shown later that the PML-BC region could be defined using a complex change of coordinates [105–112]. Inside the computational domain the light is propagated according to Maxwell's equations. In the PML region the light is subject to Maxwell's equations that have been transformed by complex coordinate stretching, this change of coordinates simulates the presence of an absorbing region to prevent numerical reflections from accumulating inside the computational domain.

To apply PML-BC for optical wave propagation a change of coordinates is performed via $x_i' = s_i \, x_i$, where x_i corresponds to any of the coordinate axes, the parameter s defines the conductivity of the PML region along a particular direction [96–98, 105–110] and is defined by

$$s = 1 - i \frac{\sigma_e}{\omega \, \epsilon_0 \, n^2} = 1 - i \frac{\sigma_m}{\omega \, \mu_0} \tag{3.35}$$

where σ_e and σ_m are the electrical and magnetic conductivities respectively. In the non-PML region $s_i = 1$, which will leave Maxwell's equations unchanged [96–98]. In practical implementations a parabolic conductivity profile is assumed. This changes the definition of the

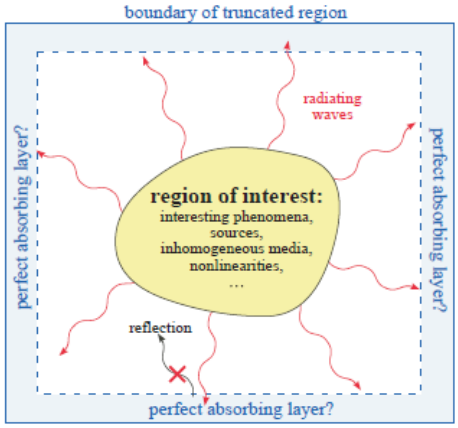


Figure 3.1: Object being studied surrounded by a perfectly matched layer region.

Table 3.1: Values of s_x and s_y

Region	s_x	s_y	s_x^2/s	s_y^2/s
I	1	s	$1/s$	s
II	s	1	s	$1/s$
III	1	1	$1/s$	$1/s$

parameter s so that it includes the effect of the perfectly matched layer reflectivity. With a parabolic conductivity profile the parameter s is defined as

$$s = 1 - i\,\frac{3\,\lambda}{4\,\pi\,n\,d}\left(\frac{\rho}{d}\right)^2 \log\frac{1}{R} \tag{3.36}$$

where n is the refractive index of the medium, ρ is the distance from the beginning of the PML region and d is the total thickness of the PML region [96–98].

Application of the complex change of coordinates defines a new gradient operator.

$$\nabla' = \left(\frac{\partial}{\partial x'}, \frac{\partial}{\partial y'}, \frac{\partial}{\partial z'}\right) = \left(s_x\frac{\partial}{\partial x}, s_y\frac{\partial}{\partial y}, s_z\frac{\partial}{\partial z}\right) \tag{3.37}$$

Substitution of this operator into Maxwell's equations (1.7) and (1.8) allows for a Helmholtz type equation to be derived that is valid in the transformed coordinates of the PML region [96–98, 107].

$$\frac{s_x}{s}\frac{\partial}{\partial x}\left(P\,s_x\frac{\partial\phi}{\partial x}\right) + s_y\frac{\partial}{\partial y}\left(P\,\frac{s_y}{s}\frac{\partial\phi}{\partial y}\right) + s\frac{\partial}{\partial z}\left(P\frac{\partial\phi}{\partial z}\right) + k_0^2\,Q\,s\,\phi = 0 \tag{3.38}$$

This equation is of the same type as (1.50) with the added "s" parameters. The ratios s_x/s and s_y/s take on different values depending on the region being considered, see Figure 3.2 and Table 3.1 both taken from [98]. It is assumed that the field can be decomposed according to $\phi(x,\,y,\,z) = \phi(x,\,y,\,z)\,e^{-i\,\gamma\,z}$, this expression is substituted into equation (3.39) and the FE-BPM is applied in order to determine a numerical approximation to the solution along the direction of propagation.

Since curved optical waveguides are being analysed, PML-BC are incorporated into a FE-BPM code for computing the solution of equation (3.1). Upon application of the complex coordinate

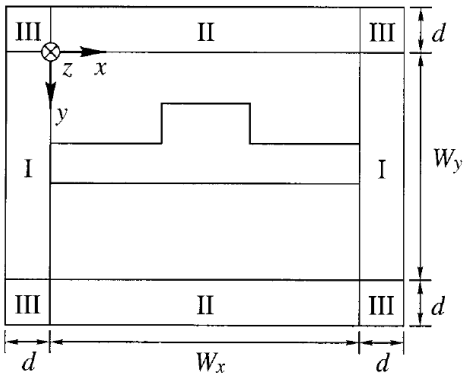


Figure 3.2: Computational domain with a rib waveguide, surrounded by a PML region.

stretching transformation and the FE-BPM the following global matrices are determined

$$\hat{\mathbf{M}} = \sum_{e=1}^{M} P^e \, s^e \, A^e \tag{3.39}$$

$$\hat{\mathbf{K}} = \sum_{e=1}^{M} k_0^2 \, Q^e \, s^e \, \Gamma^e \, A^e \; - \; P^e \left(\frac{s_x}{s}\right)^e B^e \; - \; P^e \left(\frac{s_y}{s}\right)^e \Gamma^e \, C^e \tag{3.40}$$

The matrices A^e, B^e and C^e are defined according to equations (2.18) - (2.20), see page 27, for propagation in two-dimensional optical waveguides. For propagation in one-dimensional structures define A^e and B^e according to (3.34). In one-dimensional waveguides the C^e contribution is not present.

Equations (3.39) and (3.40) define a system of linear equations, via equation (3.22), whose solution describes the propagation of a wave in a curved three-dimensional optical waveguide assuming PML-BC. To the author's knowledge this is the first time that this set of equations has been presented. If the term Γ is allowed to vary along the direction of propagation then this scheme can also simulate curved optical waveguides for which the curvature varies along the path-length of the waveguide.

3.5 SFEM_Propagation: An object oriented waveguide mode propagator

So far the mathematical details behind the FE-BPM have been presented. This section provides a description of an object oriented C++ implementation of the FE-BPM with PML-BC that was written as part of this PhD for the purpose of computing a solution of equation (3.1). *SFEM_Propagation* is built on top of *SFEM_Modes*, i.e. *SFEM_Propagation* inherits *SFEM_Modes* so that all the code that was written for *SFEM_Modes* can be used with only slight alterations by *SFEM_Propagation*.

3.5.1 The propagation algorithm

To propagate a beam using *SFEM_Propagation* discretise the waveguide cross-section using the method described in Section 2.4.1. Algorithms 1 and 2 are altered to extend the mesh so

that the surrounding PML region can be incorporated. The alteration consists of adding a loop, after lines 18 of Algorithms 1 and 2, to define the node positions inside the PML region.

Once the mesh is defined the elemental properties can be defined, when PML-BC are included the elements of the mesh must contain information to define the s-parameter, see equation (3.35), since the elements are defined using objects it is an easy task to extend the information required by each element.

The next step is to define the initial condition on the mesh. This can be any type of wave but is usually chosen to be a Gaussian beam or a mode of the waveguide. When waveguides are being studied it is best to launch a mode of the waveguide, this requires the optical modes of the waveguide to be computed prior to launch. The reason being that other types of wave take a very long time to settle into a bound state of the waveguide.

Once the initial condition has been defined the beam propagation algorithm can be applied. The global matrices are defined according to equations (3.39) and (3.40). The global matrices are computed according to Algorithm 6 assuming equations (3.39) and (3.40) in Appendix D. If the waveguide properties do not change along the path-length of the waveguide then this step need only be computed once. Next the propagation constant is defined in terms of the input field according to equation (3.28). Once the beam is propagating γ is updated using the propagated field profile.

The most important step, construction of the system of linear equations (3.22), is accomplished in four parts. From the definitions of the matrices $\hat{\mathbf{A}}$ and $\hat{\mathbf{B}}$, see equations (3.23) and (3.24), it can be seen that there are factors common to both $\hat{\mathbf{A}}$ and $\hat{\mathbf{B}}$. To this end two new matrices are defined

$$\hat{\mathbf{L}} = \hat{\mathbf{K}} - \gamma^2 \hat{\mathbf{M}}, \quad \hat{\mathbf{M}}_2 = \hat{\mathbf{M}} + \frac{\gamma}{4}\hat{\mathbf{L}}$$

This allows the matrices $\hat{\mathbf{A}}$ and $\hat{\mathbf{B}}$ to be defined according to

$$\hat{\mathbf{A}} = (2\,i\,\gamma)\,\hat{\mathbf{M}}_2 - \alpha\,dz\,\hat{\mathbf{L}}, \quad \hat{\mathbf{B}} = (2\,i\,\gamma)\,\hat{\mathbf{M}}_2 + (1-\alpha)\,dz\,\hat{\mathbf{L}}$$

The last step requires the formation of the right-hand side vector

$$\hat{\mathbf{R}} = \hat{\mathbf{B}} \cdot \hat{\phi}_{old}$$

$\hat{\phi}_{old}$ in this case is assumed to be the field from the previous step, or the input field in the case of the first step. To ensure stability α is defined in the range $\frac{1}{2} \leq \alpha \leq 1$.

Equations (3.22) can now be solved by application of a suitable linear system solver. Given the sparse nature and large size of the matrices involved the author has chosen to use the bi-conjugate gradient method (BCGM) to solve equation (3.22). This method can be implemented very efficiently using the sparse matrix object discussed in Appendix C. In effect BCGM iteratively searches for a minimum of the function

$$f(\hat{\mathbf{x}}) = \frac{1}{2}\hat{\mathbf{x}} \cdot \hat{\mathbf{A}} \cdot \hat{\mathbf{x}} - \hat{\mathbf{b}} \cdot \hat{\mathbf{x}}$$

since this function attains a minimum when [40, 72]

$$\nabla f(\hat{\mathbf{x}}) = \hat{\mathbf{A}} \cdot \hat{\mathbf{x}} - \hat{\mathbf{b}} = \hat{\mathbf{0}}$$

The details of the implementation used by the author can be found in [40].

In broad terms the search for the solution starts with an approximate solution of equation (3.22), the input field for the FE-BPM is chosen, then the solution is updated according to

$$\hat{\mathbf{x}}^{new} = \hat{\mathbf{x}}^{old} + t\,\hat{\mathbf{v}}$$

$\hat{\mathbf{v}}$ is the direction taken to search for the minimum of $f(\hat{\mathbf{x}})$, not necessarily the direction of steepest descent, and t is a parameter that enables this search to converge quickly. t and $\hat{\mathbf{v}}$ are chosen so as to satisfy bi-conjugacy and mutual orthogonality conditions [40, 71, 72]. There is no unique method for choosing t and $\hat{\mathbf{v}}$. One method is provided in [72] and another, more advanced, method is provided in [40]. In each case the process of pre-conditioning is applied to ensure the numerical stability of the BCGM. A description of the method is provided in Algorithm 9. The solution of equation (3.22) represents the field a distance dz down the waveguide. The propagation process is described algorithmically in Algorithm 10.

3.6 Testing SFEM_Propagation

To ensure that *SFEM_Propagation* produces physically sensible results some test simulations were run. For the two-dimensional version a Gaussian beam was launched into free space. The results of the 2D simulations are presented in Section 3.6.1. Once a beam could be propagated in 3D the code could be tested to ensure that it was producing realistic results. To this end a Gaussian beam was launched into a rib waveguide to show that the code works. The results of the 3D simulations are presented in Section 3.6.2.

3.6.1 Free-Space simulations in two-dimensions

A Gaussian beam of width $\omega = 0.5$ was launched into air with wavelength $\lambda = 1.55\,(\mu m)$. The width of the computational domain was $L_x = 10\,(\mu m)$. A 500 element mesh was constructed across the width of the computational domain. The total propagation distance was $100\,(\mu m)$ and the propagation step size was $dz = 0.1\,(\mu m)$. Three scenarios were considered, these are

- propagation with no boundary conditions.
- propagation with transparent boundary conditions.
- propagation with perfectly-matched layer boundary conditions.

For propagation with PML-BC 20 perfectly matched layers, spaced $0.1\,(\mu m)$ apart were added to the left and right mesh boundaries.

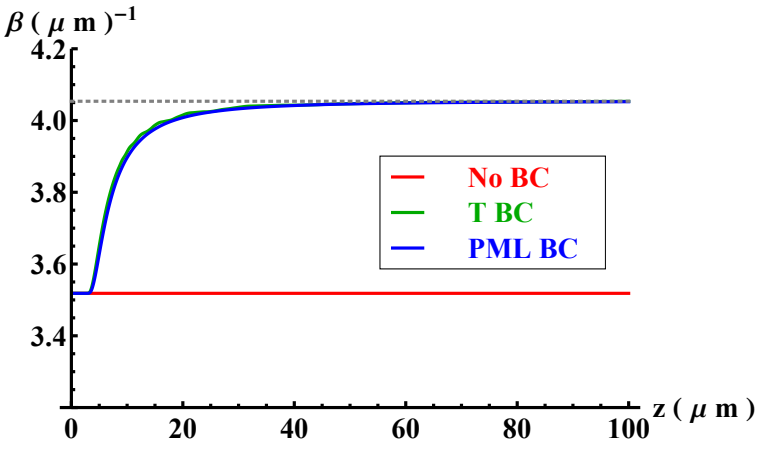
Firstly, the beam was allowed to propagate straight ahead under each of the three scenarios. Figures 3.3(a) - 3.3(c) show the beam properties. In Figure 3.3(a) the real part of the propagation constant is shown. It is seen that when the transparent and perfectly matched layer boundary conditions are used the real part of the propagation constant converges to what would be expected for a beam propagating in air. No change in the propagation constant is observed when no boundary conditions are applied.

Figure 3.3(b) shows the imaginary part of the propagation constant. When the transparent and perfectly matched layer boundary conditions are used the imaginary part of the propagation

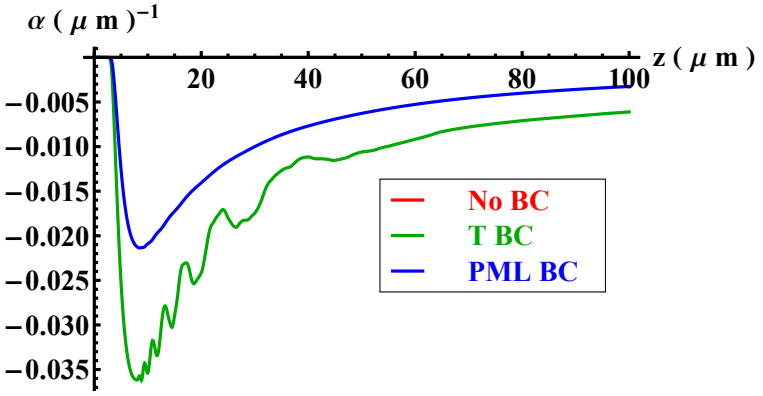
constant shows the beam losing energy as it diffracts and eventually settling into a steady state. This is not observed when no boundary conditions are applied.

Figure 3.3(c) shows the total power in the beam as it propagates. In the case of the perfectly matched layer boundary condition the beam power decays as would be expected, however, this is not observed in the case of the transparent and no boundary conditions. This indicates that radiation is not being allowed to leave the computational domain as is physically required.

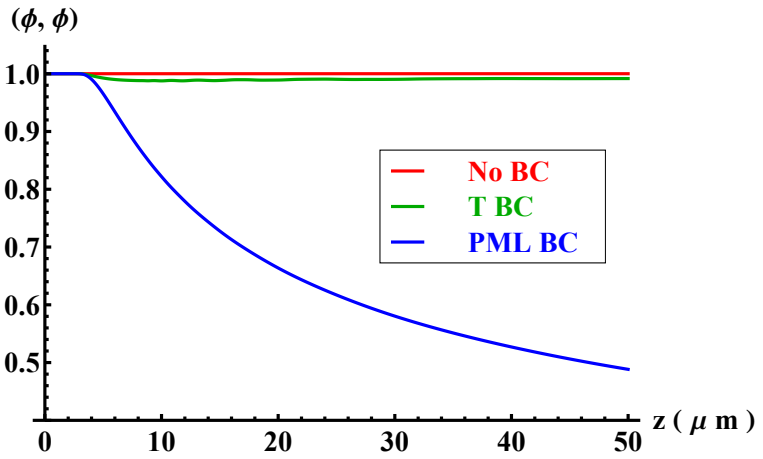
Figures 3.4(a) - 3.4(c) show the propagated beam in each of the three cases. Figure 3.4(a) shows the high level of reflections that occur at the computational domain boundary in the absence of absorbing boundary conditions. Figure 3.4(b) shows some reflection from the computational domain boundary but it is clear that application of the transparent boundary condition is an improvement upon no boundary condition. Figure 3.4(c) shows the beam propagating as would be expected, no reflection from the computational domain boundary is observed and the beam is decaying as expected.



(a) Real propagation constant

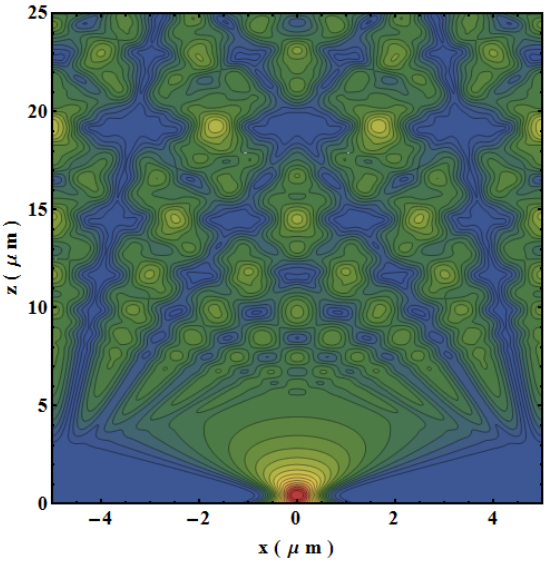


(b) Imaginary propagation constant

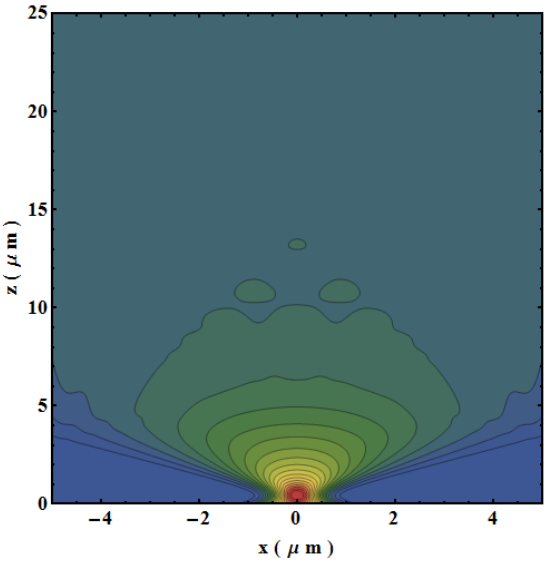


(c) Total power

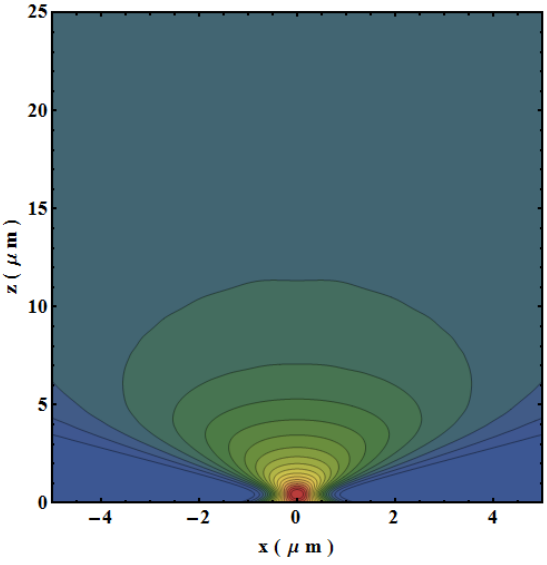
Figure 3.3: Properties of the wave propagating straight ahead in free space



(a) No BC

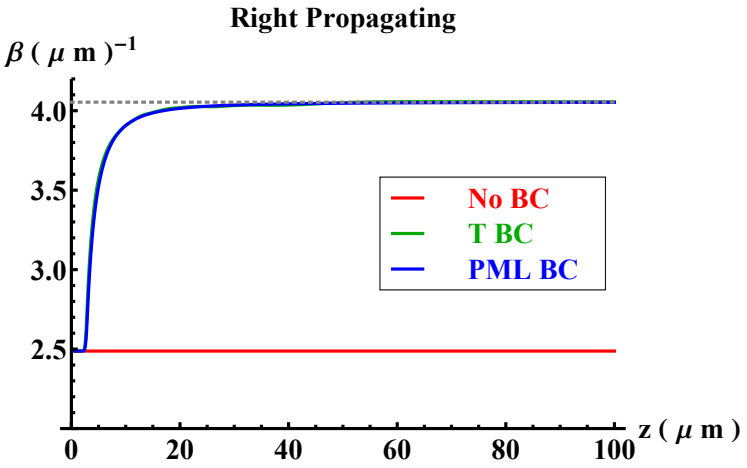


(b) Transparent BC

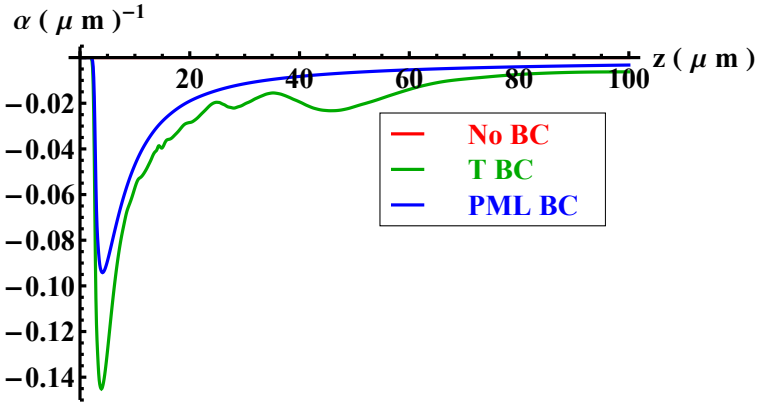


(c) Perfectly matched layer BC

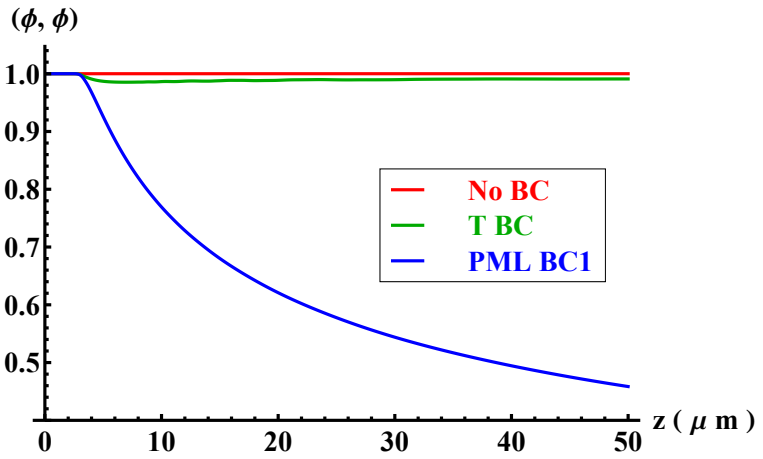
Figure 3.4: Free space propagation straight ahead under different boundary conditions



(a) Real propagation constant

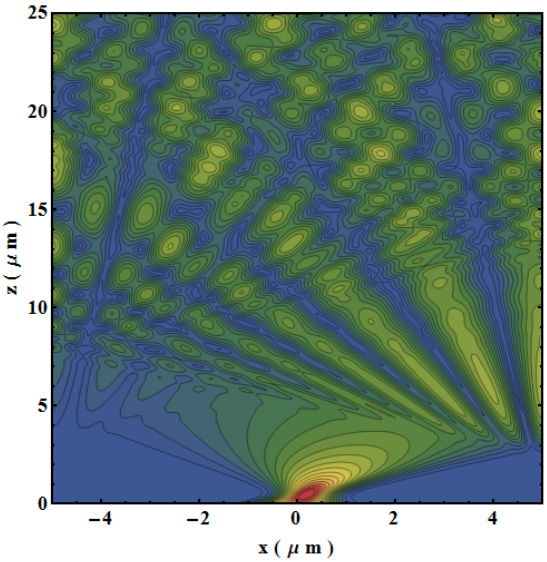


(b) Imaginary propagation constant

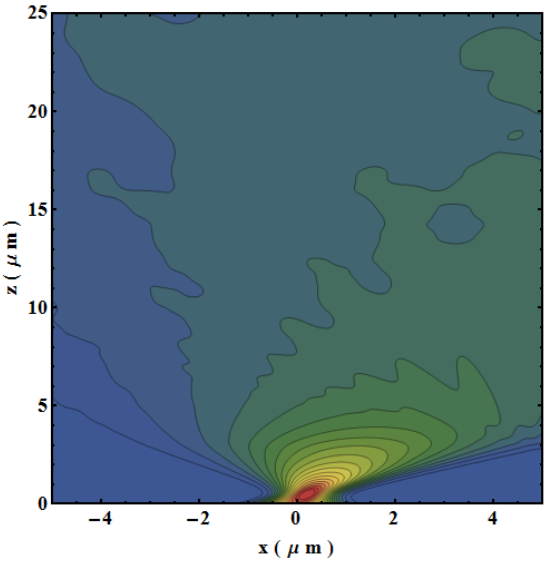


(c) Total power

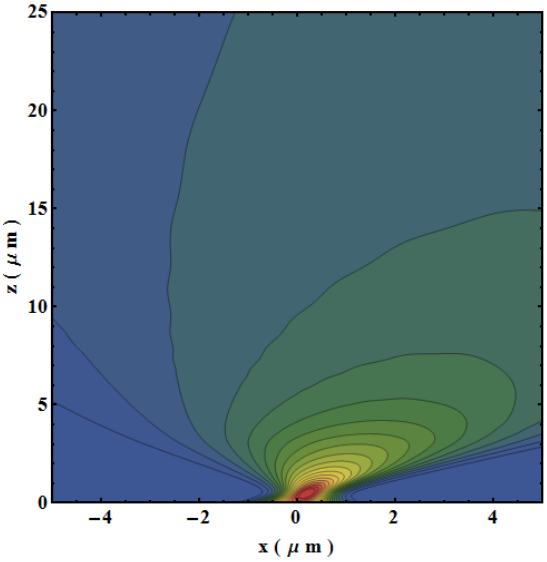
Figure 3.5: Properties of the wave propagating 45° to the right in free space



(a) No BC

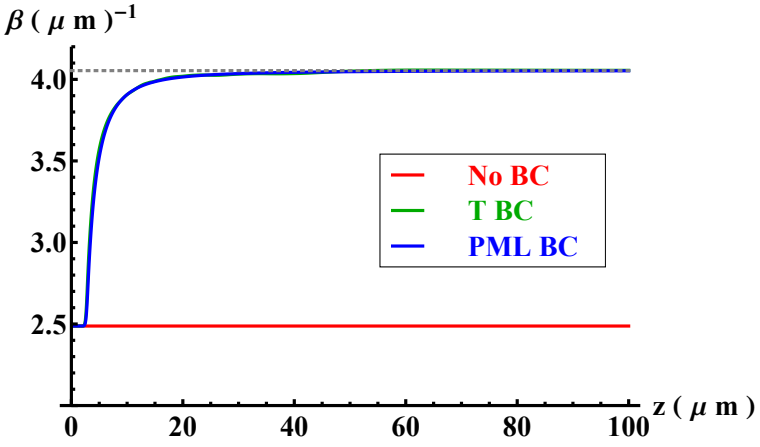


(b) Transparent BC

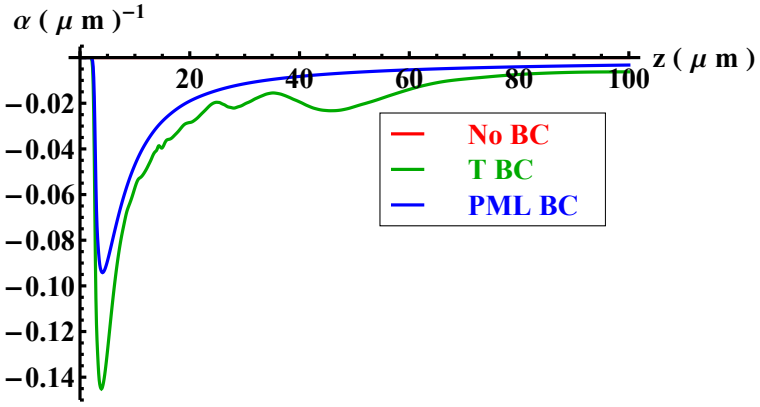


(c) Perfectly matched layer BC

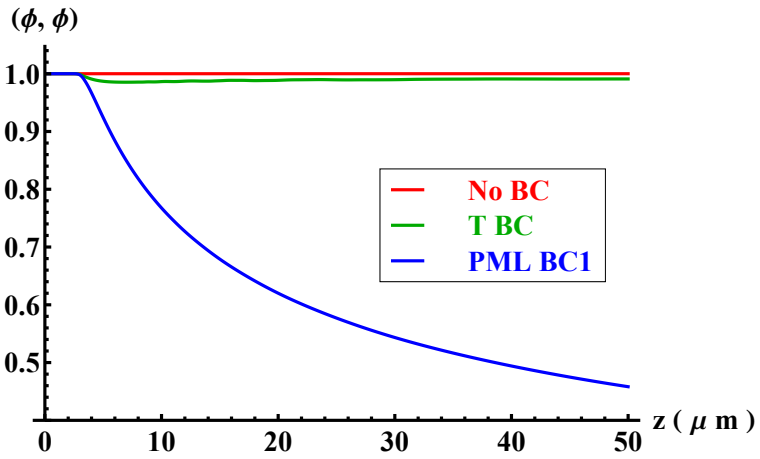
Figure 3.6: Free space propagation 45° to the right under different boundary conditions



(a) Real propagation constant



(b) Imaginary propagation constant

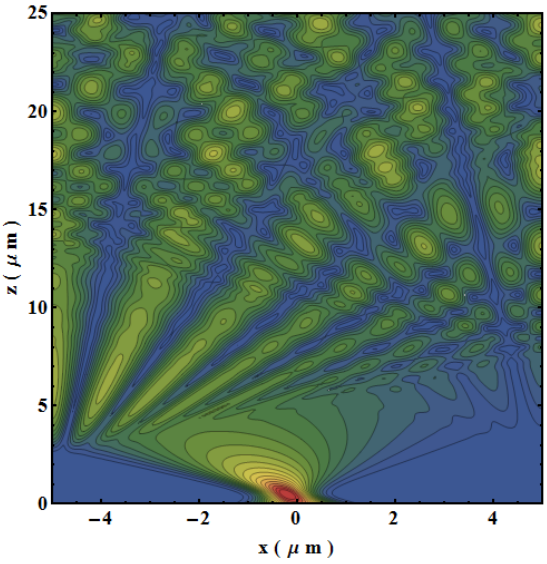


(c) Total power

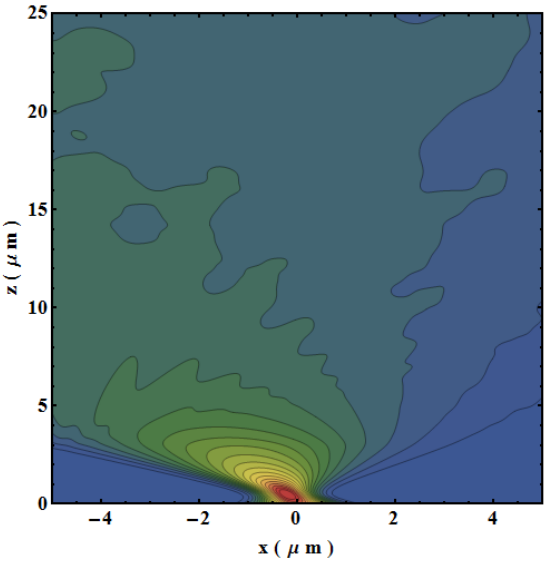
Figure 3.7: Properties of the wave propagating 45° to the left in free space

The Gaussian beam simulation was repeated to allow the beam to propagate at $\pm 45°$ to the original direction of propagation. The aim is to show that the perfectly matched layer boundary condition can absorb radiation from any direction.

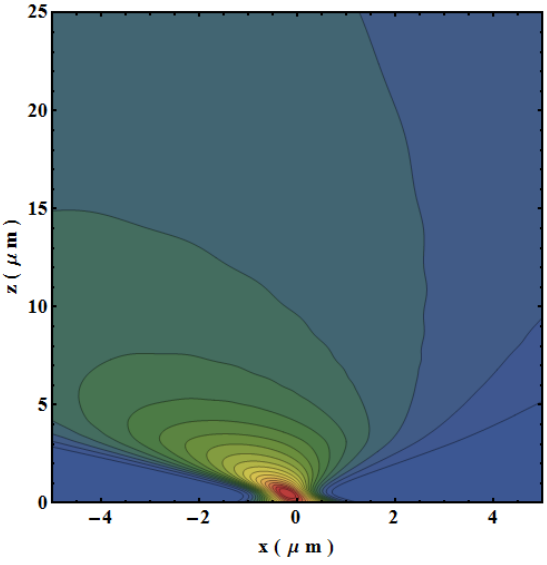
Figures 3.5(a) - 3.5(c) and 3.7(a) - 3.7(c) show the computed beam parameters in the case of right and left propagation respectively. The curves are the same in both cases indicating that the transparent and perfectly matched layer boundary conditions absorb radiation independent of the direction from which it came. Figures 3.6(a) - 3.6(c) and 3.8(a) - 3.8(c) show the computed beam profiles as they propagate to the right and left respectively. The symmetry of the beam profiles is a good indication that all is well with the boundary conditions. Figures 3.6(a) and 3.8(a), beam profiles in the case of no boundary conditions, clearly demonstrate the need for absorbing boundary conditions. Figures 3.6(b) and 3.8(b) indicate that there is some reflection from the transparent boundary conditions. Figures 3.6(c) and 3.8(c) show that the perfectly-matched layer boundary conditions do not permit any reflection.



(a) No BC



(b) Transparent BC



(c) Perfectly matched layer BC

Figure 3.8: Free space propagation 45° to the left under different boundary conditions

Table 3.2: Device parameter for the Gaussian beam propagation calculation

n_{core} 3.44	n_{sub} 3.34	n_{clad} 1.0	
W (µm) 2.0	E (µm) 1.1	T (µm) 0.2	
x_{ll} (µm) -5.5	x_l (µm) -4.5	x_u (µm) 4.5	x_{uu} (µm) 5.5
y_{ll} (µm) -5.55	y_l (µm) -4.55	y_u (µm) 5.6175	y_{uu} (µm) 6.6175

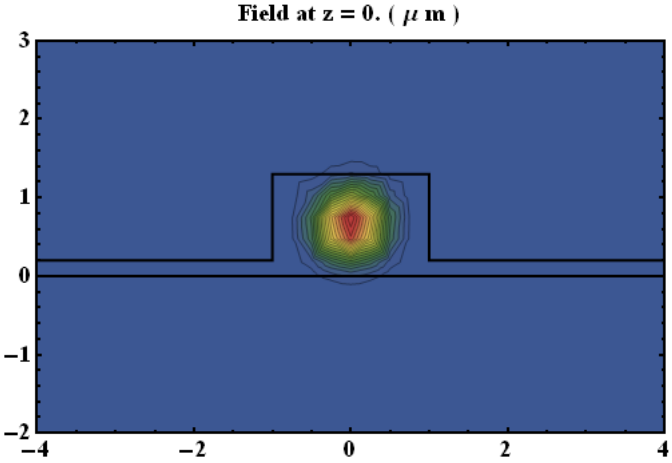


Figure 3.9: Gaussian beam with $\omega = 0.3$ (µm) and $\lambda = 1.55$ (µm) injected into rib waveguide for propagation.

3.6.2 Gaussian beam propagation in a rib waveguide

The waveguide chosen was a rib waveguide with the properties listed in Table 3.2 [94]. 3760 linear finite elements were used to discretise the computational domain, 10 perfectly matched layers, spaced 0.1 (µm) apart, formed the absorbing layer around the waveguide. The step-size along the direction of propagation was $dz = 0.05$ (µm). The average time taken for each propagation step was 5.6 s. the total number of propagation steps was 10001, this required 15.6 hours of computation time.

A Gaussian beam of width $\omega = 0.3$ (µm) and wavelength $\lambda = 1.55$ (µm) was launched into the waveguide, this input beam is shown in Figure 3.9. As the beam is propagated the FE-BPM algorithm updates the complex propagation constant for the mode developing in the waveguide. The real part of the propagation constant, as a function of waveguide path-length, is shown in Figure 3.10. It is seen that the propagated value of β eventually converges to the propagation constant that is computed from a modal analysis of the same waveguide using the finite element method (FEM) [37, 38]. The fact that β converges to β_{SFEM} demonstrates that the code is providing valid results.

The imaginary part of the propagation constant, the loss-factor, is shown in Figure 3.11, it shows how the beam radiates energy as it propagates enabling a guided rib waveguide mode to form. The power in the beam being propagated is computed by integrating the beam intensity over the computational domain, the power versus path length is shown in Figure 3.12. The loss due to propagation decreases as the beam is transformed into a guided mode.

As the beam propagates it oscillates inside the waveguide structure, this can be seen by plotting

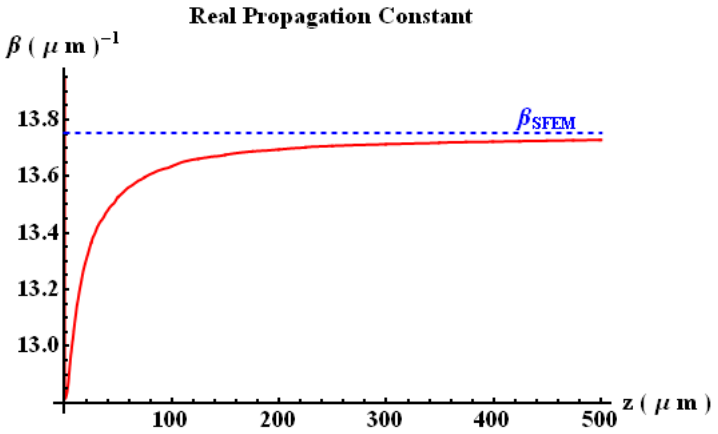


Figure 3.10: Beam propagation constant as function of path-length, as computed by FE-BPM, also shown for comparison is the value of the waveguide mode propagation constant computed by SFEM.

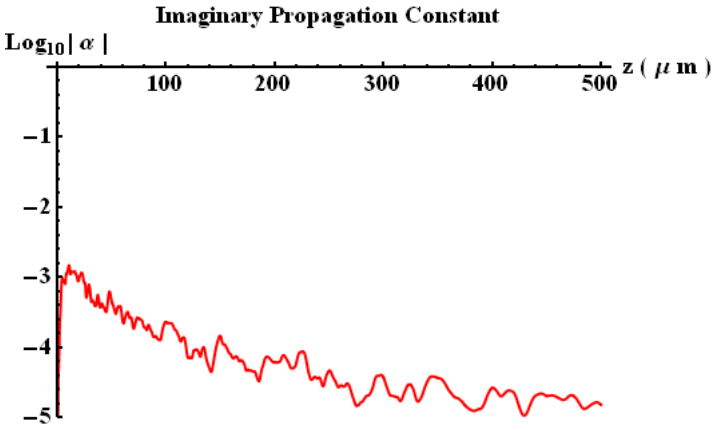


Figure 3.11: Beam loss-factor as a function of path-length, as computed by FE-BPM, α decreases in magnitude as the beam is transformed into a guided rib waveguide mode.

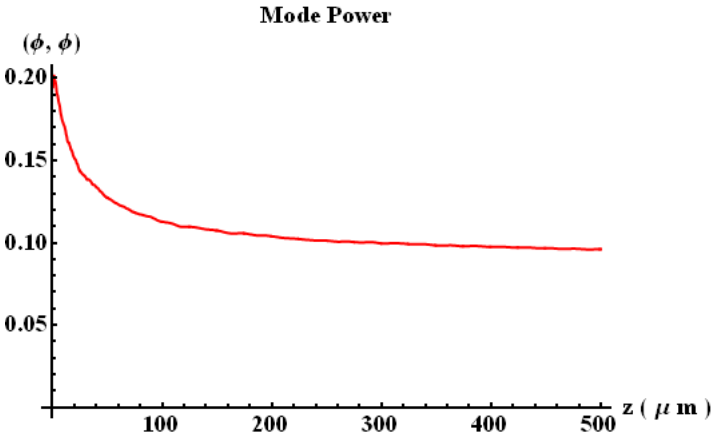


Figure 3.12: Power versus path-length for the propagated beam. The initial losses are due to radiation from the Gaussian beam. The power settles to a constant value as the initial beam is transformed into a guided rib waveguide mode.

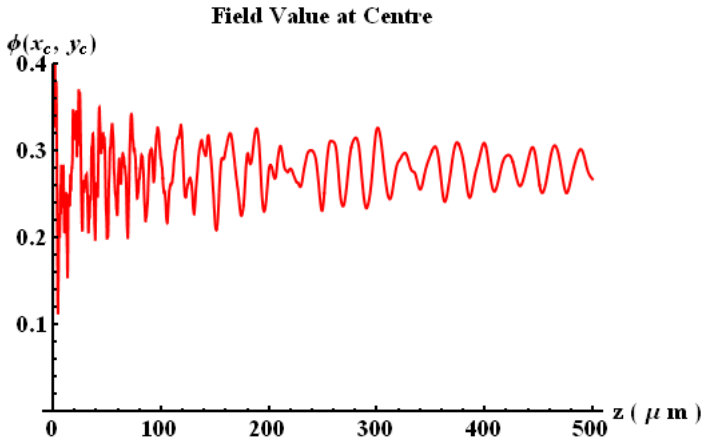
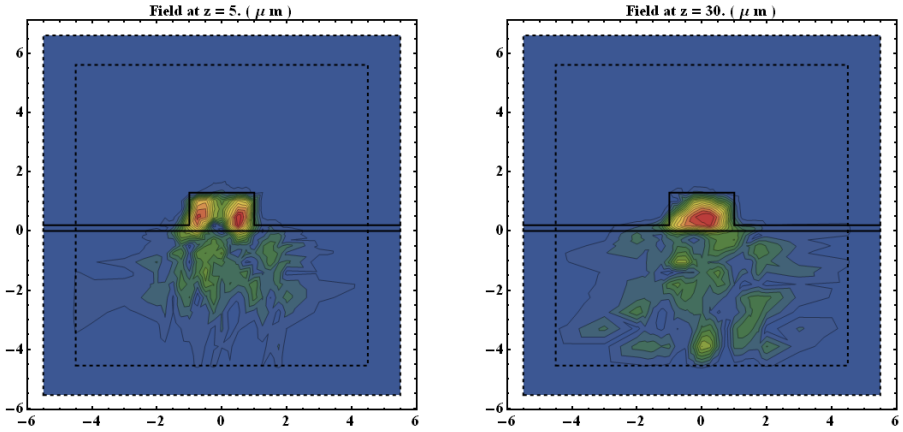


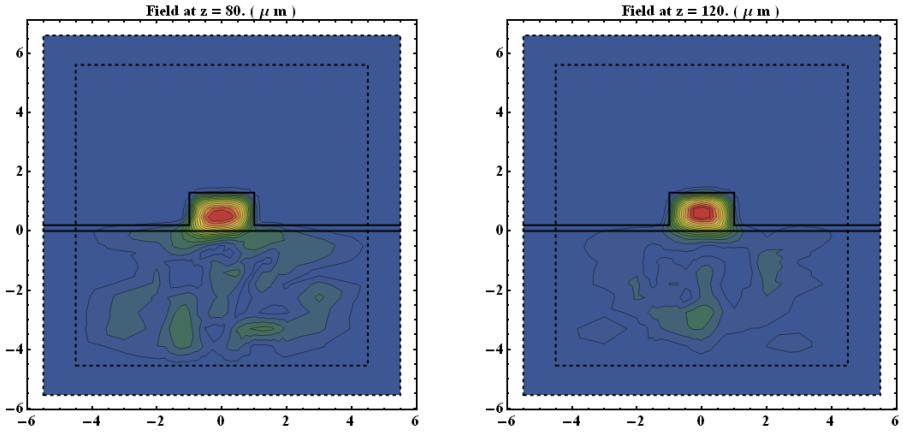
Figure 3.13: Field value at waveguide centre as a function of path-length. Amplitude oscillation indicates oscillation of beam inside waveguide.

the value of the field at the waveguide centre. The amplitude of the field oscillations is plotted in Figure 3.13. As the beam is transformed into a guided mode of the waveguide the amplitude of the field oscillations start to decrease.

The period of the oscillation also increases as the beam tends to a waveguide mode. The transformation of the Gaussian beam into a waveguide mode is shown at different positions along the length of the waveguide in Figures 3.14(a) - 3.15(d).

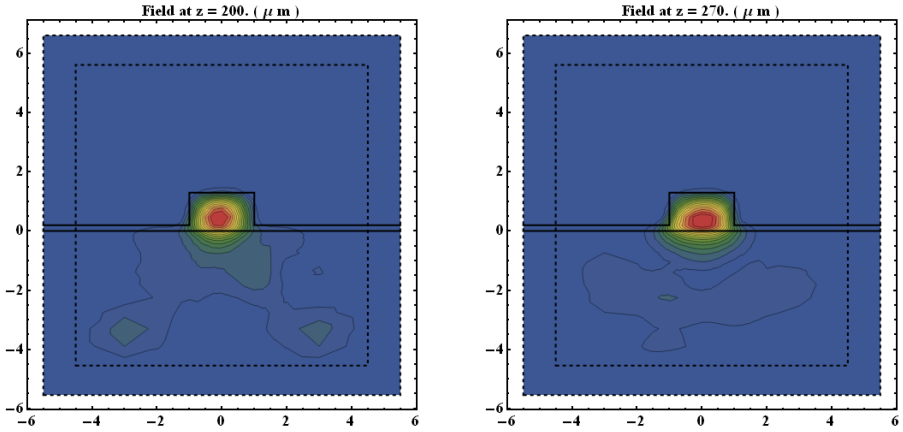


(a) Propagated beam at $z = 5$ (µm) (b) Propagated beam at $z = 30$ (µm)

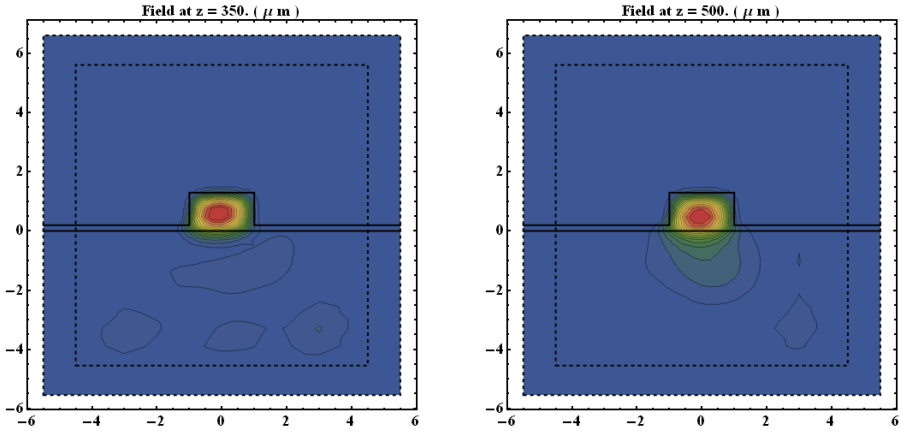


(c) Propagated beam at $z = 80$ (µm) (d) Propagated beam at $z = 120$ (µm)

Figure 3.14: Steps in the Gaussian beam propagation



(a) Propagated beam at $z = 200$ (µm) (b) Propagated beam at $z = 270$ (µm)



(c) Propagated beam at $z = 350$ (µm) (d) Propagated beam at $z = 500$ (µm)

Figure 3.15: Steps in the Gaussian beam propagation

3.7 Discussion

The finite element beam propagation method as it is applied to curved optical waveguides has been developed. It has also been shown, for the first time, how to incorporate perfectly matched layer boundary conditions into the propagation code for a curved waveguide in the conformal mapping model. An implementation of the propagation scheme has been written in C++. The code is capable of performing propagation simulations in any passive optical device. The code has been shown to produce reliable results from its application to the test problems.

In the next chapter a new method for designing curved optical waveguides is developed. The technique will ensure that it is possible to design curved optical waveguides with reduced transition loss.

Chapter 4

The Design of Optical Waveguide Bends

Summary: *A technique for designing waveguide bend paths that ensure very low transition loss is presented. A review of current curved waveguide design methodology is given. The new bends are developed using an existing method in an uncomplicated manner. It is shown how the new bend types have a different shape from standard waveguides, this new shape explains why the bends exhibit very low transition loss.*

4.1 Introduction

The standard waveguide bend is composed of a straight waveguide followed by a circular bend section of radius R, ending in another straight section, see Figure 4.5. It is intended that the new bend type should replace the standard bend section. To this end the notion of an equivalent circle is introduced. The equivalent circle is that bend connecting two points in the plane that would otherwise be connected by a circle of radius R subtending an angle θ at its origin.

The current methods used to optimise waveguide bends are discussed in Section 4.2. The various techniques used to reduce losses in curved waveguides are presented in a paper by Ladouceur and Labeye [43]. Optimisation in this case means a reduction in the intrinsic loss associated with the bend; either through a reduction of transition loss or bending loss or both. The simplest way to obtain a reduction in bending loss is to increase the radius of curvature of the bend. This leads to devices that are much longer than desired which means that they cannot be effectively contained in a photonic integrated circuit (PIC).

To achieve a reduction in bend loss a variety of techniques are used to ensure an increase in mode confinement along the bend. The simplest way to reduce bend loss is to perform a deep etch parallel to the waveguide bend section [13, 115]. Another technique is to increase the width of the waveguide in the bend section [14, 15]. Other methods that have been developed take advantage of the material parameters to ensure a high confinement of a mode in a bend section [116–121].

Transition loss minimisation is obtained by maximising coupling efficiency between the fundamental mode in the straight section and the fundamental mode in the bend section. Bend

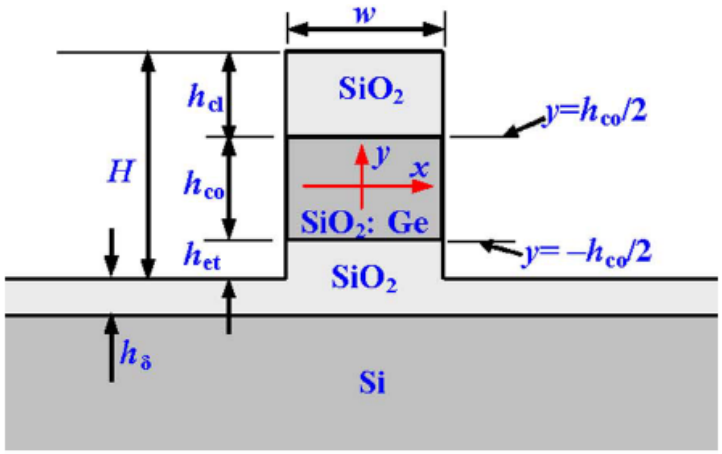


Figure 4.1: Deep etched SiO_2 ridge waveguide

offsetting requires that a waveguide bend be translated laterally from a straight section by some amount δ that allows for the peak position of the mode in the straight section to be matched with the peak position of the mode in the bend section [12, 14, 15, 43]. A method that has been developed recently is that of bend matching [122–125]. By setting the bend length to be an integer multiple of the beat length of the modes propagating in the bend section the modes in the bend exit the bend in phase with each other, thus reducing overall loss.

Mode matching can also be achieved with the introduction of a waveguide taper at the straight-bend junction [120] and also through the manipulation of the waveguide path. The technique developed in this chapter is derived from waveguide path manipulation. The idea behind the technique is to alter the shape of the waveguide path so that the mode transitions from the straight section into the bend section in a gradual manner, effectively allowing the mode from the straight section to transform into the mode in the bend section. This idea was originally introduced in the study of s-bend design [126–130]. The idea was applied to single waveguide bends by the author in [49–52]. The technique is developed in Section 4.3. It will be seen that the technique is easy to understand, very easy to implement and not limited to slab waveguides. It will also be seen that the technique will not require any dramatic and difficult waveguide alterations or fabrication steps. The proposed technique is also waveguide independent.

4.2 Techniques for the Reduction of Losses in Waveguide Bends

Reduction of bend loss is achieved by ensuring that a waveguide contains as much light as possible in its core region. The simplest way to ensure a very high mode confinement is to design a waveguide with a very large etch depth that provides a high index contrast, see Figure 4.1 taken from [120]. This has been applied by Dai and Shi to achieve a loss of 0.06 dB in a SiO_2-SiO_2:Ge-SiO_2 waveguide bend with a radius of $R \approx 10\,\mu m$ [120]. The high confinement provided by silicon based waveguides enables the realisation of passive devices with very low bend loss with very small bend radii. In each of the papers [117–119] the authors report losses in and around 0.06 dB for $R \approx 10\,\mu m$ on silicon-on-insulator (SOI).

If the material platform is not SOI, other methods have to be applied. A trench can be etched parallel to the waveguide bend, see Figure 4.2 taken from [13], the aim of the trench is to confine light inside the waveguide bend as it propagates in the bend. The trench works because

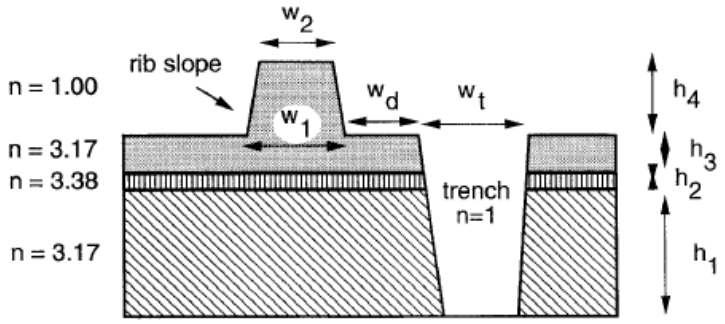


Figure 4.2: Deep etched SiO_2 ridge waveguide with trench section

light cannot exit the bend because of an induced refractive index contrast. The trench can be incorporated into a device by direct etching [13,115] or by chemical diffusion [116]. A 0.225 dB reduction in loss was reported by [115] when a trench was etched parallel to a 3 µm wide InP-InGaAsP-InP ridge waveguide with a bend radius of $R \approx 1500$ µm. A measured loss reduction of between 6 dB and 1 dB for 15 mm $< R <$ 25 mm was reported for a Ti:$LiNbO_3$ waveguide with a trench formed by diffusion of MgO parallel to the bend section [116]. Including a trench will incur transition loss at the straight-bend junction on both sides of the bend because of mode mis-match. There may also be errors because of over / under etching and it may not always be possible to include a trench either by etching or diffusion on a dense PIC.

The width of a waveguide bend may be increased to ensure higher confinement of the bend mode. Application of curved waveguide widening in a Al_2O_3-SiO_2 waveguide for $R \approx 100$ µm, when the width was increased from the original 2 µm in the straight to 3 µm in the bend, resulted, along with waveguide offsetting, a measured loss of 0.35 dB [14]. The details of the optimisation are discussed in [15]. Once again it may not be possible to increase the width of a waveguide bend depending on the application. For example, in an arrayed waveguide grating (AWG) the phase properties may be altered by changing the waveguide width [131,132]. Given that each arm of an AWG requires a bend with a slightly different radius the width-optimisation would have to be performed for each arm of an AWG.

Another approach to bend loss reduction is to change the path of the waveguide bend. This has generally been applied to the problem of designing a connecting waveguide between two straight sections that are laterally offset from one another, for example in an s-bend device [20,127,128]. The aim there was to design a waveguide bend section in such a way that the bending loss from the section was minimised. Marcuse reported a total bend loss of 0.04 dB for a bend section connecting two low-index contrast 3 µm wide waveguides are separated by 50 µm [20]. Baets and Lagasse report a loss of 0.2 dB for their scheme for designing a connection between two waveguides spaced 10 mm apart [127]. Lerner reports a 20% reduction in loss for his method, that includes waveguide offsetting, of computing the optimum connection between very low index contrast, $\Delta = 0.003$, 3 µm wide waveguides spaced 50 µm apart [128]. A variation of these bend design methods that reduces intermodal coupling has recently been published [133].

These bend manipulation techniques have also been applied to the calculation of the connecting waveguide for the standard bend [43,130]. Ladouceur and Labeye combine width optimisation with bend shape optimisation but their scheme assumes knowledge of the bending loss of the waveguide, which is applicable for slab waveguides, but not for real structures. The method of Hu and Lu reports a total loss of 0.6 dB for $R = 200$ µm in a 1 µm wide waveguide with index contrast of $\Delta = 0.02$. These bend shape optimisation schemes are derived from an analysis of

the waveguide curvature along the direction of propagation.

The other side of loss reduction for curved waveguides is to attempt to reduce the transition loss that occurs as a mode propagates across a straight-bend junction. Transition loss occurs because the mode in the straight waveguide and the mode in the curved waveguide have different shapes, see Figure 4.3. To minimise transition loss two conditions must be satisfied [12]:

1. the amplitude distributions of the two modes must be matched
2. the phase distributions of the modes propagating in the bends must be matched

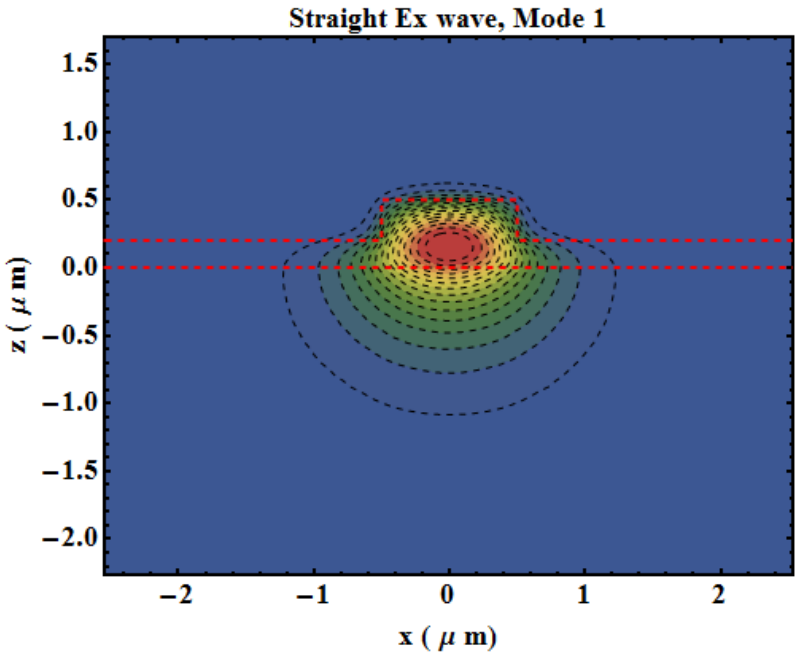
The phase distributions are generally assumed to be matched if the mode is only considered in the region where its phase front is flat, i.e. inside the caustic. In general the amplitude distributions are not matched. To match the amplitude distributions, the curved waveguide is laterally offset by some distance to ensure that the center of the mode in the straight section matches the centre of the mode in the bend section. To determine the location of optimum offset compute the overlap integral between the mode in the straight section and the mode in the curved section while the offset between the straight and curved sections is varied. The optimal location is determined by the point at which the overlap integral is a maximum. For slab waveguides this distance is determined approximately by the formula

$$\delta = \frac{\pi^2 n_{eff}^2 w_0^4}{\lambda^2 R}$$

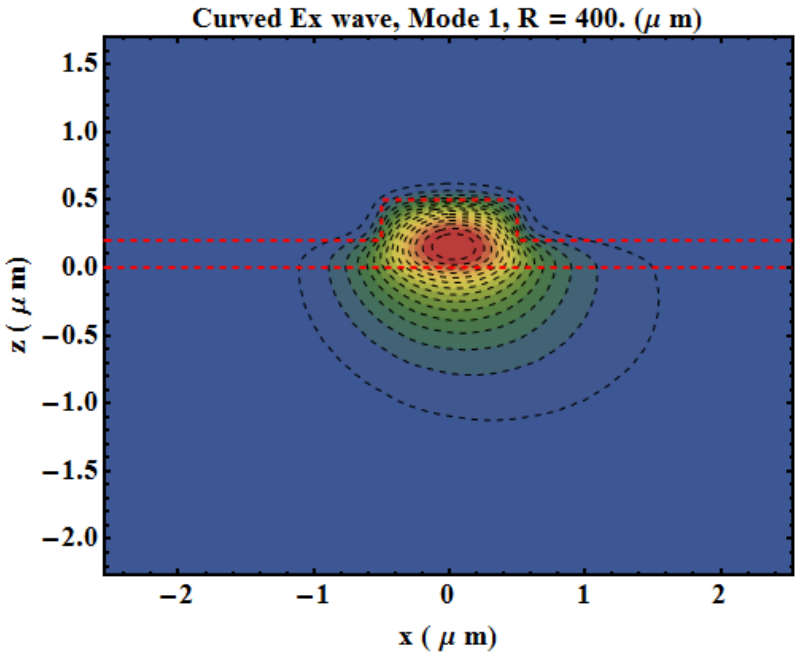
where n_{eff} is the effective index of the straight waveguide, w_0 is the width of the waveguide mode, λ is the wavelength and R is the bend radius [12]. No equivalent formula for real waveguides exists but the analysis can be performed using numerical tools, such as those developed in Chapters 2 and 3. Figure 4.4 shows the computed optimal waveguide offset positions for waveguide WG9A computed as a function of the bend radius. If a fabrication tolerance of 0.1 µm is assumed, not unreasonable for the InGaAsP-InP platform, it can be seen that it may not always be possible to fabricate a waveguide located at the optimal position. In any case there will still be transition loss because although the mode centre positions will match their shapes will still be different.

Bend matching is a relatively new technique for designing curved waveguides. As a mode propagates in a bend on constant radius it excites higher order modes in the bend and beats with itself. The key to designing a matched bend is to position the output straight waveguide at a distance equal to an integer number of mode beat lengths. This design criterion reduces transition loss at the output junction since the modes propagating in the bend leave that bend in phase with each other [122–125].

The remainder of this chapter is dedicated to describing a method for bend design that will ensure a reduction of transition loss. It is also expected that the proposed technique will reduce the bending loss. The technique is derived from the curvature based bend-shape optimisation schemes introduced in [127, 128, 130]. The aim is to ensure that the bend curvature is matched to the straight section curvature at the start and end of the bend. This will allow the mode to pass from the straight section into the bend section without experiencing transition loss. The proposed method is simple to implement, material independent, does not require any alterations in waveguide geometry and does not require extra fabrication processes. The technique is so successful that is has been recently used to design bends whose effective radius of curvature is less than 10 (µm) and whose losses are less than 0.02 (dB/90°) [134].



(a) Straight waveguide, $\beta = 12.988\,(\mu\text{m})^{-1}$



(b) Curved waveguide $R = 400\,\mu\text{m}$ $\beta = 12.99\,(\mu\text{m})^{-1}$

Figure 4.3: Fundamental E^x modes of waveguide WG1. The index contrast and waveguide dimensions are available in Table 2.1.

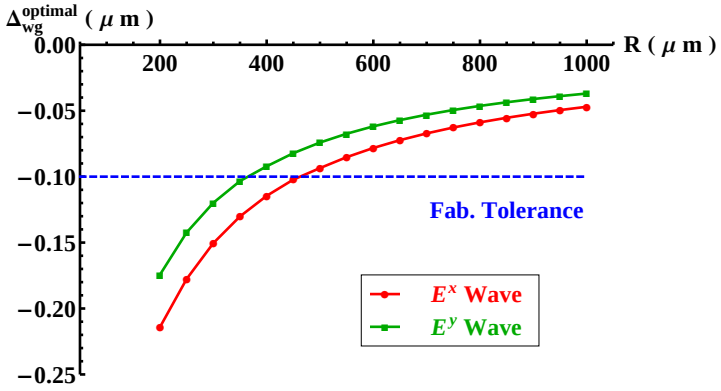


Figure 4.4: Optimal offset positions for a straight-curve waveguide transition in WG9A

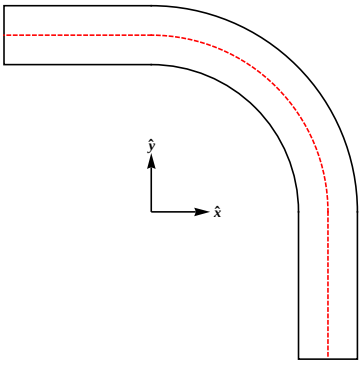


Figure 4.5: Standard waveguide bend composed of a straight followed by a circular bend to connect back onto a straight section

4.3 Curvature Based Bend Construction

A curve in the plane has a curvature κ associated with each point along its path-length. This is called the curvature profile of the curve. The curvature versus path-length profile of a waveguide bend describes the curvature at each point along a curve running through the centre of that waveguide, see Figure 4.5. Using the curvature profile as a starting point, a parametric representation of waveguide path can be constructed. By prescribing a desired curvature profile for a waveguide, the path for that waveguide can be computed. To construct a path from a given curvature requires Euler's method of natural equations [135]. Euler's method requires the evaluation of three integrals; the first integral yields the bending angle as a function of path-length, the second pair of integrals yield a parametric representation of a curve that has the prescribed curvature along its path-length.

An arbitrary curve in the plane has curvature profile κ along its path-length s. If $\kappa(s)$ is integrated along the length of the curve the result is the bending angle for that curve. The bending angle is the angle that a tangent drawn to any point on a curve makes with the horizontal axis, see Figure 4.6. It is denoted by $\phi(s)$ and defined by

$$\phi(s) = \int_{s_0}^{s} \kappa(u)\, du \tag{4.1}$$

To determine the parametric representation of the bend consider a short length ds along the

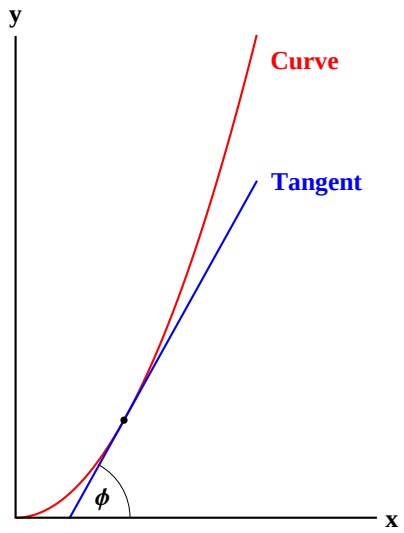


Figure 4.6: Illustration of the bending angle associated with a curve in the plane

bend. ds can be determined from horizontal and vertical progressions along the bend via $ds^2 = dx^2 + dy^2$, where dx and dy are given by

$$dx = \cos\phi\, ds \tag{4.2}$$

$$dy = \sin\phi\, ds \tag{4.3}$$

Summation over all of the dx and dy along the bend provides the parametric representation of the bend. The horizontal coordinates are given by

$$x(s) = \int_{s_0}^{s} \cos\phi(u)\, du \tag{4.4}$$

the vertical coordinates are given by

$$y(s) = \int_{s_0}^{s} \sin\phi(u)\, du \tag{4.5}$$

Equations (4.1), (4.4) and (4.5) are used to construct parametric representations of curves having curvature $\kappa(s)$.

4.3.1 Constant curvature bends

The first curve to be considered is one that has a constant curvature along its length see Figure 4.7. Take the value of this curvature to be $1/R$.

$$\kappa_{cc}(s) = \frac{1}{R} \text{ if } 0 \leq s \leq L_{cc} \tag{4.6}$$

The bending angle for this curve is found by applying (4.1) to (4.6). The result, upon integration, shows that for a constant curvature bend the bending angle varies linearly along its length.

$$\phi_{cc}(s) = \frac{1}{R}\int_0^s du = \frac{s}{R} \text{ if } 0 \leq s \leq L_{cc} \tag{4.7}$$

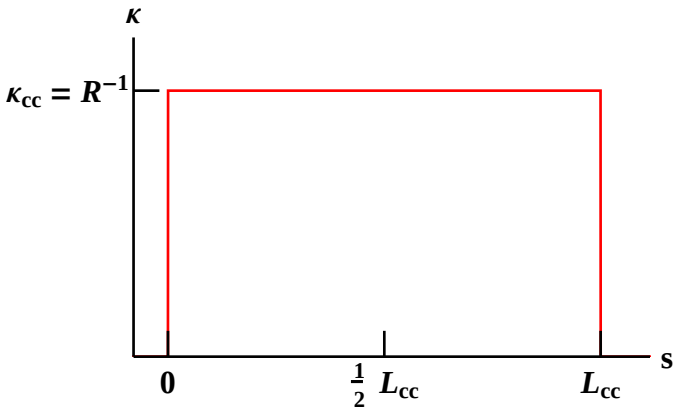


Figure 4.7: Curvature profile associated with a constant curvature bend

The parameterisation of this curve is obtained with the application of (4.4) and (4.5) to equation (4.7) to yield $(x_{cc}(s),\, y_{cc}(s))$.

$$x_{cc}(s) \;=\; \int_0^s \cos\left\{\frac{u}{R}\right\} du \tag{4.8}$$

$$y_{cc}(s) \;=\; \int_0^s \sin\left\{\frac{u}{R}\right\} du \tag{4.9}$$

Calculation of the integrals (4.8) and (4.9) gives the parameterisation of the constant curvature bend. The curve in this case is a circle of radius R.

$$x_{cc}(s) \;=\; R\,\sin\left(\frac{s}{R}\right) \tag{4.10}$$

$$y_{cc}(s) \;=\; R\,\left(1-\cos\left(\frac{s}{R}\right)\right) \tag{4.11}$$

4.3.2 Linear curvature bends

The next case to be considered is a curve with a linear curvature profile. The curvature varies as

$$\kappa_{lc}(s) \;=\; \begin{cases} \alpha_l\, s, & \text{if } 0 \le s \le \dfrac{L_{lc}}{2} \\[2ex] \alpha_l\,(L_{lc}-s), & \text{if } \dfrac{L_{lc}}{2} \le s \le L_{lc} \end{cases} \tag{4.12}$$

This "tent"-like profile ensures that the curve is symmetric about its midpoint, see Figure 4.8.

The slope α_l is chosen to ensure that the linear curvature waveguide bend will turn through the same angle as an equivalent constant curvature waveguide bend. If a constant curvature bend must turn through some angle θ, then α_l is determined by solving

$$\int_0^{L_{lc}/2} \alpha_l\, u\, du \;=\; \frac{\theta}{2} \Rightarrow \frac{1}{8}\,\alpha_l\, L_{lc}^2 \;=\; \frac{\theta}{2} \tag{4.13}$$

Assuming $L_{lc} \approx L_{cc} = R\,\theta$, then $\alpha_l = 4/R\,L_{lc}$[1]. With this definition for α_l the peak curvature

[1] It will be seen in Section 4.3.5 how the lengths for bends having different curvature profiles are determined

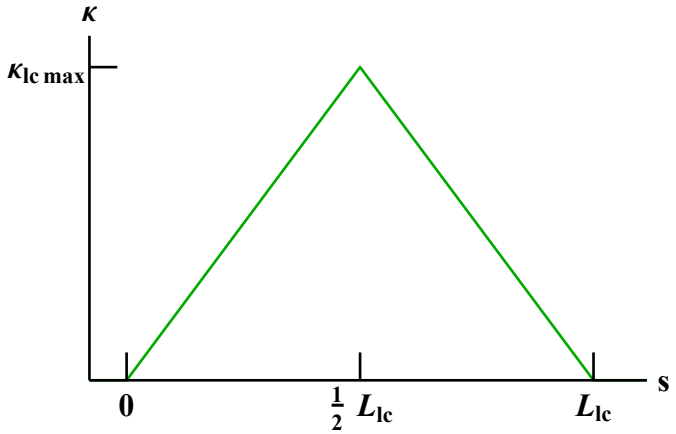


Figure 4.8: Curvature profile associated with a linear curvature bend

of the linear curvature bend is roughly twice that of an equivalent circle, $\kappa_{lc}(L_{lc}/2) \approx 2/R$, where it is required that $\kappa_{lc}(s)$ be a continuous function of path-length.

The bending angle for the linear curvature bend is determined by evaluating (4.1) with $\kappa(s)$ defined by equation (4.13).

$$\phi_{lc}(s) = \begin{cases} \displaystyle\int_0^s \alpha_l \, u \, du, & \text{if } 0 \leq s \leq \frac{L_{lc}}{2} \\ \displaystyle\int_{L_{lc}/2}^s \alpha_l \, (L_{lc} - u) \, du, & \text{if } \frac{L_{lc}}{2} \leq s \leq L_{lc} \end{cases}$$

Two integral evaluations are required to define $\phi_{lc}(s)$. To ensure continuity of $\phi_{lc}(s)$ at the midpoint of the bend the value $\phi_{lc(-)}(L_{lc}/2)$, i.e. $\phi_{lc}(L_{lc}/2)$ evaluated on $0 \leq s \leq L_{lc}/2$, is added to the second branch of the bend. The bending angle for a linear curvature bend is then given by

$$\phi_{lc}(s) = \begin{cases} \dfrac{2s^2}{RL_{lc}}, & \text{if } 0 \leq s \leq \dfrac{L_{lc}}{2} \\ \dfrac{2s^2}{RL_{lc}} - \dfrac{4s}{R} + \dfrac{L_{lc}}{R}, & \text{if } \dfrac{L_{lc}}{2} \leq s \leq L_{lc} \end{cases} \tag{4.14}$$

$\phi_{lc}(s)$ is zero at the start of the waveguide, continuous at the mid-point and equals θ at the end. The parameterisation of the linear curvature bend can be computed from the integrals

$$x_{lc}(s) = \begin{cases} \displaystyle\int_0^s \cos\left\{\frac{2u^2}{RL_{lc}}\right\} du, & \text{if } 0 \leq s \leq \frac{L_{lc}}{2} \\ \displaystyle\int_{L_{lc}/2}^s \cos\left\{\frac{2u^2}{RL_{lc}} - \frac{4u}{R} + \frac{L_{lc}}{R}\right\} du, & \text{if } \frac{L_{lc}}{2} \leq s \leq L_{lc} \end{cases} \tag{4.15}$$

$$y_{lc}(s) = \begin{cases} \displaystyle\int_0^s \sin\left\{\frac{2u^2}{RL_{lc}}\right\} du, & \text{if } 0 \leq s \leq \frac{L_{lc}}{2} \\ \displaystyle\int_{L_{lc}/2}^s \sin\left\{\frac{2u^2}{RL_{lc}} - \frac{4u}{R} + \frac{L_{lc}}{R}\right\} du, & \text{if } \frac{L_{lc}}{2} \leq s \leq L_{lc} \end{cases} \tag{4.16}$$

The integrals (4.15) and (4.16) can be written in terms of the Fresnel integrals. The Fresnel

cosine and sine integrals are defined by (4.17) and (4.18) respectively [41].

$$C(x) = \sqrt{\frac{2}{\pi}} \int_0^x \cos t^2 \, dt = \int_0^x \cos \frac{\pi \, t^2}{2} \, dt \tag{4.17}$$

$$S(x) = \sqrt{\frac{2}{\pi}} \int_0^x \sin t^2 \, dt = \int_0^x \sin \frac{\pi \, t^2}{2} \, dt \tag{4.18}$$

To evaluate (4.15) and (4.16) the following integrals are required [41].

$$\int_{x_1}^{x_2} \cos\{ax^2\} \, dx = \sqrt{\frac{\pi}{2a}} \; C\left(\sqrt{\frac{2a}{\pi}} \, x\right)\Bigg|_{x_1}^{x_2} \tag{4.19}$$

$$\int_{x_1}^{x_2} \sin\{ax^2\} \, dx = \sqrt{\frac{\pi}{2a}} \; S\left(\sqrt{\frac{2a}{\pi}} \, x\right)\Bigg|_{x_1}^{x_2} \tag{4.20}$$

$$\int_{x_1}^{x_2} \cos\{a\,x^2 + 2\,b\,x + c\} \, dx = \sqrt{\frac{\pi}{2\,a}} \left\{ \cos\left(\frac{b^2 - a\,c}{a}\right) C\left(\sqrt{\frac{2}{a\,\pi}} \, (a\,x + b)\right) + \sin\left(\frac{b^2 - a\,c}{a}\right) S\left(\sqrt{\frac{2}{a\,\pi}} \, (a\,x + b)\right) \right\}\Bigg|_{x_1}^{x_2} \tag{4.21}$$

$$\int_{x_1}^{x_2} \sin\{a\,x^2 + 2\,b\,x + c\} \, dx = \sqrt{\frac{\pi}{2\,a}} \left\{ \cos\left(\frac{b^2 - a\,c}{a}\right) S\left(\sqrt{\frac{2}{a\,\pi}} \, (a\,x + b)\right) + \sin\left(\frac{b^2 - a\,c}{a}\right) C\left(\sqrt{\frac{2}{a\pi}} \, (a\,x + b)\right) \right\}\Bigg|_{x_1}^{x_2} \tag{4.22}$$

Using (4.19) and (4.21) the parameterisation of the horizontal coordinates can be computed. Upon evaluation of (4.15) it is seen that the horizontal coordinates of a linear curvature bend are computed from

$$x_{lc}(s) = c_1 \begin{cases} C\left(\dfrac{s}{c_1}\right), & \text{if } 0 \le s \le \dfrac{L_{lc}}{2} \\ \cos\left(\dfrac{L_{lc}}{R}\right)\left(C\left(\dfrac{s - L_{lc}}{c_1}\right) + C(c_2)\right) & \\ + \sin\left(\dfrac{L_{lc}}{R}\right)\left(S\left(\dfrac{s - L_{lc}}{c_1}\right) + S(c_2)\right) + C(c_2) & , \text{ if } \dfrac{L_{lc}}{2} \le s \le L_{lc} \end{cases} \tag{4.23}$$

Similarly, the parameterisation of the vertical coordinates can be computed using (4.20) and (4.22). So from (4.16) it is seen that the parameterisation of the vertical coordinates of a linear curvature bend are defined by

$$y_{lc}(s) = c_1 \begin{cases} S\left(\dfrac{s}{c_1}\right), & \text{if } 0 \le s \le \dfrac{L_{lc}}{2} \\ \sin\left(\dfrac{L_{lc}}{R}\right)\left(C\left(\dfrac{s - L_{lc}}{c_1}\right) + C(c_2)\right) & \\ - \cos\left(\dfrac{L_{lc}}{R}\right)\left(S\left(\dfrac{s - L_{lc}}{c_1}\right) + S(c_2)\right) + S(c_2) & , \text{if } \dfrac{L_{lc}}{2} \le s \le L_{lc} \end{cases} \tag{4.24}$$

In equations (4.23) and (4.24) the following constants are used

$$c_1 = \frac{1}{2}\sqrt{\pi \, R \, L_{lc}}, \quad c_2 = \sqrt{\frac{L_{lc}}{\pi \, R}}$$

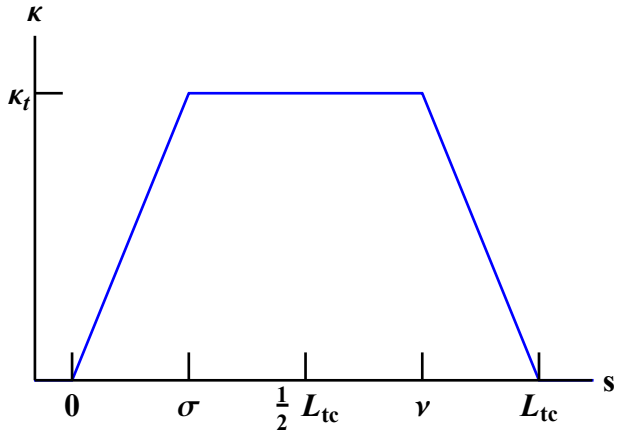


Figure 4.9: Curvature profile associated with a trapezoidal curvature bend

The functions for $x_{lc}(s)$ and $y_{lc}(s)$ are discontinuous at $s = \frac{L_{lc}}{2}$ when the integrals are initially evaluated. To ensure continuity of $x_{lc}(s)$ and $y_{lc}(s)$ at $s = \frac{L}{2}$ the value of the limit of the function to the left of $s = \frac{L_{lc}}{2}$ must be added to the function on the right of $s = \frac{L_{lc}}{2}$ for each of $x_{lc}(s)$ and $y_{lc}(s)$, this ensures that the linear curvature bend is a continuous function of path-length. Equations (4.23) and (4.24) have already been adjusted to ensure continuity at $s = L_{lc}/2$.

4.3.3 Trapezoidal curvature bends

The trapezoidal curvature bend has a three-part curvature profile defined by equation (4.25) see Figure 4.9.

$$\kappa_{tc}(s) = \begin{cases} \alpha_t\, s, & \text{if } 0 \leq s \leq \sigma \\ \kappa_t, & \text{if } \sigma \leq s \leq \nu \\ \alpha_t\,(L_{tc} - s), & \text{if } \nu \leq s \leq L_{tc} \end{cases} \tag{4.25}$$

where σ defines the length of the linear portion of the bend and ν is defined by σ. The parameters α_t, κ_t, σ and ν must be chosen so that the curvature profile is continuous and that the area under the curve equals the bend angle for an equivalent circle.

The locations of the points σ and ν define the length of the linear curvature portion of the curve. To start with, choose $0 < \sigma < \frac{L_{tc}}{2}$. If $\sigma = 0$ the constant curvature profile is recovered, if $\sigma = L_{tc}/2$ the linear curvature profile is recovered. The curvature must satisfy $\kappa_{tc}(0) = \kappa_{tc}(L_{tc}) = 0$ and $\kappa_{tc}(\sigma) = \kappa_{tc}(\nu) = \kappa_t$. To ensure continuity at $s = \sigma$ the limits from the left and the right must be calculated. By defining $\sigma = \frac{\kappa_t}{\alpha}$ the curvature profile (4.25) is continuous at $s = \sigma$. This defines the parameter ν to be $\nu = L_{tc} - \sigma$. With σ defined the curvature profile is also continuous at $s = \nu$. The curvature of the equivalent circle is given by $\kappa_{cc} = \frac{1}{R}$. As was seen in section 4.3.2 the maximum curvature of a linear curvature waveguide is $\kappa_{lc\,max} \sim \frac{2}{R}$, here the maximum value of the trapezoidal curvature bend must lie above that of the equivalent circle and below that of the linear waveguide, therefore $\kappa_t \sim \frac{\gamma}{R}$, by choosing $0 < \gamma < 2$ the curvature profile will maintain its trapezoidal shape.

The slope of the linear curvature region α_t needs to be determined. This is done by invoking the equal bend-angle condition. By symmetry, only the first half of the bend need be considered.

The trapezoidal curvature bend will turn through the correct angle if the condition

$$\int_0^{L_{tc}/2} \kappa_{tc}(s)\, ds \;=\; \frac{\theta}{2} \tag{4.26}$$

is valid. Substitution of (4.25) in (4.26) results in

$$\begin{aligned}\frac{\theta}{2} &= \int_0^{\sigma} \alpha_t\, s\, ds + \int_{\sigma}^{L_{tc}/2} \kappa_t\, ds \\ &= \frac{1}{2}\alpha_t \sigma^2 + \frac{1}{2}\kappa_t\, L_{tc} - \kappa_t\, \sigma\end{aligned}$$

Working through the algebra results in the following expression for the slope of the linear curvature region

$$\alpha_t \;=\; \frac{\kappa_t^2}{\kappa_t\, L_{tc} - \theta} \tag{4.27}$$

At this point only the curvature scaling parameter γ remains unknown[2]. To determine γ the fraction of the total bend length to be given over to linear curvature must be decided. Assume that the linear portion is some fraction f of the total length of the bend, $\sigma = fL_{tc}$, where $0 < f < \frac{1}{2}$. Taking α_t as it's defined by (4.27), σ can be written in terms of L_{tc} and γ.

$$\sigma \;=\; \frac{\kappa_t}{\alpha_t} \;=\; L_{tc}\left(1 - \frac{1}{\gamma}\right)$$

Since this must equal $\sigma = fL_{tc}$ the curvature scaling parameter can be defined in terms of the fraction of the bend whose curvature is linear.

$$\gamma \;=\; \frac{1}{1-f}$$

Choosing f between 0 and 1/2 will ensure the profile maintains its trapezoidal shape. For the moment a value of $f = 1/4$ is chosen, this means that 50% of each TC bend has linear curvature, and 50% has constant curvature and also that for TC bends $\gamma = 4/3$. This is not to say that the choice $f = 1/4$ is the best one, it may be that a bend with a different value of f might yield lower optical losses than the bend being proposed here.

Now that the curvature profile parameters are defined, the bending angle, and hence the parameterisation of the trapezoidal curvature bend can be computed. Computation of the bending angle requires the evaluation of three integrals, and confirmation of continuity at the points σ and ν. The integrals that define the bending angle are

$$\phi_{tc}(s) \;=\; \begin{cases} \displaystyle\int_0^s \alpha_t\, u\, du, & \text{if } 0 \le s \le \sigma \\ \displaystyle\int_{\sigma}^s \kappa_t\, du, & \text{if } \sigma \le s \le \nu \\ \displaystyle\int_{\nu}^s \alpha_t\, (L_{tc} - u)\, du, & \text{if } \nu \le s \le L_{tc} \end{cases} \tag{4.28}$$

The result upon integration is a discontinuous function of path-length, but it can be made continuous at $s = \sigma$ by adding $\phi_{lc(-)}(\sigma) = \frac{\kappa_t^2}{2\,\alpha_t}$ to the portion defined on $\sigma \le s \le \nu$. Similarly, at $s = \nu$ add $\phi_{lc(-)}(\nu) = \kappa_t\, L_{tc} - \frac{3\,\kappa_t^2}{2\,\alpha_t}$ to the portion defined on $\nu \le s \le L_{tc}$. The

[2]Leaving aside the fact that $L_{tc} \neq L_{cc}$, which we will come to in Section 4.3.5

resulting function satisfies $\phi_{tc}(0) = 0$, $\phi_{tc}(L_{tc}) = \theta$ and is continuous at $s = \sigma$ and $s = \nu$.

$$\phi_{tc}(s) = \begin{cases} \dfrac{1}{2}\,\alpha_t\,s^2, & \text{if } 0 \leq s \leq \sigma \\ \kappa_t\left(s - \dfrac{\kappa_t}{\alpha_t}\right) + \dfrac{\kappa_t^2}{2\,\alpha_t}, & \text{if } \sigma \leq s \leq \nu \\ \dfrac{1}{2\,\alpha_t}(\kappa_t^2 - \alpha_t^2\,(L_{tc} - s)^2) + \kappa_t\,L_{tc} - \dfrac{3\,\kappa_t^2}{2\,\alpha_t}, & \text{if } \nu \leq s \leq L_{tc} \end{cases} \tag{4.29}$$

The parameterisation of the trapezoidal curvature bend can be computed by substituting (4.29) into equations (4.4) and (4.5). The integrals to be evaluated are listed here.

$$x_{tc}(s) = \begin{cases} \displaystyle\int_0^s \cos\left\{\frac{1}{2}\,\alpha_t\,u^2\right\} du, & \text{if } 0 \leq s \leq \sigma \\ \displaystyle\int_\sigma^s \cos\left\{\kappa_t\left(u - \frac{\kappa_t}{\alpha_t}\right) + \frac{\kappa_t^2}{2\,\alpha_t}\right\} du, & \text{if } \sigma \leq s \leq \nu \\ \displaystyle\int_\nu^s \cos\left\{\frac{1}{2\,\alpha_t}(\kappa_t^2 - \alpha_t^2\,(L_{tc} - u)^2) + \kappa_t\,L_{tc} - \frac{3\,\kappa_t^2}{2\,\alpha}\right\} du, & \text{if } \nu \leq s \leq L_{tc} \end{cases} \tag{4.30}$$

$$y_{tc}(s) = \begin{cases} \displaystyle\int_0^s \sin\left\{\frac{1}{2}\,\alpha_t\,u^2\right\} du, & \text{if } 0 \leq s \leq \sigma \\ \displaystyle\int_\sigma^s \sin\left\{\kappa_t\left(u - \frac{\kappa_t}{\alpha}\right) + \frac{\kappa_t^2}{2\,\alpha_t}\right\} du, & \text{if } \sigma \leq s \leq \nu \\ \displaystyle\int_\nu^s \sin\left\{\frac{1}{2\,\alpha_t}(\kappa_t^2 - \alpha_t^2(L_{tc} - u)^2) + \kappa_t\,L_{tc} - \frac{3\,\kappa_t^2}{2\,\alpha}\right\} du, & \text{if } \nu \leq s \leq L_{tc} \end{cases} \tag{4.31}$$

The integrals on $[0, \sigma]$ can be evaluated using (4.19) in the case of the horizontal coordinates and (4.20) in the case of the vertical coordinates.

$$\begin{aligned} \int_0^s \cos\left\{\frac{1}{2}\alpha_t\,u^2\right\} du &= \sqrt{\frac{\pi}{\alpha_t}}\,C\left(\sqrt{\frac{\pi}{\alpha_t}}\,s\right) \\ \int_0^s \sin\left\{\frac{1}{2}\alpha_t\,u^2\right\} du &= \sqrt{\frac{\pi}{\alpha_t}}\,S\left(\sqrt{\frac{\pi}{\alpha_t}}\,s\right) \end{aligned}$$

The integrals on $[\sigma, \nu]$ can be evaluated exactly because the argument of the cosine and sine function in each case is a linear function of u. Simplifying the arguments and evaluating the integrals results in

$$\begin{aligned} \int_\sigma^s \cos\left\{\kappa_t\left(u - \frac{\kappa_t}{\alpha_t}\right) + \frac{\kappa_t^2}{2\,\alpha_t}\right\} du &= \int_\sigma^s \cos\left\{\kappa_t\,u - \frac{\kappa_t^2}{2\,\alpha_t}\right\} du \\ &= \frac{2}{\kappa_t}\sin\left(\frac{1}{2}\left(\kappa_t\,s - \frac{\kappa_t^2}{\alpha_t}\right)\right)\cos\left(\frac{1}{2}\,\kappa_t\,s\right) \end{aligned} \tag{4.32}$$

for the horizontal coordinates, and

$$\begin{aligned} \int_\sigma^s \sin\left\{\kappa_t\left(u - \frac{\kappa_t}{\alpha_t}\right) + \frac{\kappa_t^2}{2\,\alpha_t}\right\} du &= \int_\sigma^s \sin\left\{\kappa_t\,u - \frac{\kappa_t^2}{2\,\alpha_t}\right\} du \\ &= \frac{2}{\kappa_t}\sin\left(\frac{1}{2}\left(\kappa_t\,s - \frac{\kappa_t^2}{\alpha_t}\right)\right)\sin\left(\frac{1}{2}\,\kappa_t\,s\right) \end{aligned} \tag{4.33}$$

for the vertical coordinates. The resulting functions for the middle portion of the x and y parameterisations must be continuous at $s = \sigma$. The limits from the right hand side of σ are

$$x_+\left(\frac{\kappa_t}{\alpha_t}\right) = \lim_{s\to\sigma} x(s) = \frac{2}{\kappa_t}\sin\left(\frac{1}{2}\left(\kappa_t\frac{\kappa_t}{\alpha_t} - \frac{\kappa_t^2}{\alpha_t}\right)\right)\cos\left(\frac{1}{2}\kappa_t\frac{\kappa_t}{\alpha_t}\right) = 0$$
$$y_+\left(\frac{\kappa_t}{\alpha}\right) = \lim_{s\to\sigma} y(s) = \frac{2}{\kappa_t}\sin\left(\frac{1}{2}\left(\kappa_t\frac{\kappa_t}{\alpha_t} - \frac{\kappa_t^2}{\alpha_t}\right)\right)\sin\left(\frac{1}{2}\kappa_t\frac{\kappa_t}{\alpha_t}\right) = 0$$

The limits from the left hand side of σ are

$$x_-\left(\frac{\kappa_t}{\alpha_t}\right) = \lim_{s\to\sigma} x(s) = \sqrt{\frac{\pi}{\alpha_t}}\,C\left(\sqrt{\frac{\alpha_t}{\pi}}\frac{\kappa_t}{\alpha_t}\right)$$
$$y_-\left(\frac{\kappa_t}{\alpha_t}\right) = \lim_{s\to\sigma} y(s) = \sqrt{\frac{\pi}{\alpha_t}}\,S\left(\sqrt{\frac{\alpha_t}{\pi}}\frac{\kappa_t}{\alpha_t}\right)$$

In order to ensure continuity at $s = \sigma$ add $x_-(\sigma)$ to the middle portion of the x parameterisation and add $y_-(\sigma)$ to the middle portion of the y parameterisation. The integrals $[\nu,\, L_{tc}]$ are evaluated using equation (4.21) for the horizontal coordinates and (4.22) for the vertical coordinates.

$$\int_\nu^s \cos\left\{\frac{1}{2\,\alpha_t}(\kappa_t^2 - \alpha_t^2\,(L_{tc}-u)^2) + \kappa_t\,L_{tc} - \frac{3\,\kappa_t^2}{2\,\alpha}\right\}du =$$

$$\sqrt{\frac{\pi}{\alpha_t}}\left\{\cos\left(\kappa_t\,L_{tc} - \frac{\kappa_t^2}{\alpha_t}\right)\left[C\left(\sqrt{\frac{\alpha_t}{\pi}}\,(s-L)\right) + C\left(\frac{\kappa_t}{\sqrt{\pi\,\alpha_t}}\right)\right]\right.$$
$$\left. + \sin\left(\kappa_t\,L_{tc} - \frac{\kappa_t^2}{\alpha_t}\right)\left[S\left(\sqrt{\frac{\alpha_t}{\pi}}\,(s-L_{tc})\right) + S\left(\frac{\kappa_t}{\sqrt{\pi\,\alpha_t}}\right)\right]\right\}$$
$$+ \frac{1}{\kappa_t}\sin\left(\kappa_t\,L_{tc} - \frac{3\kappa_t^2}{2\,\alpha_t}\right) - \frac{1}{\kappa_t}\sin\left(\frac{\kappa_t^2}{2\,\alpha_t}\right) + \sqrt{\frac{\pi}{\alpha_t}}\,C\left(\frac{\kappa_t}{\sqrt{\pi\,\alpha_t}}\right)$$

$$\int_\nu^s \sin\left\{\frac{1}{2\,\alpha_t}(\kappa_t^2 - \alpha_t^2(L_{tc}-u)^2) + \kappa_t\,L_{tc} - \frac{3\,\kappa_t^2}{2\,\alpha}\right\}du =$$

$$\sqrt{\frac{\pi}{\alpha_t}}\left\{\sin\left(\kappa_t\,L_{tc} - \frac{\kappa_t^2}{\alpha_t}\right)\left[C\left(\sqrt{\frac{\alpha_t}{\pi}}\,(s-L_{tc})\right) + C\left(\frac{\kappa_t}{\sqrt{\pi\,\alpha_t}}\right)\right]\right.$$
$$\left. - \cos\left(\kappa_t\,L_{tc} - \frac{\kappa_t^2}{\alpha_t}\right)\left[S\left(\sqrt{\frac{\alpha_t}{\pi}}\,(s-L_{tc})\right) + S\left(\frac{\kappa_t}{\sqrt{\pi\,\alpha_t}}\right)\right]\right\}$$
$$- \frac{1}{\kappa_t}\cos\left(\kappa_t\,L_{tc} - \frac{3\kappa_t^2}{2\,\alpha_t}\right) + \frac{1}{\kappa_t}\cos\left(\frac{\kappa_t^2}{2\,\alpha_t}\right) + \sqrt{\frac{\pi}{\alpha_t}}\,S\left(\frac{\kappa_t}{\sqrt{\pi\,\alpha_t}}\right)$$

These integrals were corrected for discontinuity at $s = \nu$ after they were evaluated. The value of x on the left of $s = \nu$ was added to the value on the right, similarly for y. The parameterisation of the trapezoidal curvature bend is provided by the equation describing the

horizontal coordinates

$$x_{tc}(s) = \begin{cases} d_1\, C\left(\dfrac{s}{d_1}\right), & \text{if } 0 \leq s \leq \sigma \\ \dfrac{2}{\kappa_t}\sin\left(\dfrac{1}{2}\left(\kappa_t\, s - \dfrac{\kappa_t^2}{\alpha_t}\right)\right)\cos\left(\dfrac{1}{2}\,\kappa_t\, s\right) + d_1\, C\left(d_2\right), & \text{if } \sigma \leq s \leq \nu \\ d_1\left\{\cos\left(d_3\right)\left[C\left(\dfrac{s-L_{tc}}{d_1}\right) + C\left(d_2\right)\right]\right. & \\ \quad \left. + \sin\left(d_3\right)\left[S\left(\dfrac{s-L_{tc}}{d_1}\right) + S\left(d_2\right)\right]\right\}, & \text{if } \nu \leq s \leq L_{tc} \\ \quad + \dfrac{1}{\kappa_t}\sin\left(d_4\right) - \dfrac{1}{\kappa_t}\sin\left(\dfrac{\kappa_t^2}{2\,\alpha_t}\right) + d_1\, C\left(d_2\right) & \end{cases} \tag{4.34}$$

and the vertical coordinates

$$y_{tc}(s) = \begin{cases} d_1\, S\left(\dfrac{s}{d_1}\right), & \text{if } 0 \leq s \leq \sigma \\ \dfrac{2}{\kappa_t}\sin\left(\dfrac{1}{2}\left(\kappa_t\, s - \dfrac{\kappa_t^2}{\alpha_t}\right)\right)\sin\left(\dfrac{1}{2}\,\kappa_t\, s\right) + d_1\, S\left(d_2\right), & \text{if } \sigma \leq s \leq \nu \\ d_1\left\{\sin\left(d_3\right)\left[C\left(\dfrac{s-L_{tc}}{d_1}\right) + C\left(d_2\right)\right]\right. & \\ \quad \left. - \cos\left(d_3\right)\left[S\left(\dfrac{s-L_{tc}}{d_1}\right) + S\left(d_2\right)\right]\right\}, & \text{if } \nu \leq s \leq L_{tc} \\ \quad - \dfrac{1}{\kappa_t}\cos\left(d_4\right) + \dfrac{1}{\kappa_t}\cos\left(\dfrac{\kappa_t^2}{2\,\alpha_t}\right) + d_1\, S\left(d_2\right) & \end{cases} \tag{4.35}$$

In equations (4.34) and (4.35) the following constants were used

$$d_1 = \sqrt{\frac{\pi}{\alpha_t}}, \quad d_2 = \frac{\kappa_t}{\sqrt{\pi\,\alpha_t}}, \quad d_3 = \kappa_t\, L_{tc} - \frac{\kappa_t^2}{\alpha_t}, \quad d_4 = \kappa_t\, L_{tc} - \frac{3\kappa_t^2}{2\,\alpha_t}$$

4.3.4 Mode optimised bends

A choice of a linear or trapezoidal curvature profile will remove the problem of the abrupt mode transition between straight and curved sections. In this section a technique for constructing a waveguide bend from the profiles of the modes in that bend is presented [50–52]. It will be seen that the resulting curves will have a non-linear curvature profile.

The idea behind this method is that you construct a bend that is composed of a set of concatenated waveguide bend sections, each of which has a slightly different curvature. If the curvature in each section differs by a small but finite amount with respect to the previous section then the optical mode can propagate smoothly along the bend. Since the mode in each section will be very similar this will allow light to propagate with very little mode mismatch and hence less loss than is otherwise possible. This is essentially the same reasoning behind the linear and trapezoidal curvature bends, the difference in this case is that the curvature profile of the proposed waveguide is computed directly from the mode profile data.

To construct such a waveguide the first step is to compute a set of waveguide modes for waveguides whose curvature differs by a small amount. The modes are to be computed using the

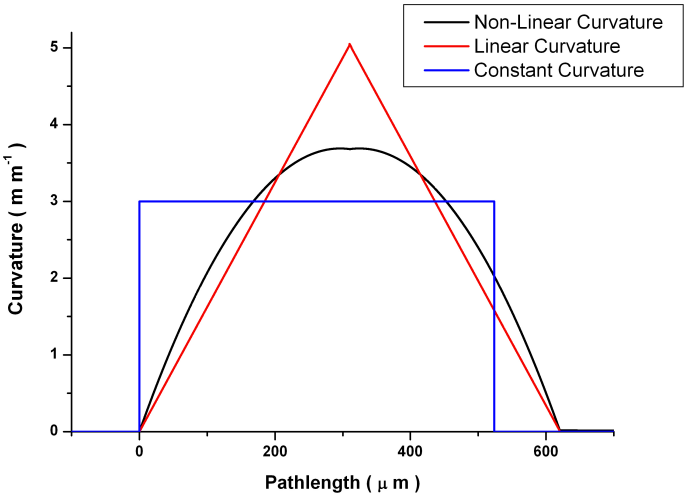


Figure 4.10: A constructed non-linear curvature profile with equivalent constant and linear curvature profiles.

finite element method, as described in Chapter 2. The range of curvatures considered starts at $\kappa = 0\,\mathrm{mm}^{-1}$, corresponding to a straight waveguide, and increases in steps of $\Delta\kappa$ up to some maximum curvature κ_{max}. The value of κ_{max} equals the inverse of the smallest bend radius for which light can propagate in a given waveguide structure. κ_{max} depends on the waveguide parameters. Its value is generally determined by numerical experimentation, either by mode computation for successively smaller values of bend radius, or by simulated mode propagation.

The next step is to generate a surface such that each point on the surface represents the value of the overlap integral T between a mode from a waveguide of curvature κ, and a mode from a waveguide of curvature $\kappa + \Delta\kappa$. The surface is plotted with the overlap integral values as heights, curvature values along one axis, and curvature difference values along a perpendicular axis.

Once the overlap surface is generated for a given waveguide the level curves of the surface are computed. This data consists of a set of (κ, $\kappa + \Delta\kappa$, T) values in which T is constant for every (κ, $\kappa + \Delta\kappa$) pair. A curvature profile is numerically constructed via the simple algorithm (4.36).

$$\begin{aligned} \kappa_{i+1} &= \kappa_i + F(\kappa_i) \quad 1 \leq i \leq N \\ \kappa_0 &= 0 \quad \text{initial condition} \end{aligned} \tag{4.36}$$

In (4.36) $F(\kappa_i)$ represents a curvature value that is obtained by interpolation over the (κ, $\kappa + \Delta\kappa$) data set, N represents the number of data points required. The curve that is constructed using (4.36) represents the curvature for the first half of our proposed curve, the second half of the curvature being symmetric about the mid-point. The full waveguide bend is assumed to be represented by the continuously changing curvature versus path-length profile, and not as a finite number of constant curvature bends. It should be noted that the proposed length of this curve has not been specified. Initially the curve will have the same length as the equivalent circle $L = R\,\theta$, this length will change according to the bend-construction algorithm of Section 4.3.5. Once the curvature profile has been specified the shape of the bend can be constructed via a numerical integration with Euler's method, i.e. equations (4.1) - (4.5). An example of a constructed non-linear curvature profile is provided in Figure 4.10.

4.3.5 A bend construction algorithm

Given an input bend radius R_{bend}, bend angle θ_{bend} and a curvature profile equations (4.1) - (4.5) can be evaluated in each case to return N positions, (x_i, y_i), $1 \leq i \leq N$, that represent the central path of a waveguide of assumed length $L = R\theta$. The first point on the waveguide is the origin, $(x_1, y_1) = (0, 0)$, the last point (x_N, y_N) is generally unknown. If a continuous curvature waveguide bend is to replace the constant curvature bend then the first and last points of each bend must be the same, otherwise different bends will end at different positions. All bends can be constructed from the same starting point, so the final position of the equivalent bend is used as a control point, this will ensure that all bends start and finish at the same position. The location of the control point, labelled (x_c, y_c), will cause the length of each bend to be determined, since the coordinates along the bend will all be scaled to ensure that $(x_N, y_N) = (x_c, y_c)$ for each of the different curvature schemes.

The algorithm for computing the coordinates of a continuous curvature bend that must replace a constant curvature bend described by an equivalent circle is described by Algorithm 11 in Appendix D. The algorithm proceeds by computing the path followed by an equivalent circle, using the routine *define_eqc_coords()*. This provides the location of the control point (x_c, y_c). The routine *define_bend_coords()* computes the positions of the centre of a bend with a specified curvature profile using (4.1) - (4.5) initially assuming a length $L_{bend} = R_{bend}\,\theta_{bend}$. Once the coordinates of the new bend are known the endpoint control test is applied by the routine *re_scale_coords()*. The routine compares (x_N, y_N) from the computed bend positions with the known endpoint from the equivalent circle (x_c, y_c). Scaling parameters for the horizontal and vertical coordinates are defined in *re_scale_coords()*. For the horizontal coordinates the scaling parameter is $x_s = x_c/x_N$, for the vertical coordinates use $y_s = y_c/y_N$. If $x_s = y_s = 1$, the algorithm is complete because the initial and final positions of the continuous curvature bend and the equivalent circle match. If x_s and y_s are not both equal to one, the horizontal coordinates are scaled by x_s, and the vertical coordinates are scaled by y_s. The length of the bend is then computed from (4.37).

$$L_{bend} = \int ds = \int \sqrt{dx^2 + dy^2} \tag{4.37}$$

Since $x_s \neq y_s \neq 1$ the loop starts again by computing the bend coordinates assuming the newly computed bend length L_{bend}. The scaling is also repeated, and another bend length is computed from the new set of coordinates. This process is repeated until the bend length has converged to within a specified tolerance, ϵ. Upon convergence of the bend length the horizontal and vertical scaling parameters will be very close to unity and the result will be a set of coordinates that describe the centre of a bend that has a specified curvature profile.

Once the bend-length is known, curvature and bend-angle profiles can be computed from the analytical formulae for a particular bend type, or numerically from the bend coordinate data. To obtain the curvature from the bend coordinate data, a geometric technique is employed. Assume that every point is contained by a circle of some, as yet, unknown radius, the inverse of this radius at each point along the bend will provide the curvature data for the bend. Given a point B on the curve, pick two points at either side of B and label them A and C as shown in Figure 4.11. These points form a triangle, $\triangle_{ABC}$, of area Q. If the lengths of the arms of the triangle are labelled as d_{AB}, for the distance between A and B, d_{BC}, for the distance between B and C, and d_{AC}, for the distance between A and C, by the sine rule the radius of the circle

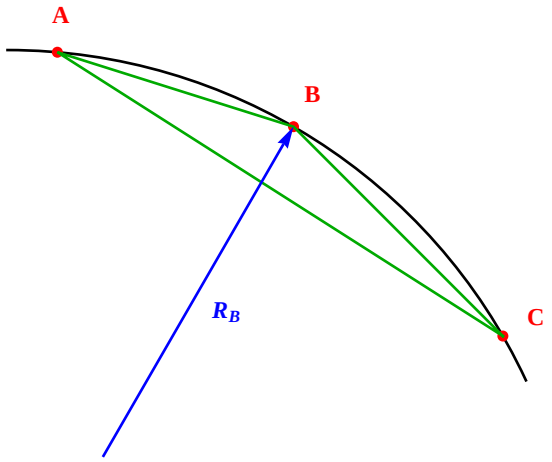


Figure 4.11: The curvature at the point B equals the inverse of the radius of the circle circumscribing $\triangle_{ABC}$.

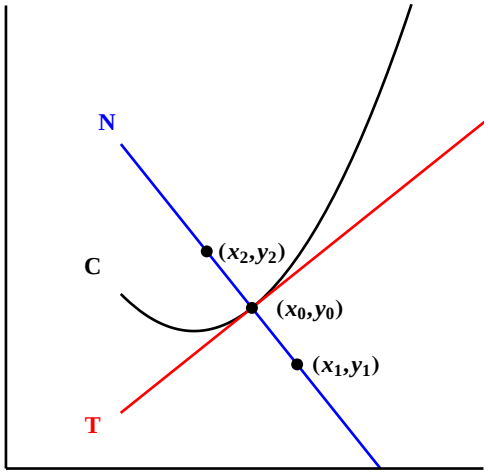


Figure 4.12: Construction for generating the outline of a curve a fixed distance from a given curve.

circumscribing $\triangle_{ABC}$ is given by [136]

$$R_B = \frac{d_{AB}\, d_{BC}\, d_{AC}}{4\,Q} \tag{4.38}$$

while the curvature at that point given by $\kappa_B = 1/R_B$. Using this method, the curvature profile for an arbitrary curve can be computed.

It is not enough to simply generate the curve that describes the centre of the proposed waveguide, the outline of the waveguide shape will also be required. If the waveguide has width W then that width must be maintained along its length. The position of the central axis cannot be shifted by an amount $W/2$, since this will lead to some parts of the waveguide not having the required width. Another geometric technique is employed to solve this problem.

Consider a curve C in the plane, as shown in Figure 4.12. If tangent T is drawn to this curve at the point $(x_0,\, y_0)$, there will also be a normal N to that tangent at the same point. The points $(x_1,\, y_1)$, and $(x_2,\, y_2)$ on the normal can be chosen so that they are a fixed distance from the point $(x_0,\, y_0)$. By moving the point $(x_0,\, y_0)$ along the curve C two other curves could be generated, one above C and one below, that would always be a fixed distance away from the

curve C. In this manner the outline of a waveguide of width W, with its central axis described by some set of points, can be defined.

The coordinates of the upper and lower curves are determined using simple coordinate geometry. Taking the equation of the tangent line as $T : y = m_1 x + c_1$, where $m_1 = \arctan \phi$, obtained by dividing (4.3) by (4.2), and $c_1 = y_0 - m_1 x_0$. The equation of the normal line is $N : y = m_2 x + c_2$, where $m_2 = -1/m_1$, and $c_2 = y_0 - m_2 x_0$. The distance between the point (x_0, y_0) on the curve and the point (x, y) on the normal is given by

$$d^2 = (x - x_0)^2 + (y - y_0)^2 \tag{4.39}$$

Expanding the r.h.s. of (4.39) and substituting for the equation of the normal line results in a quadratic equation in x.

$$\begin{aligned} A_2 x^2 + A_1 x + A_0 &= 0 \\ A_0 &= x_0^2 + y_0^2 + c_2^2 - d^2 - 2 y_0 c_2 \\ A_1 &= 2 m_2 c_2 - 2 x_0 - 2 y_0 m_2 \\ A_2 &= 1 + m_2^2 \end{aligned} \tag{4.40}$$

The roots of equation (4.40) provide the horizontal coordinates for points above and below C that are a fixed distance from C. The required vertical coordinates can be computed from the equation for the normal line. By generating a set of these points the upper and lower edges of a waveguide of width W can be determined. Special cases, such as $x_0 = 0$ and $m_1 = \pi/2$, can be dealt with as required.

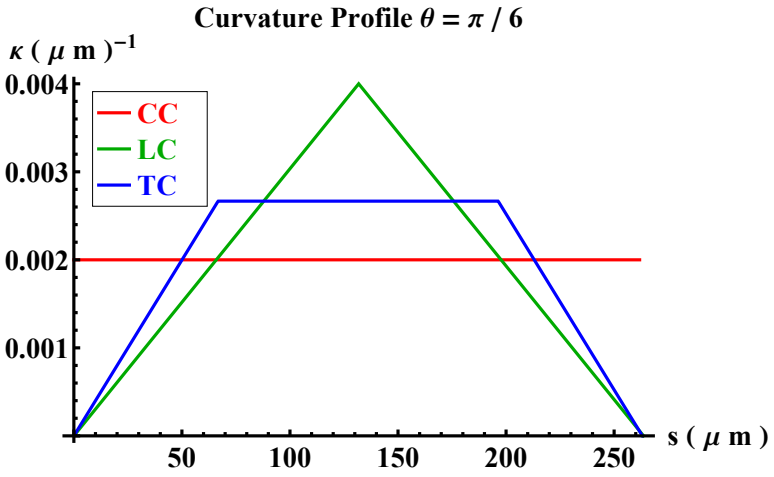
4.3.6 Application of the bend construction algorithm

To demonstrate the application of the bend construction algorithm technique waveguide bend paths were computed. CC, LC and TC bends with an equivalent radius of $R = 500\,(\mu\text{m})$ were considered for the bend angles $\theta = \{\pi/6, \pi/3, \pi/2\}$.

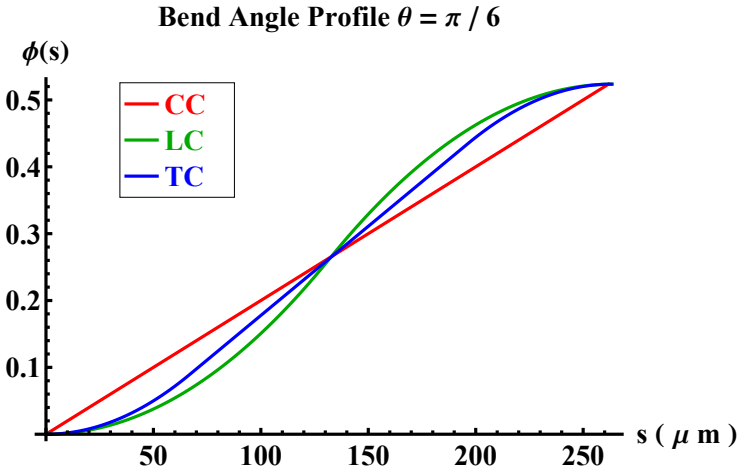
In the case of the $\theta = \pi/6$ bends the curvature profiles for each of the bends is given in Figure 4.13(a). The length of the CC bend is $L_{CC} = 261.8\,(\mu\text{m})$, the length of the LC bend is $L_{LC} = 263.6\,(\mu\text{m})$ and the length of the TC bend is $L_{TC} = 263.1\,(\mu\text{m})$. The maximum curvature of the LC bend is $\kappa_{LC}^{max} = 0.004\,(\mu\text{m})^{-1}$, the maximum curvature of the TC bend is $\kappa_{TC}^{max} = 0.00267\,(\mu\text{m})^{-1}$. The bending angle for the $\theta = \pi/6$ bends is shown in Figure4.13(b). For each of the bends $\phi(L/2) = \pi/12$ and $\phi(L) = \pi/6$ as required.

In the case of the $\theta = \pi/3$ bends the curvature profiles for each of the bends is given in Figure 4.14(a). The length of the CC bend is $L_{CC} = 523.59\,(\mu\text{m})$, the length of the LC bend is $L_{LC} = 538.14\,(\mu\text{m})$ and the length of the TC bend is $L_{TC} = 534.63\,(\mu\text{m})$. The maximum curvature of each bend has not changed because the same radius is being used. The bending angle for the $\theta = \pi/3$ bends is shown in Figure 4.14(b). For each of the bends $\phi(L/2) = \pi/6$ and $\phi(L) = \pi/3$ as required.

In the case of the $\theta = \pi/2$ bends the curvature profiles for each of the bends is given in Figure 4.15(a). The length of the CC bend is $L_{CC} = 785.39\,(\mu\text{m})$, the length of the LC bend is $L_{LC} = 835.216\,(\mu\text{m})$ and the length of the TC bend is $L_{TC} = 827.281\,(\mu\text{m})$. The maximum curvature of each bend has not changed. The bending angle for the $\theta = \pi/2$ bends is shown



(a) κ versus pathlength



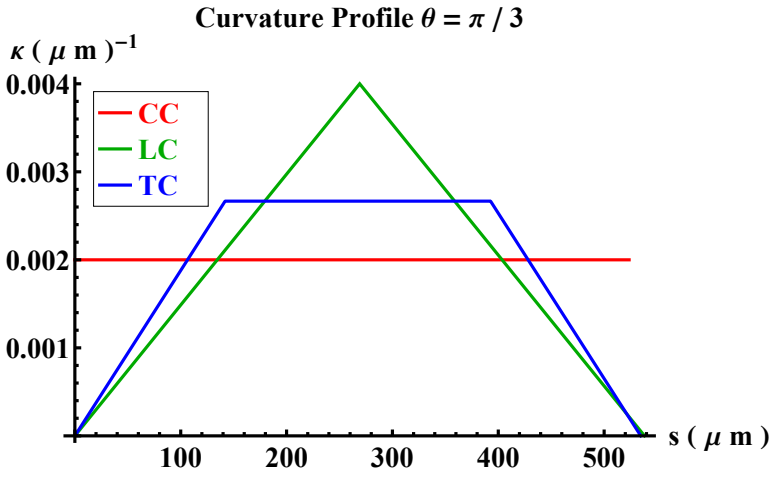
(b) ϕ versus pathlength

Figure 4.13: Curvature and bending angle profiles for a $\pi/6$ waveguide bend.

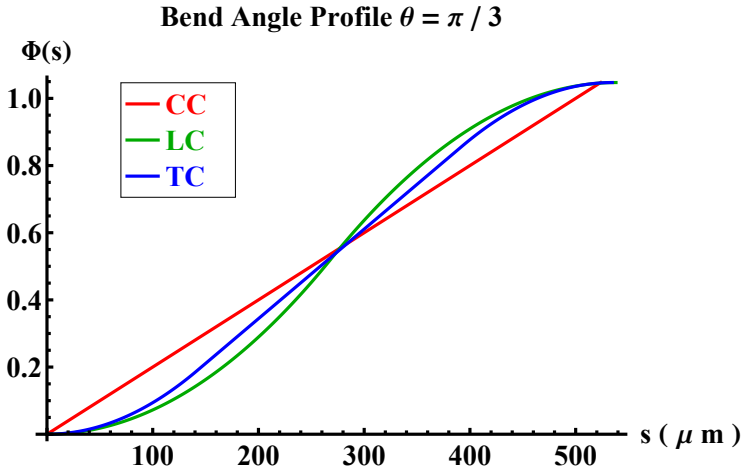
in Figure 4.15(b). For each of the bends $\phi(L/2) = \pi/4$ and $\phi(L) = \pi/2$ as required.

The paths of the waveguide centres are shown for the LC case in Figure 4.16(a) and for the TC case in Figure 4.16(b). The CC bend will follow the path of the black dashed circle for $0 \leq \theta \leq \pi/2$. Figures 4.16(a) and 4.16(b) show the difference between the path taken by the constant curvature bend and the paths taken by the LC and TC bends for the angles $\theta = \{\pi/6, \pi/3, \pi/2\}$ assuming $R = 500\,(\mu\text{m})$. These figures show that the start and end positions of the LC and TC bends are the same as those of the CC bend, this will allow for any CC bends to be replaced by an equivalent LC or TC bend should the need arise.

The waveguide outline, assuming a width of 25 (µm), for the $\pi/2$ bend can be seen in Figure 4.17. This figure shows the difference in the waveguide shape produced by each of the three bend types. Near the start and end of the LC and TC bends, the waveguide has low curvature that enables a mode to propagate with reduced transition loss. This is in contrast to the CC bend where a mode wanting to propagate will encounter a jump in waveguide curvature that causes transition loss. The width of each the waveguides is constant along the length of the bend. This can be shown by computing the distance between points on either side of the centre of the waveguide bend, i.e. points from the upper and lower arms of the waveguides. When this calculation is carried out the difference between the generated waveguide width and the actual



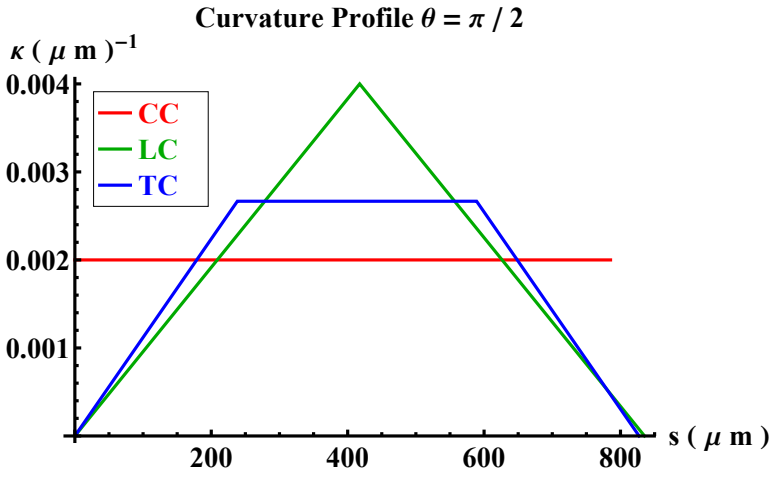
(a) κ versus pathlength



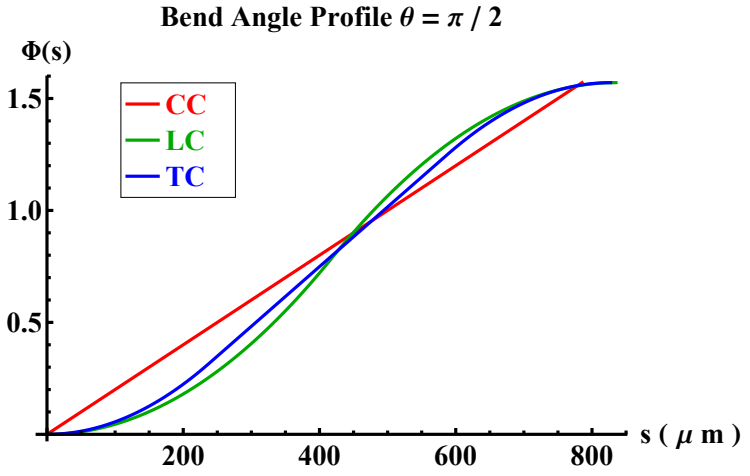
(b) ϕ versus pathlength

Figure 4.14: Curvature and bending angle profiles for a $\pi/3$ waveguide bend.

waveguide width, i.e. $|W_{actual} - d(upper, lower)|$, is $O(10^{-11})$ for each of the bend structures along the entire length of the bend.

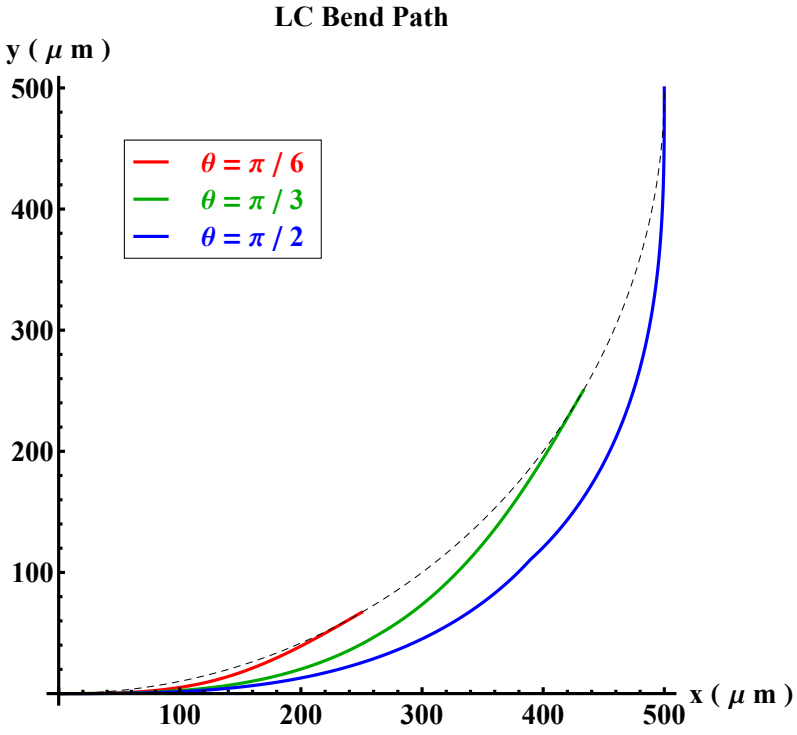


(a) κ versus pathlength

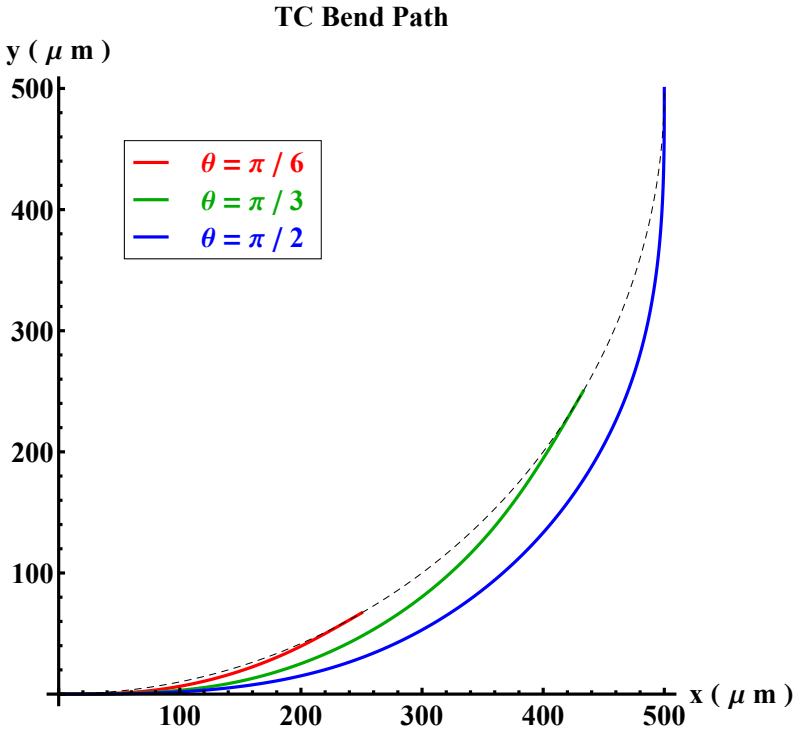


(b) ϕ versus pathlength

Figure 4.15: Curvature and bending angle profiles for a $\pi/2$ waveguide bend.



(a) LC bend paths



(b) TC bend paths

Figure 4.16: LC and TC bend paths with the CC bend path included for reference.

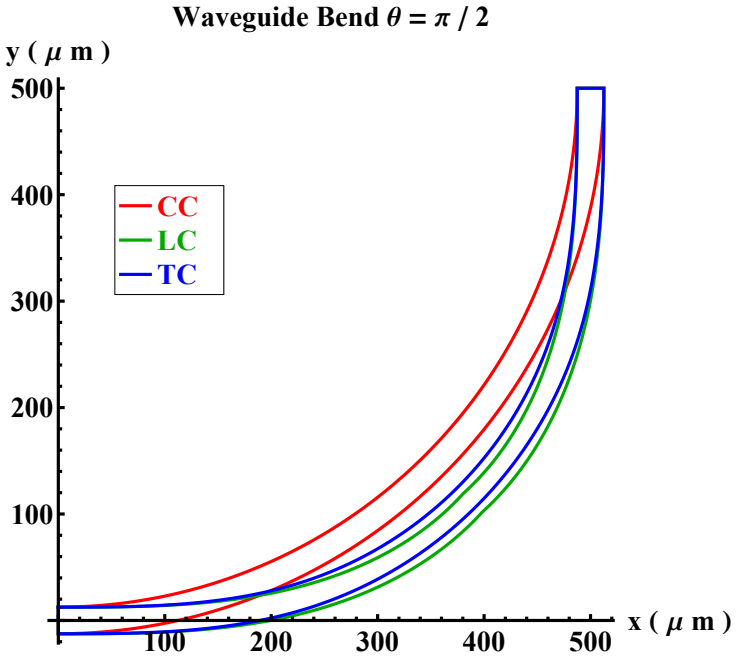


Figure 4.17: Outline of a $\pi/2$ waveguide bend with radius $R = 500\,(\mu\text{m})$ computed according to the CC, LC and TC design schemes.

4.4 Discussion

A method for designing curved optical waveguide with very low transition loss has been presented. The method allows for a waveguide to be designed without having to resort to alterations of cross-section geometry; the method will not require extra fabrication steps; and the waveguide path can be computed independently of the waveguide geometry.

In the next chapter the results from a series of simulations will be presented. The simulations involved the calculation of waveguide modes in curved optical waveguides. Application of the mode optimised bend technique to the design of a waveguide bend and finally the comparison of the CC, LC and TC bend design schemes will be made.

Chapter 5

Results

Summary: *Modal properties for curved optical waveguides are presented, along with a case of the breakdown of the one-dimensional curved slab waveguide model. The mode-optimised bend technique is used to construct a curved waveguide bend. A comparison is made between the CC, LC and TC bend design schemes using the beam propagation method.*

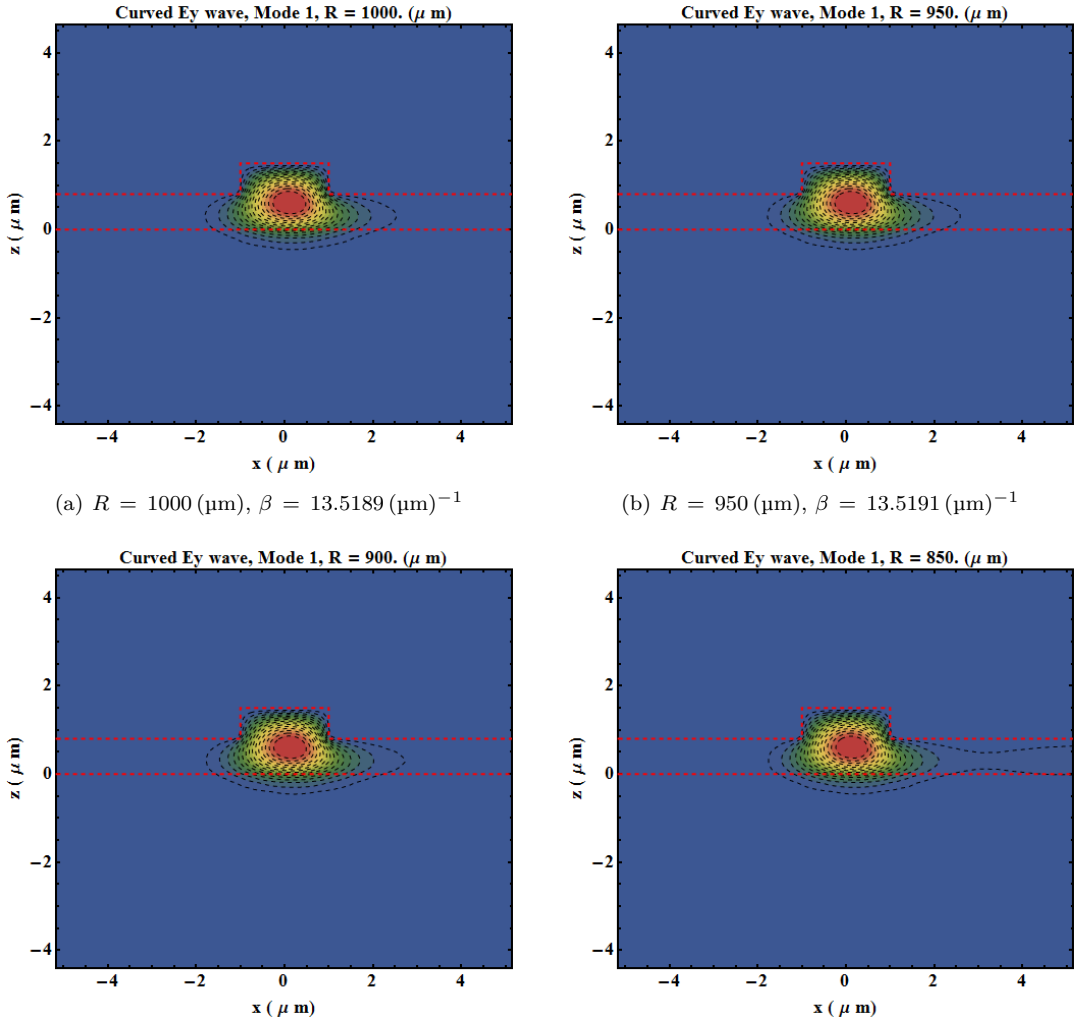
5.1 Introduction

The tools required to analyse the relative merits of each of the bend design schemes have been developed. In this chapter attention is focused on the application of those tools to the problem of bend design. By application of *SFEM_Modes* and *SFEM_Propagation* it should be possible to determine the optimum scheme for designing waveguide bends.

In Section 5.2 it is shown how *SFEM_Modes* can be used to analyse the properties of curved optical waveguides. The breakdown of the one-dimensional curved waveguide model when it is applied to real waveguides is also discussed. In Section 5.3 the mode optimised bend design scheme is applied to the curved waveguide problem. It is shown that waveguides designed using the mode optimised bend design scheme result in far lower power attenuation losses than is possible with other bend design schemes. Finally, in Section 5.4 comparison is made between the three different curvature based bend design schemes. Results from beam propagation simulations in two and three dimensions are presented.

5.2 Curved Waveguide Modes and Propagation Constants

SFEM_Modes was used to perform a modal analysis for a series of curved waveguides. Figures 5.1(a) - 5.2(d) show the general features of modes in curved optical waveguides. It can be seen that bends with larger radii have almost the same shape as the straight waveguide modes. As the bend radius decreases the mode profile shifts towards the direction of maximum curvature and mode confinement decreases [31].



(a) $R = 1000\,(\mu\text{m})$, $\beta = 13.5189\,(\mu\text{m})^{-1}$

(b) $R = 950\,(\mu\text{m})$, $\beta = 13.5191\,(\mu\text{m})^{-1}$

(c) $R = 900\,(\mu\text{m})$, $\beta = 13.5193\,(\mu\text{m})^{-1}$

(d) $R = 850\,(\mu\text{m})$, $\beta = 13.5195\,(\mu\text{m})^{-1}$

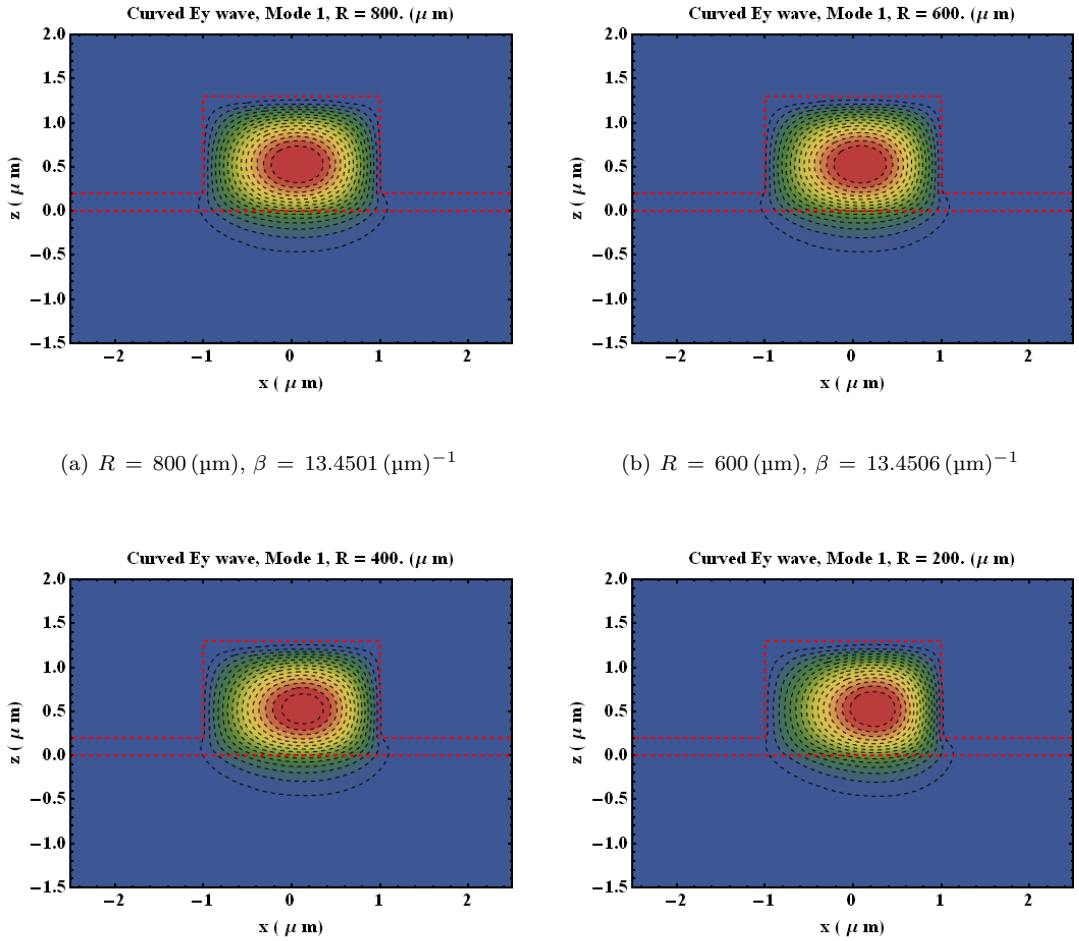
Figure 5.1: Lowest order E^y mode in a curved WG8A for various values of R. The waveguide materials and dimensions are available in Table 2.1.

SFEM_Modes can also be used to highlight problems that can occur when curved waveguides are viewed using only the one-dimensional conformal mapping model. Using the one-dimensional model a mode is said to be guided by both waveguide walls if its effective index satisfies

$$n_{eff} < n_{core} \exp\left\{-\left(\frac{W}{2R}\right)\right\} \tag{5.1}$$

If a mode does not satisfy this condition then it is in the whispering gallery regime [11]. The effective index data for WG8A and WG9A is plotted in Figures 5.3(a) and 5.3(b) respectively.

Figure 5.3(a) shows the computed lowest order mode effective index data for E^y waves in WG8A in green. Also shown in Figure 5.3(a) limiting value that a waveguide mode must have for it to be considered bound in WG8A, as computed from equation (5.1). According to Figure 5.3(a) waveguide WG8A should contain a guided fundamental mode for $R > 600$ (μm). However, upon examination of the mode profiles it is seen that for $R \leq 800$ (μm) the mode profile associated with the largest propagation constant is not a guided mode of the waveguide, even though the propagation constant satisfies the guiding condition. For waveguide WG9A the guiding condition is satisfied for $R \geq 200$ (μm). This analysis says that the guiding



(a) $R = 800\,(\mu\text{m})$, $\beta = 13.4501\,(\mu\text{m})^{-1}$

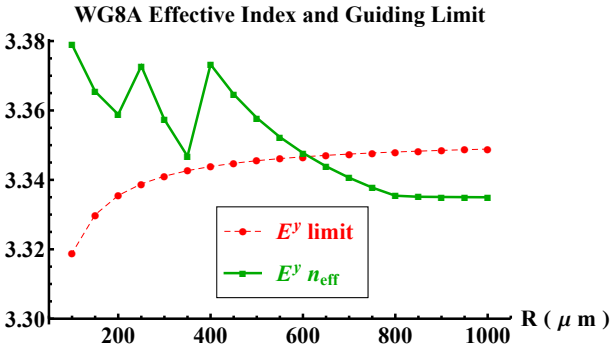
(b) $R = 600\,(\mu\text{m})$, $\beta = 13.4506\,(\mu\text{m})^{-1}$

(c) $R = 400\,(\mu\text{m})$, $\beta = 13.4521\,(\mu\text{m})^{-1}$

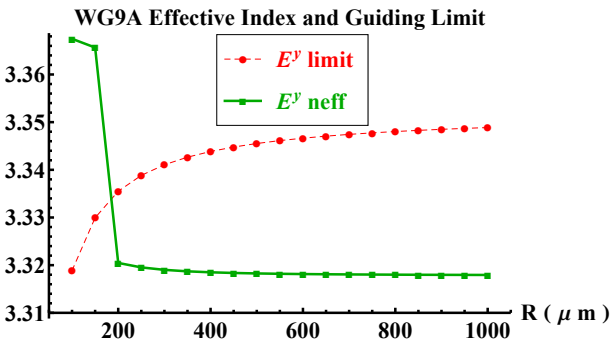
(d) $R = 200\,(\mu\text{m})$, $\beta = 13.4601\,(\mu\text{m})^{-1}$

Figure 5.2: Lowest order E^y mode in a curved WG9A for various values of R. The waveguide materials and dimensions are available in Table 2.1.

conditions derived from the one-dimensional curved waveguide model are only applicable to two-dimensional waveguides in cases where the waveguide geometry will permit high confinement, i.e. in general they should not be used to decide on the boundedness or otherwise of modes in real waveguides.



(a) WG8A n_{eff} and guiding limit



(b) WG9A n_{eff} and guiding limit

Figure 5.3: Effective index and guiding condition data for WG8A and WG9A. The waveguide materials and dimensions are available in Table 2.1.

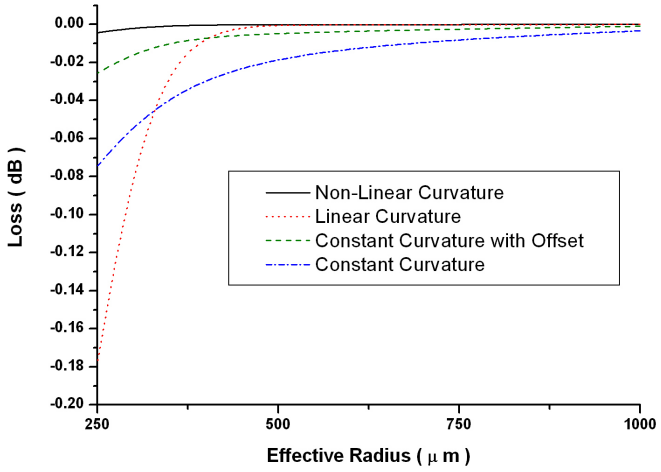


Figure 5.4: Loss in a $\pi/2$ single mode waveguide bend versus effective radius of curvature for different bend design schemes.

5.3 Mode Optimised Bend Construction

To compare the performance of the continuous curvature waveguide bend to constant curvature waveguides the losses in four types of bends are considered. These are are the constant curvature bend, the constant curvature bend with offset [15], the linear continuous curvature bend and the non-linear continuous curvature bend. The waveguide used in this discussion is a single mode slab waveguide operating at $\lambda = 1.55\,(\mu m)$, whose width is $d = 0.9\ (\mu m)$, core refractive index is $n_{core} = 3.35222$ and cladding refractive index is $n_{clad} = 3.27156$ [52].

Using the one-dimensional finite difference beam propagation method with transparent boundary conditions the bending loss in a curved waveguide structure can be determined [137]. Using an implementation written by the author in C++, the loss of the four types of curved waveguide structures were examined. The loss in this case was measured by comparing the input power to the output power. From Figure 5.4 it is seen that over a broad range of effective radius of curvature the non-linear continuous curvature waveguide bends lose less power than the other three types of waveguide. At an effective radius of $R_c = 400\,\mu m$ the constant curvature bend with offset performs better than the linear curvature waveguide bend. This shows that for optimal performance the curvature must vary in a non-linear fashion along the length of the waveguide [52].

While it is possible to construct a bend with very low loss by the mode-optimisation technique the amount of work required to generate the bend shape makes this method impractical. A large amount of mode calculations must be performed to generate the overlap surface, shown in Figure 5.5, and this can take a significant amount of time.

The waveguide offset approach to optimisation will not yield any practical differences from that of the CC bend due to the small offsets required which might not be realised due to the limitations of fabrication technology, see Section 4.2. To that end the remainder of this chapter will focus on results obtained from the CC, LC and TC bends only.

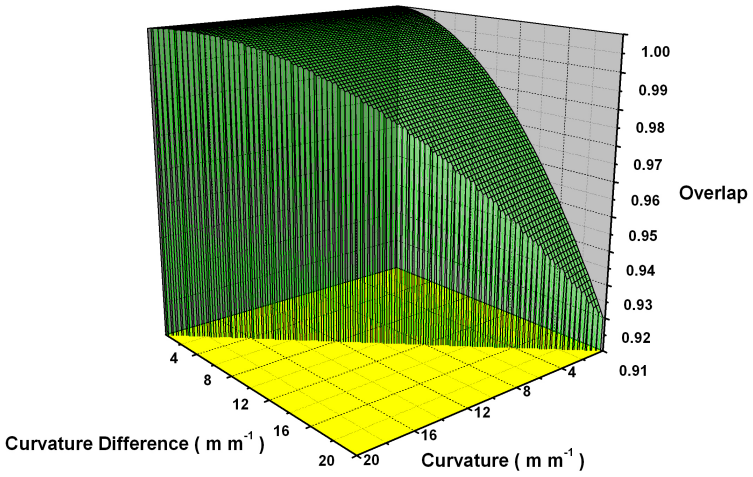


Figure 5.5: Overlap integral surface for the waveguide used in these simulations

5.4 Comparison of the Bend Design Schemes

To compare the CC, LC and TC bends a series of beam propagation simulations were performed in two and three dimensions. The waveguide device used comprised an initial straight section of length 10 (µm), followed by a bend of some effective radius R and bend angle $\theta = \pi/2$ that is defined according to the CC, LC or TC scheme described in Section 4.3, the device is finished by a straight section of length 500 (µm). A plan view of the device is given in Figure 5.6. The 3D simulations proceed by launching the fundamental E^y mode of the straight waveguide section into the device and solving equation (3.1) for that device. In 2D the fundamental TM mode of the device is launched. The mode was allowed to propagate along the length of the device. The device was discretised along the direction of propagation. The curvature at each point along the bend was incorporated into the simulation using the conformal mapping technique. This has the effect of causing the slope of the refractive index profile to vary along the direction of propagation. The simulations were carried out using *SFEM_Propagation*, with PML-BC. In total, a set of 10 radii were considered $100 < R < 1000$ with $\Delta R = 100$ (µm). The lengths of the bends in each case are given in Figure 5.7.

The aim of these simulations was to estimate the loss associated with each of the bend types. Since the initial and final straight sections were common to all devices any difference in loss is attributed to the different bend types. Firstly, the bending loss is estimated from the propagation constant data. Recall that the complex propagation constant $\gamma = \beta + i\,\alpha$ is updated along the length of the device by equation (3.28). However, depending on the bend type α never assumes a single value, see Figure 5.8. The simplest way, in the author's opinion, was to use an average value of α over the length of the bend section and apply equation (1.4). This allows for an estimate of the waveguide bending loss to be computed over a series of bend radii.

During the propagation calculation, the power in the mode being propagated is computed at each propagation step. This is done by numerical integration over the computed field. Over the course of a propagation the power would be expected to decrease as light is radiated away. Unfortunately, due to the presence of numerical reflections in the 3D calculations, the value of the integrated power oscillates, see Figure 5.9. This is a problem that remains to be resolved

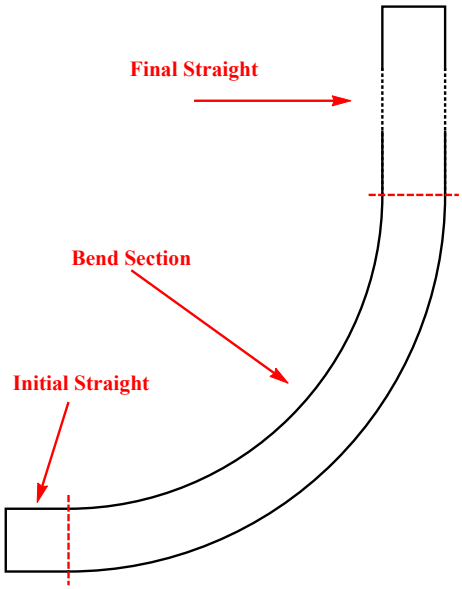


Figure 5.6: Layout of the test device for the BPM simulations

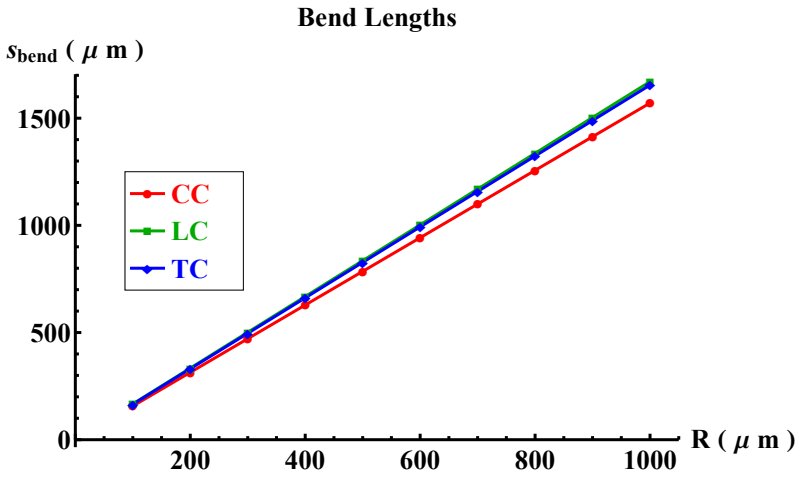


Figure 5.7: Lengths of the bend sections used in the BPM simulations

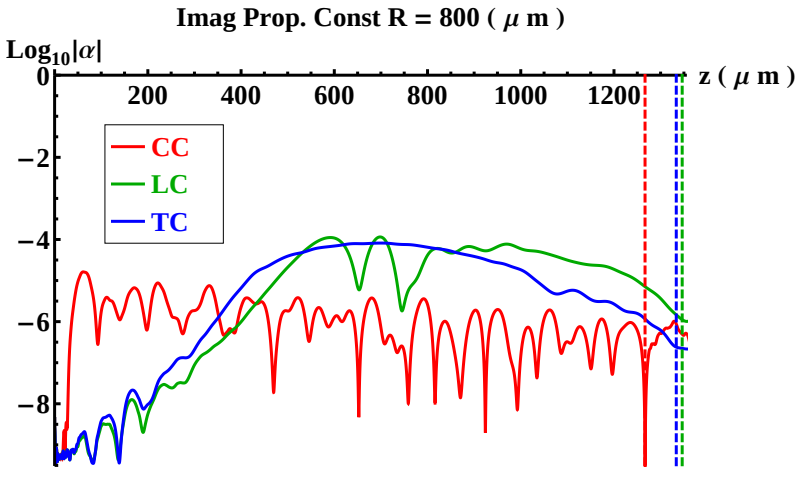


Figure 5.8: Imaginary propagation constant versus waveguide path-length for WG8A with a bend radius of 800 (µm)

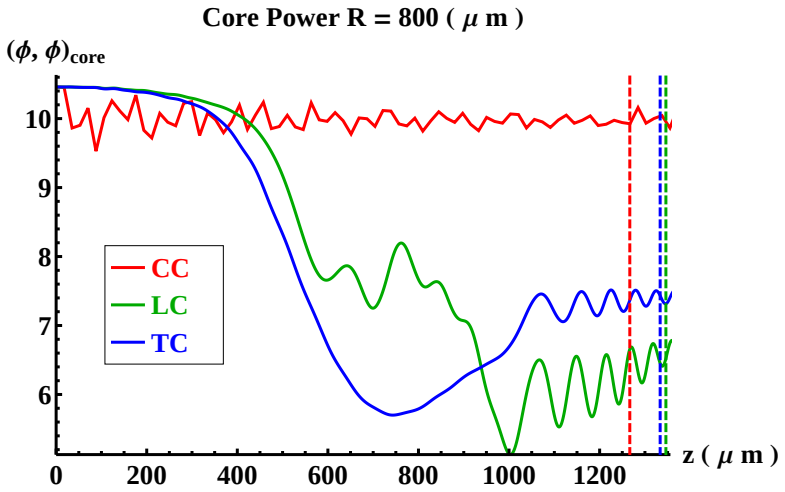


Figure 5.9: Mode power versus waveguide path-length for WG8A with a bend radius of 800 (µm)

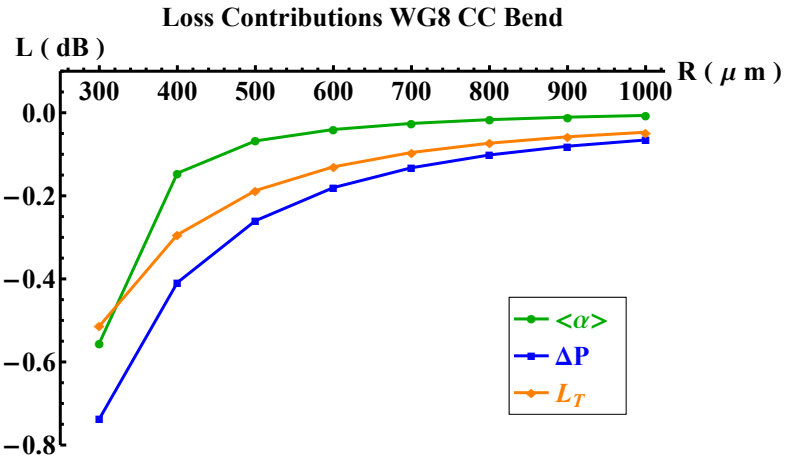
but could not be tackled during this thesis. In order to be able to determine an estimate of the power attenuation coefficient from equation (1.6) the ratio of the minimum power in the bend section to the power in the straight section was used. Therefore, the loss estimates for the shallow etch waveguides are a worst case estimate. If the numerical problems could be resolved it is expected that reduced losses would be observed. Propagation calculations in straight waveguides do not seem to suffer from significant numerical reflections from the computational domain boundaries.

There is a standard technique for computing an estimate of the transition loss. The method involves computing the modes in a straight waveguide section and a curved waveguide section for multiple values of the radius of curvature. The overlap integral between the straight waveguide modes and the curved waveguides modes is computed and the transition loss is estimated from equation (1.2). This process works fine as long as the technique being used to compute the waveguide modes returns an answer at all radii, see Section 5.2. Using *SFEM_Propagation* a mode can always be launched into a curved waveguide from a straight waveguide. This means that an estimate of the transition loss should be possible even if the mode does not propagate the full length of the bend. For the LC and TC bends the mode does not change shape as it crosses the straight-bend junction, therefore, there is no transition loss in those bend types.

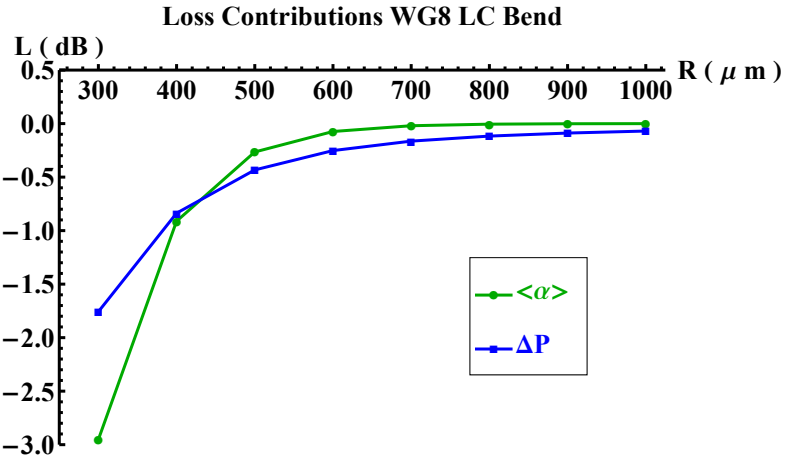
Simulations were carried out in shallow and deep etch waveguides. The contribution of each loss mechanism to the total loss was analysed from the data collected. The loss due to bending is labelled $< \alpha >$, the loss due to power attenuation is labelled ΔP and the loss due to mode transition is labelled L_T. The total loss L is the sum of each of these contributions.

5.4.1 Shallow etch waveguides

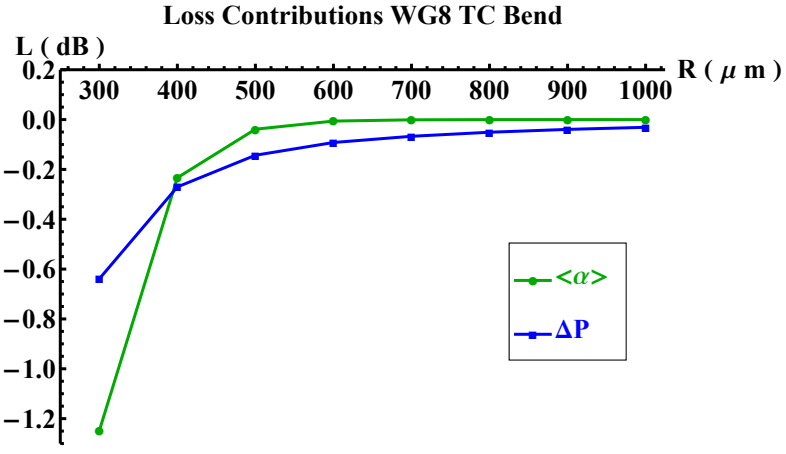
Simulations were carried using the parameters of the shallow etch waveguide WG8A. The waveguide materials and dimensions are available in Table 2.1. Simulations were performed in two and three dimensions. From the 2D simulations it was observed that the mode was not confined in any of the bend types for a bend radius of $R = 100\,(\mu m)$, the mode was also observed to have fully leaked from the LC bend when $R = 200\,(\mu m)$. In all other cases light was able to propagate the full length of the device. Figures 5.10(a) - 5.10(c) show the loss contributions for each of the different bend types.



(a) CC bend

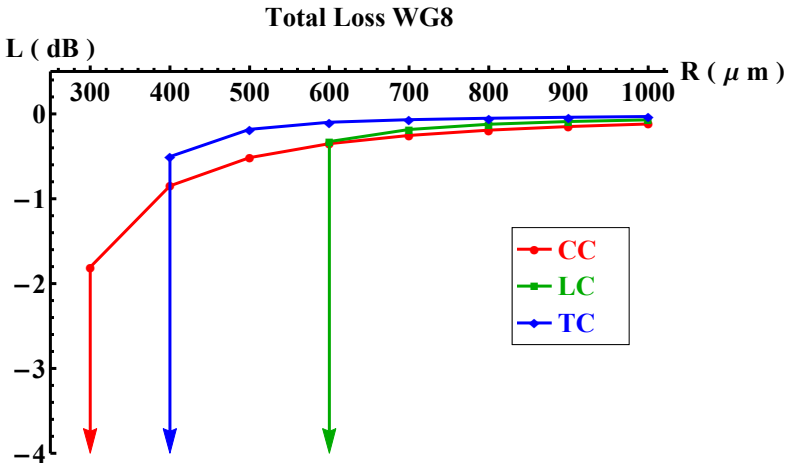


(b) LC bend

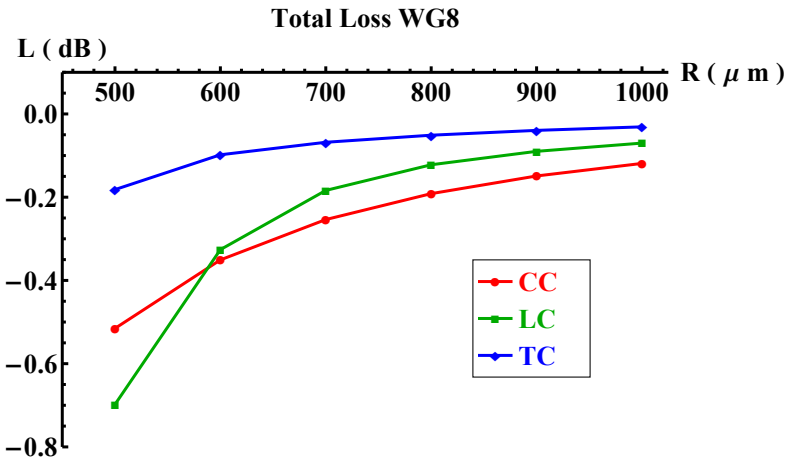


(c) TC bend

Figure 5.10: Loss contributions for the shallow etch waveguide computed from 2D simulations. The index contrast for the waveguides used in these simulations is available in Table 2.2.



(a) Losses over the range $300 \leq R \leq 1000$



(b) Losses over the range $500 \leq R \leq 1000$

Figure 5.11: Total loss for the shallow etch waveguide computed from 2D simulations. The index contrast for the waveguides used in these simulations is available in Table 2.2.

The dominant loss contribution in the CC case is the power attenuation loss. ΔP for the CC bend ranges from 0.74 (dB) at $R = 300\,(\mu m)$ to 0.066 (dB) at $R = 1000\,(\mu m)$. In the LC and TC cases the power attenuation loss and the bending loss are of a similar magnitude. In the LC case the power attenuation loss ranges from 1.77 (dB) at $R = 300\,(\mu m)$ to 0.07 (dB) at $R = 1000\,(\mu m)$ and in the TC case the power attenuation loss ranges from 0.64 (dB) at $R = 300\,(\mu m)$ to 0.03 (dB) at $R = 1000\,(\mu m)$.

The contribution from the bending loss is much lower in the CC case than it is in either of the LC or TC cases, this seems reasonable since the curvature in the CC bend is lower than that of the LC or TC bends. The transition loss that is present in the CC bend reflects the fact that in the CC bend the mode shape must change abruptly as it transitions from the straight to the curved region. This abrupt transition is not present in the LC or TC bends.

In Figure 5.11(a) it can be seen that the total loss associated with the LC bend is greater than that of the CC or TC bend for $R \leq 600\,(\mu m)$. The arrows indicate the radius for which the mode in the bend exits the waveguide completely, according to the 3D simulations. In Figure 5.11(b) it can be seen that the loss in the LC bend reduces below that of the CC bend

for $R > 600\,(\mu m)$. In the cases $R \geq 400\,(\mu m)$ the TC bend loses less light than either of the CC or LC bends.

From the 3D simulations it was observed that the mode was not confined in the CC bend for bend radii of $R \leq 300\,(\mu m)$. In the TC bend the mode was also observed to have fully leaked for $R \leq 400\,(\mu m)$, and in the LC bend the mode leaked from the device at all bend radii $R \leq 600\,(\mu m)$. In all other cases light was able to propagate the full length of the device. Figures 5.12(a) - 5.12(c) show the loss contributions for each of the different bend types.

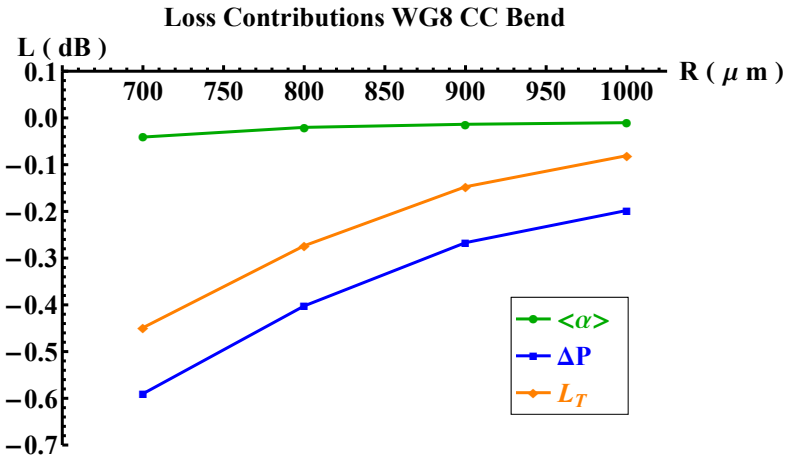
The dominant loss contribution in all cases is the power attenuation loss. In the CC case this ranges from 0.6 (dB) at $R = 700\,(\mu m)$ to 0.2 (dB) at $R = 1000\,(\mu m)$. In the LC case the power attenuation loss ranges from 2.5 (dB) at $R = 700\,(\mu m)$ to 3.3 (dB) at $R = 1000\,(\mu m)$ and in the TC case the power attenuation loss ranges from 2.6 (dB) at $R = 700\,(\mu m)$ to 0.15 (dB) at $R = 1000\,(\mu m)$. The power attenuation losses are much higher in this case because of the shallow etch depth of the waveguide. Light is able to leave the waveguide via the side slab that is 0.8 (µm) high. This is not accounted for correctly by the 2D model.

The contribution from the bending loss is lower in the CC case than it is in either of the LC or TC cases, this is reasonable because the curvature in the CC bend is lower than that of the LC or TC bends. The transition loss in the CC bend ranges from 0.45 (dB) at $R = 700\,(\mu m)$ to 0.08 (dB) at $R = 1000\,(\mu m)$.

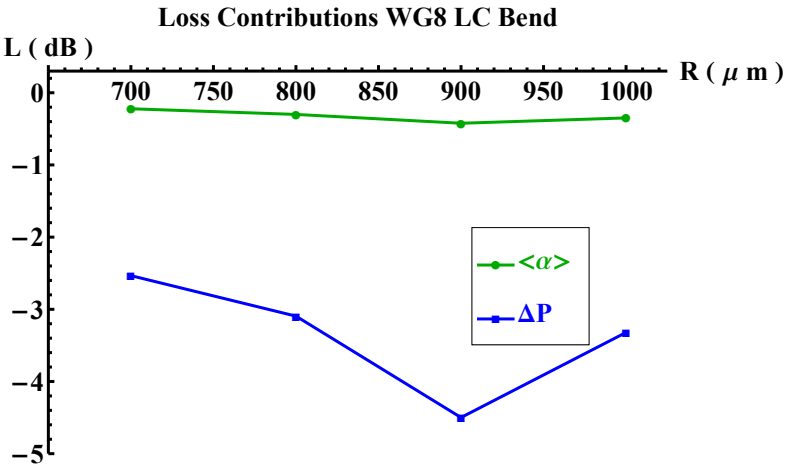
The total losses associated with propagation in WG8A can be seen in Figure 5.13. The figure shows that for $R = 700$, 800 (µm) the difference between the light lost by the CC bend and the light lost by the LC and TC bends is around 2 dB. This is due to the very high power loss from the LC and TC bends, caused by the low confinement and higher curvatures experienced by the light in those bends. As R approaches lower curvatures the TC and the CC bend start to resemble each other in the amount of light they each lose, but the LC bend is still losing more light.

Another advantage of the LC and TC bends is that they are very likely to ensure that the propagating mode exits the bend section with the same propagation it had when it entered. This is because the mode propagation constant changes symmetrically about the centre of the bend. This means that there is no transition loss as light exits the LC and TC bends. Figure 5.14 shows the difference between the initial and final values of the real part of the mode propagation constant for various values of the bend radius. For $R \geq 300\,(\mu m)$ $\Delta\,\beta$ is $O(10^{-5})$ in the LC and TC bends.

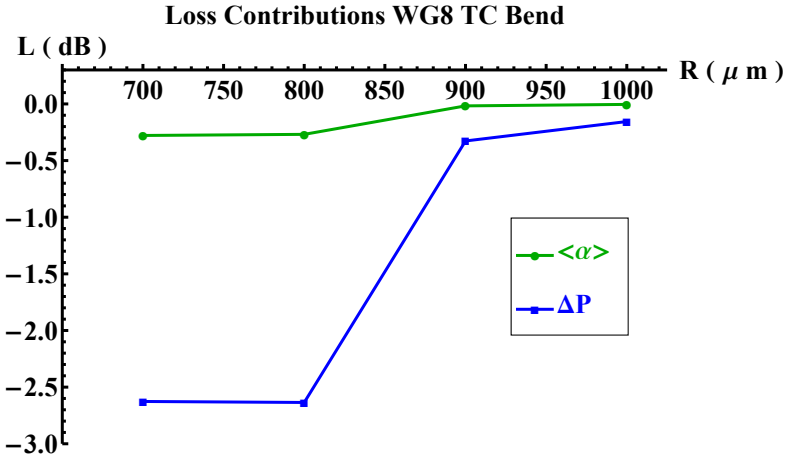
It should also be noted that during 3D simulations of waveguide WG8A a substantial reflection of the computed field was observed at the interface of the computational domain and the PML region. It has not been possible to correct for this anomalous reflection. It is suspected that the magnitude of the reflection is related to the amplitude of the field as it hits the interface because these types of reflections are not observed during the 3D simulations in the deep etch waveguide. This problem requires further analysis which is beyond the scope of this thesis. The reason it is being mentioned is that the reflections from the interface are interfering with the propagating field and this may explain the deviations of the computed power from what would be intuitively expected.



(a) CC bend



(b) LC bend



(c) TC bend

Figure 5.12: Loss contributions for the shallow etch waveguide computed from 3D simulations. The index contrast for the waveguides used in these simulations is available in Table 2.1.

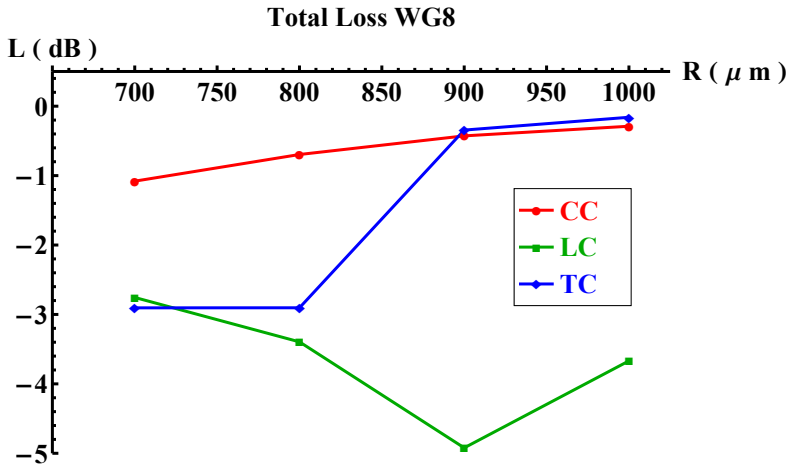


Figure 5.13: Total loss for the shallow etch waveguide computed from 3D simulations. The index contrast for the waveguides used in these simulations is available in Table 2.1.

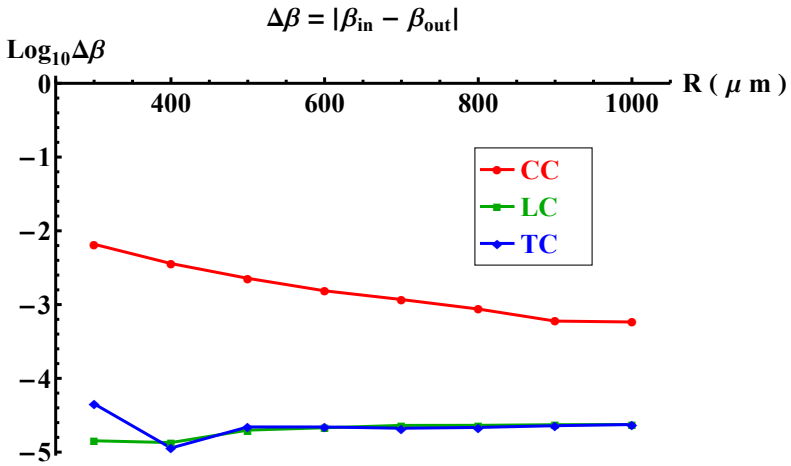


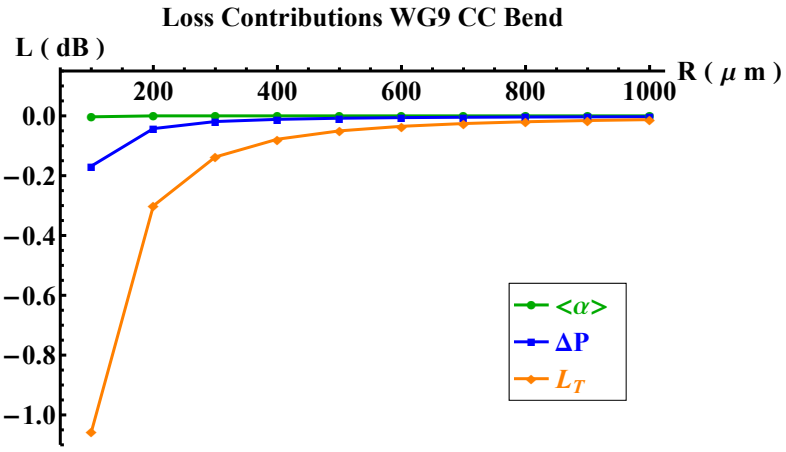
Figure 5.14: Difference between the input and output values of the real part of the propagation constant for a 2D approximation of WG8A. The index contrast for the waveguides used in these simulations is available in Table 2.2.

5.4.2 Deep etch waveguides

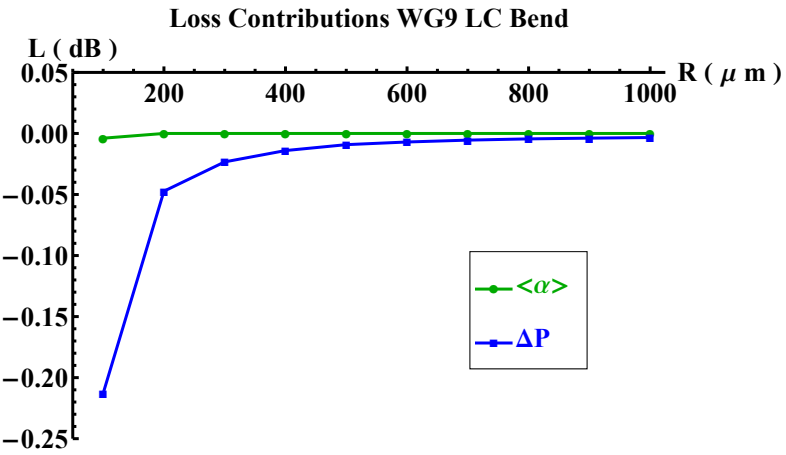
Simulations were carried using the parameters of the deep etch waveguide WG9A. The index contrast for the waveguides used in these simulations is available in Table 2.1 Simulations were performed in two and three dimensions. From the 2D simulations it was observed that the mode was able to propagate the full length of the device in all bend types at all radii. Figure 5.15(a) - 5.15(c) shows the loss contributions for each of the different bend types.

The dominant loss contribution in the CC case is the transition loss that occurs as the mode enters the bend, this ranges from 1.05 (dB) at $R = 100\,(\mu m)$ to 0.013 (dB) at $R = 1000\,(\mu m)$. In the LC and TC cases the transition loss is not present because the mode does not undergo an abrupt transition.

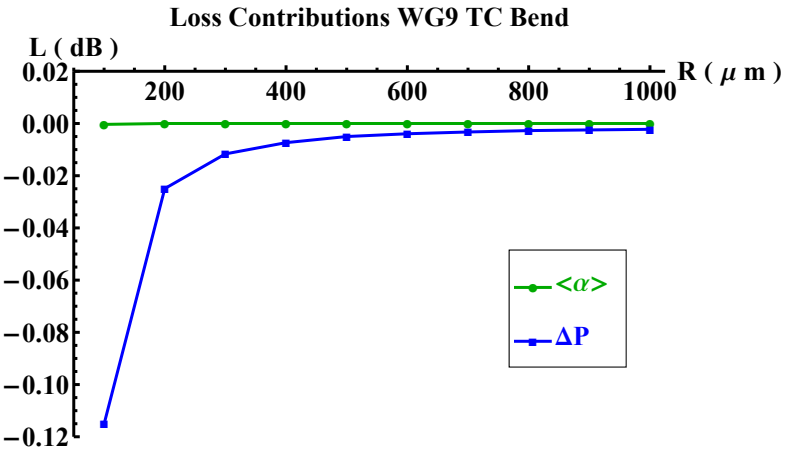
For the LC and TC bends the dominant loss factor is the power attenuation loss, this is also of a similar magnitude in the CC bend. For the CC bend the power attenuation loss ranges from 0.17 (dB) at $R = 100\,(\mu m)$ to to 0.003 (dB) at $R = 1000\,(\mu m)$. In the LC case the



(a) CC bend

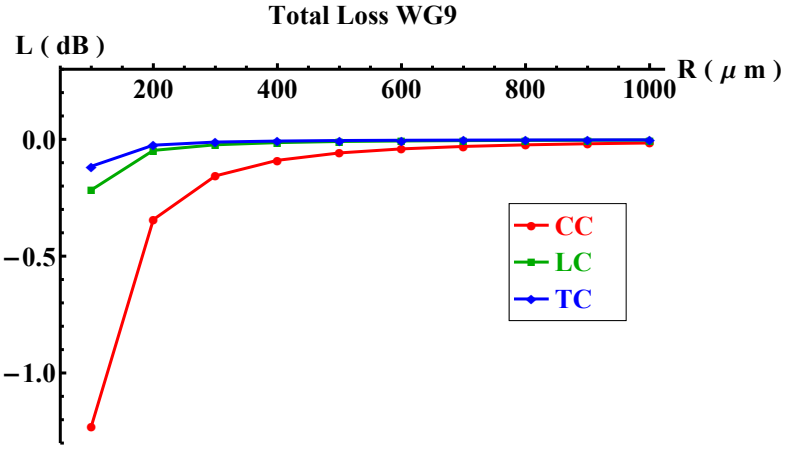


(b) LC bend

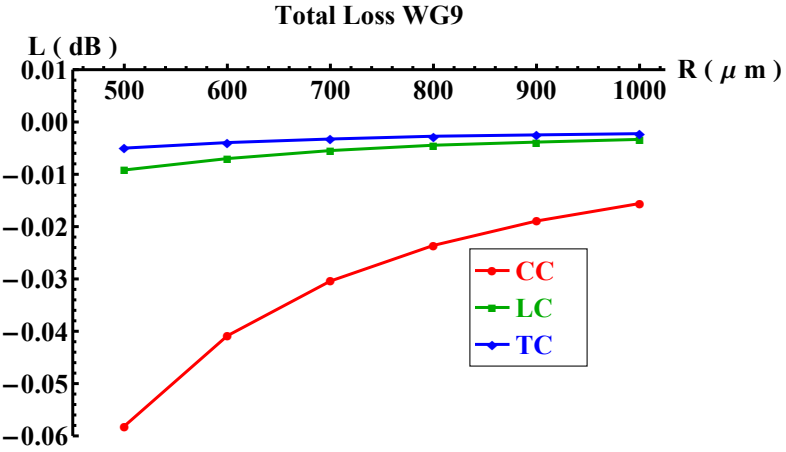


(c) TC bend

Figure 5.15: Loss contributions for the deep etch waveguide computed from 2D simulations. The index contrast for the waveguides used in these simulations is available in Table 2.2.



(a) Losses over the range $300 \leq R \leq 1000$



(b) Losses over the range $500 \leq R \leq 1000$

Figure 5.16: Total loss for the deep etch waveguide computed from 2D simulations. The index contrast for the waveguides used in these simulations is available in Table 2.2.

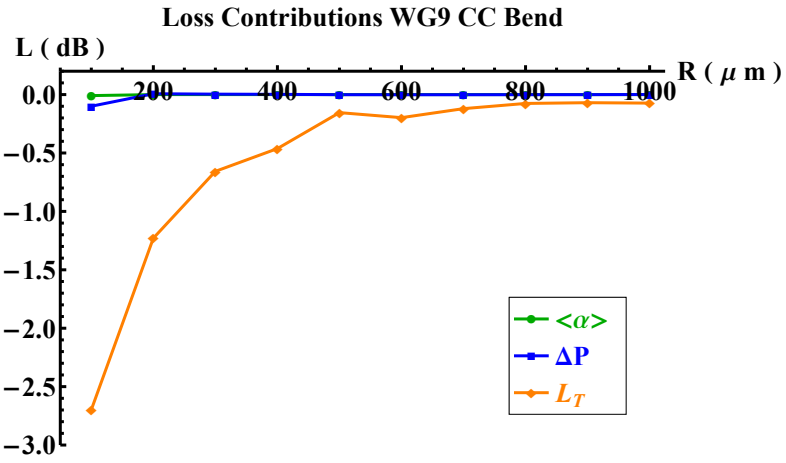
power attenuation loss is 0.21 (dB) at $R = 100$ (µm) and 0.003 (dB) at $R = 1000$ (µm). In the TC case the power attenuation loss varies from 0.12 (dB) at $R = 100$ (µm) to 0.002 (dB) at $R = 1000$ (µm).

The contribution from the bending loss is of a similar magnitude in all cases but at a much lower level than either the transition loss or the power attenuation loss. In each of the bend types the bending loss at $R = 100$ (µm) is approximately 0.004 (dB).

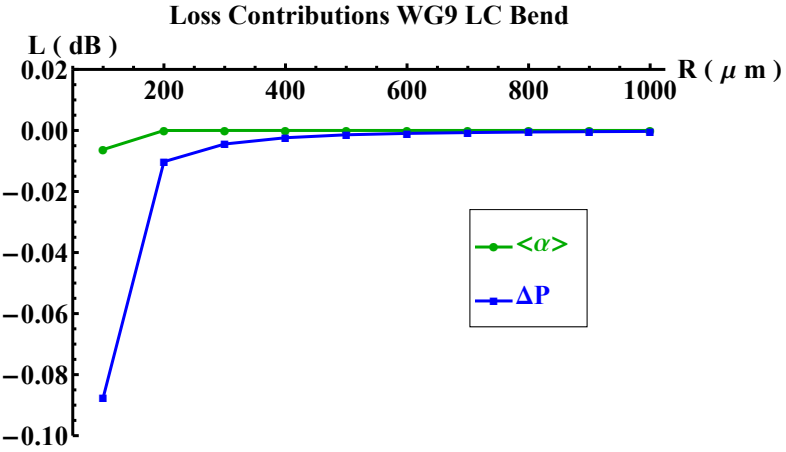
In Figure 5.16(a) it can be seen that the total loss associated with the CC bend is greater than that of the LC or TC bend for all bend radii. This is reinforced by Figure 5.16(b) which shows that the LC and TC bends have similar losses that are much lower than those in the CC bend.

From the 3D simulations it was observed that the mode was able to propagate the full length of the device in all bend types at all radii. This is possible because the high confinement in the waveguide prevents any light from exiting the bend. Figures 5.17(a) - 5.17(c) show the loss contributions for each of the different bend types.

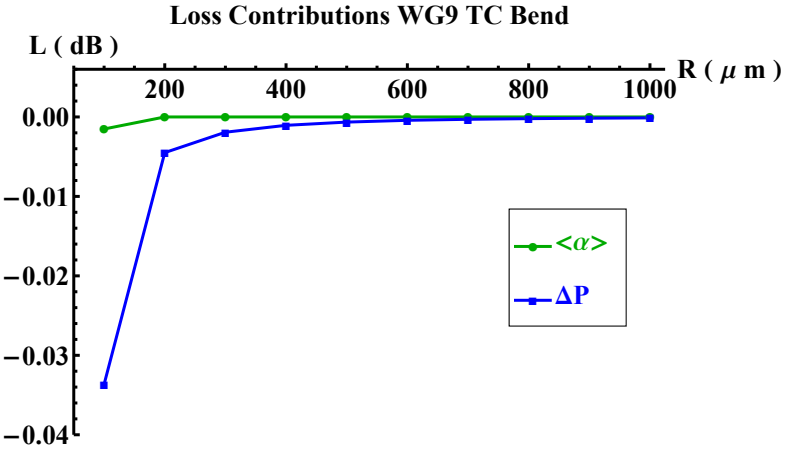
The dominant loss contribution in the CC case is the transition loss that occurs as the mode



(a) CC bend

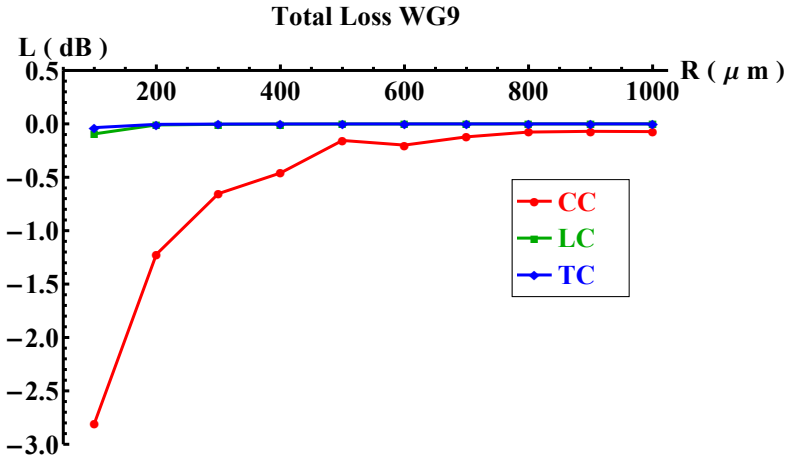


(b) LC bend

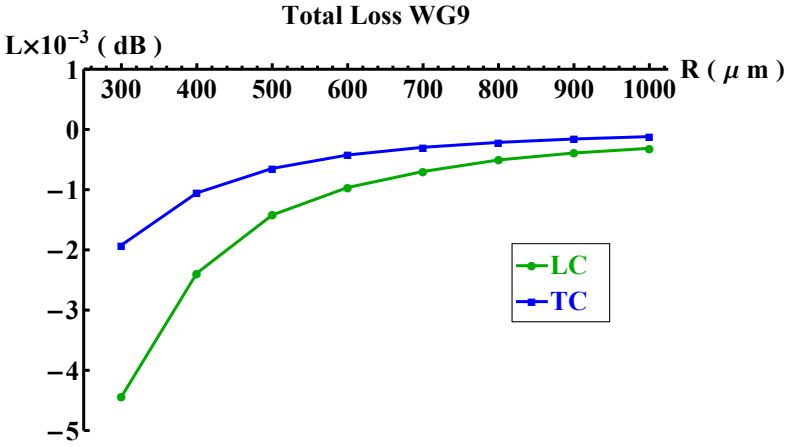


(c) TC bend

Figure 5.17: Loss contributions for the deep etch waveguide computed from 3D simulations. The index contrast for the waveguides used in these simulations is available in Table 2.1.



(a) Total loss over full range



(b) Total loss for LC and TC bends for $R \geq 300\,(\mu m)$

Figure 5.18: Total loss for the deep etch waveguide computed from 3D simulations. The index contrast for the waveguides used in these simulations is available in Table 2.1.

enters the bend, this ranges from 2.7 (dB) at $R = 100\,(\mu m)$ to to 0.036 (dB) at $R = 1000\,(\mu m)$. In the LC and TC cases the transition loss is not present because the mode does not undergo an abrupt transition.

For the LC bend the dominant loss factor is the power attenuation loss. At $R = 100\,(\mu m)$ the power attenuation loss is 0.087 (dB) while at $R = 1000\,(\mu m)$ its value is 0.0003 (dB). The CC bend displays a similar level of power attenuation loss having a value 0.09 (dB) at $R = 100\,(\mu m)$ and 0.0005 (dB) at $R = 1000\,(\mu m)$. The power attenuation loss is lower in the TC bend taking the values 0.033 (dB) at $R = 100\,(\mu m)$ and 0.0001 (dB) at $R = 1000\,(\mu m)$.

The contribution from the bending loss is highest in the CC bend case with $\Delta P = 0.0087\,(dB)$ at $R = 100\,(\mu m)$. The bending loss in the LC bend is lower than that of the CC bend and the TC bend has the lowest bending loss of all. The values for the bending loss in the LC bend and the TC bend at $R = 100\,(\mu m)$ are 0.0062 (dB) and 0.001 (dB) respectively.

In Figure 5.18(a) it can be seen that the total loss associated with the CC bend is far in excess of that in the LC or TC bends for all bend radii. Figure 5.18(b) shows that the total losses

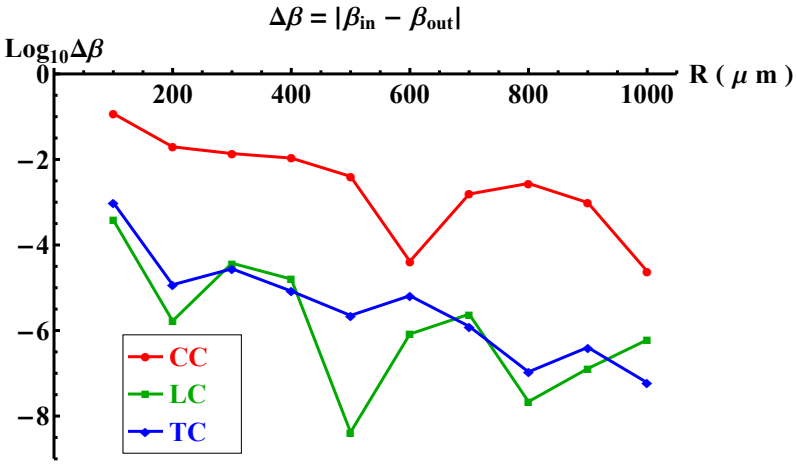
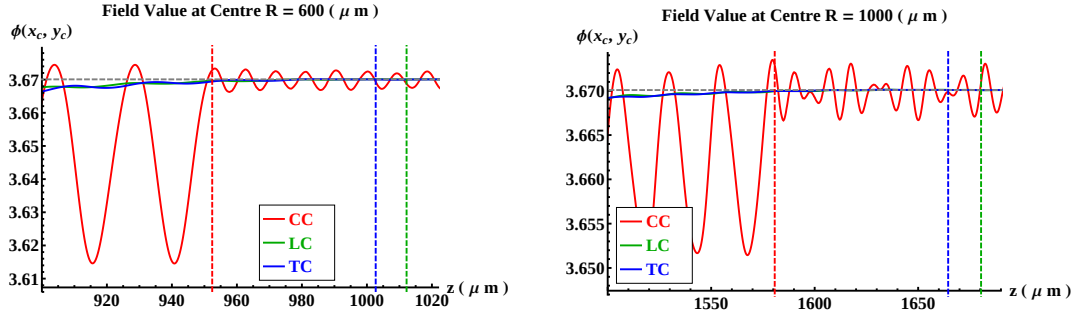


Figure 5.19: Difference between the input and output values of the propagation constant for WG9A. The index contrast for the waveguides used in these simulations is available in Table 2.1.



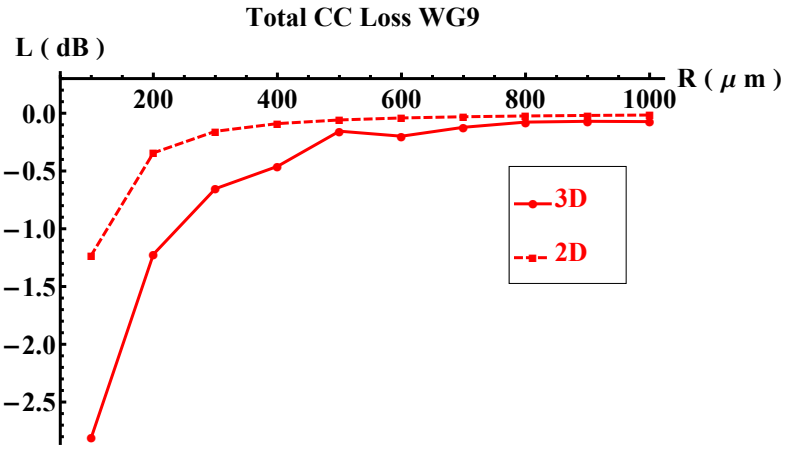
(a) $R = 600\,(\mu\text{m})$ (b) $R = 1000\,(\mu\text{m})$

Figure 5.20: Field value at the centre of WG9A near the bend-straight junction. The vertical lines indicate the position of the bend-straight junction. The index contrast for the waveguides used in these simulations is available in Table 2.1.

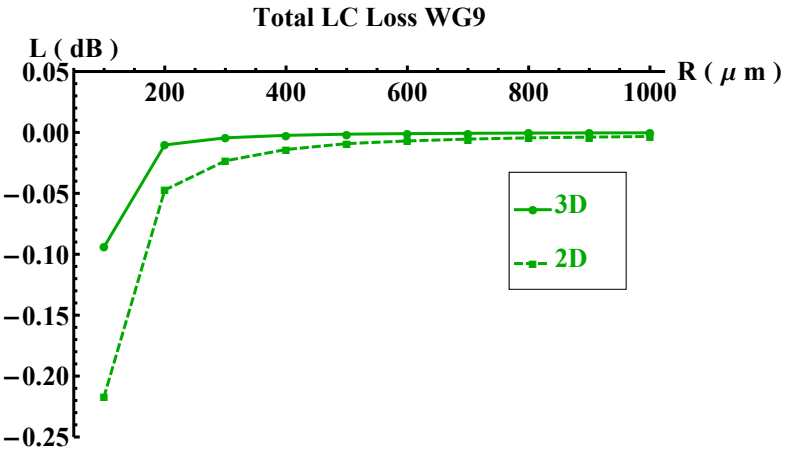
associated with the LC and TC bends are $O(10^{-3})\,(\text{dB})$ for $R \geq 300\,(\mu\text{m})$ and the TC bend exhibits a lower loss than the LC bend over that range of bend radii.

Figure 5.19 shows the change in the real part of the propagation constant between the input and the output of the device. It can be seen that in the LC and TC cases $\Delta\beta$ is lower than it is for the CC bend. This indicates that the field at the output of the bend section has the same propagation it had when it entered the bend. In the case of $R = 600\,(\mu\text{m})$ the field at the end CC bend has roughly the same propagation constant, see Figure 5.20(a), similarly for $R = 1000\,(\mu\text{m})$, see Figure 5.20(b). This is indicative of the fact that the higher order modes, excited by propagation in the CC bends, are nearly in phase with each other as they exit the bend [124]. This symmetric variation of the mode means that there is no transition loss when propagating in LC and TC bends.

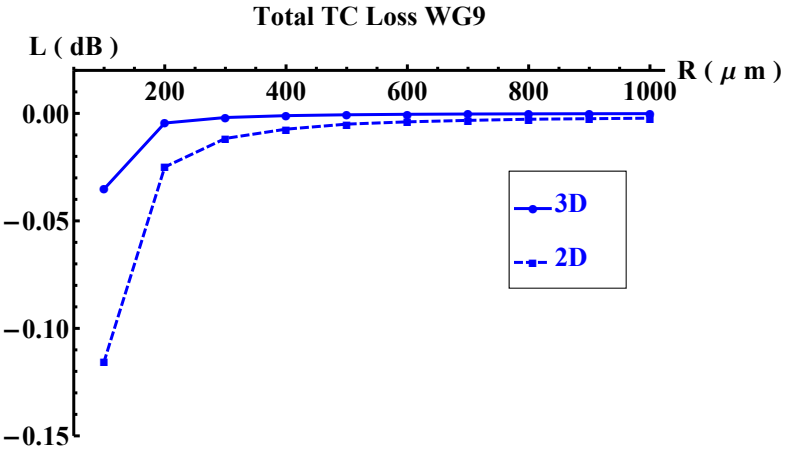
Since there were no anomalous reflections in the 3D simulations for WG9A it is possible to compare the computed total losses obtained from the 2D and 3D simulations. Figures 5.21(a) - 5.21(c) show the total losses in each the bends as computed from the 2D and 3D beam propagation analyses. For the CC bend, the loss predicted by the 2D analysis is lower than that computed from the 3D analysis over the range $100 \leq R \leq 600$. Although for $R > 600$ the loss values seem to be in general agreement. For the LC and TC bends, the loss predicted by the



(a) CC total losses



(b) LC total losses



(c) TC total losses

Figure 5.21: Comparison of the total losses in WG9A predicted by 2D and 3D beam propagation analysis. The index contrast for the 3D waveguides used in these simulations is available in Table 2.1. The index contrast for the 2D waveguides used in these simulations is available in Table 2.2.

3D analysis is lower than that computed from the 2D analysis for $100 \leq R \leq 600\,(\mu m)$, again there seems to be general agreement between the estimates in both cases for $R > 400\,(\mu m)$. The difference between the loss estimates arises from the fact that in moving from 3D to 2D some features of the waveguide properties are lost.

5.5 Discussion

The calculation of modes in curved optical waveguides has been discussed. A bend was designed, and its properties discussed, according to the mode optimised design scheme. Simulations were performed to compare the losses that arise as a result of the application of bend design based on CC, LC and TC schemes.

When light is well confined, the LC and TC bends perform better than the CC bend, and also the TC bend performs better than the LC bend. The LC and TC bends enable a mode to be propagated around a curved waveguide section with lower loss than would be obtained from using a CC bend section. Also the light propagating in the LC and TC bends exits the bend section in phase with the mode in the straight section. For shallow etched waveguides it appears that switching to continuous curvature waveguide bends may help to reduce transition losses. So in order to minimise the total bending losses the best strategy may be to adopt a design based on the TC design scheme which offers a bend with reduced transition loss at lower curvature.

Chapter 6

Conclusions and Future Work

6.1 Conclusions

From the work that has been carried out for this thesis numerous conclusions can be drawn from the work. The one dimensional conformal mapping model can be extended to two dimensions. It has been shown that the new model reproduces the known physics of modes in curved optical waveguides. The mode profiles and propagation constants of curved waveguides can be computed using the finite element method. The results of calculations using *SFEM_Modes* agree very well with expectations

Reduction of dimension approximations to simplify analysis of waveguides should only be applied to waveguides whose mode confinement is very high, i.e. deep etched waveguides. It has been shown that conditions derived from one-dimensional models can lead to erroneous predictions in the case of shallow etched waveguides.

Waveguide bends designed according to the mode optimised bend scheme will ensure that the losses obtained are lower than is possible by other methods. However, the large amount of work required to generate the optimal bend shape is burdensome, so while the technique produces very good results it may not be practical.

On the other hand the techniques used to generate the LC and TC bends require very little labour. The results of the 2D and 3D propagation simulations, using *SFEM_Propagation*, show that a CC bend can be replaced by an equivalent TC bend leading to reduced transition and bending losses when the mode confinement is very high. The 2D simulations in the shallow etched waveguides also predict that losses can be reduced by adopting bends designed according to the TC scheme. The TC scheme is a combination of both CC and LC bends. It combines the mode transitioning properties available from the LC bend with the low maximum curvature available from the CC bend. It may be possible to further optimise the design of the TC bend but the evidence provided in this thesis seems to indicate that it does provide an optimal choice of bend design.

The techniques developed in this thesis have already been used to enable the fabrication of photonic integrated circuits. Using the mask layout software *PICDraw* the design of a multi-mode interference device integrated with a slotted Fabry-Perot laser [138, 139] has been realised by Messrs. William Cotter and Padraic Morrissey and Dr. Hua Yang of the Integrated Photonics

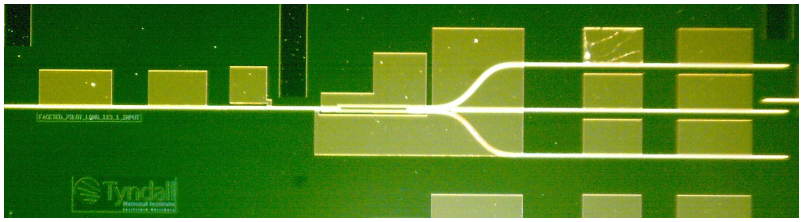


Figure 6.1: MMI integrated with slotted Fabry-Perot Lasers

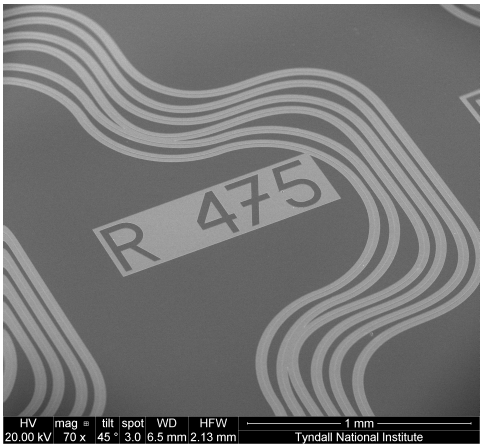


Figure 6.2: SEM image of a fabricated waveguide bend test chip

Group at Tyndall National Institute, see Figure 6.1. This device is capable of generating multiple channels of coherent output from a single injection locked laser. There is also an on-going collaboration with the Intel Corporation to develop multiplexing / de-multiplexing devices on the silicon platform. This project requires the design of arrayed waveguide gratings and Echelle gratings. The application of CC, LC and TC bends in those devices is being investigated by Dr. David Goulding, now at the Centre for Advanced Photonics and Process Analysis at Cork Institute of Technology. Outside of Cork the techniques discussed in Chapter 4 are being used to fabricate waveguides with very low loss at very tight bend radii. A group from Finland has recently published results for a waveguide bend with a 1.27 (µm) bend radius that exhibits 0.09 (dB) loss [134].

6.2 Future Work

It is the author's opinion that the work performed in this thesis can provide a stepping stone to a number of further projects. It is hoped that some of these topics may be solved as the results presented here are prepared for publication.

First off should be the experimental verification of the results obtained as part of this thesis. Previous attempts at experimental verification ended in failure due to insufficient modelling efforts. The aim was to fabricate a set of waveguide bends designed according to the different schemes, with the bends laid out in a parallel configuration, see Figure 6.2. However, the properties of those devices were analysed using a 2D approach. When the test device was fabricated using a shallow etch waveguide the measured losses were far in excess of those that were predicted by the 2D model. A repeat of the experiment with the new design tools and knowledge available could produce positive results.

The next problem to be solved is the removal of the anomalous reflection that occurs in *SFEM_Propagation* as a mode hits the interface between the computational domain and the PML-BC region. The evidence to date appears to show that the reflection does not occur during straight waveguide calculations, so it is believed that the reflection may depend on the amplitude of the wave that hits the interface. In order to examine the causes of this reflection some of the calculations for waveguide WG8A were repeated using a larger value for the width of the computational domain. It was expected that this may reduce the amplitude of the reflected waves. However, the expected reduction was not observed in any of the cases tested. It was later suspected that the reflection may be caused by differences in the value of the "s"-parameter in the PML region caused by the curvature dependent refractive index profile, see equation (3.36) in Section 3.4.2. However, an examination of the "s"-parameter for straight and curved waveguides shows that no difference is present. A calculation involving a curvature independent "s"-parameter reveals that the reflection is still present. Further work will be required to understand this problem.

Plans are in place to incorporate the beam propagation software into the photonic device design studio currently under development by the integrated photonics group. The software, called *PICDraw* has been under development for a number of years. Its primary purpose has been to aid in the drawing of masks through automation of device rendering and the development of a set of design libraries for drawing commonly used structures. The mode solver code *SFEM_Modes* has already been added to *PICDraw* and this is now being used by the integrated photonics group at Tyndall National Institute. The addition of a beam propagation tool would greatly enhance the, already formidable, capabilities of *PICDraw*.

Appendix A

Complex Analysis

The conformal mapping theorem, Theorem 1.3.1, is used in Section 1.3 of Chapter 1 to map an equation valid on a curved waveguide onto an equivalent straight waveguide. The complex analysis required to understand the theorem and its proof is presented here. Start by establishing what a complex number is, how functions of complex numbers are defined and also how differentiation of complex valued functions is defined. Finally, the proof of Theorem 1.3.1 is presented. For a more thorough discussion of complex variable theory consult [53, 54].

A.1 Complex valued functions and their derivatives

The complex variable ζ is formed from pairs of numbers in the (x, z) plane. ζ is defined as $\zeta = x + iz$, where $i = \sqrt{-1}$. The (x, z) plane is referred to as the complex plane and is labelled by $\mathbb{C}$. A subset of $\mathbb{C}$ is a region of the plane called a domain and labelled $\mathbb{D}$.

Definition A.1.1 (Complex valued function)**.** If to each value which a complex variable ζ can assume there corresponds one or more values of a complex variable w, it is said that w is a function of ζ. This is written $w = f(\zeta)$.

Definition A.1.2. If $w = f(\zeta)$ then we can consider ζ as a function of w, written $\zeta = f^{-1}(w)$. The function f^{-1} is the inverse function corresponding to f.

Definition A.1.3. If $w = u + iv$ is a single valued function of $\zeta = x + iz$, with $x, z \in \mathbb{R}$, then $u + iv = f(x + iz)$. Equating the real and imaginary parts this is seen to be equivalent to

$$u = u(x, z) \quad v = v(x, z) \tag{A.1}$$

The set of equations (A.1) is called a transformation.

Now that the definition of a complex valued function has been presented the derivative of such a function can be discussed. The most important points here are the concept of the analytic function, the Cauchy-Riemann equations and harmonic functions.

Definition A.1.4 (Derivative of a complex valued function)**.** If $f(\zeta)$ is single-valued in some region $\mathbb{D} \subseteq \mathbb{C}$, the derivative $f'(\zeta)$ is defined by

$$f'(\zeta) = \frac{df}{d\zeta} = \lim_{\Delta\zeta \to 0} \frac{f(\zeta + \Delta\zeta) - f(\zeta)}{\Delta\zeta} \tag{A.2}$$

provided that the limit exists independent of the manner in which $\Delta\zeta \to 0$. If the limit exists

it is said that the function $f(\zeta)$ is differentiable at ζ.

Definition A.1.5 (Analytic function)**.** If the derivative $f'(\zeta)$ exists at all points ζ of a region $\mathbb{D}$, then $f(\zeta)$ is said to be analytic in $\mathbb{D}$.

Let $w = f(\zeta) = u(x, z) + i\,v(x, z)$. If $f'(\zeta)$ exists then $\lim_{\Delta\zeta\to 0} \frac{\Delta w}{\Delta\zeta}$ exists, so define $\Delta\zeta = \Delta x + i\,\Delta z$ and $\Delta w = \Delta u + i\,\Delta v$ and the derivative of $f(\zeta)$ is equation (A.2) by Definition A.1.4.

$$f'(\zeta) = \lim_{\Delta x\to 0,\,\Delta z\to 0} \frac{\Delta u + i\,\Delta v}{\Delta x + i\,\Delta z} \tag{A.3}$$

This limit must be calculated in a manner which is independent of how $\Delta x \to 0$ and $\Delta z \to 0$. Let $\Delta z \to 0$ first and then let $\Delta x \to 0$.

$$\begin{aligned} f'(\zeta) &= \lim_{\Delta x\to 0}\left(\lim_{\Delta z\to 0} \frac{\Delta u + i\,\Delta v}{\Delta x + i\,\Delta z}\right) \\ &= \lim_{\Delta x\to 0}\left(\frac{\Delta u}{\Delta x} + i\,\frac{\Delta v}{\Delta x}\right) \\ &= \frac{\partial u}{\partial x} + i\,\frac{\partial v}{\partial x} \end{aligned} \tag{A.4}$$

Now reverse the order, let $\Delta x \to 0$ first and then let $\Delta z \to 0$.

$$\begin{aligned} f'(\zeta) &= \lim_{\Delta z\to 0}\left(\lim_{\Delta x\to 0} \frac{\Delta u + i\,\Delta v}{\Delta x + i\,\Delta z}\right) \\ &= \lim_{\Delta z\to 0}\left(\frac{1}{i}\frac{\Delta u}{\Delta z} + \frac{\Delta v}{\Delta z}\right) \\ &= \frac{\partial v}{\partial z} - i\,\frac{\partial u}{\partial z} \end{aligned} \tag{A.5}$$

Since the derivative $f'(\zeta)$ exists and is independent of how $\Delta z \to 0$ equation (A.4) and equation (A.5) must be equal. Equating the real parts and the imaginary parts we arrive at the Cauchy-Riemann Equations.

$$\frac{\partial u}{\partial x} = \frac{\partial v}{\partial z} \qquad \frac{\partial v}{\partial x} = -\frac{\partial u}{\partial z} \tag{A.6}$$

Definition A.1.6. A necessary and sufficient condition that $w = f(\zeta) = u + i\,v$ be analytic in some region $\mathbb{D}$ is that, in $\mathbb{D}$, $u(x, z)$ and $v(x, z)$ satisfy the Cauchy-Riemann equations. If the partial deivatives, (A.6), are continuous in $\mathbb{D}$ then the Cauchy-Riemann equations are sufficient conditions that $f(\zeta)$ be analytic in $\mathbb{D}$.

Definition A.1.7. A continuous function $\phi(x, z)$ that satisfies Laplace's equation in a domain $\mathbb{D} \subseteq \mathbb{C}$ is said to be harmonic in $\mathbb{D}$. In other words the function $\phi(x, z)$ is harmonic in $\mathbb{D}$ if $\nabla^2\phi = \dfrac{\partial^2\phi}{\partial x^2} + \dfrac{\partial^2\phi}{\partial z^2} = 0$.

Theorem A.1.1. *Let $f(\zeta) = u(x, z) + i\,v(x, z)$ be an analytic function in a domain $\mathbb{D} \subseteq \mathbb{C}$. If the 2^{nd} order partial derivatives of $u(x, z)$ and $v(x, z)$ with respect x and z exist and are continuous in $\mathbb{D}$ then $u(x, z)$ and $v(x, z)$ are harmonic in $\mathbb{D}$ [54].*

$$\begin{aligned} \frac{\partial^2 u}{\partial x^2} + \frac{\partial^2 u}{\partial z^2} &= 0 \\ \frac{\partial^2 v}{\partial x^2} + \frac{\partial^2 v}{\partial z^2} &= 0 \end{aligned}$$

Proof. $f(\zeta)$ is analytic in the domain, therefore $u(x, z)$ and $v(x, z)$ satisfy the Cauchy-Riemann

Equations (A.6). Differentiate (A.6) with respect to x and z.

$$\frac{\partial^2 u}{\partial x^2} = \frac{\partial^2 v}{\partial x\,\partial z} \tag{A.7}$$

$$\frac{\partial^2 u}{\partial x\,\partial z} = -\frac{\partial^2 v}{\partial x^2} \tag{A.8}$$

$$\frac{\partial^2 u}{\partial z\,\partial x} = \frac{\partial^2 v}{\partial z^2} \tag{A.9}$$

$$\frac{\partial^2 u}{\partial z^2} = -\frac{\partial^2 v}{\partial z\,\partial x} \tag{A.10}$$

Combining equations (A.7) and (A.10) and equations (A.8) and A.9 together completes the proof.

$$\frac{\partial^2 u}{\partial x^2} = -\frac{\partial^2 u}{\partial z^2} \Rightarrow \nabla^2 u = 0$$
$$\frac{\partial^2 v}{\partial z^2} = -\frac{\partial^2 v}{\partial x^2} \Rightarrow \nabla^2 v = 0$$

□

A.2 Proof of the conformal mapping theorem

With the establishment of harmonic functions the proof of the conformal mapping theorem can be given. Here Theorem A.2.1 is the same as Theorem 1.3.1.

Theorem A.2.1. *Suppose that $\mathbb{D}$, $\mathbb{D}' \subseteq \mathbb{C}$ are domains of the complex plane and that $f : \mathbb{D} \to \mathbb{D}'$ is a one-to-one and onto analytic function. Suppose also that for every $\zeta \in \mathbb{D}$ we write $w = f(\zeta)$, where $\zeta = x + i\,z$ and $w = u + i\,v$, with x, z, u, $v \in \mathbb{R}$. Then for every function $\phi(x, z)$ in $\mathbb{D}$ $\nabla^2_{x,\,z}\phi = |f'(z)|^2\,\nabla^2_{u,\,v}\phi$ [53, 54].*

$$\frac{\partial^2 \phi}{\partial x^2} + \frac{\partial^2 \phi}{\partial z^2} = |f'(\zeta)|^2 \left(\frac{\partial^2 \phi}{\partial u^2} + \frac{\partial^2 \phi}{\partial v^2}\right)$$

Proof. The function $\phi(x, z)$ is transformed into a function $\phi(x(u, v), z(u, v))$ by $f : \mathbb{D} \to \mathbb{D}'$. Evaluate the derivatives of ϕ with respect to x, z using the chain rule.

$$\frac{\partial \phi}{\partial x} = \frac{\partial \phi}{\partial u}\frac{\partial u}{\partial x} + \frac{\partial \phi}{\partial v}\frac{\partial v}{\partial x}$$
$$\frac{\partial \phi}{\partial z} = \frac{\partial \phi}{\partial u}\frac{\partial u}{\partial z} + \frac{\partial \phi}{\partial v}\frac{\partial v}{\partial z}$$

The second derivatives are also computed using the chain rule.

$$\begin{aligned}\frac{\partial^2 \phi}{\partial x^2} =& \frac{\partial \phi}{\partial u}\frac{\partial^2 u}{\partial x^2} + \frac{\partial u}{\partial x}\left(\frac{\partial^2 \phi}{\partial u^2}\frac{\partial u}{\partial x} + \frac{\partial^2 \phi}{\partial u\,\partial v}\frac{\partial v}{\partial x}\right) \\ &+ \frac{\partial \phi}{\partial v}\frac{\partial^2 v}{\partial x^2} + \frac{\partial v}{\partial x}\left(\frac{\partial^2 \phi}{\partial u\,\partial v}\frac{\partial u}{\partial x} + \frac{\partial^2 \phi}{\partial z^2}\frac{\partial v}{\partial x}\right)\end{aligned} \tag{A.11}$$

$$\begin{aligned}\frac{\partial^2 \phi}{\partial z^2} =& \frac{\partial \phi}{\partial u}\frac{\partial^2 u}{\partial z^2} + \frac{\partial u}{\partial x}\left(\frac{\partial^2 \phi}{\partial u^2}\frac{\partial u}{\partial z} + \frac{\partial^2 \phi}{\partial u\,\partial v}\frac{\partial v}{\partial z}\right) \\ &+ \frac{\partial \phi}{\partial v}\frac{\partial^2 v}{\partial z^2} + \frac{\partial v}{\partial z}\left(\frac{\partial^2 \phi}{\partial u\,\partial v}\frac{\partial u}{\partial z} + \frac{\partial^2 \phi}{\partial z^2}\frac{\partial v}{\partial z}\right)\end{aligned} \tag{A.12}$$

Adding equations (A.11) and (A.12) yields

$$\begin{aligned}\frac{\partial^2\phi}{\partial x^2}+\frac{\partial^2\phi}{\partial z^2} &= \frac{\partial^2\phi}{\partial u^2}\left(\left(\frac{\partial u}{\partial x}\right)^2+\left(\frac{\partial u}{\partial z}\right)^2\right)+\frac{\partial^2\phi}{\partial v^2}\left(\left(\frac{\partial v}{\partial x}\right)^2+\left(\frac{\partial v}{\partial z}\right)^2\right)\\ &+\frac{\partial\phi}{\partial u}\left(\frac{\partial^2 u}{\partial x^2}+\frac{\partial^2 u}{\partial z^2}\right)+\frac{\partial\phi}{\partial v}\left(\frac{\partial^2 v}{\partial x^2}+\frac{\partial^2 v}{\partial z^2}\right)\\ &+2\frac{\partial^2\phi}{\partial u\,\partial v}\left(\frac{\partial u}{\partial x}\frac{\partial v}{\partial x}+\frac{\partial u}{\partial z}\frac{\partial v}{\partial z}\right)\end{aligned} \tag{A.13}$$

The functions $u(x,y)$ and $v(x,y)$ are harmonic by Theorem A.1.1 this implies $\nabla^2_{x,\,z}u = \nabla^2_{x,\,z}y = 0$, so (A.13) is reduced to (A.14).

$$\begin{aligned}\frac{\partial^2\phi}{\partial x^2}+\frac{\partial^2\phi}{\partial z^2} &= \frac{\partial^2\phi}{\partial u^2}\left(\left(\frac{\partial u}{\partial x}\right)^2+\left(\frac{\partial u}{\partial z}\right)^2\right)+\frac{\partial^2\phi}{\partial v^2}\left(\left(\frac{\partial v}{\partial x}\right)^2+\left(\frac{\partial v}{\partial z}\right)^2\right)\\ &+2\frac{\partial^2\phi}{\partial u\,\partial v}\left(\frac{\partial u}{\partial x}\frac{\partial v}{\partial x}+\frac{\partial u}{\partial z}\frac{\partial v}{\partial z}\right)\end{aligned} \tag{A.14}$$

By the Cauchy-Riemann equations, equation (A.6), (A.15) is valid.

$$\frac{\partial u}{\partial x}\frac{\partial v}{\partial x}+\frac{\partial u}{\partial z}\frac{\partial v}{\partial z} = \left(\frac{\partial v}{\partial z}\right)\frac{\partial v}{\partial x}+\left(-\frac{\partial v}{\partial v}\right)\frac{\partial v}{\partial z} = 0 \tag{A.15}$$

The crossed partial derivative in equation (A.14) is eliminated and the result is (A.16).

$$\frac{\partial^2\phi}{\partial x^2}+\frac{\partial^2\phi}{\partial z^2} = \frac{\partial^2\phi}{\partial u^2}\left(\left(\frac{\partial u}{\partial x}\right)^2+\left(\frac{\partial u}{\partial z}\right)^2\right)+\frac{\partial^2\phi}{\partial v^2}\left(\left(\frac{\partial v}{\partial x}\right)^2+\left(\frac{\partial v}{\partial z}\right)^2\right) \tag{A.16}$$

The Cauchy-Riemann equations are used to evaluate the r.h.s.

$$\begin{aligned}\left(\frac{\partial u}{\partial x}\right)^2+\left(\frac{\partial u}{\partial z}\right)^2 &= \left(\frac{\partial u}{\partial x}\right)^2+\left(-\frac{\partial v}{\partial x}\right)^2\\ &= \left|\frac{\partial u}{\partial x}+i\,\frac{\partial v}{\partial x}\right|^2\\ &= |f'(\zeta)^2| \quad \because \text{(A.4)}\end{aligned} \tag{A.17}$$

$$\begin{aligned}\left(\frac{\partial v}{\partial x}\right)^2+\left(\frac{\partial v}{\partial z}\right)^2 &= \left(\frac{\partial v}{\partial x}\right)^2+\left(\frac{\partial v}{\partial z}\right)^2\\ &= \left|\frac{\partial v}{\partial z}-i\,\frac{\partial u}{\partial z}\right|^2\\ &= |f'(\zeta)^2| \quad \because \text{(A.5)}\end{aligned} \tag{A.18}$$

By equations (A.17) and (A.18) the following is valid

$$\frac{\partial^2\phi}{\partial x^2}+\frac{\partial^2\phi}{\partial z^2} = |f'(\zeta)^2|\left(\frac{\partial^2\phi}{\partial u^2}+\frac{\partial^2\phi}{\partial v^2}\right) \tag{A.19}$$

This completes the proof of the theorem. □

Appendix B

The Variational Principle

The variational principle allows us to cast a differential equation, ordinary or partial, into an equivalent functional. By the variational principle computing the stationary points of a functional is the same as computing the solutions to that differential equation [63, 64, 70]. The finite element method uses this process to compute a numerical solution to a differential equation.

Definition B.0.1 (Inner Product)**.** The inner product of two functions, ϕ and ψ, over the domain Ω is denoted by $(\phi,\, \psi)$ and defined by the integral

$$(\phi,\, \psi) \,=\, \int_{\Omega} \phi\, \psi \, d\Omega \tag{B.1}$$

This operator is commutative $(\phi,\, \psi) \,=\, (\psi,\, \phi)$.

Definition B.0.2 (Self-Adjoint)**.** An operator $\mathfrak{L}$ is self-adjoint if $(\mathfrak{L}\,\phi,\, \psi) \,=\, (\phi,\, \mathfrak{L}\,\psi)$

B.1 Proof of the variational principle

Theorem B.1.1 (Variational Principle)**.** *Given a boundary value problem defined by $\mathfrak{L}\,\phi \,=\, f$, where $\mathfrak{L}$ is a self-adjoint operator, its solution can be obtained by computing the stationary points of the functional $F(\phi)$ defined by*

$$F(\phi) \,=\, \frac{1}{2}(\mathfrak{L}\,\phi,\, \phi) - (\phi,\, f) \tag{B.2}$$

Proof. To prove that the solution of $\mathfrak{L}\,\phi \,=\, f$ is given by the stationary points of $F(\phi)$ it is sufficient to show that $\mathfrak{L}\,\phi \,=\, f$ is the necessary consequence of $\delta\, F \,=\, 0$, where $\delta\, F$ is defined as the first variation of the functional $F(\phi)$.

The first variation of $F(\phi)$ is given by

$$\delta\, F \,=\, F(\phi + \delta\phi) - F(\phi) \;\text{ where } \delta\phi \,\neq\, 0$$

By definition $F(\phi+\delta\phi) \,=\, \frac{1}{2}(\mathfrak{L}\,(\phi+\delta\phi),\, \phi+\delta\phi) - (\phi+\delta\phi,\, f)$. Expand $F(\phi+\delta\phi)$ by employing

the inner product (B.1).

$$\begin{aligned}
F(\phi+\delta\phi) &= \frac{1}{2}\int_\Omega \mathfrak{L}(\phi+\delta\phi)(\phi+\delta\phi)\,d\Omega - \int_\Omega (\phi+\delta\phi) f\,d\Omega \\
&= \frac{1}{2}\int_\Omega (\mathfrak{L}\,\phi+\mathfrak{L}\,\delta\phi)(\phi+\delta\phi)\,d\Omega - \int_\Omega (\phi\, f+\delta\phi\, f)\,d\Omega \\
&= \frac{1}{2}\int_\Omega (\mathfrak{L}\,\phi\,\phi+\mathfrak{L}\,\phi\,\delta\phi+\mathfrak{L}\,\delta\phi\,\phi+\mathfrak{L}\,\delta\phi\,\delta\phi)\,d\Omega - \int_\Omega (\phi\, f+\delta\phi\, f)\,d\Omega \\
&= \frac{1}{2}(\mathfrak{L}\,\phi,\,\phi)+\frac{1}{2}(\mathfrak{L}\,\phi,\,\delta\phi)+\frac{1}{2}(\mathfrak{L}\,\delta\phi,\,\phi)+\frac{1}{2}(\mathfrak{L}\,\delta\phi,\,\delta\phi)-(\phi,\,f)-(\delta\phi,\,f)
\end{aligned}$$

The first variation must be given by

$$\begin{aligned}
\delta F &= F(\phi+\delta\phi)-F(\phi) \\
&= \frac{1}{2}(\mathfrak{L}\,\phi,\,\phi)+\frac{1}{2}(\mathfrak{L}\,\phi,\,\delta\phi)+\frac{1}{2}(\mathfrak{L}\,\delta\phi,\,\phi)+\frac{1}{2}(\mathfrak{L}\,\delta\phi,\,\delta\phi) \\
&\quad -(\phi,\,f)-(\delta\phi,\,f)-\frac{1}{2}(\mathfrak{L}\,\phi,\,\phi)+(\phi,\,f) \\
&= \frac{1}{2}(\mathfrak{L}\,\phi,\,\delta\phi)+\frac{1}{2}(\mathfrak{L}\,\delta\phi,\,\phi)-(\delta\phi,\,f)+O((\delta\phi)^2)
\end{aligned}$$

Since the operator $\mathfrak{L}$ is self-adjoint $(\mathfrak{L}\,\delta\phi,\,\phi) = (\delta\phi,\,\mathfrak{L}\,\phi)$. Also by definition the inner product is commutative, so $(\mathfrak{L}\,\phi,\,\delta\phi) = (\delta\phi,\,\mathfrak{L}\,\phi)$. By the self-adjoint property and the inner product commutativity the first variation is

$$\begin{aligned}
\delta F &= (\delta\phi,\,\mathfrak{L}\,\phi)-(\delta\phi,\,f) \\
&= (\delta\phi,\,\mathfrak{L}\,\phi-f) \;\because \text{ inner product is a linear operator}
\end{aligned}$$

The functional $F(\phi)$ is stationary when $\delta F = 0$, therefore $\mathfrak{L}\,\phi - f = 0$ because $\delta\phi \neq 0$. □

Appendix C

Sparse Matrix Manipulation

To numerically propagate a mode in an optical waveguide the beam propagation method, presented in Chapter 3, requires the solution of a system of equations of the form $\hat{\mathbf{A}} \cdot \hat{\mathbf{x}} = \hat{\mathbf{b}}$ at every propagation step. The matrix $\hat{\mathbf{A}}$ in that system is large and sparse. The size of the system is determined by the number of nodes in the mesh discretisation of the waveguide cross-section, i.e. if the mesh contains N nodes then the matrix $\hat{\mathbf{A}}$ has size $N \times N$. A sparse matrix is one which contains a large number of zero elements. These zero elements do not contribute to the solution but they must be accounted for by the computer. Standard matrix manipulation would require that the zero elements be stored in a large contiguous block of memory that has been dynamically allocated [79], and in some cases be accounted for in a matrix product calculation. Since the number of nodes required for an accurate solution is $O(10^3)$, it is not practical, or sometimes even possible, to store the entire matrix $\hat{\mathbf{A}}$. The storage requirements for these large arrays, and the time required for processing them, can be reduced by adopting a different approach to matrix storage and access.

The technique used here is the row-indexed sparse storage mode (RISSM) [40]. Other storage schemes certainly exist but this scheme was used because it came with an implementation of the bi-conjugate gradient method in the C programming language [40]. What follows here is a description of row-indexed sparse storage mode, followed by some results showing the advantages of using RISSM.

C.1 Row-indexed Sparse Storage Mode

The aim of RISSM is to replace a large sparse two-dimensional array $\hat{\mathbf{A}}$ with two one-dimensional arrays. One array holds the non-zero values of the sparse array, call this *val_arr*, the other array holds values used to index into *val_arr* to simulate indexing into $\hat{\mathbf{A}}$, call this *index_arr*.

For a two-dimensional array of size $N \times N$ take the diagonal values of $\hat{\mathbf{A}}$ and store them in positions $1 \leq k \leq N$ of *val_arr*. Then scan the rows of $\hat{\mathbf{A}}$ and store the non-zero off-diagonal elements in positions $N+2 \leq k \leq N_{non-zero}$ of of *val_arr*. The non-zero off-diagonal elements are ordered row-wise and within each row are ordered column-wise. Note position $N+1$ of *val_arr* is never used.

To fill *index_arr* store the column numbers associated with each off-diagonal element in po-

Table C.1: *val_arr* and *index_arr* for the sparse matrix in equation (C.1).

k	*val_arr*$[k]$	*index_arr*$[k]$	Explanation of *index_arr*$[k]$
1	1	7	Matrix size+ 2
2	5	9	Index of 1^{st} non-zero element of row 2
3	8	11	Index of 1^{st} non-zero element of row 3
4	10	12 + 1 = 13	Index of last non-zero off-diagonal element of previous row + 1
5	12	13	Index of 1^{st} non-zero element of row 5
6	X	14	Index of the last element of *val_arr* incremented by 1
7	2	2	Col. num. of 1^{st} non-zero off-diagonal element of row 1
8	3	5	Col. num. of 2^{nd} non-zero off-diagonal element of row 1
9	4	1	Col. num. of 1^{st} non-zero off-diagonal element of row 2
10	6	3	Col. num. of 2^{nd} non-zero off-diagonal element of row 2
11	7	2	Col. num. of 1^{st} non-zero off-diagonal element of row 3
12	9	5	Col. num. of 2^{nd} non-zero off-diagonal element of row 3
13	11	1	Col. num. of 1^{st} non-zero off-diagonal element of row 5

sitions $N+2 \leq k \leq N_{non-zero}$. Position 1 of *index_arr* always contains the value $N+2$, *index_arr*$[1]$ is used to return the size of the original array. For positions $2 \leq k \leq N$ store the *val_arr* index of the first non-zero element in row k. If a row contains no non-zero elements store the index of the most recent element from the previous row incremented by 1. At position $N+1$ of *index_arr* store the index of the last element of *val_arr* incremented by 1, *index_arr*$[N+1]$ is used to return the number of non-zero elements in the original array.

To illustrate how RISSM is applied in practice consider the following sparse array of size $N = 5$.

$$A = \begin{pmatrix} 1 & 2 & 0 & 0 & 3 \\ 4 & 5 & 6 & 0 & 0 \\ 0 & 7 & 8 & 0 & 9 \\ 0 & 0 & 0 & 10 & 0 \\ 11 & 0 & 0 & 0 & 12 \end{pmatrix} \tag{C.1}$$

The arrays *val_arr* and *index_arr* for this array are contained in Table C.1. From Table C.1 it can be seen that the original size of the array is *index_arr*$[1] - 2 = 5$ and that the number of non-zero elements is given by *index_arr*$[6] - 1$.

To implement this scheme in C++ the RISSM sub-routines provided in [40] were adapted for use with an array object of arbitrary type. A class was written that allows for RISSM objects to be created from matrices that are input to an instance of the class. The RISSM class has the capability to perform matrix→RISSM and RISSM→matrix transformations.

An implementation of the bi-conjugate gradient method (BCGM) that iteratively solves the linear system $\hat{\mathbf{A}} \cdot \hat{\mathbf{x}} = \hat{\mathbf{b}}$ was also made part of the class. The principle advantage of this technique is that it allows for $\hat{\mathbf{x}}$ to be efficiently computed because the matrix $\hat{\mathbf{A}}$ is only ever accessed through its action on some vector $\hat{\mathbf{x}}$. The matrix-vector product $\hat{\mathbf{A}} \cdot \hat{\mathbf{x}}$ can be computed

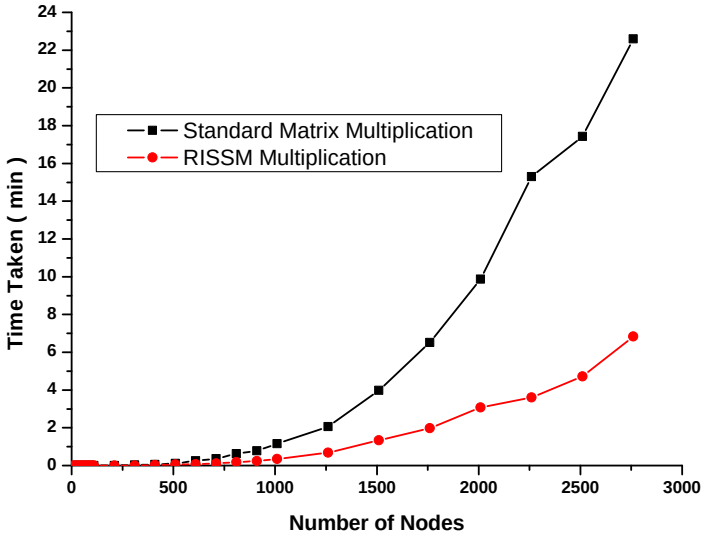


Figure C.1: Comparing the calculation time for a triple matrix product using standard matrix multiplication and multiplication via the RISSM object

very quickly when $\hat{\mathbf{A}}$ is in RISSM format, as described in [40].

C.2 Testing the objects

To test the implementation of the RISSM object the product of three sparse $N \times N$ matrices was computed for different values of N, a matrix product of this type is required by the mode solver *SFEM_Modes*. Banded matrices, in which the upper and lower bandwidths were set equal to $N/4$, were used as the test matrices, the non-zero elements were assigned random values. It was observed that the use of RISSM objects for performing the multiplication leads to a factor of three reduction in calculation time, see Figure C.1, the original matrix size equals (Number of Nodes)^2. For matrices of size 3700×3700 standard matrix multiplication requires 23 minutes to compute the matrix triple product, the same multiplication can be computed in 7 minutes when the matrices are in RISSM format.

In the propagation simulations for WG8A and WG9A each propagation step requires the solution of a system of equations of sizes 3339×3339 and 3969×3969 respectively. Solution of systems of equations of this magnitude using standard techniques would require far too much time. Testing has shown that BCGM with RISSM can compute the solution these large sparse systems in, on average, less than 6 seconds per propagation step, see Figure C.2, this includes the formation of the system of equations required by *SFEM_Propagation*.

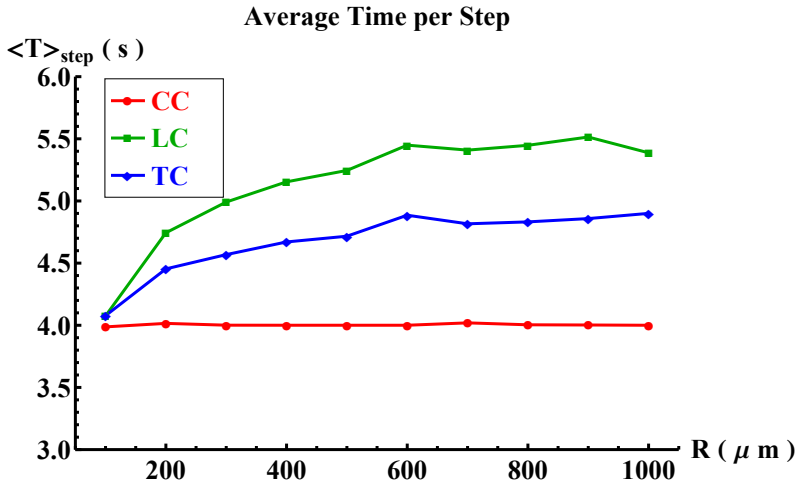


Figure C.2: Average time per propagation step for the bend propagation simulations in WG8A

C.3 Discussion

Implementation and use of the RISSM object is justified by the significant reduction in time required to perform certain operations essential to the calculation of waveguide modes and propagation simulations. With more effort it may be possible to further reduce the amount of calculation time required.

Appendix D

Algorithms

The various algorithms referenced throughout the text are included in this appendix. The algorithms are presented in a language independent form known as pseudo-code.

Algorithm 1 Waveguide discretisation in the horizontal direction

Require: L_x, n_w, W

```
dw ← (W/2)/(n_w − 1) {Compute central node spacing}
lim ← (W/2) + 4dw {Assign limit for uniform node spacing}

{Compute node positions for x ≥ 0}
pos ← 0
xpos.push_back(pos)

while n < n_max do

  if pos < lim then
    pos ← pos + dw {Update position, uniform spacing}
  else
    δ ← 2 dw pos
    pos ← pos + δ {Update position, non-uniform spacing}
  end if

  xpos.push_back(pos) {Store position}

  {Ensure that mesh is defined within limits}
  if pos > L_x/2 then
    break
  end if
end while

npos ←xpos.size()
for i = npos to 1 do
  xnodes.push_back(-xpos[i]) {Store node positions for −(L_x/2) ≤ x ≤ 0}
end for

for i = 2 to npos do
  xnodes.push_back(xpos[i]) {Store node positions for 0 < x ≤ (L_x/2)}
end for

{Update the value of L_x}
L_x ← 2 xnodes.last()

return xnodes[]
```

Algorithm 2 Waveguide discretisation in the vertical direction

Require: L_y, n_e, n_t, E, T

{Compute node spacing in each layer}
$de \leftarrow E/(n_e - 1)$, $dt \leftarrow T/(n_t - 1)$, $d_{max} \leftarrow \max(de, dt)$
$lim \leftarrow E + T + 4\,d_{max}$ {Assign limit for uniform node spacing}
$low \leftarrow -(L_y/2)$, $high \leftarrow (L_y/2)$

$pos \leftarrow 0$ {Compute node positions for $y < 0$}
while $n < n_{max}$ **do**
  $\delta \leftarrow n\,d_{max}$, $pos \leftarrow pos - \delta$
  {Ensure that mesh is defined within limits}
  if $pos < low$ **then**
    break
  else
    yneg.push_back(pos) {Store position}
  end if
end while

$nneg \leftarrow$ yneg.size()

$pos \leftarrow 0$ {Compute node positions for $y \geq 0$}
yplus.push_back(pos)
while $n < n_{max}$ **do**
  if $pos \geq 0$ **and** $pos < T$ **then**
    $pos \leftarrow pos + dt$
  else if $pos \geq T$ **and** $pos < lim$ **then**
    $pos \leftarrow pos + de$
  else
    $\delta \leftarrow 4\,d_{max}\,pos$, $pos \leftarrow pos + \delta$
  end if
  {Ensure that mesh is defined within limits}
  if $pos > high$ **then**
    break
  else
    yplus.push_back(pos) {Store position}
  end if
end while

$nplus \leftarrow$ yplus.size()

for $i = nplus$ **to** 1 **do**
  ynodes.push_back(yplus[i]) {Store node positions for $0 < y \leq (L_y/2)$}
end for

for $i = 1$ **to** $nneg$ **do**
  ynodes.push_back(yneg[i]) {Store node positions for $-(L_y/2) \leq x \leq 0$}
end for

$L_y \leftarrow$ ynodes.first()+fabs(ynodes.last()) {Update the value of L_y}

return ynodes[]

Algorithm 3 Cartesian product to form node array

Require: xnodes[], ynodes[]

```
{Construct a 2D array of node positions from the horizontal and vertical node sets}
N_y ← ynodes.size(), N_u ← xnodes.size()
N_nodes ← N_u N_y
nodearr.nrows ← N_y
nodearr.ncols ← N_u
for s = 1 to N_y do
    for r = 1 to N_u do
        nodearr[s][r] ← node(xnodes[r], ynodes[s])
    end for
end for

{Number each node in the mesh according to (2.8)}
for s = 1 to N_y do
    for r = 1 to N_u do
        nodearr[s][r].global ← (r − 1)N_y + s
    end for
end for
return nodearr[][]
```

Algorithm 4 Construction of the finite element mesh from the node array

Require: nodearr[][]

```
{Start by creating arrays of odd and even numbered elements from the 2D array of node positions}
for r = 1 to N_u do
    for s = 1 to N_y do
        odd.push_back(element(nodearr[s][r],nodearr[s+1][r],nodearr[s][r+1]))

        even.push_back(element(nodearr[s+1][r],nodearr[s+1][r+1],nodearr[s][r+1]))
    end for
end for

{Store the constructed elements in a 1D array}
N_elems ← 2(xnodes.size()-1)(ynodes.size()-1)
themesh.size ← N_elems

for i = 1 to odd.size() do
    themesh[2i-1] ← odd[i] {Store the odd numbered elements}
end for

for i = 1 to even.size() do
    themesh[2i] ← even[i] {Store the even numbered elements}
end for

return themesh[]
```

Algorithm 5 Building the connectivity matrix for a mesh

Require: themesh[]

{Create the connectivity matrix}
cmatrix.nrows $\leftarrow$ N_{elems}, cmatrix.ncols $\leftarrow 3$

for $e = 1$ **to** N_{elems} **do**
    {Each row of cmatrix contains the global numbers of the nodes associated with element e}
    cmatrix[e][1] $\leftarrow$ themesh[e].node(1).global()
    cmatrix[e][2] $\leftarrow$ themesh[e].node(2).global()
    cmatrix[e][3] $\leftarrow$ themesh[e].node(3).global()
end for

return cmatrix[][]

Algorithm 6 Construct the global matrices from the elementary matrices

Require: themesh[], cmatrix[][]

{Compute the elemental matrices K^e and M^e according to (2.30) and (2.31)}
for $e = 1$ **to** N_{elems} **do**
    themesh[e].define_Ke();
    themesh[e].define_Me();
end for

for $e = 1$ **to** N_{elems} **do**
    for $i = 1$ **to** 3 **do**
        $m \leftarrow$ cmatrix[e][i]
        for $j = 1$ **to** 3 **do**
            $n \leftarrow$ cmatrix[e][j]

            K[m][n] $\leftarrow$ K[m][n] + themesh[e].Ke[i][j]

            M[m][n] $\leftarrow$ M[m][n] + themesh[e].Me[i][j]
        end for
    end for
end for

Algorithm 7 Steps in the calculation of the propagation constants and mode profiles of an optical waveguide

Require: Global matrices $\hat{\mathbf{K}}$ and $\hat{\mathbf{M}}$

{Cholesky decompose $\hat{\mathbf{M}}$}
$(\hat{\mathbf{L}}, \hat{\mathbf{L}}^T) \leftarrow$ choldc($\hat{\mathbf{M}}$);

{Invert Cholesky factors}
$(\hat{\mathbf{L}}^{-1}, \hat{\mathbf{L}}^{-T}) \leftarrow$ choldinv($\hat{\mathbf{L}}$, $\hat{\mathbf{L}}^T$);

{Compute the triple product (2.39)}
$rissmLinv \leftarrow$ matrix_to_rissm($\hat{\mathbf{L}}^{-1}$);
$rissmLTinv \leftarrow$ matrix_to_rissm($\hat{\mathbf{L}}^{-T}$);
$rissmK \leftarrow$ matrix_to_rissm($\hat{\mathbf{K}}$);
$\hat{\mathbf{C}} \leftarrow$ compute_triple_product(rissmLinv, rissmK, rissmLTinv);

{Perform Householder reduction on $\hat{\mathbf{C}}$}
tred2($\hat{\mathbf{d}}$, $\hat{\mathbf{e}}$, $\hat{\mathbf{C}}$);

{Diagonalise $\hat{\mathbf{C}}$ using QR method}
tqli($\hat{\mathbf{d}}$, $\hat{\mathbf{e}}$, $\hat{\mathbf{C}}$);

{Sort eigenvalues and eigenvectors by absolute value}
eigsrt($\hat{\mathbf{d}}$, $\hat{\mathbf{C}}$)

{Get the bound state propagation constants}
retrieve_eigvals();

{Compute the bound state mode profiles}
retrieve_eigvecs();

Algorithm 8 Multi-parameter calculation of waveguide properties

{Input waveguide dimensions, material parameters and wavelength}
{Commence loop over the parameters that effect the computational domain}
$L \leftarrow L_{min}$

while $L < L_{max}$ **do**
  {Loop over the length of the domain}

  $n_w \leftarrow n_{min}$

  while $n_w < n_{max}$ **do**
    {Loop over the number of sub-divisions}

    compute_solution(n_w, L)

    $n_w \leftarrow n_w + \Delta n$

  end while

  $L \leftarrow L + \Delta L$

end while

Algorithm 9 Pre-Conditioned Bi-Conjugate Gradient Algorithm for the solution of $\hat{\mathbf{A}} \cdot \mathbf{x} = \mathbf{b}$

print Input, matrix $\hat{\mathbf{A}}$, vector $\mathbf{b}$, initial approximation $\mathbf{x}^{(0)}$,
Pre-Conditioning matrix $\hat{\mathbf{C}}$, tolerance ϵ, max iterations $itmax$

$\mathbf{x}_{old} \leftarrow \mathbf{x}^{(0)}$ {Initialise the approximation}
$\mathbf{r}_{old} \leftarrow \mathbf{b} - \hat{\mathbf{A}}\mathbf{x}_{old}$ {Define initial residual}
$\mathbf{v}_{old} \leftarrow \mathbf{r}_{old}$ {Initialise the search direction to be the direction of steepest}

$k \leftarrow 1$ {Loop control variable}
while $k < itmax$ **do**

  if $k == 1$ **then**
    $\mathbf{w}_{old} \leftarrow \hat{\mathbf{C}}^{-1}\mathbf{r}_{old}$ {Initialise $\mathbf{w}$}
  else
    $\mathbf{w}_{old} \leftarrow \mathbf{w}_{new}$ {Update $\mathbf{w}$ and $\mathbf{v}$}
    $\mathbf{v}_{old} \leftarrow \mathbf{v}_{new}$
  end if

  $t \leftarrow \dfrac{(\mathbf{w}_{old}, \mathbf{w}_{old})}{(\mathbf{v}_{old}, \hat{\mathbf{A}}\mathbf{v}_{old})}$
  $\mathbf{x}_{new} \leftarrow \mathbf{x}_{old} + t\,\mathbf{v}_{old}$ {Compute an approximation for $\mathbf{x}$}
  $\mathbf{r}_{new} \leftarrow \mathbf{r}_{old} - t\,\hat{\mathbf{A}}\mathbf{v}_{old}$ {Update the residual}

  {Check to see if the solution has converged}
  if $||\mathbf{r}_{new}||_{\infty} < \epsilon$ **then**
    print Calculation has converged
  else
    {Continue the iterations}
    $\mathbf{w}_{new} \leftarrow \hat{\mathbf{C}}^{-1}\mathbf{r}_{new}$ {Update $\mathbf{w}$}
    $s \leftarrow \dfrac{(\mathbf{w}_{new}, \mathbf{w}_{new})}{(\mathbf{w}_{old}, \mathbf{w}_{old})}$
    $\mathbf{v}_{new} \leftarrow \hat{\mathbf{C}}^{-T}\mathbf{w}_{new} + s\,\mathbf{v}_{old}$ {Update the search direction $\mathbf{v}$}
    $k \leftarrow k + 1$ {Count iterations}
  end if

end while

Algorithm 10 Steps in the beam propagation algorithm

Require: Waveguide parameters, BC parameters, Propagation parameters

{Build the mesh according to Algorithms 1 - 5}
generate_mesh();

{Define the initial condition}
define_input_field($\hat{\phi}_{old}$, γ);

{Start propagating}
$z \leftarrow 0.0$
for $s = 1$ **to** N_{steps} **do**
  {Define global matrices according to equations (3.39) and (3.40)}
  define_globals();

  {Define propagation constant according to equation (3.28)}
  set_beta();

  {Define the matrices $\hat{\mathbf{A}}$ and $\hat{\mathbf{B}}$ according to (3.23) and (3.24)}
  define_L(); {$\hat{\mathbf{L}} = \hat{\mathbf{K}} - \gamma^2\hat{\mathbf{M}}$}
  define_M2(); {$\hat{\mathbf{M}}_2 = \hat{\mathbf{M}} + (\gamma/4)\hat{\mathbf{L}}$}

  {$\hat{\mathbf{A}} = (2\,i\,\gamma)\hat{\mathbf{M}}_2 - \alpha\,dz\,\hat{\mathbf{L}}$}
  {$\hat{\mathbf{B}} = (2\,i\,\gamma^{old})\hat{\mathbf{M}}_2 + (1\,-\,\alpha)\,dz\,\hat{\mathbf{L}}$}
  define_A_B();

  {Define right hand side vector according to equation (3.22)}
  define_R(); {$\hat{\mathbf{R}} = \hat{\mathbf{B}} \cdot \hat{\phi}_{old}$}

  {Compute $\hat{\phi}_{new}$ by solving $\hat{\mathbf{A}} \cdot \hat{\phi}_{new} = \hat{\mathbf{R}}$}
  $rissmA \leftarrow$ matrix_to_rissm($\hat{\mathbf{A}}$);
  solve_system(rissmA, $\hat{\phi}_{new}$, $\hat{\mathbf{R}}$);

  {Compute power values}
  integrate_mode();

  {Update solution vector for next step}
  $\hat{\phi}_{old} = \hat{\phi}_{new}$

  {Output solution information}
  output_info();

  $z \leftarrow z + dz$
end for

Algorithm 11 Algorithm for computing the coordinates of a continuous curvature bend that replaces an equivalent constant curvature bend

{Input bend radius, bend angle, bend type}
Require: $R \leftarrow R_{bend}$, $T \leftarrow \theta_{bend}$, $BT \leftarrow type$

{If bend type is mode-optimised then curvature data for the bend is required}
Require: $K[] \leftarrow \kappa[]$

{Define the coordinates that make up the equivalent circle}
{This step corresponds to evaluating (4.10) and (4.11) for a circle of radius R, and bend angle θ}
define_eqc_coords()

{Proceed with continuous curvature bend calculation}
$L_{bend} \leftarrow RT$, $L_{bendold} \leftarrow 0.0$
$n_{iter} \leftarrow 1$, $max_{iter} \leftarrow 30$
while $n_{iter} < max_{iter}$ **do**
  {Initialise the convergence condition}
  $L_{bendold} \leftarrow L_{bend}$

  {Evaluate the appropriate integrals depending on the value of BT}
  define_bend_coords()

  {Rescale the coordinate positions if necessary}
  re_scale_coords()

  {Compute the bend length from (4.37)}
  $L_{bend} \leftarrow 0.0$
  for $i = 2$ **to** N **do**
    $L_{bend} \leftarrow L_{bend} + ((X[i] - X[i-1])^2 + (Y[i] - Y[i-1])^2)^{1/2}$
  end for

  {Apply convergence test}
  if $|L_{bend} - L_{bendold}| < \epsilon$ **then**
    print Algorithm has converged
  else
    $n_{iter} \leftarrow n_{iter} + 1$
  end if

end while

{Output the positions of the centre of the bend}
return $X[], Y[]$

Bibliography

[1] L. A. Coldren, S. C. Nicholes, L. Johannsson, S. Ristic, R. S. Guzzon, E. J. Norberg, and U. Krishnamachari, "High Performance InP-Based Photonic ICs-A Tutorial," *J. Lightwave Technol.*, vol. 29, no. 4, pp. 554 – 570, 2011.

[2] A. Biberman, H. L. Lira, K. Padmaraju, N. Ophir, J. Chan, M. Lipson, and K. Bergman, "Broadband silicon photonic electrooptic switch for photonic interconnection networks," *Photon. Technol. Lett.*, vol. 23, no. 8, pp. 504 – 506, 2011.

[3] D. Dai, J. Bauters, and J. E. Bowers, "Passive technologies for future large-scale photonic integrated circuits on silicon: polarization handling, light non-reciprocity and loss reduction," *Nature Light: Science and Application*, vol. 1, pp. 1 – 12, 2012.

[4] Infinera, "Photonic integrated circuits (PICs): Scaling next generation optical networks." `http://www.infinera.com/technology/files/infinera-IEEE-PIC.pdf`.

[5] G. R. Fowles, *"Introduction to Modern Optics"*. Dover, 2^{nd} ed., 1989.

[6] K. Okamoto, *"Fundamentals of Optical Waveguides"*. Elsevier, 2^{nd} ed., 2006.

[7] M. J. Adams, *"An Introduction to Optical Waveguide Theory"*. Wiley, 1981.

[8] S. L. Chuang, *"The Physics of Optoelectronic Devices"*. Wiley Series in Pure and Applied Optics, Wiley, 1995.

[9] J. M. Liu, *"Photonic Devices"*. Cambridge University Press, 2007.

[10] W. A. Gambling, D. N. Payne, and H. Matsumura, "Radiation from curved single mode fibres," *Electron. Lett.*, vol. 12, no. 21, pp. 567 – 569, 1976.

[11] W. A. Gambling and H. Matsumura, "Modes in curved step index optical fibres," *Electron. Lett.*, vol. 13, no. 18, pp. 532 – 535, 1977.

[12] E. G. Neumann, "Curved dielectric optical waveguides with reduced transition losses," *IEE Proc. H (Microwaves, Optics and Antennas)*, vol. 129, no. 5, pp. 278 – 280, 1982.

[13] C. Seo and J. C. Chen, "Low transition losses in bent rib waveguides," *J. Lightwave Technol.*, vol. 14, no. 10, pp. 2255 – 2259, 1996.

[14] E. C. M. Pennings, G. H. Manhoudt, and M. K. Smit, "Low-loss bends in planar optical ridge waveguides," *Electron. Lett.*, vol. 24, no. 16, pp. 998 – 999, 1988.

[15] M. K. Smit, E. C. M. Pennings, and H. Blok, "A normalized approach to the design of low-loss optical waveguide bends," *J. Lightwave Technol.*, vol. 11, no. 11, pp. 1737 – 1742, 1993.

[16] W. Berglund and A. Gopinath, "WKB analysis of bend losses in optical waveguide," *J. Lightwave Technol.*, vol. 18, no. 8, pp. 1161 – 1166, 2000.

[17] D. Dai and S. He, "Analysis of characteristics of bent rib waveguides," *J. Opt. Soc. Am. A*, vol. 21, no. 1, pp. 113 – 121, 2004.

[18] A. W. Snyder and J. D. Love, *Optical Waveguide Theory.* Kluwer Academic Publishers, 1983.

[19] E. A. J. Marcatilli, "Bends in optical dielectric guides," *Bell Syst. Tech. J.*, vol. 48, Sept. 1969.

[20] D. Marcuse, "Bending losses of the asymmetric slab waveguide," *Bell Syst. Tech. J.*, vol. 50, no. 8, pp. 2551 – 2563, 1971.

[21] L. Lewin, "Radiation from curved dielectric slabs and fibers," *IEEE Trans. Microwave Theory Tech.*, vol. MTT-22, pp. 718 – 727, July 1974.

[22] A. W. Snyder and J. D. Love, "Reflection at a curved dielectric interface - electromagnetic tunneling," *IEEE Transaction Microwave Theory Tech.*, vol. MTT-23, no. 1, pp. 134 – 141, 1974.

[23] E. G. Neumann and H.-D. Rudolph, "Radiation from bends in dielectric rod transmission lines," *IEEE Trans. Microwave Theory Tech.*, vol. MTT-23, no. 1, pp. 142 – 149, 1975.

[24] A. W. Snyder, I. White, and D. J. Mitchell, "Radiation from bent optical waveguides," *Electron. Lett.*, vol. 11, no. 15, pp. 332 – 333, 1975.

[25] M. W. Austin, "GaAs/GaAlAs curved rib waveguides," *IEEE J. Quantum Electron.*, vol. QE-18, no. 4, pp. 795 – 800, 1982.

[26] P. C. Kendall, P. N. Robson, and J. E. Stitch, "Rib waveguide curvature loss: the scalar problem," *IEE Proc. J*, vol. 132, no. 2, pp. 140 – 145, 1985.

[27] P. C. Kendall, M. S. Stern, and P. N. Robson, "A new curvature loss formula of Huygens-type for rib waveguides," *IEE Proc. J*, vol. 135, no. 1, pp. 11 – 16, 1988.

[28] A. H. Badar and T. S. M. MacLean, "Transition and pure bending losses in multimode and single-mode bent optical fibres," *IEE Proc.-J*, vol. 138, no. 4, pp. 261 – 268, 1991.

[29] T. Yamamoto and M. Koshiba, "Numerical analysis of curvature loss in optical waveguides by the finite-element method," *J. Lightwave Technol.*, vol. 11, no. 10, pp. 1579 – 1583, 1993.

[30] P. D. Sewell and T. M. Benson, "Efficient curvature analysis of buried waveguides," *J. Lightwave Technol.*, vol. 18, no. 9, pp. 1321 – 1329, 2000.

[31] K. R. Hiremath, M. Hammer, R. Stoffer, L. Prkna, and J. Čtyroký, "Analytical approach to dielectric optical bent slab waveguide," *Opt. Quant. Electron.*, vol. 37, pp. 37 – 61, 2005.

[32] T. N. Trinh and R. Mittra, "Field profile in a single-mode curved dielectric waveguide of rectangular cross section," *IEEE Trans. Microwave Theory Tech.*, vol. MTT - 29, no. 12, pp. 1315 – 1318, 1981.

[33] S. J. Garth, "Mode behaviour on bent planar dielectric waveguides," *IEE Proc. Optoelectronics*, vol. 142, no. 2, pp. 115 – 120, 1995.

[34] M. Heiblum and J. H. Harris, "Analysis of curved optical waveguides by conformal transformation," *IEEE J. Quant. Elecron.*, vol. 11, no. 2, 1975.

[35] D. K. Cheng, *"Field and Wave Electromagnetics"*. Addison Wesley, 1989.

[36] E. A. J. Marcatilli, "Dielectric rectangular waveguide and directional coupler for integrated optics," *Bell Syst. Tech. J.*, vol. 48, 1969.

[37] K. Kawano and T. Kitoh, *"Introduction to Optical Waveguide Analysis"*. Wiley, 2001.

[38] M. Koshiba, H. Saitoh, M. Eguchi, and K. Hirayama, "Simple scalar finite element approach to optical rib waveguides," *IEE Proc.*, vol. 139, no. 2, pp. 166 – 171, 1992.

[39] D. Marcuse, *"Theory of Dielectric Optical Waveguides"*. Academic Press, 1991.

[40] W. H. Press, S. A. Teukolsky, W. T. Vetterling, and B. P. Flannery, *"Numerical Recipes in C"*. Cambridge University Press, 2^{nd} ed., 1992.

[41] M. Abramowitz and I. Stegun, *"Handbook of Mathematical Functions"*. National Bureau of Standards, 1965.

[42] K. Thyagarajan, M. R. Shenoy, and A. K. Ghatak, "Accurate numerical method for the calculation of bending loss in optical waveguides using a matrix approach," *Opt. Lett.*, vol. 12, no. 4, pp. 296 – 298, 1987.

[43] F. Ladouceur and P. Labeye, "A new general approach to optical waveguide path design," *J. Lightwave Technol.*, vol. 13, no. 3, pp. 481 – 492, 1995.

[44] M.-L. Wu, P.-L. Fan, J.-M. Hsu, and C.-T. Lee, "Design of ideal structures for lossless bends in optical waveguides by conformal mapping," *J. Lightwave Technol.*, vol. 14, no. 11, pp. 2604 – 2614, 1996.

[45] P.-L. Fan, M.-L. Wu, and C.-T. Lee, "Analysis of abrupt bent waveguides by the beam propagation method and the conformal mapping method," *J. Lightwave Technol.*, vol. 15, no. 6, pp. 1026 – 1031, 1997.

[46] M. Krause, H. Renner, and E. Brinkmeyer, "Polarization-dependent curvature loss in silicon rib waveguides," *J. Selected Topics Quant. Electron.*, vol. 12, no. 6, pp. 1359 – 1362, 2006.

[47] C. Durniak and J. D. Love, "Bending effects in finite-cladding single-mode slab waveguides," *J. Lightwave Technol.*, vol. 25, no. 11, pp. 3634 – 3640, 2007.

[48] D. M. Shyroki, "Exact equivalent straight waveguide model for bent and twisted waveguides," *IEEE Trans. Microwave Theory Tech.*, vol. 56, no. 2, pp. 414 – 419, 2008.

[49] R. N. Sheehan and F. H. Peters, "Curvature based optimisation of waveguide bends for integrated photonics," Proc. Photonics Ireland, 2007.

[50] R. N. Sheehan and F. H. Peters, "The design of continuous curvature waveguides," Proc. 8^{th} International Conference on Numerical Simulation of Optoelectronic Devices, pp. 27 – 28, 2008.

[51] R. N. Sheehan and F. H. Peters, "Low-loss curved optical waveguide design for integrated photonics," Proc. Photonics Ireland, 2009.

[52] R. N. Sheehan, S. Horne, and F. H. Peters, "The design of low-loss curved waveguides," *Opt. Quant. Electron.*, vol. 40, pp. 1211 – 1218, 2009.

[53] M. J. Ablowitz and A. S. Fokas, *"Complex Variables: Introduction and Applications"*. Cambridge University Press, 1997.

[54] M. R. Spiegel, *"Complex Variables"*. McGraw Hill, 1999.

[55] K. Bierwirth, N. Schulz, and F. Arndt, "Finite-difference analysis of rectangular dielectric waveguide structures," *IEEE Trans. Microwave Theory Tech.*, vol. MTT-34, no. 11, pp. 1104 – 1114, 1986.

[56] C. Vassallo, "Improvement of finite difference methods for step-index optical waveguides," *IEE Proc.-J*, vol. 139, no. 2, pp. 137 – 142, 1992.

[57] J. Yamauchi, M. Sekiguchi, O. Uchiyama, J. Shibayama, and H. Nakano, "Modified finite-difference formula for the analysis of semivectorial modes in step-index optical waveguides," *IEEE Photon. Technol. Lett.*, vol. 9, no. 7, pp. 961 – 963, 1997.

[58] N. Mabaya, P. E. Lagasse, and P. Vandenbulcke, "Finite element analysis of optical waveguides," *IEEE Trans. Microwave Theory Tech.*, vol. 26, no. 6, 1981.

[59] B. M. A. Rahman and J. B. Davies, "Finite-element solution of integrated optical waveguides," *J. Lightwave Technol.*, vol. LT-2, no. 5, pp. 682 – 687, 1984.

[60] K. Hayata, M. Koshiba, and M. Suzuki, "Finite element solution of arbitrarily nonlinear, graded-index slab waveguides," *Electron. Lett.*, vol. 23, no. 8, pp. 429 – 431, 1987.

[61] T. P. Young, "Design of integrated optical circuits using finite-elements," *IEE Proc.*, vol. 135-A, no. 3, pp. 135 – 144, 1988.

[62] K. Hayata, M. Nagai, and M. Koshiba, "Finite-element formalism for nonlinear slab-guided waves," *IEEE Trans. Microwave Theory Tech.*, vol. 36, no. 7, pp. 1207 – 1215, 1988.

[63] G. Strang and G. Fix, *"An Analysis of the Finite Element Method"*. Prentice Hall, 1973.

[64] C. Johnson, *"Numerical Solution of Partial Differential Equations by the Finite Element Method"*. Cambridge University Press, 1987.

[65] C. H. Henry and B. H. Verbeek, "Solution of the scalar wave equation for arbitrarily shaped dielectric waveguides by two-dimensional fourier analysis," *J. Lightwave Technol.*, vol. 7, no. 2, pp. 308 – 313, 1989.

[66] H. Diestel, "A method for calculating the guided modes of strip-loaded optical waveguides with arbitrary index profile," *IEEE J. Quantum Electron.*, vol. QE-20, no. 11, pp. 1288 – 1292, 1984.

[67] P. Bienstman, E. Six, M. Roelens, M. Vanwolleghem, and R. Baets, "Calculation of bending losses in dielectric waveguides using eigenmode expansion and perfectly matched layers," *IEEE Photon. Technol. Lett.*, vol. 14, no. 2, pp. 164 – 166, 2002.

[68] H. Shu and M. Bass, "Calculating the guided modes in optical fibers and waveguides," *J. Lightwave Technol.*, vol. 25, no. 9, pp. 2693 – 2699, 2007.

[69] A. Taflove, *"Computational Electrodynamics: The Finite Difference Time Domain Method"*. Norwood, MA.: Artech House, 1995.

[70] J. Jin, *"The Finite Element Method in Electromagnetics"*. Wiley, 2^{nd} ed., 2002.

[71] G. Golub and C. V. Loan, *"Matrix Computations"*. Johns Hopkins University Press, 1989.

[72] J. D. Faires and R. Burden, *"Numerical Methods"*. Brooks - Cole, 1998.

[73] A. Ralston and P. Rabinowitz, *"A First Course in Numerical Analysis"*. Dover, 2^{nd} ed., 2001.

[74] P. P. Silvester and R. L. Ferrari, *"Finite Elements for Electrical Engineers"*. Cambridge University Press, 1986.

[75] `http://www.rsoftdesign.com/`.

[76] `http://www.photond.com/`.

[77] `http://www.ansys.com/`.

[78] P. E. Morrissey, D. Goulding, R. Sheehan, B. Roycroft, and F. H. Peters, "Experimental technique for quick and efficient lensed fiber to ridge waveguide coupling," *IET Optoelectronics*, vol. 7, no. 2, pp. 57 – 61, 2013.

[79] D. Capper, *"Introducing C++ for Scientists, Engineers and Mathematicians"*. Springer, 2^{nd} ed., 2001.

[80] `http://www.freefem.org/`.

[81] M. D. Feit and J. J. A. Fleck, "Light propagation in graded-index optical fibers," *Appl. Opt.*, vol. 17, no. 24, pp. 3990 – 3998, 1978.

[82] J. V. Roey, J. van der Donk, and P. E. Lagasse, "Beam-propagation method: analysis and assessment," *J. Opt. Soc. Amer.*, vol. 71, no. 7, pp. 803 – 810, 1981.

[83] C. R. Doerr, "Beam propagation method tailored for step-index waveguides," *IEEE Photon. Technol. Lett.*, vol. 13, no. 2, pp. 130 – 132, 2001.

[84] D. Yevick and B. Hermansson, "Split-step finite difference analysis of rib waveguides," *Electron. Lett.*, vol. 25, no. 7, pp. 461 – 462, 1989.

[85] R. Accornero, M. Artiglia, G. Coppa, P. D. Vita, G. Lapenta, M. Potenza, and P. Ravetto, "Finite difference methods for the analysis of integrated optical waveguides," *Electron. Lett.*, vol. 26, no. 23, pp. 1959 – 1960, 1990.

[86] J. Yamauchi, T. Ando, and H. Nakano, "Beam propagation analysis of optical fibres by alternating direction implicit method," *Electron. Lett.*, vol. 27, no. 18, pp. 1663 – 1665, 1991.

[87] W. P. Huang and C. L. Xu, "Simulation of three-dimensional optical waveguides by a full-vector beam propagation method," *IEEE J. Quantum Electron.*, vol. 29, no. 10, 1993.

[88] T. B. Koch, J. B. Davies, F. A. Fernandez, and R. Maerz, "Computation of wave propagation in integrated optical devices using z-transient variational principles," *IEEE Trans. Magnetics*, vol. 27, no. 5, pp. 3876 – 3879, 1991.

[89] F. Schmidt, "An adaptive approach to the numerical solution of fresnel's wave equation," *J. Lightwave Technol.*, vol. 11, no. 9, pp. 1425 – 1434, 1993.

[90] Y. Arai, A. Maruta, and M. Matsuhara, "Transparent boundary for the finite-element beam-propagation method," *Opt. Lett.*, vol. 18, no. 10, pp. 765 – 766, 1993.

[91] M. Koshiba and Y. Tsuji, "A wide-angle finite-element beam propagation method," *IEEE Photon. Technol. Lett.*, vol. 8, no. 9, pp. 1208 – 1210, 1996.

[92] Y. Tsuji and M. Koshiba, "A finite element beam propagation method for strongly guiding and longitudinally varying optical waveguides," *J. Lightwave Technol.*, vol. 14, no. 2, pp. 217 – 222, 1996.

[93] Y. Tsuji, M. Koshiba, and T. Tanabe, "A wide-angle beam propagation method based on a finite element scheme," *IEEE Trans. Magnetics*, vol. 33, no. 2, pp. 1544 – 1547, 1997.

[94] Y. Tsuji, M. Koshiba, and T. Shiraishi, "Finite element beam propagation method for three-dimensional optical waveguide structures," *J. Lightwave Technol.*, vol. 15, no. 9, pp. 1728 – 1734, 1997.

[95] D. Schulz, C. Glingener, M. Bludszuweit, and E. Voges, "Mixed finite element beam propagation method," *J. Lightwave Technol.*, vol. 16, no. 7, pp. 1336 – 1342, 1998.

[96] M. Koshiba, Y. Tsuji, and M. Hikari, "Finite element beam propagation method with perfectly matched layer boundary conditions," *IEEE Trans. Magnetics*, vol. 35, no. 3, pp. 1482 – 1485, 1999.

[97] S. Yoneta, M. Koshiba, and Y. Tsuji, "Combination of beam propagation method and finite element method for optical beam propagation analysis," *J. Lightwave Technol.*, vol. 17, no. 11, pp. 2398 – 2404, 1999.

[98] Y. Tsuji and M. Koshiba, "Finite element beam propagation method with perfectly matched layer boundary conditions for three-dimensional optical waveguides," *Int. J. Numer. Modelling: Electronic Networks, Devices and Fields*, vol. 13, pp. 115 – 126, 2000.

[99] L. Vincetti, A. Cucinotta, S. Selleri, and M. Zoboli, "Three-dimensional finite-element beam propagation method: assessments and developments," *J. Opt. Soc. Amer. A*, vol. 17, no. 6, pp. 1124 – 1131, 2000.

[100] J. S. Gu, P. A. Besse, and H. Melchior, "Method of lines for the analysis of the propagation characteristics of curved optical rib waveguides," *IEEE J. Quantum Electron.*, vol. 27, no. 3, pp. 531 – 537, 1991.

[101] R. Scarmozzino, A. Gopinath, R. Pregla, and S. Helfert, "Numerical techniques for modeling guided-wave photonic devices," *IEEE J. Select. Top. Quantum Electron.*, vol. 6, no. 1, pp. 150 – 162, 2000.

[102] H. Zhang, J. Mu, and W.-P. Huang, "Improved bidirectional beam-propagation method by a fourth-order finite-difference scheme," *J. Lightwave Technol.*, vol. 25, no. 9, pp. 2807 – 2813, 2007.

[103] G. R. Hadley, "Transparent boundary condition for the beam propagation method," *IEEE J. Quant. Electron.*, vol. 28, no. 1, pp. 363 – 370, 1992.

[104] J. P. Bérenger, "A perfectly matched layer for the absorption of electromagnetic waves," *J. Comp. Phys.*, vol. 114, no. 2, pp. 185 – 200, 1994.

[105] W. C. Chew and W. H. Wheedon, "A 3d perfectly matched medium from modified maxwell's equations with stretched coordinates," *Microwave Opt. Technol.*, vol. 7, no. 13, pp. 599 – 604, 1994.

[106] C. M. Rappaport, "Perfectly matched absorbing boundary conditions based on anisotropic lossy mapping of space," *IEEE Microwave and Guided Wave Lett.*, vol. 5, no. 3, pp. 90 – 92, 1995.

[107] $\ddot{U}$. Pekel and R. Mittra, "An application of the perfectly matched layer (pml) concept to the finite element method frequency domain analysis of scattering problems," *IEEE Microwave and Guided Wave Letters*, vol. 5, pp. 258 –260, aug 1995.

[108] W. P. Huang, C. L. Xu, W. Lui, and K. Yokohama, "The perfectly matched layer (pml) boundary condition for the beam propagation method," *IEEE Photon. Technol. Lett.*, vol. 8, no. 5, pp. 649 – 651, 1996.

[109] C. M. Rappaport, "Interpreting and improving the pml absorbing boundary condition using anisotropic lossy mapping of space," *IEEE Trans. Magn.*, vol. 32, no. 3, pp. 968 – 974, 1996.

[110] W. C. Chew, J. Jin, and E. Michielssen, "Complex coordinate stretching as a generalized absorbing boundary condition," *Microwave Opt. Technol.*, vol. 15, no. 6, pp. 363 – 369, 1997.

[111] D. Jiménez, C. Ramírez, F. Pérez-Murano, and A. Guzmán, "Implementation of Bérenger layers as boundary conditions for the beam propagation method: applications to integrated devices," *Opt. Comm.*, vol. 159, pp. 43 – 48, 1999.

[112] S. G. Johnson, "Notes on perfectly matched layers (pmls)." `http://math.mit.edu/~stevenj/`.

[113] G. R. Hadley, "Wide-angle beam propagation using Padé approximant operators," *Opt. Lett.*, vol. 17, no. 20, pp. 1426 – 1428, 1992.

[114] W. P. Huang and H. A. Haus, "A simple variational approach to optical rib waveguides," *IEEE J. lightwave Technol.*, vol. 9, no. 1, pp. 56 – 61, 1991.

[115] C. Seo and Y.-J. Sim, "Optical bent rib waveguide with reduced transition losses," *IEEE Trans. Magn.*, vol. 32, no. 3, pp. 930 – 933, 1996.

[116] M. Majd, B. Schüpert, and K. Petermann, "Low-loss Ti:$LiNbO_3$ waveguide bends prepared by MgO indiffusion," *J. Lightwave Technol.*, vol. 8, no. 11, pp. 1670 – 1674, 1990.

[117] M. Popović, K. Wada, S. Akiyama, H. A. Haus, and J. Michel, "Micron-size bending radii in silica-based waveguides," *Proc. SPIE Integrated Optics: Devices, Materials, and Technologies VI*, pp. 54 – 63, 2002.

[118] W. Bogaerts, D. Taillaert, B. Luyssaert, P. D. J. van Campenhout, P. Bienstman, D. van Thourhout, R. B. V. Wiaux, and S. S. Beckx, "Basic structures for photonic integrated circuits in silicon-on-insulator," *Opt. Express*, vol. 12, no. 8, pp. 1583 – 1591, 2004.

[119] W. Bogaerts, R. Baets, P. Dumon, V. Wiaux, S. Beckx, D. Taillaert, B. Luyssaert, J. V. Campenhout, P. Bienstman, and D. V. Thourhout, "Nanophotonic waveguides in silicon-on-insulator fabricated with CMOS technology," *J. Lightwave Technol.*, vol. 23, no. 1, pp. 401 – 412, 2005.

[120] D. Dai and Y. Shi, "Deeply etched SiO_2 ridge waveguides for sharp bends," *J. Lightwave Technol.*, vol. 24, no. 12, pp. 5019 – 5024, 2006.

[121] C. Koos, C. G. Poulton, L. Zimmermann, L. Jacome, J. Leuthold, and W. Freude, "Ideal bend contour trajectories for singlemode operation of lowloss overmoded waveguides," *Photon. Technol. Lett.*, vol. 19, no. 11, pp. 819 – 821, 2007.

[122] A. Melloni, P. Monguzzi, R. Costa, and M. Martinelli, "Design of curved waveguides: the matched bend," *J. Opt. Soc. Amer. A*, vol. 20, no. 1, pp. 130 – 137, 2003.

[123] A. Melloni, G. Cusmai, and M. Martinelli, "Experimental confirmation of matched bends," *Opt. Lett.*, vol. 29, no. 5, pp. 465 – 467, 2004.

[124] W. Yuan and D. C. Hall, "A general scaling rule for matched bend waveguides," *J. lightwave Technol.*, vol. 29, no. 4, pp. 3786 – 3796, 2011.

[125] W. Yuan, C. S. Seibert, and D. C. Hall, "Single facet teardrop laser with matched-bends design," *IEEE J. Selected Topics Quant. Electron.*, vol. 17, no. 6, pp. 1662 – 1669, 2011.

[126] D. Marcuse, "Length optimization of an S-shaped transition between offset optical waveuides," *Appl. Opt.*, vol. 17, no. 5, pp. 763 – 768, 1978.

[127] R. Baets and P. E. Lagasse, "Loss calculation and design of arbitrarily curved integrated-optic waveguides," *J. Opt. Soc. Am.*, vol. 73, no. 2, pp. 177 – 182, 1983.

[128] L. Lerner, "Minimum bending loss interconnection for integrated optics waveguides," *Electron. Lett.*, vol. 29, no. 9, pp. 733 – 735, 1993.

[129] Y. Y. Lu and P. L. Ho, "Beam propagation modeling of arbitrarily bent waveguides," *IEEE Photon. Technol. Lett.*, vol. 14, no. 12, pp. 1698 – 1700, 2002.

[130] Y. Y. Lu and Y. Y. Lu, "Computing optimal waveguide bends with constant width," *J. Lightwave Technol.*, vol. 25, no. 10, pp. 3161 – 3167, 2007.

[131] M. K. Smit and C. van Dam, "PHASAR-based WDM devices: Principles, design and applications," *IEEE Selected Topics in Quant. Electron.*, vol. 2, no. 2, 1996.

[132] D. P. P. Muñoz and J. Capmany, "Modeling and design of arrayed waveguide gratings," *J. Lightwave Technol.*, vol. 20, no. 4, 2002.

[133] T. Chen, H. Lee, J. Li, , and K. J. Vahala, "A general design algorithm for low optical loss adiabatic connections in waveguides," *Opt. Express*, vol. 20, no. 20, pp. 22819 – 22829, 2012.

[134] M. Cherchi, S. Ylinen, M. Harjanne, M. Kapulainen, and T. Aalto, "Dramatic size reduction of waveguide bends on a micron-scale silicon photonic platform," *Opt. Expr.*, vol. 21, no. 15, pp. 17814 – 17823, 2013.

[135] D. J. Struik, *"Lectures on Classical Differential Geometry"*. Dover, 1988.

[136] D. Zwillinger, *"CRC Standard Mathematical Tables and Formulae"*. CRC Press, 31^{st} ed., 2003.

[137] M. Rivera, "A finite difference bpm analysis of bent dielectric waveguides," *J. Lightwave Technol.*, vol. 13, pp. 233 – 238, 1995.

[138] P. E. Morrissey, W. Cotter, J. O'Callaghan, H. Yang, B. Roycroft, D. Goulding, B. Corbett, and F. H. Peters, "Multiple coherent outputs from single growth monolithically integrated injection locked tunable lasers," *International Conf. Indium Phosphide and Related Materials*, pp. 281 – 284, 2012.

[139] H. Yang, P. Morrissey, W. Cotter, C. L. M. Daunt, J. O'Callaghan, B. Roycroft, N. Ye, N. Kelly, B. Corbett, and F. H. Peters, "Monolithic integration of single facet slotted laser, soa, and mmi coupler," *IEEE Photon. Technol. Lett.*, vol. 25, no. 3, pp. 257 – 260, 2013.